THE UNIVERSITY
of EDINBURGH

Mapping the lifetime of PSD95 at single-synapse resolution across the mouse brain in health and disease

Edita Bulovaitė

Ph.D. Thesis

The University of Edinburgh

2021

Declaration

I declare that this thesis and the work described herein is my own unless indicated otherwise and has not been submitted for any other degree.

Edita Bulovaitė

October 2021

Acknowledgements

Firstly, I would like to thank my supervisor Prof Seth Grant for providing me with an opportunity to learn from him and for believing in my abilities. Thank you for giving me the challenge to develop and carry out this project. I would also like to thank my thesis committee, Prof Michael Cousin and Prof Paul Skehel, for your impartial advice and support throughout my PhD.

I owe a big thank you to Dr Malik Yousuf and Prof Erik Fransén for the friendship, advice and guidance in my PhD and the most exciting and heated scientific discussions I have had to date. Additional thank you to Malik for being there for me both, at good times and at times I struggled. Thank you to Dr Noboru Komiyama for all the advice and interesting scientific discussions. I would like to thank Dr Mathew Horrocks for getting me involved in fun side projects and supporting my microscope building workshop idea and implementation. I would also like to thank Prof Rob Phillips for inspiring me to think creatively about science and encouraging to try out solving problems that I never thought I had the skills to solve.

I would like to thank Prof Margarete Heck, Prof Karen Chapman and Prof Patrick Hadoke for all your help and incredible support, without which I likely would not be here today.

Thank you, Bev Notman, Will Mungall and Theresa Wong for your friendship and lab assistance throughout my PhD. Thank you for being such wonderful people! I would like to thank all members of the Grant Lab, past and present: Dr Zhen Qiu, Dr Ragini Gokhale, Dr Babis Koniaris, Adrianna Zgraj, Dr Emma Sigfridsson, Dimitra Koukaroudi, Gabor Varga, Dr Rand Dahan, Dr Sarah Lempriere, Cathy McLaughlin, Dr Colin Davey and others. Thank you to Dr Marc Vendrell, Dr Lorena Tapia Mendive and Dr Fabio De Moliner for your help with the chemistry of dye coupling and for your patience with my never-ending questions.

I owe a big thank you to Dhanya Baird for being a wonderful friend. Our conversations, adventures and creative endeavours is what kept me sane these past four years.

I would like to thank my parents, Meilutė and Arnoldas, my brother Edvardas, and my grandparents Danutė Misevičienė, Onutė Bulovienė and Virgilijus Bulovas for your patience, support and love. Thank you to my puppies, Juta and Haikis, for their affection and ability to make me laugh. Thank you to my ladies, Burbulė and Bunzulė, who greatly assisted me in painful times of thesis writing and are wonderful little friends.

I would like to dedicate this thesis to my grandpa Jonas Misevičius, the greatest friend I ever had. I miss you very much.

List of Figures

List of Tables

Abbreviations

18M	18-month-old
2P microscopy	Two-photon excitation microscopy
3M	3-month-old
3W	3-week-old
95% CI	95% confidence interval
ACB	Nucleus accumbens
ACN	Acetonitrile
Adam 22	ADAM metallopeptidase domain 22
AKAP79/150	A-kinase-anchoring protein 79/150
Ala	Alanine (symbol A)
AMPA	α-amino-3-hydroxy-5-methyl-4-isoxazole propionic acid
AMPAR	α-amino-3-hydroxy-5-methyl-4-isoxazole propionic acid receptor
ANcr2gr	Crus 2, granular layer
ANcr2mo	Crus 2, molecular layer
AON1	Anterior olfactory nucleus, layer 1
AON2	Anterior olfactory nucleus, layer 2
APN	Anterior pretectal nucleus
Arc	Activity-regulated cytoskeleton-associated protein
Arg	Arginine, also known as l-arginine (symbol R)
ASD	Autism spectrum disorder
Asp	Aspartic acid (symbol D)
ATP	Adenosine triphosphate
BBB	Blood-brain-barrier
BIC	Bicuculline
C2 domain	Ca2+-dependent membrane-targetting module
CA1	Cornu Ammonis 1
CA1slm	Field CA1, stratum lacunosum-moleculare
CA1so	Field CA1, stratum oriens
CA1sp	Field CA1, pyramidal layer
CA1sr	Field CA1, stratum radiatum
CA2	Cornu Ammonis 2

CA2slm	Field CA2, stratum lacunosum-moleculare
CA2so	Field CA2, stratum oriens
CA2sp	Field CA2, pyramidal layer
CA2sr	Field CA2, stratum radiatum
CA3	Cornu Ammonis 3
CA3slm	Field CA3, stratum lacunosum-moleculare
CA3slu	CA3 stratum lucidum
CA3so	Field CA3, stratum oriens
CA3sp	Field CA3, pyramidal layer
CA3sr	Field CA3, stratum radiatum
CamKII	Calcium/calmodulin-dependent protein kinase II
CASK	Calcium/calmodulin dependent serine protein kinase
CB	Cerebellum
CDK-5	Cyclin dependent kinase 5
CDKL5	Cyclin dependent kinase like 5
CENT3gr	Lobule III, granular layer
CENT3mo	Lobule III, molecular layer
CLA	Claustrum
COPYgr	Copula pyramidis, granular layer
COPYmo	Copula pyramidis, molecular layer
CP	Caudoputamen
CSU	Confocal spinning disc unit
CTX	Isocortex
CTXsp	Cortical subplate
CUL4,5gr	Lobules IV-V, granular layer
CUL4,5mo	Lobules IV-V, molecular layer
CYFIP1	Cytoplasmic FMR1 interacting protein 1
DABCO	1,4-diazobicyclo-[2.2.2]-octane
DCM	Dichloromethane
ddH2O	Double-distilled water
DG-mo	Dentate gyrus, molecular layer
DG-po	Dentate gyrus, polymorph layer
DG-sg	Dentate gyrus, granule cell layer
DIPEA	N,N-diisopropylethylamine

DLG	Discs large
DMF	Dimethylformamide
DMSO	Dimethyl sulfoxide
DNA	Deoxyribonucleic acid
E.coli	*Escherichia coli*
E3.5	Embryonic day 3.5
EE	Environmental enrichment
eGFP	Enhanced green fluorescent protein
EM gain	Electron-multiplying gain
EMCCD camera	Electron-multiplying CCD camera
EPd	Endopiriform nucleus, dorsal part
EPSC	Excitatory postsynaptic current
ES cells	Embryonic stem cells
fEPSP	Field excitatory postsynaptic potential
Fmr1	Fragile X mental retardation 1, a gene that encodes FMRP protein
FMRP	Fragile X mental retardation protein
FRAP	Fluorescence recovery after photobleaching
FRP1	Frontal pole, layer 1
FRP2-3	Frontal pole, layer 2/3
FS	Fundus of striatum
FTD	Frontotemporal dementia
GABAA	γ-aminobutyric acid type A
GAP domain	GTPase activating protein domain
GK	Guanylate kinase-like domain
GKAP/SAPAP	Guanylate kinase-associated protein / SAP90/PSD95 associated protein
Gly	Glycine (symbol G)
GPi	Globus pallidus, internal segment
HD	Huntington's disease
HPF	Hippocampal formation
HPLC	High-performance liquid chromatography
HY	Hypothalamus
IC	Inferior colliculus
ID	Intellectual disability

IP	Interposed nucleus
IV injection	Intravenous injection
JF526	Janelia Fluor 526
JF549	Janelia Fluor 549
JF646	Janelia Fluor 646
KCl	Potassium chloride
KI	Knock-in
Kir2.3	Potassium inwardly rectifying channel
KO	Knock out
LD	Lateral dorsal nucleus of the thalamus
Leu	Leucine (symbol L)
LHA	Lateral hypothalamic area
LoxP	Locus of X-over P1
LP	Lateral posterior nucleus of the thalamus
LPL	Long protein lifetime
LTP	Long-term potentiation
Lys	Lysine (symbol K)
MA	Magnocellular nucleus
MAGUK	Membrane-associated guanylate kinase
MB	Midbrain
Mdm2	Mouse double minute 2 homolog
MECP2	Methyl-CpG-binding protein 2
MeOH	Methanol
Met	Methionine (symbol M)
mGluR	Metabotropic glutamate receptor
mKO2	Monomeric kusabira-orange 2 fluorescent protein
MO1	Somatomotor areas, layer 1
MO2-3	Somatomotor areas, layer 2/3
MO5	Somatomotor areas, layer 5
MO6a	Somatomotor areas, layer 6a
MO6b	Somatomotor areas, layer 6b
MOBgl	Main olfactory bulb, glomerular layer
MOBgr	Main olfactory bulb, granule layer
MOBipl	Main olfactory bulb, inner plexiform layer

MOBmi	Main olfactory bulb, mitral layer
MOBopl	Main olfactory bulb, outer plexiform layer
MOWIOL	Poly(vinyl alcohol)
MRN	Midbrain reticular nucleus
mRNA	Messenger ribonucleic acid
MY	Medulla
Nedd8	Neural precursor cell-expressed developmentally regulated gene 8
NLGN-3	Neuroligin-3
NMDA	N-methyl-D-aspartate
NMDAR	N-methyl-D-aspartate receptor
nNOS	Neuronal nitric oxide synthase
NO	Nitric oxide
NOT	Nucleus of the optic tract
OCT	Optimal cutting temperature compound
OLF	Olfactory areas
ORB1	Orbital area, layer 1
ORB2-3	Orbital area, layer 2/3
ORB5	Orbital area, layer 5
ORB6a	Orbital area, layer 6a
ORB6b	Orbital area, layer 6b
OT1	Olfactory tubercule, molecular layer
OT2	Olfactory tubercule, pyramidal layer
OT3	Olfactory tubercule, polymorph layer
P	P-value
P	Pons
P11-13	Postnatal day 11-13
P14-16	Postnatal day 14-16
P8-10	Postnatal day 8-10
PAL	Pallidum
Par1	Protease-activated receptor 1
PBS	Phosphate buffered saline
PCR	Polymerase chain reaction
PDZ domain	PSD95/Dlg/ZO-1 domain

PEST domain	Domain rich in proline (P), glutamic acid (E), serine (S) and threonine (T).
PFA	Paraformaldehyde
Phe	Phenylalanine (symbol F)
PIR1	Piriform area, molecular layer
PIR2	Piriform area, pyramidal layer
PIR3	Piriform area, polymorph layer
PO	Posterior complex of the thalamus
PP1	Protein phosphatase 1
PPN	pedunculopontine nucleus
PPT	Posterior pretectal nucleus
PRMgr	Paramedian lobule, granular layer
PRMmo	Paramedian lobule, molecular layer
PSD93	Postsynaptic density protein 93
PSD95	Postsynaptic density protein 95
PTLp1	Posterior parietal association areas, layer 1
PTLp2-3	Posterior parietal association areas, layer 2/3
PTLp4	Posterior parietal association areas, layer 4
PTLp5	Posterior parietal association areas, layer 5
PTLp6a	Posterior parietal association areas, layer 6a
PTLp6b	Posterior parietal association areas, layer 6b
PTM	Post-translational modification
PyBOP	Benzotriazol-1-yl-oxytripyrrolidinophosphonium hexafluorophosphate
R	Correlation coefficient
Rap	Ras proximate family of proteins
Ras	Rat sarcoma virus family of proteins
Ribo-seq	Ribosome profiling
RNA	Ribonucleic acid
RNAi	RNA interference
ROI	Region of interest
RR	Midbrain reticular nucleus, retrorubral area
RSPd1	Retrosplenial area, dorsal part, layer 1
RSPd2-3	Retrosplenial area, dorsal part, layer 2/3
RSPd5	Retrosplenial area, dorsal part, layer 5

RSPv1	Retrosplenial area, ventral part, layer 1
RSPv2-3	Retrosplenial area, ventral part, layer 2/3
RSPv5	Retrosplenial area, ventral part, layer 5
RSPv6a	Retrosplenial area, ventral part, layer 6a
RT	Reticular nucleus of the thalamus
RT	Room temperature
SAP102	Synapse associated protein 102
SAP97	Synapse associated protein 97
SCm	Superior colliculus, motor related
SCs	Superior colliculus, sensory related
SD	Standard deviation
SDS PAGE	Sodium dodecyl sulphate-polyacrylamide gel electrophoresis
SeNBD	Selenium-nitrobenzodioxazole
sEPSC	Spontaneous excitatory postsynaptic current
Ser	Serine (symbol S)
SH3	Src Homology 3
Shank	SH3 and multiple ankyrin repeat domains protein
SI	Substantia innominata
SILAC	Stable isotope labeling by amino acids in cell culture
SIMgr	Simple lobule, granular layer
SIMmo	Simple lobule, molecular layer
SiR	Silicon-rhodamine
SiR-COOH	Silicon-rhodamine carboxylic acid
SNc	Substantia nigra, compact part
SNr	Substantia nigra, reticular part
SPAR	Spine-associated Rap-specific GTPase-activating protein
SPFp	Subparafascicular nucleus, parvicellular part
SPL	Short protein lifetime
SS1	Somatosensory areas, layer 1
SS2-3	Somatosensory areas, layer 2/3
SS4	Somatosensory areas, layer 4
SS5	Somatosensory areas, layer 5
SS6a	Somatosensory areas, layer 6a
SS6b	Somatosensory areas, layer 6b

STN	Subthalamic nucleus
STR	Striatum
SUB	Subiculum
SynGAP	Synaptic Ras GTPase activating protein
SynMAP	Synaptome mapping pipeline
SZ	Schizophrenia
TARP	Transmembrane AMPA receptor regulatory protein
TH	Thalamus
Thr	Threonine (symbol T)
TLC	Thin-layer chromatography
TMR	Tetra-methyl-rhodamine
Tris	Tris(hydroxymethyl)aminomethane
TTX	Tetrodotoxin
Tween	Polyoxyethylene sortbitol ester
Ube3A	Ubiquitin-protein ligase E3A
Val	Valine (symbol V)
VGlut1	Vesicular glutamate transporter 1
VIS1	Visual areas, layer 1
VIS2-3	Visual areas, layer 2/3
VIS4	Visual areas, layer 4
VIS5	Visual areas, layer 5
VIS6a	Visual areas, layer 6a
VIS6b	Visual areas, layer 6b
VPL	Ventral posterolateral nucleus of the thalamus
VPM	Ventral posteromedial nucleus of the thalamus
WT	Wild type
ZI	Zona incerta
β-gal	Beta-galactosidase

Abstract

A continuous renewal of synaptic proteins is required for healthy functioning and activity-dependent synapse adaptations in the brain. Disruptions to protein turnover lead to impairments in learning and memory and contribute to age-related cognitive decline and dementia. Protein turnover is thought to be tightly regulated in space and time, however, no technology to date has been able to visualise protein turnover and lifetime at individual synapses across the brain. In this thesis, we present insights into the architecture and temporal changes to the lifetime of an abundant post-synaptic density scaffolding protein PSD95 at single-synapse resolution using a newly developed method.

Transgenic mice carrying a HaloTag domain fused to the endogenous PSD95 protein were intravenously injected with a fluorescent ligand that covalently binds the HaloTag domain. Fluorescent protein levels were visualized in brain sections using confocal microscopy, with loss of fluorescence over time used for estimating PSD95 protein decay. We employed Synaptome mapping pipeline to quantify the changes in numbers and morphological parameters of synaptic puncta. We performed a detailed examination of: (a) the lifetime of PSD95 in synapses of 110 brain regions, (b) the changes in protein lifetime with age of an animal, and (c) the effects of disease-relevant mutations in PSD95-interacting synaptic proteins on the turnover and lifetime of PSD95.

Strikingly, a vast majority of PSD95 protein in synapses is replaced within two weeks and the synapses with longer lived protein reside in cortical and hippocampal brain regions, areas involved with long-term memory storage. PSD95-positive puncta half-life ranges more than 6-fold between brain regions in adult mice, from ~1-2 days in olfactory bulb and thalamic nuclei to ~10-12 days in the superficial layers of the cortex.

PSD95 lifetime increases with age across the brain and the protein lasts at least twice as long in synapses of ageing 18-month-old animals compared to synapses in developing 3-week-old mice. Between developing and adult brain, the most striking changes in turnover are observed in the cortical brain areas

which are known to undergo extensive synaptic pruning and remodelling during the first month of life in mice. With ageing, the largest increase in protein lifetime is detected in cerebellar areas.

Disease-relevant mutations in post-synaptic density proteins interacting with PSD95 showed differing effects on PSD95 lifetime. The mice carrying a schizophrenia- and autism-relevant deletion of a gene that codes for PSD93 protein showed a substantially increased lifetime of PSD95 compared to wild-type animals, with a gene dose-dependent effect. In contrast, mice carrying an autism and intellectual disability-relevant mutation in a gene coding for SynGAP protein showed minor changes to PSD95 turnover displaying the sensitivity of the method to detect disease-specific effects on protein turnover and lifetime.

In summary, synapse protein dynamics show a conserved spatial architecture with longest protein lifetime observed in regions involved with memory storage. Age-related increase in protein lifetime may contribute to memory impairments and dementia risk. The atlas of synaptic protein lifetimes will serve as a novel resource with applications in molecular neuroscience and brain disease research.

Lay Summary

The proteins in connection sites between nerve cells need to be replaced with new on a regular basis in order to support healthy functioning of the brain. When proteins stay for too long or too short at the connection sites, called synapses, our ability to learn and remember becomes impaired and can lead to dementia and other brain diseases.

In this thesis, we present a novel technology allowing us to visualize the dynamics of synapse proteins across the whole brain which was never before possible. We have mapped protein dynamics across 110 brain regions and show that, on average, we replace most of our synapse proteins every couple of weeks. We find that proteins last the longest in synapses in brain regions that process and store our memories. Protein dynamics slow down drastically with age which may explain more frequent memory problems in the elderly. Our results also indicate that genetic mutations that cause Schizophrenia make proteins stay for too long in synapses which may influence the ability to efficiently learn new information in Schizophrenic patients.

Our results highlight the important aspects of synapse protein dynamics and their relevance to disease and ageing. The comprehensive maps of whole brain synapse protein dynamics will become a useful resource for researchers working on synapse biology and brain disorders.

Contents

Chapter 1 Introduction

1.1 Protein turnover

1.1.1 "The dynamic state of body constituents"

Up until late 1930s, living organisms were assumed to be like stable chemical engines, burning exogenous fuels but not undergoing metabolic transformations (Schoenheimer, 1942, Goldberg and Dice, 1974, Hawkins, 1991). The shift in thinking came when Schoenheimer and colleagues for the first time showed that fatty acids, building blocks of fat, when fed to adult mice get incorporated into fat tissues of the body instead of being used up for energy and excreted (Schoenheimer, 1942, Rittenberg and Schoenheimer, 1937). Schoenheimer was able to detect exogenously supplied fatty acids by pioneering the use of heavy isotope labelling of organic compounds and in this study labelled fatty acids with a heavy isotope deuterium. The evidence for continuous replacement of body constituents was strengthened by the fact that the overall weight of fat tissue did not change after feeding isotope-labelled fatty acids suggesting that old fatty acids in the body got replaced by new (Schoenheimer, 1942, Rittenberg and Schoenheimer, 1937). The studies of metabolism were soon expanded into the field of proteins and protein turnover to show that proteins, too, incorporate isotope-labelled amino acids fed to adult mice (Ratner et al., 1940, Schoenheimer, 1942). In his last book Schoenheimer coins the term "the dynamic state of body constituents" that goes on to fuel future research into the continual renewal and remodeling of living things.

1.1.2 Definitions: protein turnover and half-life

Before proceeding into interesting aspects of protein turnover, several terms should be defined to avoid future confusion:

- Protein synthesis refers to the ribosome-mediated assembly of amino acids as guided by a protein-specific mRNA sequence.
- Protein degradation refers to the reduction of protein into its constituent amino acids. Protein degradation may occur via two major pathways: ubiquitin-proteasome system (UPS) and autophagy.

- Protein turnover is the balance between protein synthesis and degradation.
- Half-life is the average time it takes for a quantity to reduce to half of its original value.

Previous studies have often referred to protein turnover when describing the movement or redistribution of molecules within a cellular compartment, inactivation of protein by posttranslational modifications or the turnover of whole cells. In this thesis, protein turnover will strictly refer to the processes of synthesis and degradation of proteins.

1.1.3 Relationship between protein synthesis and degradation

Maintaining a set rate of protein turnover and a consistent protein lifetime requires coordinated actions of protein synthesis and degradation machineries. Franklin and Johnson (1998) observed that inhibiting protein synthesis rate by a specific percentage with protein synthesis inhibitors led to an almost equivalent percentage reduction in the rate of protein degradation. Similarly, when protein degradation was inhibited with inhibitors of proteasome activity, a coordinated reduction in protein synthesis was observed (Alvarez-Castelao et al., 2020). While the detailed mechanism of the relationship or coupling of protein synthesis and degradation is not yet known, several molecular interactions linking the two processes have now been identified. Protein translation initiation factor eIF3 was found to interact with proteasomal subunit 19S as revealed by affinity purification of eIF3 protein complexes in yeast (Sha et al., 2009). Another regulator of protein translation initiation, eIF2$\boldsymbol{\alpha}$, was found to undergo increased phosphorylation in response to inhibition of proteasomal activity (Alvarez-Castelao et al., 2020). Heme-regulated inhibitory kinase (HRI) facilitated the phosphorylation of eIF2$\boldsymbol{\alpha}$ resulting in downregulation of protein synthesis. A recent study by Pandey et al. (2021) revealed a link between protein degradation via autophagy pathway and protein synthesis. The inhibitory avoidance learning task in rats led to upregulation in autophagy and lysosomal degradation proteins which was not

due to increased levels of the mRNA of these proteins but was fuelled by increased translation of the already existing mRNAs.

Tight coupling of protein synthesis and degradation machineries might be particularly important for removal of misfolded or otherwise defective newly made proteins. Over 30% of newly synthesized proteins get rapidly degraded due to defects in their structure, and close physical proximity of ribosome and proteasome may be needed for quick and effective degradation (Schubert et al., 2000, Sha et al., 2009). Future studies should aim to further dissect the molecular mechanisms that couple protein synthesis and degradation pathways, assess their interaction, and investigate whether there are different coupling mechanisms for regulating the lifetime of healthy versus defective proteins.

1.1.4 Possible physiological roles of protein turnover

Protein turnover has been shown to occur in eukaryotes and prokaryotes, all tissues, cell types and proteins (Ross et al., 2021, Hinkson and Elias, 2011, Hawkins, 1991). Since protein turnover is an energetically expensive process (Hawkins, 1991, Bier, 1999), there must be an evolutionary advantage to continuously degrading and replacing cellular proteins. While the precise role of protein turnover is not yet known, several potential benefits of the process are described below.

1.1.4.1 Removal of abnormal proteins

Protein turnover is important for removal of aberrantly folded or faulty proteins (Goldberg and Dice, 1974, Santra et al., 2019). While protein translation is a highly accurate process (error rate only one per 10^3-10^4 codons), occasional mistakes that are left unfixed result in faulty proteins that cause cytotoxicity in the cell and need to be promptly degraded (Drummond and Wilke, 2008, Ogle and Ramakrishnan, 2005, Bucciantini et al., 2002). Some of the mutant proteins also tend to misfold and aggregate causing aberrant protein deposits well-documented in neurodegenerative diseases such as Alzheimer's, Parkinson's and Huntington's disease (Soto and Pritzkow, 2018, Hartl, 2017). Proteolytic machinery in cells quickly responds to such mutated and misfolded

proteins and selectively degrades them (Goldberg, 2003, Goldberg, 1972, Hanna et al., 2019). The feature of aberrant protein degradation is particularly important for non-dividing cells, such as neurons, which cannot dilute the concentration of faulty proteins by cell division (Goldberg and Dice, 1974).

1.1.4.2 Adaptation to changing environment

Continuous turnover of proteins may contribute to organism's ability to adapt to changes in its environment. Adaptation to environmental changes often occurs through upregulation of specific molecular pathways or increased synthesis of protective enzymes (Bleuven and Landry, 2016). The rate at which these adaptations occur at least in part depends on the turnover rate of molecular components involved (Berlin and Schimke, 1965). Studies looking into the responses of rat liver enzymes to cortisone administration have pointed out the positive relationship between the rate of enzyme turnover and the rate at which the concentration of the enzyme can change in response to stimulation (Berlin and Schimke, 1965). Enzymes that turn over faster were able to adjust their concentration to hormonal stimulation quicker compared to slower turning over enzymes. Interestingly, enzymes involved in rate-limiting or catalytic reactions were shown to have shorter lifetimes compared to those involved in regulatory activity (Martin-Perez and Villén, 2017, Goldberg and Dice, 1974, Berlin and Schimke, 1965). Rapid upregulation or downregulation of catalytic enzymes would be important for initiating biochemical reactions in response to changes in environment.

Protein turnover must be particularly important when an organism attempts to adapt to poor environments or lack of nutrients. Rates of protein turnover have been shown to increase with starvation or changes in diet, activity and cellular environment (Schimke and Doyle, 1970, Martin-Perez and Villén, 2017, Heo et al., 2018b, Fornasiero et al., 2018). In such cases, upregulation of protein turnover may be useful for providing essential amino acids for the synthesis of required proteins (Schimke and Doyle, 1970).

1.1.4.3 Energy reservoir

To follow on from the points above, protein turnover can help organisms withstand difficult times such as starvation (Goldberg and Dice, 1974). Carbohydrates and fats are preferentially utilised for energy in cells, but when the intake of glucose and fatty acids is insufficient, amino acids get broken down for emergency energy (Hayamizu, 2017, Felig et al., 1969, Goldberg and Dice, 1974). In such cases, protein degradation and turnover would allow the organism to rapidly mobilize and supply protein resources.

1.1.5 Factors influencing protein turnover

Protein turnover and lifetime can be affected by a number of factors, some inherent to the amino acid sequence and protein structure while others imposed by the external environment. Some of the experimentally identified relationships between protein lifetime and intrinsic and extrinsic factors are described below.

1.1.5.1 Intrinsic factors

1.1.5.1.1 Protein structure and conformation

Proteins that fail to fold properly or have large exposed disordered regions tend to be preferentially targeted for degradation (Needham et al., 2019, Fishbain et al., 2015, van der Lee et al., 2014, Goldberg, 1972). Studies have found that in cases of premature termination of protein translation, frequent errors in translation or substitution of amino acids with their analogs can all affect protein lifetime (Goldberg, 1972). *E. coli* cells treated with puromycin, an agent that causes premature polypeptide chain termination by getting incorporated into the translated protein, show substantially increased protein degradation. Cells in which frequent mistranslation is common due to ribosomal protein ram1 mutation, also display shortened protein lifetimes. Similar situation is seen when amino acid analogs get incorporated into newly translated proteins. All of these modifications are thought to cause conformational changes or misfolding of the proteins thus promoting their degradation.

Even in cases of healthy and unmutated proteins, inappropriate folding or large sequences of disorder lead to premature protein degradation. While

information for protein's tertiary structure is contained within amino acid sequence, the exposure to cytosolic environment, as happens when the protein is being translated, can often interfere with folding of the peptide. Molecular chaperones help proteins through the folding and maturation process but are also there to detect the proteins that fail to fold (Needham et al., 2019). Chaperones recognize the surface-exposed hydrophobic sequences that should be hidden within the protein and initiate ubiquitination of the peptide. An internal disordered sequence is also essential for proteasome docking (Fishbain et al., 2015). In proteins that lack disordered regions, or such regions are not big enough for the proteasome to dock, the degradation does not proceed.

1.1.5.1.2 Accessible surface area

Several studies have pointed to the relationship between protein size and its half-life (Fornasiero et al., 2018, Miller et al., 1987, Goldberg and Dice, 1974). Large proteins tend to have bigger surface areas exposed to the cytosol which correlates positively with susceptibility to quicker degradation (Fornasiero et al., 2018). Interestingly, when proteins are assembled into oligomers or protein complexes, their accessible surface area tends to decrease thus increasing protein stability (Buchler et al., 2005, Miller et al., 1987).

1.1.5.1.3 N-terminus amino acid

The presence of certain amino acids in the N-terminus of a protein has been found to correlate with rapid turnover and short lifetime of the protein (Bachmair et al., 1986, Gawron et al., 2016, Martin-Perez and Villén, 2017). Bachmair et al. (1986) directly tested the role of amino acids at the N-terminus of the protein by constructing a gene in which yeast ubiquitin was linked to βgal of *Escherichia coli* and expressed in yeast cells. Through site-directed mutagenesis the researchers exchanged the original ATG codon at the ubiquitin-βgal junction into codons specifying 15 other amino acids and examined the lifetime of modified βgal protein in yeast after the original deubiquitination. Proteins with Arg, Lys, Phe, Leu, or Asp at the N-terminus had very short lifetimes, with half-lives of 2-3 minutes. In contrast, proteins

containing Met, Ser, Ala, Thr, Val, or Gly showed half-lives of ~20 hours. These findings have since been supported by further studies in yeast (Martin-Perez and Villén, 2017) and human cell lines (Gawron et al., 2016) and the phenomenon is often referred to as 'N-end rule'. The presence of amino acids that correlate with fast turnover is thought to provide a supporting environment for N-terminal acetylation, which may be recognized by the N-end rule pathway and thus targeted to degradation (Gibbs et al., 2014, Martin-Perez and Villén, 2017).

1.1.5.1.4 Short linear sequence motifs

Several peptide motifs, including PEST sequence, KFERQ motif, D-box and others, have been found to selectively target proteins for degradation (Rechsteiner and Rogers, 1996, Boisvert et al., 2012, Martin-Perez and Villén, 2017). For PEST regions, by closely examining rapidly degrading proteins (Myc, Fos, Jun, p53 and others), researchers found regions of the proteins to be selectively enriched in proline (P), glutamate (E), serine (S) and threonine (T) (Rechsteiner and Rogers, 1996). PEST sequences were found to be hydrophilic stretches of at least 12 amino acids uninterrupted by positively charged residues. The knockout of PEST sequences from proteins resulted in dramatically increased protein stability and lifetime (Tsurumi et al., 1995, Ghoda et al., 1989, Colledge et al., 2003, Rechsteiner and Rogers, 1996). For example, wild-type c-Fos is a rapidly turned over protein with a half-life of around 10 minutes but a mutant c-Fos in which PEST sequence was removed could last 4-5 times longer (Tsurumi et al., 1995). Similarly, postsynaptic density protein PSD95 was also found to contain a PEST sequence at its N-terminus (Colledge et al., 2003). While wild-type PSD95 gets ubiquitinated in response to NMDA receptor activation, ubiquitination and therefore degradation of PSD95 lacking the PEST sequence was dramatically reduced thus increasing protein lifetime (Colledge et al., 2003).

Activity-dependent ubiquitination observed in PSD95 suggests that the activation of PEST sequence-dependent degradation may be conditional (Colledge et al., 2003, Ehlers, 2003). Indeed, researchers suggest that protein

degradation is often increased by the conformational changes in the proteins and subsequent increased exposure of PEST sequences to the cytosol (Rechsteiner and Rogers, 1996). Ligand binding, phosphorylation and other modifications have been found to promote degradation of PEST sequence-containing proteins via 26S proteasome (**Figure 1.1**).

Figure 1.1: A comic illustration of 26S proteasome targeting the PEST sequence-containing protein. *Reprinted from Rechsteiner and Rogers (1996), Copyright (1996), with permission from Elsevier.*

1.1.5.2 Extrinsic factors

1.1.5.2.1 Protein localization

Protein lifetimes differ between tissue and cell types as well as cellular compartments (Fornasiero et al., 2018, Dörrbaum et al., 2018, Mathieson et al., 2018, Price et al., 2010, Lajtha et al., 1976, Lajtha, 1959). Out of heart, liver, muscle and brain tissues examined, brain tissue displays longest protein lifetimes (Lajtha, 1959, Lajtha et al., 1976, Fornasiero et al., 2018, Price et al., 2010). At the level of cell types, in the brain neurons have longer protein lifetimes compared to glial cells (Fornasiero et al., 2018, Dörrbaum et al.,

2018). Within individual cells, longest protein lifetimes are detected for nucleosome proteins, such as histones, which can last up to 1 year (Price et al., 2010). Mitochondrial proteins, myelin and extracellular matrix components are also long lived while proteins of cytosol, endoplasmic reticulum and proteins involved in DNA binding, RNA processing and protein production are significantly less stable (Fornasiero et al., 2018, Dörrbaum et al., 2018). In neurons, same set of proteins display longer lifetimes in synaptic fractions compared to whole-tissue homogenates (Heo et al., 2018b, Fornasiero et al., 2018). Location-dependent differences in protein turnover may arise due to: (a) activity-dependent patterns, (b) crowdedness of the intracellular environment and resulting interconnectedness of proteins, (c) localization of different protein isoforms carrying specific susceptibility to degradation.

1.1.5.2.2 Active use of protein

When the protein is used actively, its turnover rate increases (Martin-Perez and Villén, 2017). Martin-Perez and Villén (2017) directly tested this relationship in yeast cells by tuning up activity in molecular pathway-specific manner and measuring protein turnover in activated versus non-activated cells. In the case of activating arginine biosynthetic pathway, only the proteins that were directly involved in metabolically synthesizing arginine were upregulated in cells not supplied with this amino acid with food. All other proteins did not show change in turnover between the two conditions. Similarly, (Ehlers, 2003) discovered that changes in activity levels in primary neuronal cells led to parallel changes in turnover rates of some of postsynaptic proteins, including NMDA receptor subunits NR1 and NR2B, scaffolding protein SAP102, AKAP79/150 and PP1. Interestingly, the relationship between activity and protein turnover was not straightforward for some of the proteins. For scaffolding protein PSD95, increased activity induced higher levels of ubiquitination of the protein and thus presumably degradation, but the overall turnover rate was not changed (Ehlers, 2003, Yi and Ehlers, 2005). Such disparity between rates of degradation and rates of turnover could be explained by changes in protein synthesis that do not co-ordinate with protein degradation in some cases.

1.1.5.2.3 Complex membership

Proteins that belong to same molecular complexes on average tend to have similar half-lives (Mathieson et al., 2018, Martin-Perez and Villén, 2017, Price et al., 2010). Subunits of proteasome, ATP synthase, ribosome, and chaperonin complexes are among those to show the smallest variation of their half-lives, a result that has been observed in yeast (Martin-Perez and Villén, 2017), a range of human non-diving cells (Mathieson et al., 2018) and mouse liver and brain tissue (Price et al., 2010). In the neuronal excitatory synapse, protein half-lives were found to be similar for subunits of mGluR, NMDA and AMPA receptors among others (Dörrbaum et al., 2018). Assembled complexes are thought to increase the stability of individual member subunits (Hinkson and Elias, 2011, Buchler et al., 2005) but it is not yet known if complex members turn over individually or all together. It has been suggested that some subunits may undergo targeted regulation of turnover that controls the activity of the whole complex (Hinkson and Elias, 2011). By adjusting the abundance of the critical subunit, cells could shift the balance between complex assembly and disassembly. Not all complexes, however, show homogeneous half-lives. Complexes composed of more heterogeneous proteins, such as microtubule and nucleosome complexes, display largely varied half-lives (Price et al., 2010). The difference in homogeneity of half-lives in different complexes should be further investigated to uncover patterns and rules to the phenomenon.

1.1.6 Summary

All cells in living organisms undergo continuous protein replacement. Protein turnover allows for removal of abnormal proteins, contributes to adaptations in response to changing environment and acts as an emergency energy reservoir in cells. Protein stability and lifetime is determined by a number of protein-intrinsic factors, including protein structure and conformation, accessible protein surface area, N-terminus amino acids and short linear sequence motifs that make protein susceptible to degradation by proteasome. External factors such as protein localization, active use of protein and complex membership can also influence the stability and lifetime of a cellular protein.

Given the dynamic nature of proteins in all living organisms, an interesting question arises about the stability of molecular substrates that store information in cells and organisms, including the storage of memory in neural systems.

1.2 Neuronal synapse lifetime

Learning and memory are thought to require enduring modifications in synapses, however, the resting or learning-induced stability of synapses is only now being uncovered. Below I review recent findings on structural and molecular synapse lifetime and turnover.

1.2.1 Molecular synapse lifetime

Proteins in the brain have an average half-life in the order of a few days to a couple of weeks (Price et al., 2010, Cohen et al., 2013, Fornasiero et al., 2018, Dörrbaum et al., 2018). Studies in primary cell cultures find the average protein half-life to be 4.14 days (Cohen et al, 2013) or 5.4 days as recorded by Dörrbaum et al. (2018). *In vivo*, protein lifetimes are longer and Price et al. (2010) find the median half-life to be 9 days. Most studies to date have measured protein lifetime in whole brain or whole-brain-region homogenates and only a few have looked specifically into synaptic preparations (Ehlers, 2003, Heo et al., 2018b, Fornasiero et al., 2018). These studies find the lifetime of synaptic proteins to be slightly longer compared to proteins located outside of synapses (Fornasiero et al., 2018). To put these half-life numbers into perspective, a vast majority (>99%) of a protein that has a half-life of 5 days would be replaced within just over a month (35 days). A protein that has a half-life of 9 days would be almost completely replaced (~0.7% remaining) in around two months (63 days). What this means is that neurons and synapses, structures thought to store long-term memories in the brain, replace all their molecular contents every month or two, a time period that is much shorter than that of memories that last a lifetime.

1.2.1.1 Age-related changes in protein lifetime

Changes in rates of brain protein synthesis have been observed throughout the lifespan in rodents (Fando et al., 1980, Dwyer et al., 1980, Ekstrom et al., 1980, Ingvar et al., 1985). During development, rates of protein synthesis decline in rat forebrain and cerebellum (Fando et al., 1980). During ageing, multiple studies find decreases in brain protein synthesis (Dwyer et al., 1980, Ekstrom et al., 1980, Ingvar et al., 1985). Dwyer et al. (1980) find an 11% decrease in protein synthesis in forebrain of rats between 3M and 10.5M of age and an additional 9% decrease between 16.5M and 22.5M. Ekstrom et al. (1980) record a dramatic 56% decrease in brain protein synthesis rates between 6M and 32M in rats. Ingvar et al. (1985) document changes in protein synthesis across 39 brain structures in rats and find that some but not all structures show a decrease in protein synthesis rates between 6M and 15-32M. Most notable changes in protein synthesis with ageing were detected in granule cells of dentate gyrus, nucleus accumbens, locus coeruleus, cerebellar white matter, olfactory cortex, substantia nigra, superior colliculus, inferior colliculus and visual cortex. A number of brain regions affected are involved in auditory and visual information processing and authors reasoned that the changes in protein synthesis in these regions may be due to chronic lack of sensory stimulation (Ingvar et al., 1985).

Previous studies were limited to looking into whole-brain or whole-region protein extracts and lacked synaptic specificity. Additionally, the above-mentioned studies only examined the rates of synthesis of a population of proteins all pooled together and did not distinguish protein-specific patterns. Further experiments are needed to document not only the rates of synthesis but also the rates of degradation and thus the lifetime of different synaptic proteins in the brain.

1.2.1.2 Activity-induced changes in protein lifetime

Neuronal activity and sensory stimulation affect the rates of neuronal protein synthesis and turnover (Ehlers, 2003, Schanzenbächer et al., 2016, Schanzenbächer et al., 2018, Fornasiero et al., 2018, Heo et al., 2018b,

Dörrbaum et al., 2020, Jähne et al., 2021). To increase neuronal activity in *in vitro* preparations, neuronal cell cultures are treated with competitive GABAA receptor antagonist bicuculline (BIC). BIC treatment results in reduced average protein lifetimes in Ehlers (2003) study and a slight reduction in lifetimes in Heo et al. (2018b). Activity was also found to positively correlate with turnover of presynaptic proteins at single synapse level (Jähne et al., 2021). Activity-dependent changes in turnover, however, are not universal across all proteins (Ehlers, 2003, Heo et al., 2018b, Schanzenbächer et al., 2016, Schanzenbächer et al., 2018). For example, Ehlers (2003) recorded BIC-dependent decreases in protein half-life in NMDAR subunit NR2B, scaffolding protein SAP102, AKAP79/150 and PP1 but no changes in turnover were observed for NR2A, mGluR1, PSD95, Homer and CamKII synaptic proteins. Interestingly, Dörrbaum et al. (2020) found a global slowing down of protein turnover in cells treated with BIC contradicting the results discussed above. In this study, 43% of the examined proteome showed changes in protein synthesis or degradation in response to BIC treatment and most affected proteins showed a decrease in protein synthesis and/or degradation. A small fraction of proteins displayed an opposite behavior to enhanced activity with increased rate of protein synthesis and/or degradation therefore strengthening the evidence for protein-specific responses to activity (Dörrbaum et al., 2020).

In vivo, increases in sensory stimulation which in turn increase neuronal activity result in shorter protein lifetimes of synaptic proteins (Heo et al., 2018b, Fornasiero et al., 2018). Mice exposed to environmental enrichment (EE) show an almost uniform shift towards increased turnover and shorter protein lifetimes in Heo et al. (2018b). EE exposure results in more moderate effects in Fornasiero et al. (2018) with some proteins showing an increase in turnover and a smaller fraction a decrease in turnover rates. Some of the proteins that show shorter lifetimes in response to EE include Synapsin-1, CASK, SynGAP, and Neurexin-4 (Fornasiero et al., 2018). *In vivo* findings, therefore, support those made in cell cultures and suggest that activity regulates synaptic protein turnover in a protein-specific manner.

Reduction in neuronal activity *in vitro* by an application of Na^+ channel blocker tetrodotoxin (TTX) decreases the average rate of protein turnover (Ehlers, 2003, Heo et al., 2018b, Dörrbaum et al., 2020, Schanzenbächer et al., 2016, Schanzenbächer et al., 2018). TTX affected 31% of quantified proteins in Dörrbaum et al. (2020) with most proteins showing a decrease in protein synthesis and/or degradation. Interestingly, TTX and BIC treatments appear to induce opposing effects on turnover of proteins sensitive to changes in activity (Ehlers, 2003).

1.2.1.3 Protein turnover and disease

Imbalance in protein synthesis and turnover have been implicated in a number of brain diseases (Louros and Osterweil, 2016, Soukup et al., 2018, Hipp et al., 2019, Jayaraj et al., 2020). Mutations in components of protein synthesis machinery cause several neurodevelopmental disorders, including autism spectrum disorders and intellectual disability (Louros and Osterweil, 2016). FMRP is a translational repressor protein that when mutated gives rise to Fragile X syndrome, one of the leading causes of autism spectrum disorder (ASD) and intellectual disability (ID) in children. Absence of FMRP protein results in excessive protein synthesis and affects important synaptic proteins like AMPARs and PSD95 (Qin et al., 2005, Muddashetty et al., 2007, Osterweil et al., 2010, Barnes et al., 2016). A mutation in another translational repressor protein CYFIP1 is known to cause ASD, ID and schizophrenia (Louros and Osterweil, 2016, De Rubeis et al., 2013, Haan et al., 2021). Mutation in SynGAP, an abundant postsynaptic protein, can lead to ASD and experimental models show increases in protein synthesis in dissociated cortical neurons from SynGAP mutants (Gamache et al., 2020, Wang et al., 2013).

A number of neurodevelopmental disorders have also been linked to mutations in components of protein degradation machinery (Glessner et al., 2009, Louros and Osterweil, 2016). Perhaps the most well-known mutation occurs in E3 ligase Ube3A that causes Angelman syndrome in children (Jiang et al., 1998). Ube3A regulates ubiquitination of activity-regulated protein Arc, an important player in activity-dependent molecular adaptations in synapses (Greer et al.,

2010). In addition, Ube3A controls the degradation of tumor suppressor protein p53, a protein important for genome stability, progression through the cell cycle and apoptosis (Mishra and Jana, 2008).

In ageing, dysfunctional proteostasis can cause accumulations of misfolded protein aggregates associated with neurodegenerative diseases, such as Alzheimer's disease, Parkinson's disease and Huntington's disease (Soukup et al., 2018, Hipp et al., 2019, Jayaraj et al., 2020). Additionally, mutations in members of protein degradation machinery have been directly implicated in a number of neurodegenerative diseases. For example, 5-10% of Parkinson's disease cases have a genetic association and one of the most frequent causes of disease is the mutation in Parkin protein (Arkinson and Walden, 2018, Soukup et al., 2018). Parkin is a E3 ubiquitin ligase that is involved in mitochondrial quality control and turnover (Arkinson and Walden, 2018).

1.2.1.4 Technical and biological limitations

Majority of the studies examining protein lifetime to date have relied on bulk measurements from whole-brain or whole-brain-region homogenates and have failed to extract spatial information related to protein turnover. Protein turnover may be brain region-, cell type- or even synapse-specific which may carry important implications for neural signal processing and information storage in different brain areas, cells or synapses.

I will now discuss recent findings on stability of synaptic structures in the living brain which uncover important trends in brain region- and synapse-specific regulation of structural synapse stability.

1.2.2 Structural synapse stability

Structural synapse stability refers to the stability of dendritic spines and axonal boutons, the post- and pre-synaptic sites, respectively. Studies examining structural synapse stability over time often rely on genetically or virally expressed fluorescent protein in the cytosol of a subset of neurons. The dynamics of synaptic structures is then recorded using 2-photon fluorescence

microscopy in living mice over days or weeks through a cranial window on the surface of mouse brain.

In adult brain, 50 to 96% of dendritic spines in the superficial layers of the cortex are remarkably stable and persist for over 1 month (Trachtenberg et al., 2002, Grutzendler et al., 2002, Zuo et al., 2005). The finding is consistent for different areas of the cortex, including somatosensory, visual, barrel, motor cortices and frontal areas (**Table 1.1**).

Axonal boutons also display great stability, with ~85% of boutons of thalamocortical afferents and 40% of L6 axon terminal boutons in barrel cortex persisting over 1 month in adult mice (De Paola et al., 2006). In contrast, dendritic spines in the basal dendrites of hippocampal CA1 show much shorter lifetimes, suggesting that spine stability may differ between brain regions (Attardo et al., 2015, Pfeiffer et al., 2018). Attardo et al. (2015) visualized dendritic spine dynamics in CA1 via a micro-endoscope and found 100% of spines to turn over within 3-6 weeks. Pfeiffer et al. (2018) observed 40% of spines to turn over within 4 days by applying a 'hippocampal window' technique, in which a portion of somatosensory cortex is dissected out in order to access deeper areas of the brain. Structural synapse dynamics has not been examined in other regions of the brain yet and thus the extent and role of stable dendritic spines is yet to be confirmed.

Reference	Area examined	Animal age	Findings
Trachtenberg et al. (2002)	L5 neurons of barrel cortex	1.5-2.5M	Stable spines (persist over 1 month) ~50% population
Grutzendler et al. (2002)	L5 neurons of primary visual cortex	4M	~96% spines remain stable over 1 month
Zuo et al. (2005)	L5 neurons of barrel, motor and frontal areas	4-6M	3-5% spines eliminated and formed over 2 weeks. 75% of spines present over 18.5 months.
Holtmaat et al. (2005)	L5 and L2-3 neurons of somatosensory cortex	2-4M and 6-7.5M	Persistent spines (lifetime ≧ 8 days) 66% in 2-4M and 73% in 6-7.5M
Attardo et al. (2015)	Hippocampal CA1so	2-3M	100% spine turnover within 3-6 weeks
Pfeiffer et al. (2018)	Hippocampal CA1so	4-12M	60% spine survival over 4 days.

Table 1.1: The summary of recent literature on the lifetime of synaptic structures in cortex and hippocampus.

1.2.2.1 Synapse stability with age

The stability of synaptic structures has been found to differ between developing, adult and ageing brain (**Table 1.2**). Studies in cortical brain areas in rodents reveal that dendritic spine stability increases from development to adulthood, with an increased fraction of stable spines found in adult brain (Grutzendler et al., 2002, Holtmaat et al., 2005, Zuo et al., 2005). Several reports point out that spine elimination exceeds spine formation in the brains of 1-month-old animals (Grutzendler et al., 2002, Zuo et al., 2005), the finding that aligns with extensive cortical circuit remodeling documented in developing brain (Mallya et al., 2019, Farhy-Tselnicker and Allen, 2018, Sakai, 2020, Paolicelli et al., 2011). Intriguingly, spine and axonal bouton stability was found to decrease with ageing in somatosensory cortex (Mostany et al., 2013, Grillo et al., 2013, Voglewede et al., 2019). Reduced stability here is due to an increased rate of addition and elimination of synapses but may or may not affect the fraction of stably maintained synapses, which was not assessed in the discussed studies. Changes in stability of synaptic structures across the

lifetime may point to changes in metabolic processes in neuronal cells and brain's capacity to process and store information with age.

Reference	Area examined	Animal age	Findings
Grutzendler et al. (2002)	L5 neurons of primary visual cortex	1M and 4M	↑ spine stability from 1M to 4M (73% vs ~96% stable spines).
Holtmaat et al. (2005)	L5 and L2-3 neurons of somatosensory cortex	P16-25, ~1-2M, ~2-4M and ~6-7.5M	↑ spine stability from development to adulthood
Zuo et al. (2005)	L5 neurons of barrel, motor and frontal areas	1M and 4-6M	↑ spine stability from 1M to 4-6M
Mostany et al. (2013)	L5 neurons of somatosensory cortex	<1M, 3-5M, 8-15M and >20M	↓ in dendritic spine stability from 3-5M to 8-15M and >20M
Grillo et al. (2013)	Thalamocortical and L6 axons in somatosensory cortex	4-6M and 22-24M	↓ axonal bouton stability of thalamocortical and not L6 axons
Voglewede et al. (2019)	L5 neurons of barrel cortex	3-5M and 18-21M	↓ spine stability

Table 1.2: The summary of recent literature on the changes in structural synapse stability with age.

1.2.2.2 Effects of learning and activity on synapse stability

The link between learning and changes in synapse dynamics has been strengthened by many studies exploring the effects of a range of behavioral tasks on dendritic spine stability and turnover. Motor learning via rotarod or forelimb reaching task upregulates new spine formation and selective stabilization of dendritic spines in motor cortex formed during learning (Yang et al., 2009, Xu et al., 2009). Yang et al. (2009) also observe an increase in spine elimination but over longer periods (7-30 days compared to 2 days for spine formation) and (Ma et al., 2016) detects faster turnover rates in response to motor learning. Similarly, environmental enrichment, which exposes the

animals to novel sensory experiences, increases new spine formation and stabilization (Yang et al., 2009). Increased spine formation or elimination has been observed in auditory and frontal association cortices in response to fear conditioning, in which an animal learns to associate auditory cues with a foot shock (Lai et al., 2012, Moczulska et al., 2013, Yang et al., 2016). Interestingly, Moczulska et al. (2013) and Yang et al. (2016) recorded upregulation of spine formation while (Lai et al., 2012) observed increased spine elimination, which may be due to differences in the length of time the spines were recorded for during and after learning or differences in the fear conditioning paradigm used. Conflicting observations have also been recorded in response to sensory deprivation, whether whisker trimming or monocular deprivation (Lendvai et al., 2000, Trachtenberg et al., 2002, Holtmaat et al., 2006, Ma et al., 2016, Zhou et al., 2017, Seaton et al., 2020). In early development, Lendvai et al. (2000) find that the dendritic spines in barrel cortex are sensitive to whisker trimming at P11-13 but not P8-10 or P14-16 and show increased spine stability. In mature animals, studies detect increases in spine turnover (Trachtenberg et al., 2002), preferential stabilization of newly formed spines (Holtmaat et al., 2006, Seaton et al., 2020) or decreases in spine elimination (Ma et al., 2016). Age-dependent changes in dendritic spine response to sensory stimulation was directly observed by Voglewede et al. (2019). The authors found that whisker stimulation induces upregulation of dendritic spine turnover in adult 3–5-month-old animals but a downregulation of turnover in ageing 18–21-month-old mice. Decrease in dendritic spine turnover in ageing animals may contribute to inflexibility to learn and adapt to new environments. Importantly, several reports point to selective stabilization of spines formed during learning and preferential destabilization of previously persistent spines, which possibly points to spines that host new learning and old weak memories, respectively (Holtmaat et al., 2006, Yang et al., 2009, Xu et al., 2009, Seaton et al., 2020). Such synapse specific effects are important to record and analyze in more detail to uncover the molecular mechanisms at play in ‘learning’ and ‘memory’ spines.

1.2.2.3 Structural synapse stability in disease

Changes in dendritic spine stability and turnover have been documented in multiple rodent models of neurodevelopmental and neurodegenerative diseases, diseases affecting cognition, learning and memory in the affected individuals (**Table 1.3**). Fragile X syndrome is a frequent monogenic cause of intellectual disability (ID) and autism spectrum disorder (ASD). Dendritic spine formation and elimination is elevated in somatosensory and motor cortices in mice lacking Fmr1 gene, a mouse model for Fragile X syndrome (Cruz-Martín et al., 2010, Pan et al., 2010, Padmashri et al., 2013). Similarly, mice with MECP2 duplication, a mutation that is known to cause Rett syndrome in infants, show an increased turnover of dendritic spines in somatosensory cortex (Jiang et al., 2013). ASD-associated mutations in 15q11-13 region, NLGN-3 and a BTBR mouse model all show an increased turnover of PSD95-positive dendritic spines over 2 days (Isshiki et al., 2014). Interestingly, Isshiki and colleagues find that the phenotype is specific to excitatory synapses since dendritic spines positive for an inhibitory synapse marker gephyrin do not show a change in turnover. Overall, animals carrying mutations associated with neurodevelopmental disorders display lower stability of dendritic spines in multiple areas of the cortex which may contribute to neural circuit instability in these diseases.

Decreased stability of dendritic spines has also been detected in the cortical areas in rodent models of neurodegenerative diseases, such as Alzheimer's disease and Huntington's disease (Spires-Jones et al., 2007, Murmu et al., 2013, Jackson et al., 2017). Jackson et al. (2017) show an increased turnover of dendritic spines in somatosensory cortex in a mouse model of tauopathy (mutation in rTg4510 gene). Spires-Jones et al. (2007) documented a specific increase in spine elimination in the vicinity of amyloid plaques in Tg2576 mouse model of Alzheimer's disease (AD). Murmu et al. (2013) looked into the early stages of Huntington's disease (HD) and detected an increased spine formation and elimination in the somatosensory cortex of 1-month-old R6/2 mutant mice compared to controls. Since early stages of HD are often accompanied by deficits in cognitive performance, the authors reasoned that

changes in dendritic spine stability observed prior to the onset of motor deficits could offer a biological mechanism for altered brain function (Murmu et al., 2013).

Several studies pointed to reduced numbers of persistent spines in disease mutants compared to controls in both, models of neurodevelopmental and neurodegenerative diseases (Pan et al., 2010, Della Sala et al., 2016, Murmu et al., 2013). The converging phenotype of reduced synapse stability and reduced numbers of persistent spines in brain diseases of young and old age suggests a possible requirement for a certain level of neural network stability to effectively carry out cognitive functions.

Reference	Mutation	Area examined	Animal age	Findings
Cruz-Martín et al. (2010)	Fmr1-KO (Fragile X syndrome)	L2-3 neurons	First 2 weeks	Delayed downregulation in dendritic spine dynamics during first 2 weeks
Pan et al. (2010)	Fmr1-KO (Fragile X syndrome)	L5 neurons of barrel cortex	3W and 1M	↑ spine formation and elimination. More short-lived new spines in KO
Padmashri et al. (2013)	Fmr1-KO (Fragile X syndrome)	L5 neurons of primary motor cortex	1.25M	↑ spine formation and elimination, and turnover.
Jiang et al. (2013)	MECP2 duplication (Rett syndrome)	L5 neurons of somatosensory cortex	2M-5M	↑ spine formation and elimination, and turnover.
Isshiki et al. (2014)	15q11-13, NLGN-3, and BTBR (ASD)	L2-3 neurons of somatosensory cortex and anterior frontal cortex	3M	↑ PSD95-eGFP-positive spine turnover over 2 days.
Della Sala et al. (2016)	CDKL5 (ASD / atypical Rett syndrome)	L5 neurons of somatosensory cortex	~1-2M	↓ in persistent spines over 30 days (64% persisted in mutants compared to 75% in controls).
Spires-Jones et al. (2007)	Tg2576 (AD)		8-10M and 18-24M	↑ spine elimination over 1hr in 18-24M, specifically in the vicinity of amyloid plaques.
Murmu et al. (2013)	R6/2 (HD)	L2-3 and L5 neurons of somatosensory cortex	1M	↑ spine formation and elimination over 6 weeks. ↓ probability that newly formed spines stabilized.
Jackson et al. (2017)	rTg4510 (AD, FTD, and Tauopathy)	Somatosensory cortex	4-6.5M	↑ turnover of dendritic spines. Axonal boutons stabilized in mutants.

Table 1.3: The summary of recent literature on the changes in synaptic structure stability in disease.

1.2.2.4 Technical and biological limitations

Studies examining structural synapse stability provide important insights into the lifetime and turnover of subpopulations of synapses. Structural stability, however, does not necessarily directly correspond to functional stability and the functional stability will be at least in part determined by the stability of molecular networks within the synaptic structures. Analysis of protein lifetime in individual synapses would be one of the ways to address the stability of molecular synapse components.

Dendritic spine and/or axonal bouton dynamics have not been explored in a vast majority of brain regions therefore our knowledge of synapse stability is limited to cortical and hippocampal CA1 brain areas. Additionally, the studies described above have observed and analyzed small numbers of synapses (in the order of 100s or 1000s) and therefore future studies should aim to design larger-scale unbiased surveys of synapse stability to strengthen and expand on the existing evidence.

1.2.3 Summary

Long-term memory storage is thought to require stable synaptic connections, but evidence suggests that a vast majority of synaptic structures and proteins inside them have lifetimes shorter than the life-long memories. Bulk measurements of brain or synaptic protein turnover indicate that majority of proteins get completely replaced within 1-2 months in adult rodents. Synaptic structures, including dendritic spines and axonal boutons, can last longer than proteins within them and some dendritic spines remain present throughout the mouse lifespan. Both, protein lifetime and the lifetime of synaptic structures, change throughout the lifespan, in response to activity and in cases of brain disease.

Studies into structural synapse stability highlight the subpopulations of long-lived and short-lived synapses which may have different molecular properties, including protein metabolism and lifetime. Since the traditional protein turnover studies lack the spatial resolution to identify synapse-specific differences, we propose to develop a method to visualize synaptic protein turnover at single-

synapse resolution and map the lifetime of protein across multiple brain regions. We choose to focus on mapping the lifetime of an important excitatory postsynaptic protein PSD95.

1.3 Post-synaptic density protein 95 (PSD95)

PSD95 is a scaffolding protein and one of the most abundant proteins at the PSD (Chen et al., 2005). PSD95 belongs to Disc Large Homolog (DLG) family that has an important function of linking synaptic glutamate receptors with downstream signaling pathways.

1.3.1 The DLG protein family

The DLG protein family belongs to the superfamily of membrane-associated guanylate kinases (MAGUKs). In vertebrates, the DLG family is composed of four proteins: synapse-associated protein 97 (SAP97 or DLG1), post-synaptic density protein 93 (PSD93 or DLG2) synapse-associated protein 102 (SAP102 or DLG3) and post-synaptic density protein 95 (PSD95 or DLG4). From a molecular perspective, DLG proteins contain conformationally independent modular domains that are connected with flexible polypeptide linkers (Vallejo et al., 2017). All DLGs contain 3 PSD95/Dlg/ZO-1 (PDZ) domains arranged in a tandem, a Src Homology 3 (SH3) domain and a guanylate kinase-like domain (GK). At the level of protein sequence, the 4 paralogs share 75% similarity in either mouse or human and are highly conserved between vertebrate species (Nithianantharajah et al., 2013).

1.3.2 Functions of PSD95

PSD95 has a range or roles in organizing synaptic molecular complexes, targeting glutamate receptors to synapses, ensuring the maturity and stability of synaptic contacts and in result contributing the learning, memory maintenance and brain diseases. Below I discuss the main functions of PSD95 protein at the synapse.

1.3.2.1 A ‘synapse organizer’

PSD95 makes use of its different protein binding domains to organize the molecular signaling machinery of the PSD (**Figure 1.2**). The PDZ domains of PSD95 are specialized for binding to molecular elements present in the C-terminus of other proteins, including glutamate receptors and signaling molecules (Kim and Sheng, 2004, Vallejo et al., 2017). Each PDZ domain in PSD95 has its specific binding partners but some target proteins can be promiscuous and bind to two or all three PDZ domains. Some of the interactors of PDZ domains are NMDAR subunits NR2A/B, AMPAR-binding protein stargazin, K^+ channel Kir2.3, SynGAP and others. SH3 domain is used to link PSD95 with kainite receptor subunit 2 (Garcia et al., 1998). SH3 domain usually recognizes proline-rich sequences in target proteins but alternative recognition motifs have also been documented (Teyra et al., 2017). GK domain links PSD95 with downstream scaffolding proteins, including AKAP79/150 (Colledge et al., 2000) and GKAP (Kim et al., 1997, Takeuchi et al., 1997). GK domain is homologous to yeast guanylate kinase but is catalytically inactive (Kuhlendahl et al., 1998) likely because of a point mutation, first identified in Johnston et al. (2011). SH3 and GK domains closely interact and can adopt a ‘closed’ conformation that prevents the domains from binding other proteins (Wu et al., 2017, Rademacher et al., 2019).

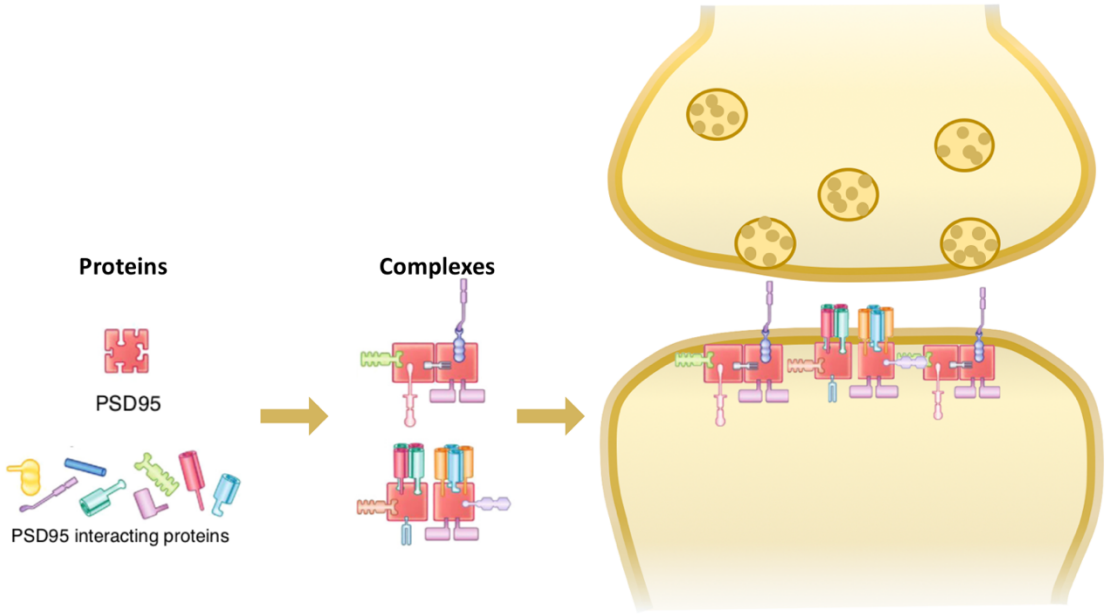

Figure 1.2: PSD95 organizes post-synaptic proteins into functional molecular signalling networks.

1.3.2.2 NMDAR complex assembly

NMDA receptors modulate glutamatergic synaptic transmission and long-lasting changes in synaptic strength though downstream molecular pathways (Husi et al., 2000). PSD95 interacts with NMDA receptors and while some studies suggest that the interaction occurs through the PDZ domain of PSD95 and C-terminus of NMDAR subunit NR2 (Kornau et al., 1995, Niethammer et al., 1996), others find that PDZ interaction is not required for complex formation (Frank et al., 2016). In addition to interaction, PSD95 and NMDAR belong to the same multimolecular complexes, composed of receptors, adaptors, signaling, cytoskeletal and other proteins that work as molecular machines to process incoming neuronal signals (Husi et al., 2000). Analysis of endogenous NMDAR complexes from mouse and human forebrains revealed a partition of the complexes into two distinct populations of ~0.8 MDa and ~1.5 MDa in size (Frank et al., 2016). While the smaller complexes contained only subunits of NMDARs, ~1.5 MDa complexes were composed NMDAR subunits, ion channels (Kir 2.3), trans-synaptic adhesion molecules (Adam 22), scaffold (PSD95 and PSD93) and signaling (CaMKIIα) proteins (Frank et al., 2016).

Authors tested the mechanisms for assembly of these complexes and uncovered that PSD95, PSD93 and NMDAR subunit NR2B were essential for the formation of ~1.5 MDa multiprotein complexes and that this interaction did not require the PDZ binding to NR2B or NR2A (Frank et al., 2016, Frank and Grant, 2017). Absence of either PSD95, PSD93 or C-terminus of NR2B resulted in absence of ~1.5 MDa molecular complexes. ~1.5 MDa complexes increased in abundance with development and formed a substantial fraction of all NMDARs therefore suggesting their physiological importance in synapse signaling (Frank et al., 2016). It is important to note that not all PSD95 participates in NMDAR multiprotein assemblies; in fact, ~1.5 MDa NMDAR complexes represent only ~3% of all multiprotein complexes containing PSD95 (Frank et al., 2017).

1.3.2.3 Synaptic clustering of AMPARs

The dynamic regulation of AMPA receptors presents a primary mechanism for modulating synaptic strength (El-Husseini et al., 2002). PSD95 interacts with AMPA receptors but indirectly, through a transmembrane AMPA receptor regulatory protein (TARP) called stargazin (Chen et al., 2000, El-Husseini et al., 2002, Schnell et al., 2002, Dakoji et al., 2003). PSD95 interaction with stargazin occurs via the PDZ domains 1 and 2 (Schnell et al., 2002, Ehrlich and Malinow, 2004) and this interaction is required for AMPA receptor targeting to the synapse (Chen et al., 2000, Bats et al., 2007). Increasing levels of PSD95 at synapses has been shown to correlate with increasing numbers of synaptically expressed AMPARs (El-Husseini et al., 2000, Schnell et al., 2002, Colledge et al., 2003, Ehrlich and Malinow, 2004). Separate studies using super-resolution microscopy have described synaptic PSD95 and AMPARs concentrate into nanoclusters of ~70-80 nm in diameter which may act as functional units within individual synapses (Nair et al., 2013, MacGillavry et al., 2013, Broadhead et al., 2016).

1.3.2.4 Synapse maturation and stability

Presence of PSD95 in synapses has been linked to synapse structural and functional maturation and increased synapse stability (Berry and Nedivi, 2017,

Cane et al., 2014, Ehrlich et al., 2007, Elias et al., 2008, El-Husseini et al., 2000). PSD95 is nearly absent in synapses early in development and only appears in the second postnatal week as it replaces its paralog SAP102 in many synapses (Cizeron et al., 2020, Sans et al., 2000). These observations suggest that PSD95 is not required for synaptogenesis per se. Indeed, Lambert et al. (2017) explore the timing of DLG protein accumulation in individual nascent spines in organotypic slice culture and find that PSD95 accumulates in the spines 12-20 hours following new spine identification. SAP102, in contrast, reaches mature levels within 3 hours of new spine formation (Lambert et al., 2017). Overexpression of PSD95 has been found to drive earlier synapse maturation through the enhancement of synaptic AMPAR levels, increased size of the presynaptic terminal and the density of the dendritic spines (El-Husseini et al., 2000). Acute knockdown of PSD95 by RNAi, in contrast, results in delayed synapse maturation and decreased number of synapses expressing functional AMPARs (Ehrlich et al., 2007, Elias et al., 2008). Accumulation of PSD95 in dendritic spines has been associated with longer spine lifetimes and the presence of PSD95 is generally thought as a marker for stable synapses (Cane et al., 2014, Berry and Nedivi, 2017).

1.3.2.5 Learning and memory

Given the role of PSD95 in clustering AMPARs and assembling NMDAR complexes, it is perhaps unsurprising that PSD95 has a major role in learning and maintenance of memories. Mutants lacking PSD95 exhibit severe deficits in spatial learning in water maze, a task dependent on hippocampal NMDA receptor function (Migaud et al., 1998). The role of PSD95 has also been tested in the formation and maintenance of fear memories (Fitzgerald et al., 2015). PSD95-KO mice did not differ from WT mice in their ability to acquire fear memory and the memory was stable 24 hours post learning. Two weeks later, however, PSD95-KO mice exhibited severe impairments in fear memory compared to controls suggesting that PSD95 is required for the long-term maintenance of memories (Fitzgerald et al., 2015). Further studies by Elkobi et al. (2008) examined the effects of acute knockdown of PSD95 by RNAi on ability to learn new tastes. PSD95 was found to be required for learning of

novel tastes but not the retrieval of already familiar ones (Elkobi et al., 2008). Finally, Nithianantharajah et al. (2013) assessed the role of PSD95 and its paralogs in several aspects of learning and cognitive functioning using touchscreen behavioral paradigms. PSD95 was shown to be required for the simplest forms of learning, such as operant conditioning, while PSD93 and SAP102 were needed for more complex forms of learning, cognitive flexibility as well as attention and response control (Nithianantharajah et al., 2013).

1.3.2.6 Brain diseases

Genes encoding PSD proteins have been implicated in over 130 human brain diseases (Bayés et al., 2011). Out of 118 core PSD95-interacting proteins, 49 genes were found to be linked to diseases, including schizophrenia, mental retardation, bipolar disease, Alzheimer's disease and others (Fernández et al., 2009). Mutations in the gene encoding PSD95 protein have more recently been associated with schizophrenia (Purcell et al., 2014, Coley and Gao, 2018), autism (Gilman et al., 2011, Stessman et al., 2017) and intellectual disability (Lelieveld et al., 2016). Reductions in PSD95 protein have been documented in grey matter of patients with schizophrenia (Catts et al., 2015) and Alzheimer's disease (Yuki et al., 2014, Curran, 2018).

1.3.3 PSD95 post-translational modifications

The degradation and turnover of PSD95 protein can, together with removing the protein, erase a number of post-translational modifications (PTMs) that govern PSD95 localization, function, multiprotein complex assembly and synaptic plasticity. Below I discuss major PTMs affecting PSD95.

1.3.3.1 Ubiquitination

Ubiquitin is a small 76 amino acid protein that covalently attaches to lysine residues of substrate proteins (Vallejo et al., 2017). Ubiquitination is best known for tagging proteins to be degraded by the proteasome system. (Bianchetta et al., 2011) have identified five ubiquitination sites on PSD95: lysine 10 at N-terminus of the protein, lysine 403 that is located between PDZ3 and SH3 domains as well as lysins 544, 672 and 679 located within GK protein binding domain. (Ma et al., 2017) identified additional ubiquitination sites at

lysines 491, 558 and 703. Authors of this study make a crucial distinction between two types of ubiquitination: K48- and K63-linked. Conventional chains linked through lysine 48 of ubiquitin target substrate proteins for degradation via the proteasome while ubiquitin chains linked through lysine 63 modulate protein interactions, activity, localization and trafficking (Ma et al., 2017). Some of PSD95 ubiquitination sites are susceptible to both K48- and K63-linked ubiquitination (e.g. K491, K544 and K672) while others are specific to either K48 (K703) or K63 (K558). K63-linked polyubiquitination in K558 was shown to be required for PSD95 interactions with proteins SPAR and GKAP/SASAP, interactions that are important for linking glutamate receptors with downstream signaling pathways. Additionally, the lack of K558 polyubiquitination affected the ability of PSD95 to localize in synapses. Ubiquitination of PSD95 was found to be activity-dependent and exposure to NMDA resulted in increase in PSD95 ubiquitination and rapid removal from synaptic sites by proteasome-dependent degradation (Colledge et al., 2003). This increase in ubiquitination, however, must be K48-specific since NMDAR activation induces a drastic decrease in K63-linked polyubiquitination levels (Ma et al., 2017). K48 and K63 may therefore have reciprocal roles in ubiquitinating PSD95.

1.3.3.2 Phosphorylation

A reversible attachment of phosphate groups on serine, threonine and tyrosine residues by kinases represents one of the most wide-spread PTMs in synapses. Tens of phosphorylation sites have been identified for PSD95, some of which are located in protein binding domains while others in the interdomain sequences (Ballif et al., 2008, Pedersen et al., 2017). Phosphorylation of PSD95 affects the localization and stability of the protein as well as its ability to interact with binding partners and couple glutamate receptors to the downstream signaling pathways (Vallejo et al., 2017, Pedersen et al., 2017). Phosphorylation of tyrosine 533 and serine 295 increase synaptic localization of PSD95 (de Arce et al., 2010, Vallejo et al., 2017, Kim et al., 2007). In contrast, phosphorylation of threonine 19 or serine 73 is required for mobilization of PSD95 in response to neuronal activity (Nelson et al., 2013, Tsui and Malenka, 2006, Steiner et al., 2008, Nowacka et al., 2020).

Phosphorylation occurring in the N-terminus or within protein binding domains often affects the ability of PSD95 to interact with other synaptic proteins. The activity of kinase CDK-5 on tyrosine 19, serine 25 and serine 35 of N-terminus balances the sizes of synaptic clusters of PSD95 and the ability of PSD95 protein to cluster neuronal ion channels (Morabito et al., 2004). Phosphorylation of serine 561, located in GK domain of PSD95, regulates a conformational switch of the protein from open to closed. Nonphosphorylatable S561A mutation or inhibition of Par1 kinase activity leads to decreased interaction between SH3 and GK domains and causes PSD95 to adopt an open conformation (Wu et al., 2017). Open conformation induces higher stability of the protein, facilitates more interactions with binding partners but in return blocks structural plasticity of the dendritic spines.

1.3.3.3 Palmitoylation

Palmitoylation is a covalent attachment of palmitic acid, a saturated fatty acid, to specific cysteine residues via the formation of a thioester bond. Attachment of lipids changes the conformation of the affected proteins, increases their hydrophobicity and affinity to plasma membranes (Vallejo et al., 2017, Mumby, 1997). PSD95 undergoes reversible palmitoylation at cysteines 3 and 5 (C3 and C5) at the N-terminus of the protein (Topinka and Bredt, 1998, Craven et al., 1999). The attachment of palmitic acid has been shown to target PSD95 to synaptic membranes and removal of the modification expels PSD95 from the PSD (Craven et al., 1999, El-Husseini et al., 2002). Palmitoylation changes the conformation of PSD95 from ‘compact’ to ‘extended’ and only in the extended conformation the protein is able to associate with AMPARs and NMDARs (Jeyifous et al., 2016, El-Husseini et al., 2002). El-Husseini et al. (2002) show that palmitoylation of PSD95 is activity-dependent and dispersal of depalmitoylated PSD95 results in a selective loss of AMPAR subunits and AMPA receptor activity at synapses. The lipid-modification of PSD95 therefore is thought to not only modulate synaptic localization and molecular interactions of PSD95 but also contribute to molecular mechanisms of synaptic plasticity through regulation of AMPAR surface expression.

1.3.3.4 S-nitrosylation

Nitric oxide (NO), a reactive oxygen species, binds to the thiol side chain of cysteine residues within proteins in a process called S-nitrosylation (Hess et al., 2005, Vallejo et al., 2017). PSD95 was found to be physiologically S-nitrosylated at C3 and C5 by NO, the same residues that get affected by palmitoylation (Ho et al., 2011). As mentioned above, activity induces depalmitoylation of PSD95. At the same time, NMDA receptor activation causes calcium to enter the cells through the ion channel and bind calmodulin associated with nNOS and form NO. Newly generated NO nitrosylates PSD95 blocking free cysteines and maintaining PSD95 in a depalmitoylated state (Ho et al., 2011, Vallejo et al., 2017). S-nitrosylation therefore dynamically regulates the balance between palmitoylated and depalmitoylated form of PSD95.

1.3.3.5 Neddylation

In neddylation, Nedd8 (neural precursor cell-expressed developmentally regulated gene 8) is conjugated to the lysine of its substrate proteins via a substrate-specific ligase, a process resembling ubiquitination (Vallejo et al., 2017). Out of the MAGUK, Homer, GKAP and Shank scaffolding proteins tested, only PSD95 was found to be neddylated (Vogl et al., 2015). Neddylation occurred specifically on lysine 202 of PSD95, a residue that is located within PDZ 2 domain. Neurons containing mutant PSD95 in which neddylation on lysine 202 was impaired, failed to form mature dendritic spines despite normal PSD95 protein trafficking and retention in the spine (Vogl et al., 2015). Furthermore, blocking neddylation interfered with AMPA receptor clustering at the synapses and affected AMPAR-mediated currents (Brockmann et al., 2019).

In summary, post-translational modifications of PSD95 affect the localization and function of the protein and, in result, the structure and function of the PSD. While most of the discussed modifications are reversible, their removal is dependent on the presence of specific proteins and/or synaptic activity. The removal and replacement of PTM-modified PSD95 with newly made protein

offers one of the ways of erasing the ‘molecular memory’ of the protein and (to some extent) the PSD and bringing forward a blank slate for future ‘molecular learning’.

1.3.4 Synthesis and degradation of PSD95

PSD95 protein synthesis occurs both, in neuronal soma and locally in the dendrites (Rangaraju et al., 2017). During mRNA translation, multiple ribosomes can associate with individual mRNA, a complex known as polysome or polyribosome, leading to multiple copies of the encoded protein (Biever et al., 2020). Polyribosomes have been shown to localize not only to neuron cell bodies but also to dendrites and axons (Bodian, 1965, Steward and Fass, 1983, Ostroff et al., 2002, Ostroff et al., 2018, Hafner et al., 2019). Similarly, functional single ribosome associations with mRNA (monosomes) have been observed across the dendritic tree and axonal processes (Biever et al., 2020). For local translation, dendritically localized ribosomes would have to associate with dendritically localized mRNA transcripts. Several studies detect dendritically localized PSD95 mRNA in primary cell cultures (Donlin-Asp et al., 2021, Ifrim et al., 2015, Cajigas et al., 2012) and in brain tissue (Cajigas et al., 2012, Subramanian et al., 2011, Zalfa et al., 2007, Muddashetty et al., 2007). Ribosome profiling (Ribo-seq) of dendritically localized polysomes and monosomes captures PSD95 mRNA as one of the substrates (Biever et al., 2020) and locally translated PSD95 can be observed *in vitro* and in fixed brain tissue (Ifrim et al., 2015, Butko et al., 2012). The extent to which local protein translation contributes to dendritic protein supply remains to be confirmed, but Cajigas et al. (2012) estimate that as much as 30% of cell’s PSD95 mRNA is located in dendrites, a measurement made in neurons of rat hippocampal CA1. Substantial contribution of local translation to neuron proteome maintenance may allow for more rapid and specific stimulus-dependent proteome adaptations.

The degradation of PSD95 is mediated by ubiquitin-proteasome system (Colledge et al., 2003, Tsai et al., 2012) and can occur in cell soma or locally in the dendrites (Bingol and Schuman, 2006). Subunits of proteasome are

detected in neuronal dendrites and spines suggesting that the molecular degradation machinery is available for local protein hydrolysis (Bingol et al., 2010, Bingol and Schuman, 2006). E3 ligase targeting PSD95 protein for degradation is Mdm2 (Colledge et al., 2003). Colledge et al. (2003) found Mdm2 to be expressed in synapses, dendrites and cell bodies in primary neuronal cell culture providing further evidence for possible local degradation of PSD95 proteins.

Overall, PSD95 protein can be synthesized and degraded either in the cell soma or in the dendrites and synapses providing two complementary mechanisms for regulating PSD95 protein amounts, protein spatial distribution and lifetime. Local regulation of protein synthesis and degradation may result in synapse-specific rates of protein turnover, an intriguing possibility that is yet to be tested.

1.3.5 PSD95 protein lifetime estimates

PSD95 protein lifetime has previously been measured in primary cell cultures (Ehlers, 2003, El-Husseini et al., 2002, Cohen et al., 2013, Kratschke, 2018, Heo et al., 2018a, Heo et al., 2018b) and *in vivo* (Fornasiero et al., 2018, Heo et al., 2018b, Price et al., 2010). Previous findings for PSD95 half-life are summarized in **Table 1.4**. PSD95 half-life was found to range from 8 hours in an *in vitro* measurement to ~30 days measured *in vivo*. On average, protein lifetime estimates were smaller *in vitro* compared to *in vivo* as is well documented (Cohen and Ziv, 2019, Alvarez-Castelao and Schuman, 2015). Even between measurements made *in vitro* (and similar for *in vivo)* we see a large variation in half-life values, the difference between the smallest and largest estimates being 11-fold. Some of the differences observed may be explained by: (a) regions of the brain and/or parts of the cell used for analysis and (b) the number and spacing of time points used for estimating the half-life. Ehlers (2003), Cohen et al. (2013) and Heo et al. (2018b) examine PSD95 lifetime in primary cortical neurons, El-Husseini et al. (2002) carry out measurements in primary hippocampal neurons, and Kratschke (2018) estimates PSD95 half-life from both, cortical and hippocampal cultures.

Additionally, Ehlers (2003) and Kratschke (2018) focus exclusively on synaptically localized PSD95 in cell cultures while El-Husseini et al. (2002) and Cohen et al. (2013) prepare extracts from whole cells which may also include non-synaptic PSD95. For *in vivo* studies, Price et al. (2010) carry out measurements on whole brain homogenates while Heo et al. (2018b) focus on synaptosomes from cortex and hippocampus and Fornasiero et al. (2018) carry out measurements on tissue homogenates and synaptosome preparations from cortex and cerebellum. All studies use different numbers of time points for sample collection after labelling and space them out over varied number of days. The number of time points used for sample collection ranges from 2 in Heo et al. (2018b) to 9 in Price et al. (2010). Larger number of time points provides more information for fitting of exponential decay function and may result in more accurate half-life values. In terms of spacing of time points, some studies followed PSD95 for a maximum of 48 hours (Ehlers, 2003, Kratschke, 2018) while others tracked protein decay for up to 32 days (Price et al., 2010). Despite the differences in experimental protocols for measuring PSD95 half-life, the studies identify PSD95 half-life to be in the order of hours (*in vitro*) or days (*in vivo*). The measurements carried out in the discussed studies, however, relied on bulk protein extracts and thus lacked spatial resolution to identify and document cell-type- or synapse-specific protein lifetimes.

Higher spatial and temporal resolution for measuring PSD95 protein lifetime was achieved using FRAP (fluorescence recovery after photobleaching). Several *in vitro* (Nakagawa et al., 2004, Sharma et al., 2006, Kuriu et al., 2006, Hruska et al., 2015) and *in vivo* (Gray et al., 2006) studies estimated PSD95 lifetime to be in the order of minutes to hours. FRAP measurements, however, are very sensitive to diffusion and other movement of molecules in addition to protein turnover which may affect the interpretation of half-life estimates.

Reference	Model system	Estimation method	PSD95 half-life
Ehlers (2003)	Rat primary cortical neurons (synaptosomes)	^{35}S - Met	8 hours
El-Husseini et al. (2002)	Rat primary hippocampal neurons	^{35}S - Met	36 hours
Cohen et al. (2013)	Rat primary cortical neurons	SILAC: lysine ($^{13}C_6$, $^{15}N_2$) and arginine ($^{13}C_6$, $^{15}N_4$).	3.67 days
Price et al. (2010)	Mouse (*in vivo*)	^{15}N-enriched Spirulina platensis	15.3 days
Heo et al. (2018b)	Mouse (*in vivo*), synaptosomes from cortex and hippocampus & rat primary cortical neurons	L-Lysine $^{13}C_6$	1.74 days (*in vitro*), ~30 days (*in vivo*)
Fornasiero et al. (2018)	Mouse (*in vivo*), synaptosome from cortex and cerebellum	L-Lysine $^{13}C_6$	Homogenate (days): cortex = 15.66, cerebellum = 11.70. Synaptosomes (days): cortex = 16.43, cerebellum = 12.73.
Kratschke (2018)	Mouse primary hippocampal and cortical neurons	HaloTag fluorescence pulse-chase	~36 hours

Table 1.4: The summary of recent literature on PSD95 protein lifetime estimates.

1.3.6 Summary

PSD95 is an important scaffolding protein and one of the most abundant proteins in the PSD. PSD95 clusters glutamate receptors at the synapse and links these receptors to downstream signaling pathways to form functional molecular networks. Maturation of synaptic connections requires PSD95 as does learning and memory storage in the brain. Mutations in PSD95 or its interacting proteins have been linked to a number of neurodevelopmental, psychiatric and neurodegenerative disorders. The localization and function of

PSD95 is modulated by multiple post-translational modifications which could in theory be erased by the replacement of 'old' PSD95 protein with 'new'. PSD95 is synthesized and degraded both, at the cell soma and locally in the dendrites, and the lifetime of PSD95 is in the order of a few hours *in vitro* or a few days *in vivo* as recorded from bulk protein preparations.

1.4 Thesis aims and outline

1.4.1 Develop methods for *in vivo* brain wide single-synapse resolution mapping of protein lifetime

In order to visualize and track synaptic protein lifetime, I propose to adapt the HaloTag technology for *in vivo* fluorescence labelling. HaloTag protein is a modified haloalkane dehalogenase, a bacterial protein that was designed to irreversibly bind to small synthetic ligands, called HaloTag ligands (Los et al., 2008b). HaloTag protein can be fused to any protein of interest and has previously in the lab been fused to endogenous PSD95 (**Figure 1.3A**). HaloTag ligands can be coupled to a variety of moieties, including fluorescent dyes, affinity tags and surface ligands for protein immobilization, through a chloaralkane linker (England et al., 2015). For this thesis, I aim to use fluorophore coupled HaloTag ligands to visualize the endogenous PSD95. I aim to inject HaloTag ligands into living animals and label PSD95 with a fluorescent date-stamp (**Figure 1.3B**). I could then measure the lifetime of PSD95 by visualizing the duration that the fluorescent label is retained.

PSD95 is primarily located in synaptic structures which are known to be dynamic and to have a lifetime of several days to several months. In my studies, it will be important to dissect the contribution of synaptic structure turnover to the protein lifetime measurement as observed by decay of fluorescently labelled PSD95. Additional markers of synapses will be required and one of the following routes could be taken: (a) employing additional fluorescent markers of stable synaptic proteins (e.g. other scaffolding proteins) and (b) labelling a subpopulation of neurons in PSD95-HaloTag mice with a fluorescent dye that fills the dendrites and reveals synaptic structures.

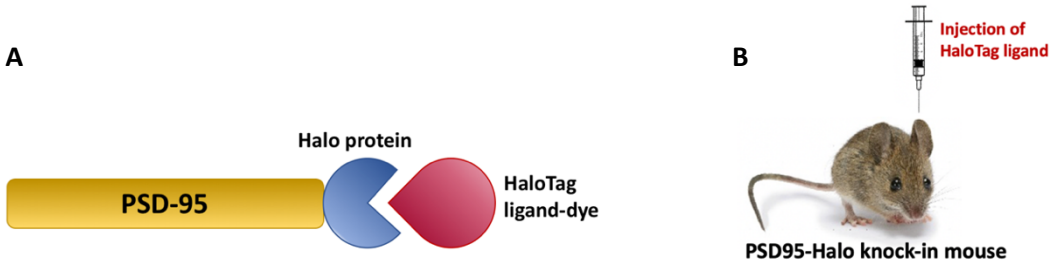

Figure 1.3: Adapting HaloTag technology to visualise and measure PSD95 protein lifetime in mouse brain. (A) *HaloTag protein is fused to the endogenous PSD95. HaloTag protein acts as a receptor for HaloTag ligand-dye compounds and forms a covalent bond with the ligands.* ***(B)*** *Injection of HaloTag ligands into living animals to fluorescently label PSD95-HaloTag fusion protein.*

In order to visualize HaloTag-labelled synaptic PSD95 across large areas of brain tissue, I could employ previously in-house developed single-synapse resolution mapping technologies (**Figure 1.4**). Here, fluorescent tags inserted into endogenous synaptic proteins can be visualized across the brain using single-synapse resolution (~280 nm in xy) fast spinning disc confocal microscopy. Synapse molecular and morphological characteristics can then be extracted for different brain regions and subregions. Several peer-reviewed studies have already documented the diversity of synapses in adult mouse brain in health and disease (Zhu et al., 2018) and the changes in synapse composition occurring throughout the lifespan (Cizeron et al., 2020). I propose to exploit the strengths of these mapping technologies in my studies to achieve single-synapse resolution large-scale mapping of fluorescent HaloTag markers.

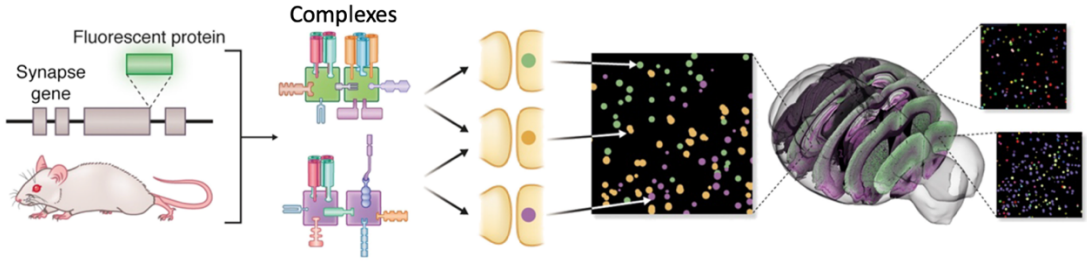

Figure 1.4: A summary of in-house developed single-synapse resolution mapping pipeline. *Fluorescently tagged endogenous proteins are visualised using single-synapse resolution confocal spinning disc microscopy. Images covering multiple brain areas can be used to uncover region-specific synapse molecular compositions and morphologies in turn revealing the diversity of synapses across the mouse brain.*

In **Chapter 2**, I summarize the materials and methods used in studies presented in this thesis.

In **Chapter 3**, I present optimization of PSD95-HaloTag labelling with fluorescent ligands in mouse brain.

1.4.2 Visualize and map the lifetime of synaptic PSD95

In **Chapters 4-6**, I focus on experimental results from mapping the lifetime of synaptic PSD95 across mouse brain.

Chapter 4 presents PSD95 lifetime estimates for 110 subregions in adult mouse brain. The study uncovers the surprising diversity of PSD95 lifetimes at the level of brain regions, subregions, cell types, different parts of the dendritic tree and individual synapses. Synapse subtype analysis reveals subpopulation of synapses with short-protein-lifetime (SPL) and subpopulation with long-protein-lifetime (LPL).

Chapter 5 describes the changes in PSD95 lifetime throughout the lifespan. The lifetime of PSD95 is assessed in and compared between developing (3-week-old), mature (3-month-old) and ageing (18-month-old) mice. Changes in SPL and LPL synapse numbers are discussed.

Chapter 6 identifies changes in PSD95 lifetime in two mouse models of brain disease: (1) mice lacking PSD93 protein which model the genetic risk for schizophrenia and autism in humans and (2) SynGAP mutants that model a genetic cause for autism spectrum disorder and intellectual disability.

Chapter 2 Materials and Methods

2.1 Ethics compliance

Animal procedures were performed in accordance with UK Home Office regulations and approved by Edinburgh University Director of Biological Services.

2.2 Mouse model

2.2.1 PSD95-Halo Knock-in (KI) mouse line

2.2.1.1 Generation of mouse line

The project centres on the use of a mouse line in which the *Psd95* (*Dlg4*) gene was modified so that the endogenous PSD95 protein is fused at its C-terminus with the HaloTag domain (**Figure 2.1**). Hereafter this model is designated as $PSD95^{HaloTag/HaloTag}$ (homozygous allele) or $PSD95^{+/HaloTag}$ (heterozygous allele) and referred to as PSD95-HaloTag (Masch et al., 2018).

The mice were previously generated by members of the laboratory (David Fricker and Ellie Tuck under the supervision of Dr Noboru Komiyama and Professor Seth Grant) and the procedure is described in detail in Kratschke (2018). The gene targeting strategy adapted from Fernández et al. (2009) was used to fuse HaloTag protein to the C-terminus of endogenous PSD95. The HaloTag coding sequence (Promega) together with a short linker were inserted into the open reading frame of the *Psd95* gene, followed by insertion of a LoxP floxed PGK-EM7-neo-pA cassette, using recombination in *Escherichia coli.* E14Tg2a ES cells (from 129P2 ola) were used for gene targeting. Positive targeting clones were identified using PCR and E3.5 blastocysts from C57BL6 mice were injected with ES cells containing the target gene. Male chimeras were crossed with C57BL6 female to produce first generation heterozygous animals. In order to remove the LoxP floxed neo cassette *in vivo*, the animals were then crossed with CAG Cre-recombinase-expressing mice. Once the neomycin cassette was removed, animals were intercrossed to produce a colony of homozygous PSD95-HaloTag mice.

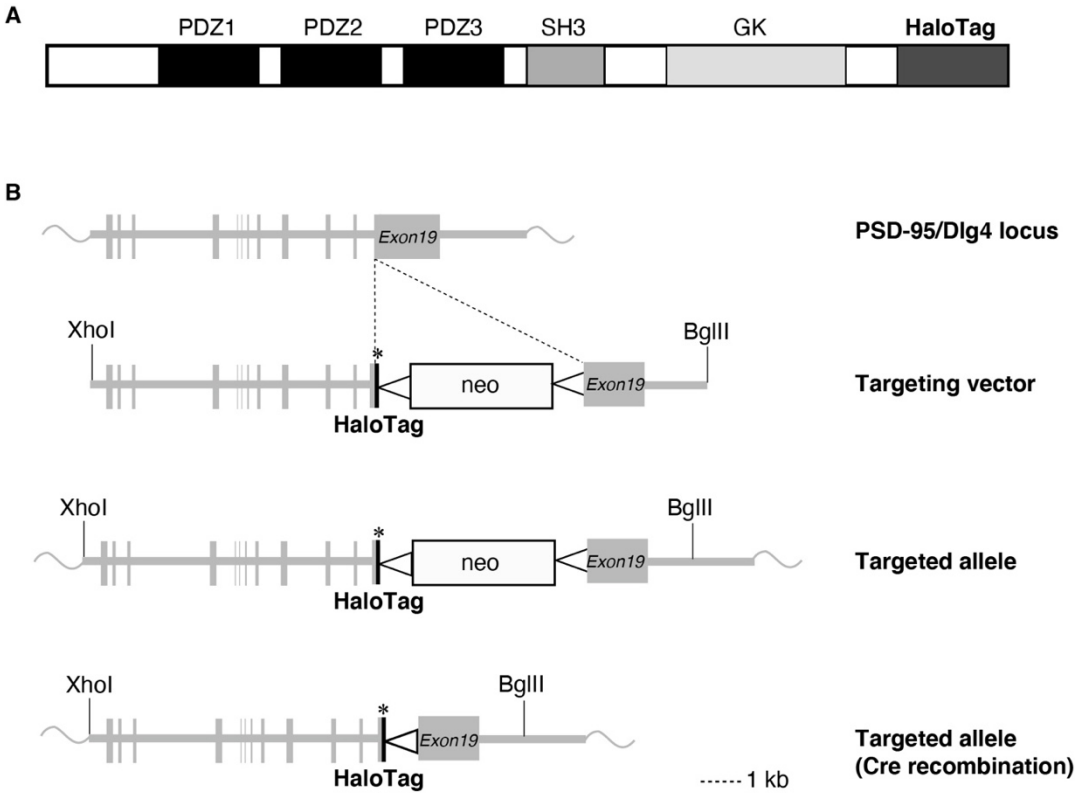

Figure 2.1: Generation of the PSD95-HaloTag knock-in mouse. (A) *PSD95-HaloTag protein domain structure. PSD95 contains three PDZ domains followed by SRC homology 3 (SH3) and guanylate kinase (GK) domains. The HaloTag is fused to the C-terminus of PSD95.* ***(B)*** *Targeting strategy used to insert the HaloTag sequence before the stop codon of Psd95 gene (asterisk). The neomycin resistance cassette (neo) was removed from between loxP sites (triangles) by crossing the PSD95-HaloTag mouse with a transgenic Cre recombinase-expressing mouse.*

2.2.1.2 Characterization of mouse line

To test the possibility that the presence of the HaloTag domain interferes with the function of PSD95, the expression of the proteins and synaptic physiological function of mice carrying the mutation were evaluated, as described below.

2.2.1.2.1 Biochemical characterisation

To biochemically test the PSD95-HaloTag knock-in mouse line for phenotypic abnormalities, PSD95 protein expression and abundance was tested in protein extracts from synaptosomes prepared from the whole-brain of wild-type, $PSD95^{+/HaloTag}$ and $PSD95^{HaloTag/HaloTag}$ mice (for further details, see Kratschke

(2018)). Three extracts per genotype were loaded into 4-12% gradient Bis-Tris gels, with 20 μl loaded into each well and gels were subsequently subjected to SDS PAGE and western blotting. The membrane was sequentially probed with antibodies recognising (a) PSD95, (b) PSD95-HaloTag and (c) alpha-Tubulin (loading control). Bands corresponding to PSD95, PSD95-HaloTag and alpha-Tubulin were then detected using the LI-COR Odyssey imaging system.

Wild type PSD-95 has a molecular weight of 80 kDa (Husi et al., 2000, Cai et al., 2006) and the band at 80 kDa was detected in all $PSD95^{+/+}$ and $PSD95^{+/HaloTag}$ samples (**Figure 2.2A**). The HaloTag protein is 33 kDa in size (Los et al., 2008b, Lang et al., 2006) and thus the PSD95-HaloTag protein is expected to have a molecular weight of 113 kDa. Results from western blot analysis revealed 113 kDa bands in $PSD95^{+/HaloTag}$ and $PSD95^{HaloTag/HaloTag}$ samples with genotype-dependent band intensity (**Figure 2.2A, B, F**). Total amounts of PSD95 protein were not different between the genotypes (single factor ANOVA, [$F(2,6) = 0.63$, $P = 0.57$) (**Figure 2.2E**). To test whether PSD95-HaloTag protein can still assemble into multiprotein complexes in the PSD, we subjected the synaptosome preparations $PSD95^{-/-}$, $PSD95^{+/+}$ and $PSD95^{HaloTag/+}$ animals to Blue native PAGE (**Figure 2.2C, D**). Separated 1.5 MDa multiprotein complexes were detected when probed with anti-PSD95 and anti-HaloTag antibodies. 1.5 MDa complexes are composed of a number of PSD proteins, including NMDA receptor subunit NR2B, PSD95's homologue PSD93 and downstream signalling molecules (Frank et al., 2016). Overall, the PSD95-HaloTag KI mutation did not affect the overall expression levels of PSD95 in mice or the ability of PSD95-HaloTag fusion protein to assemble into multiprotein complexes in the post-synapse. The discussed experiments, however, were performed on synaptosome preparations and not PSD preparations, and wild-type PSD95 protein is known to be more highly enriched in PSD fractions compared to synaptosome fractions (Bai and Witzmann, 2007, Villasana et al., 2006). With the data presented here we cannot exclude the possibility that PSD95-HaloTag protein is not localising to the PSD in the same way that the wild-type PSD95 protein would. The fact that PSD95-HaloTag is still able to assemble into multi-protein complexes involving

NMDA receptors and other signalling molecules suggests that the HaloTag does not interfere with normal function of the protein. Additional biochemical experiments on PSD fractions would be needed to confirm appropriate localisation and function of HaloTag-fused PSD95 protein. The experiments were performed by Dr Max Kratschke.

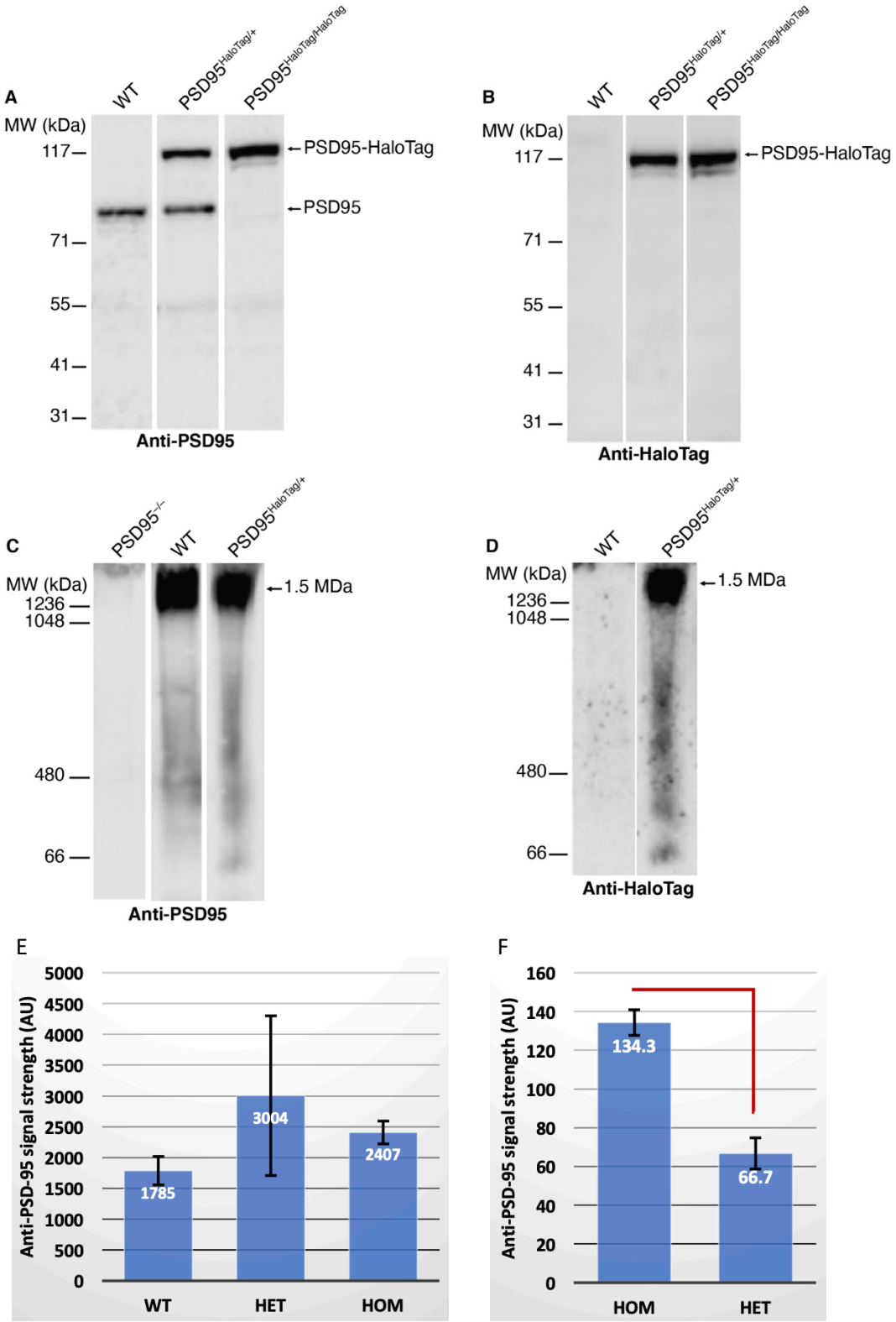

Figure 2.2: PSD95 protein expression in PSD95-HaloTag KI animals. (A) *Western blot on synaptosome preparations from PSD95$^{+/+}$, PSD95$^{HaloTag/+}$ and PSD95$^{HaloTag/HaloTag}$ mice stained with an antibody against PSD95 (Mouse, BD Bioscience, 1:5000). 80 kDa bands in PSD95$^{+/+}$ and PSD95$^{HaloTag/+}$ columns correspond to wild-type PSD95, while PSD95-HaloTag band appears at 113 kDa.* ***(B)*** *The same set of synaptosome preparations as in (A) probed with anti-*

HaloTag antibody (Mouse, Promega, 1:1000) reveals a strong band at 113 kDa in preparations from PSD95$^{HaloTag/+}$ and PSD95$^{HaloTag/HaloTag}$ animals. ***(C, D)*** *PSD95-HaloTag assembles into 1.5 MDa postsynaptic supercomplexes. Blue native PAGE was used to separate the synaptosome preparations described in (A, B) and probed with antibodies against PSD95 (C) and HaloTag (D).* ***(E)*** *Quantification of protein expression presented in (A). No significant difference found in PSD95 protein levels between PSD95$^{+/+}$, PSD95$^{HaloTag/+}$ and PSD95$^{HaloTag/HaloTag}$ samples (single factor ANOVA, [F (2,6) = 0.63, P = 0.57]).* ***(F)*** *Quantified protein levels from (B). Heterozygous animals were found to express 49.7% of the PSD95-HaloTag protein expressed by the homozygous mice (Welch's t-test: p = 0.003). Error bars: +/- SEM. N = 3 mice / genotype group. Adapted from Dr Max Kratschke's PhD thesis.*

2.2.1.2.2 Electrophysiological characterisation

Decreased expression of PSD95 protein can lead to altered electrophysiological profiles (Migaud et al., 1998). To assess whether genetic manipulation of PSD95 protein has any effects on electrophysiological properties of these mice, we examined: (1) Fibre volley/fEPSP input/output curves generated by eliciting fEPSPs, (2) paired-pulse facilitation; (3) excitatory postsynaptic currents (EPSCs); (4) ratio of NMDAR to AMPAR-mediated currents; (5) weighted decay time constants for currents; (6) examples of sEPSCs; (7) fEPSP profiles in brain slices after LTP induction (**Figure 2.3**). PSD95-HaloTag mice did not differ from WT in any of the parameters examined therefore were electrophysiologically normal. The experiments were performed by our collaborator Dr Thomas O'Dell.

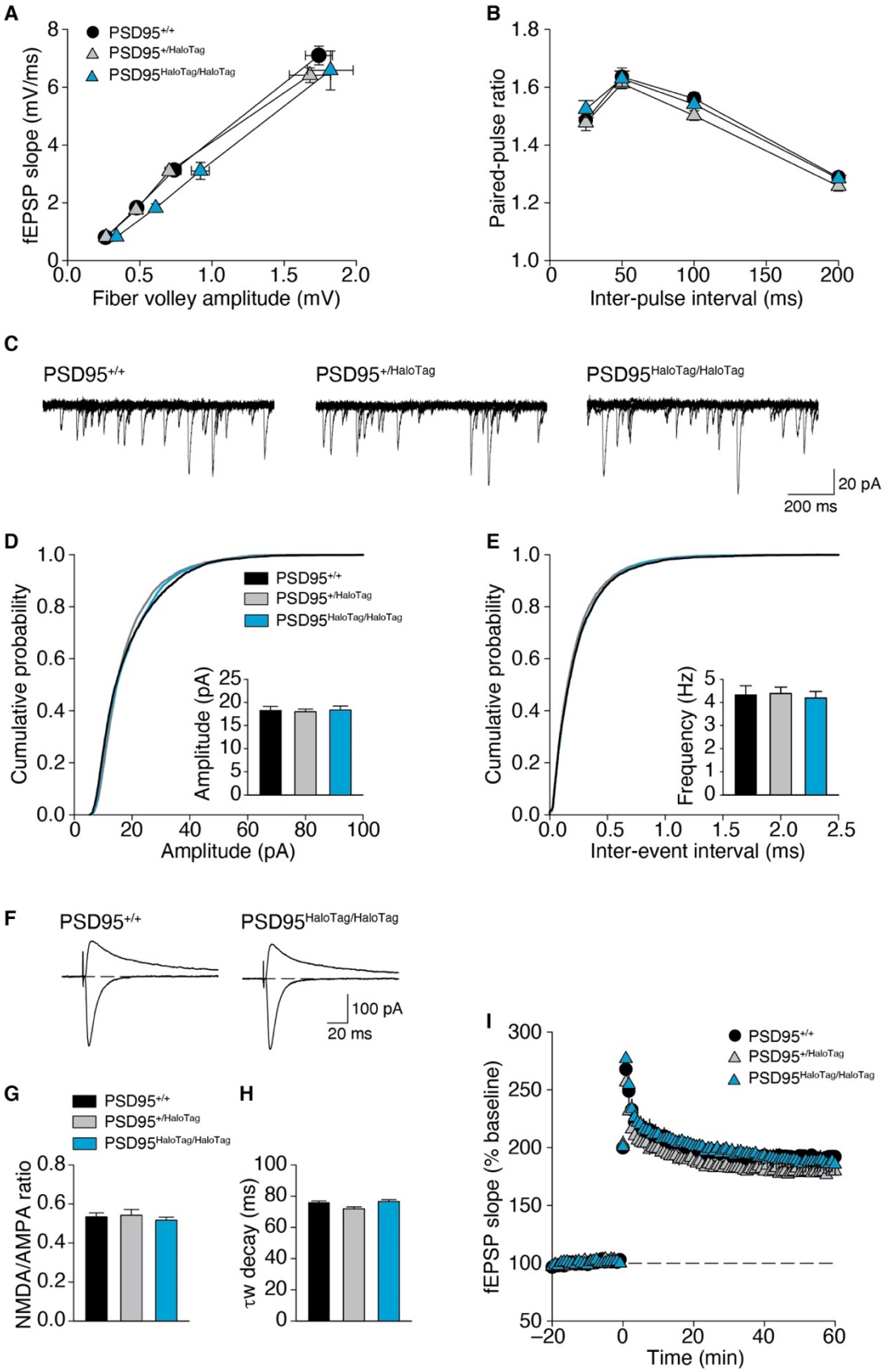
A
PSD95+/+
PSD95+/HaloTag
PSD95HaloTag/HaloTag
fEPSP slope (mV/ms)
Fiber volley amplitude (mV)
B
Paired-pulse ratio
Inter-pulse interval (ms)
C
PSD95+/+
PSD95+/HaloTag
PSD95HaloTag/HaloTag
20 pA
200 ms
D
Cumulative probability
Amplitude (pA)
Amplitude (pA)
E
Cumulative probability
Inter-event interval (ms)
Frequency (Hz)
F
PSD95+/+
PSD95HaloTag/HaloTag
100 pA
20 ms
G
NMDA/AMPA ratio
H
τw decay (ms)
I
fEPSP slope (% baseline)
Time (min)

Figure 2.3: PSD95-HaloTag KI animals do not display electrophysiological abnormalities. (A) *fEPSP curves from stratum radiatum of the CA1 generated with 100, 75, 50 and 25% of maximum stimulation of Schaffer collateral fibers.* ***(B)*** *Normal paired-pulse facilitation in mutant animals.* ***(C)*** *Representative excitatory post-synaptic currents (EPSCs) recorded in wild-type and mutant animals at -80 and +40 mV membrane potential.* ***(D, E)*** *Genetic KI did not affect the cumulative probability distributions of (D) EPSC amplitudes (1-way ANOVA, F (2,8) = 0.049, P = 0.952) and (E) inter-event intervals (F (2,8) = 0.836, P = 0.921).* ***(F)*** *Examples of EPSCs recorded at membrane potential of -80 and +40 mV.* ***(G)*** *Ratio of NMDAR to AMPAR-mediated currents is not affected in mutant animals (1-way ANOVA, F (2,11) = 0.345, P = 0.717).* ***(H)*** *No differences observed in weighted decay time constant for currents elicited at +40 mV (F (2,11) = 3.602, P = 0.071).* ***(I)*** *LTP induction did not differ between wild-type and KI animals (1-way ANOVA, F (2,11) = 1.706, P = 0.226). n (PSD95$^{+/+}$) = 3-5 animals, n (PSD95$^{HaloTag/+}$) = 3-5 animals and n (PSD95$^{HaloTag/HaloTag}$) = 3-4 animals.*

2.2.1.2.3 *In vitro* PSD95-HaloTag fluorescence labelling

HaloTag protein covalently binds exogenous HaloTag ligands coupled with fluorescent dyes and allows visualization of HaloTag fusion proteins (Los et al., 2008b, England et al., 2015). We tested the efficiency and reliability of fluorescence labelling of PSD95-HaloTag fusion proteins by applying Tetra-methyl-rhodamine-Halo (TMR-Halo) ligand to living primary neuronal cultures from PSD95$^{+/HaloTag}$ and PSD95$^{+/+}$ mice and compared this with antibody labelling for PSD95. PSD95 antibody labelling showed strong punctate expression in both PSD95$^{+/HaloTag}$ and PSD95$^{+/+}$ neuronal cultures characteristic of punctate expression of PSD95 protein in neuronal synapses (**Figure 2.4A**). TMR-Halo labelling, in contrast, was detected in PSD95$^{+/HaloTag}$ neuronal culture and not in the PSD95$^{+/+}$ culture. Importantly, TMR-Halo punctate fluorescence labelling co-localised with anti-PSD95 antibody labelling denoting the specificity of HaloTag labelling.

Next, we asked if PSD95-HaloTag protein was found in the postsynaptic terminal of excitatory synapses. We asked if the puncta containing PSD95-HaloTag labelled with TMR-Halo ligand were juxtaposed to puncta labelled with two presynaptic protein markers, Synapsin1 and VGlut1. Synapsin1 is found in most presynaptic terminals and VGlut1 is exclusively found in presynaptic terminals of excitatory synapses (Takamori et al., 2000, Wojcik et al., 2004, De Camilli et al., 1983). TMR-Halo labelling in primary neuronal cultures was indeed juxtaposed to presynaptic markers and localised to the

post-synaptic density of neuronal synapses (**Figure 2.4B, C**). Overall, the fluorescence labelling experiments *in vitro* have demonstrated specific and reliable fluorescence labelling of PSD95-HaloTag fusion protein using HaloTag ligands. The experiments were performed by Dr Max Kratschke.

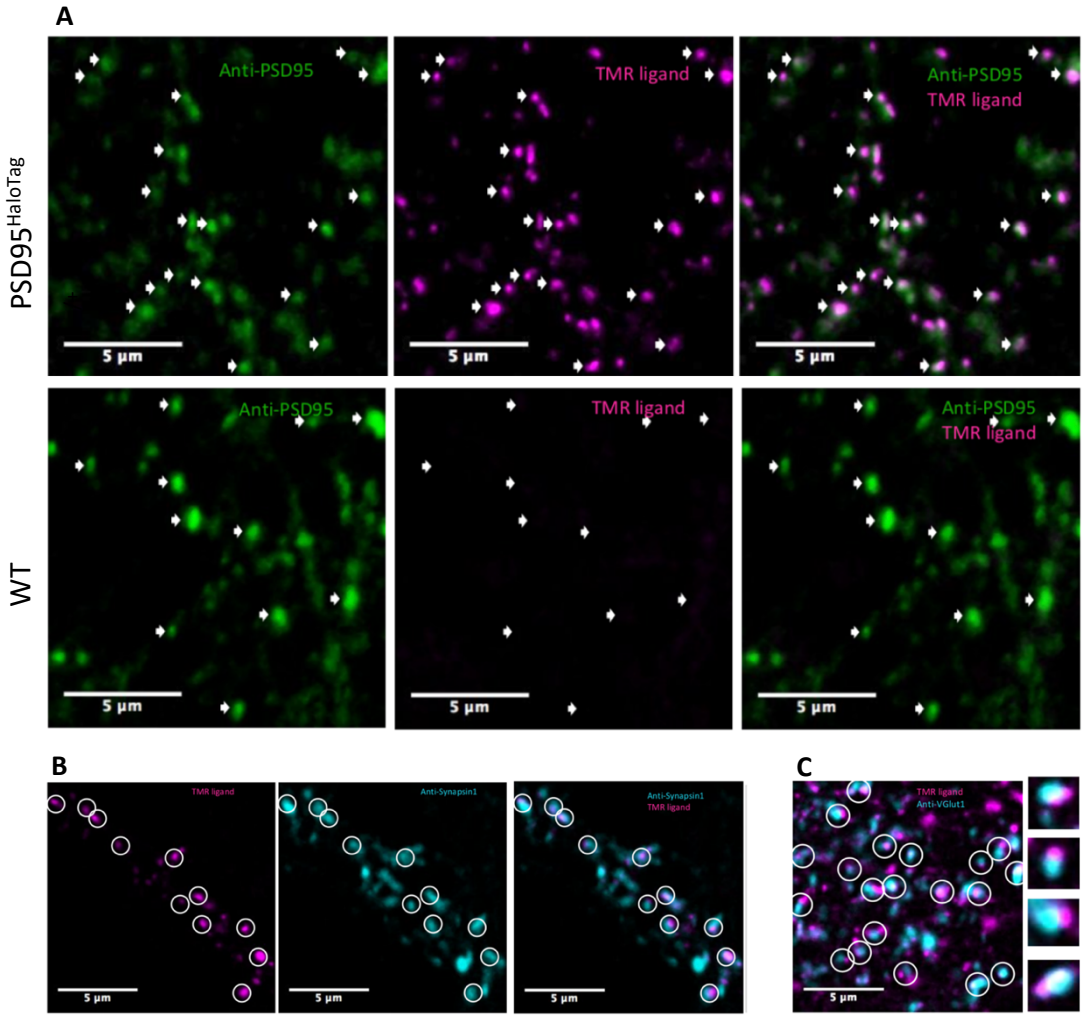

Figure 2.4: Specific and reliable PSD95-HaloTag fluorescence labelling in primary neuronal cell cultures. (A) *PSD95-HaloTag neuronal cell cultures labelled with TMR-Halo fluorescent ligand show punctate expression that co-localises with antibody labelling against PSD95. TMR-Halo does not bind and produce fluorescence in PSD95$^{+/+}$ neuronal cells.* ***(B)*** *PSD95-HaloTag fusion protein labelled with TMR-Halo juxtapositions fluorescently labelled presynaptic marker Synapsin1.* ***(C)*** *TMR-Halo labelled PSD95 juxtapositions antibody-labelled presynaptic VGlut1. Adapted from Dr. Max Kratchke's PhD thesis.*

2.2.2 Mouse breeding

2.2.2.1 PSD95-eGFP/SAP102-mKO2/PSD95-HaloTag

To create mice expressing PSD95-HaloTag, PSD95-eGFP and SAP102-mKO2, we crossed double homozygous *Psd95*$^{eGFP/eGFP}$;*Sap102*$^{mKO2/mKO2}$ mice (described previously in Zhu et al. (2018) and Cizeron et al. (2020)) were crossed with PSD95$^{HaloTag/HaloTag}$ mice. The KI strategy used for generating PSD95-eGFP and SAP102-mKO2 was as described in Fernández et al. (2009). In summary, the fluorescent protein coding sequences (eGFP for PSD95 and mKO2 for SAP102) were inserted into the C terminus of endogenous PSD95 and SAP102, respectively. The PSD95$^{HaloTag/eGFP}$;SAP102$^{mKO2/y}$ colony was used for experiments described in **Chapter 3** and **Chapter 4** of my thesis.

2.2.2.2 PSD93-KO/PSD95-HaloTag

Mice carrying a targeted 'knockout' allele of the *Dlg2* gene (*Dlg2*$^{-/-}$) lack PSD93 protein (this mouse line is referred to as PSD93$^{-/-}$). PSD93$^{-/-}$ and PSD95$^{HaloTag/HaloTag}$ mice were intercrossed to generate PSD95$^{+/HaloTag}$;PSD93$^{+/-}$ and with further inter-crosses PSD95$^{+/HaloTag}$;PSD93$^{-/-}$ mice. The PSD93$^{-/-}$ line was kindly shared with us by Prof D.S. Bredt's lab. The gene knockout mutation was induced by replacing a necessary coding exon in the second PDZ domain by a neomycin resistance cassette (McGee et al., 2001a).

For experiments described in **Chapter 6**, we used PSD95$^{+/HaloTag}$;PSD93$^{+/-}$, PSD95$^{+/HaloTag}$;PSD93$^{-/-}$ and PSD95$^{+/HaloTag}$;PSD93$^{+/+}$ The use of heterozygous and homozygous animals for PSD93 allowed us to test for effects of gene dosage on the turnover of PSD95.

2.2.2.3 SynGAP-KO/PSD95-HaloTag

Mice carrying a 'knockout' allele of the *Syngap1* gene (*Syngap1*$^{+/-}$) have reduced SynGAP protein expression (the mouse line is later referred to as SynGAP$^{+/-}$). SynGAP$^{+/-}$ mice were crossed with PSD95$^{HaloTag/HaloTag}$ to generate PSD95$^{+/HaloTag}$;SynGAP$^{+/-}$ mice. The null mutation in *Syngap1* gene was generated by constructing a targeting vector that deletes exons encoding

the C2 and GAP domains in SynGAP (Komiyama et al., 2002). PSD95$^{+/HaloTag}$;SynGAP$^{+/-}$ and PSD95$^{+/HaloTag}$;SynGAP$^{+/+}$ animals were used for the studies described in **Chapter 6**. Homozygous knockout of SynGAP is lethal therefore only animals containing a heterozygous mutation were used for the study (Komiyama et al., 2002).

2.3 Genotyping

2.3.1 Tissue collection

Initial genotyping was performed on ear clipped tissue, collected from mice at 3 weeks of age. On the day of perfusions and brain dissection, 2 samples of ~2 mm tail tissue from experimental animals was obtained following complete anaesthesia. A second round of genotyping was performed on one of the samples to confirm the genotype and the second tail sample was stored at -20^{o}C as a backup in case of any uncertainties in genotyping results from initial ear clip and tail clip samples.

2.3.2 Polymerase Chain Reaction (PCR) protocol

A tail sample for genotyping is first digested at 65 ^{o}C in 50 µL solution containing 100 mM KCl, 10 mM Tris (pH 8), 0.5% Tween 20, 1% Triton 100x and 10 U/mL of Proteinase K (NEB-P8107S). PCR reaction was set up with BioLine MyTaq^{TM} DNA Polymerase (BIO-21105). PCR mixes were prepared with 5 µL of PCR buffer, 0.5 µL of each primer (20 µM), 0.1 µL Taq enzyme, 2 µL of DNA and up to 10 µL ddH_2O to reach a final volume of 20 µL (please see **Table 2.1** for specific primers and their respective annealing temperatures). The DNA-primer solutions were then placed in a PCR machine with specific temperature cycles as per below:

95°C - 15 mins

94°C - 45 sec
Var - 45 sec } 35 cycles

72°C - 2 min

72°C - 10 mins

4°C - ∞

PCR products were resolved on 2% agarose gel stained with GelRed® Nucleic Acid Gel Stain (Biotium). PCR analyses were performed by Dr Rand Dahan and Gabor Varga.

Allele	PCR primers			
	Name	Sequence	Annealing temperature	Amplification product
PSD95-HaloTag	95GFPExF_N1	GTCACATGTCTTTGTGACCTTG	55ºC	WT 330bp
	95GFPUTRR_N1	GATACATGCAGAGAGGAGTGTC		Mut ~650bp
	HalogenF	CTGACTGAAGTCGAGATGGAC		
PSD95-eGFP	95GFPExF_N1	GTCACATGTCTTTGTGACCTTG	55ºC	WT 330bp
	95GFPUTRR_N1	GATACATGCAGAGAGGAGTGTC		Mut 514bp
	95GFP_FN2	CATCAAGGTGAACTTCAAGATC		
SAP102-mKO2	SAP102 wt F GV	CAAATCATTGAGGACCAGTCTGGGC	57ºC	WT 130bp
	SAP102 com R GV	GGAATGAAGAGGAAGGAGGGAAGAGG		Mut ~300bp
	SAP102 mKOF3-1	GCCAGATGAAGACCACCTACAAG		
PSD93-KO	PSD-93Neo	GCCTTCTATCGACTTCTTGACGAG	57ºC	WT 330bp
	PSD-93intron	GTGCGGAATGTTGTTGTGCAGTGC		Mut 750bp
	PSD-93exon-n2	ACAACAGTCTCCAATATGGGTCGC		
SynGAP-KO	FCASS1a	CTTCCTCGTGCTTTACGGTATC	55ºC	WT 591bp
	SYNcomR	CTGATCAGCCTGTCAGCAATG		Mut 1kb
	SYNwtF	GTCAGTGGGACATGGAAGTAG		

Table 2.1: Name, sequence and annealing temperatures for primers used in genotyping experimental mice.

2.4 HaloTag ligand generation

2.4.1 Fluorescent HaloTag ligands

In order to visualize the turnover of PSD95-HaloTag fusion protein, we coupled Halo ligand with a set of cell-permeable fluorophores, including silicon-rhodamine (SiR) and tetramethyl-rhodamine (TMR) dyes. The control and optimisation experiments presented in **Chapter 3** were performed with the following HaloTag-dye compounds: SiR-Halo (Lukinavičius et al., 2013, Butkevich et al., 2017), JF646-Halo (Grimm et al., 2015, Grimm et al., 2017),

TMR-Halo (Promega Ltd.) and JF549-Halo (Grimm et al., 2015). **Table 2.2** outlines further fluorescence characteristics of the dyes used.

Name	Excitation wavelength (nm)	Emission wavelength (nm)	Is the dye fluorogenic?
SiR	645	661	Yes
JF646	646	664	Yes
TMR	555	585	No
JF549	549	571	No

Table 2.2: Fluorescence properties of dyes used in the HaloTag experiments.

Experiments presented in **Chapters 3-6** were performed with SiR-Halo ligand due to its reliable *in vivo* labelling, as previously established (Masch et al., 2018). In addition, SiR-Halo and JF646-Halo offer an important advantage for intracellular application: both dyes are fluorogenic compounds which means that they only fluoresce when bound to their target (i.e. HaloTag protein). The fluorogenic property of rhodamine dyes rests in the equilibrium between the lipophilic, colourless lactone conformation and polar, fluorescent zwitterion conformation (**Figure 2.5**, Grimm et al. (2020)). Upon binding to the HaloTag protein, the conformation of SiR-Halo and JF646-Halo shift from the non-fluorescent lactone form to the fluorescent zwitterion form. The fluorogenic property of these dyes leads to a higher signal-to-noise ratio in the resulting fluorescence images due to the reduced background fluorescence.

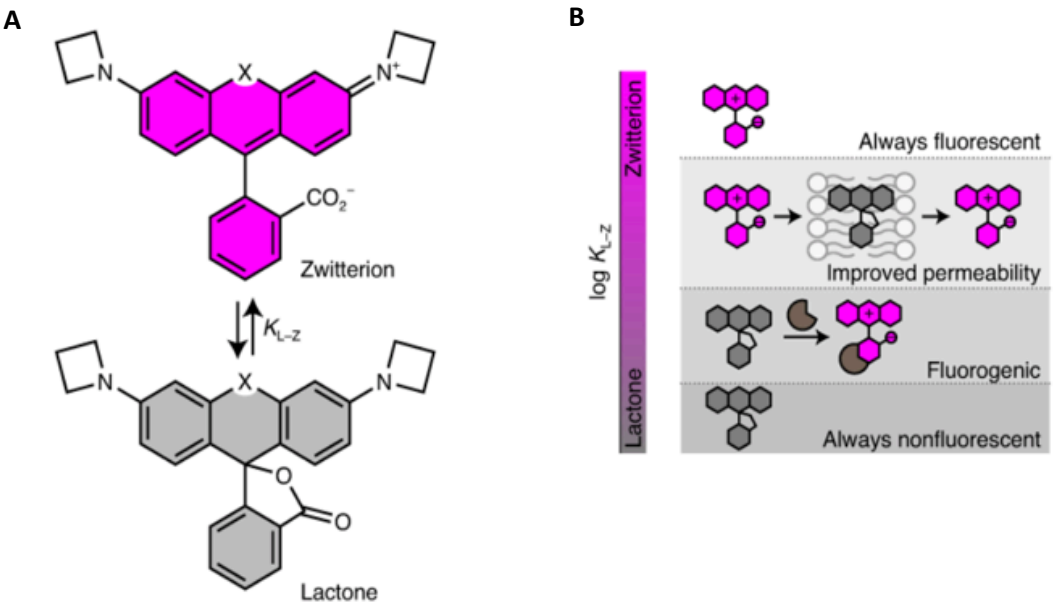

Figure 2.5: The fluorescence - non-fluorescence equilibrium in rhodamine dyes. (A) *The equilibrium between fluorescent zwitterion and non-fluorescent lactone confirmation is dependent on the equilibrium constant KL-Z.* ***(B)*** *Fluorescence and permeability properties of dyes differ based on their KL-Z. Figure taken from Grimm et al. (2020).*

TMR-Halo or JF549-Halo can be used together with SiR-Halo or JF646-Halo for pulse-chase labelling experiments because they have non-overlapping fluorescence spectra. TMR-Halo and JF549-Halo did not produce reliable labelling *in vivo* via tail-vein injection and thus in the experiments presented in **Chapter 3**, TMR-Halo and JF549-Halo were used as post-fixation “chase” ligands.

2.4.2 Coupling reaction and purification

Coupling reactions for SiR-Halo, JF646-Halo and JF549-Halo were caried out in-house while TMR-Halo was obtained from Promega Ltd. Dye coupling and purification was performed by Edita Bulovaite with the help of Dr Lorena Tapia Mendive.

2.4.2.1 SiR-Halo synthesis

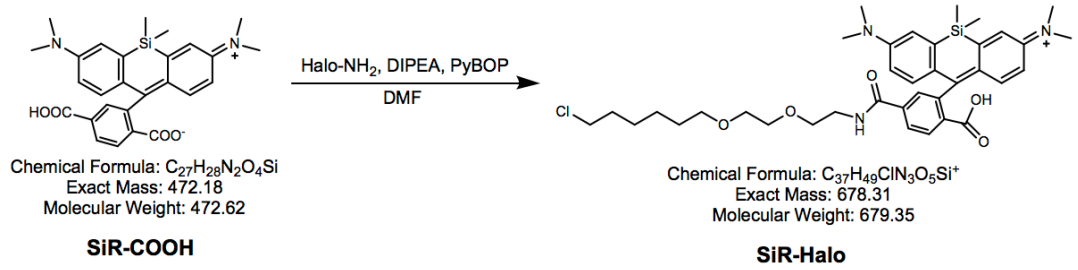

Figure 2.6: SiR-Halo coupling reaction. *Starter compounds (SiR-COOH and Halo-NH2) are mixed with catalysing reagents to produce the final product SiR-Halo.*

SiR-Halo coupling was performed as previously described (Lukinavičius et al., 2013, Butkevich et al., 2017). 50 mg (89.7 µmol) of SiR-COOH dye (Spirochrome Ltd.) and 36 mg of Amine (O2) HaloTag building block (134.6 µmol, 1.5 equivalent) were dissolved in 950 µL DMF (dimethylformamide). 90 µl of DIPEA (N,N-Diisopropylethylamine) were added into the solution at which point the blue colour of SiR-COOH disappeared from the dye solution. 70 mg of PyBOP (benzotriazol-1-yl-oxytripyrrolidinophosphonium hexafluorophosphate, 134.55 µmol, 1.5 equivalent) dissolved in 230 µL DMF was added to the SiR-COOH and Amine (O2) solution. The solution was stirred at RT for 2 hours protected from light and afterwards checked with 2% Methanol (MeOH) in DCM (dichloromethane) thin-layer chromatography (TLC) for the product.

Prior to purification, the compound was phase-separated from DMF. The compound was collected with the organic phase (diethyl ether) while the aqueous phase (brine) was discarded. 2-3 tablespoons of dried magnesium sulphate were added to the organic phase solution, mixed well and then filtered using a filter paper to remove any aqueous remains. Diethyl ether was evaporated, and the resulting powder was dissolved in the 2% MeOH in DCM. The product was purified using silica gel column chromatography (2% MeOH in DCM). The product yield: 63%.

2.4.2.2 JF646-Halo synthesis

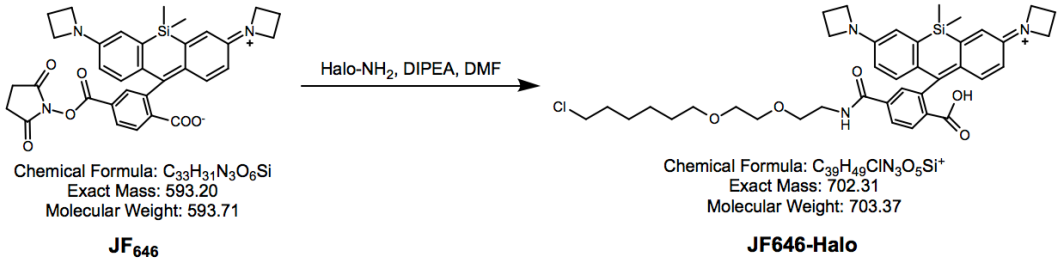

Figure 2.7: JF646-Halo coupling reaction. *JF646 and Halo-NH2 starting compounds were mixed with catalysing reagents to produce JF646-Halo.*

JF646-Halo coupling was performed as previously described (Grimm et al., 2015, Grimm et al., 2017). 2 mg (3.37 µmol) of JF_{646} NHS ester dye was dissolved in DMF (200 µL). A solution of Amine (O2) HaloTag building block (1.75 mg, 6.74 µmol, 2 equivalent) in 40 µL DMF was added, followed by DIPEA (3 µL, 16.85 µmol, 5 equivalent). The reaction was stirred at RT for 2 hours and then concentrated to dryness and purified using prep HPLC (20% ACN in H_2O initial conditions).

2.4.2.3 JF549-Halo synthesis

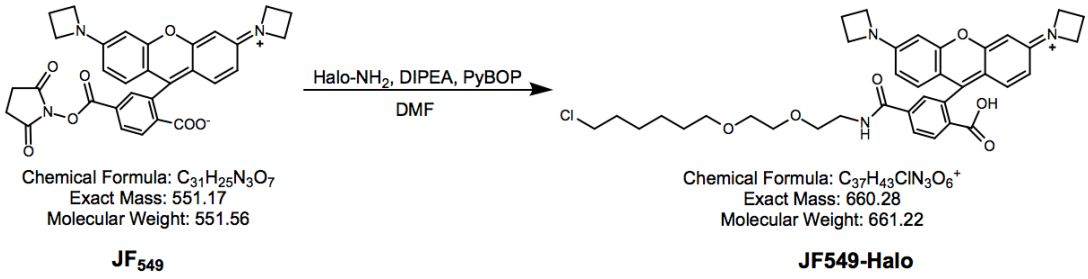

Figure 2.8: JF549-Halo coupling reaction. *JF549 was mixed with Halo-NH2 and catalysing reagents to produce JF549-Halo.*

JF549-Halo coupling was performed as previously described (Grimm et al., 2015). 2 mg (3.63 µmol) of JF_{549} NHS ester dye was dissolved in DMF (220 µL). A solution of Amine (O2) HaloTag building block (1.9 mg, 7.26 µmol, 2 equivalent) in 40 µL DMF was added, followed by DIPEA (3.16 µL, 18.15 µmol,

5 equivalent) and PyBOP (3mg dissolved in 10 µL DMF, 5.4 µmol, 1.5 equivalent). The reaction was stirred at RT for 2 hours and then concentrated to dryness and purified using prep HPLC (20% ACN in H_2O initial conditions).

2.5 *In vivo* application of HaloTag ligands

2.5.1 HaloTag ligand solution

HaloTag ligand solution was prepared as per Grimm et al. (2017), but at 1.5 mM HaloTag ligand solution for injections and total injection volume adjusted by average weight for the animal group examined. **Table 2.3** outlines the HaloTag solution composition and volumes for each age group examined.

Age group	Volume injected (µL)			
	Total	HaloTag ligand (5 mM)	Pluronic F-127	Saline
3-4 weeks old	70 µL	21 µL	7 µL	42 µL
3-4 months old	200 µL	60 µL	20 µL	120 µL
18 months old	300 µL	90 µL	30 µL	180 µL

Table 2.3: HaloTag solution composition for different age groups.

2.5.2 Intravenous (tail-vein) injection

Intravenous (IV) injections were carried out by Will Mungall. Prior to injection, animals were placed in a heat box for 5-10 minutes to allow the blood vessels of the tail to dilate and become more visible. The mice were sequentially placed in a rodent restrainer for the injection. A bolus injection of HaloTag ligand solution was performed into the lateral tail vein. Following the injection, the animals were monitored for any adverse effects twice daily for the length of the experiment.

2.6 Tissue collection and processing

2.6.1 Transcardial perfusion and brain fixation

Mice were fully anesthetized by intraperitoneally injecting 0.10-0.20 ml (age-dependent; please see **Table 2.4**) of pentobarbital (Euthatal). The thorax was opened, and an incision was made to the right atrium of the heart. Following

an insertion of a fine needle (26G, 0.45 x 100mm) into the left ventricle and the animal was transcardially perfused with 10-15 ml of 1 x PBS followed by 10-15 ml of fixative (4% PFA) and left at 4°C for 3-4 hours (age-dependent; **Table 2.4**). Samples were transferred to a 30% sucrose solution and incubated for 48-72 hours at 4°C.

Age group	Volume injected (ml)		
	Anaesthetic injected	1xPBS	4% PFA
3-4 weeks old	0.10 ml	10 ml	10 ml
3-4 months old	0.15 ml	12 ml	12 ml
18 months old	0.20 ml	15 ml	15 ml

Table 2.4: Volumes of the anaesthetic, PBS and 4% PFA injected for different age groups.

2.6.2 Tissue embedding

The brains were embedded in OCT (embedding matrix for frozen sections) solution (CellPath) inside a plastic mould (Sigma-Aldrich). Brain-containing moulds were placed in beakers containing isopentane (Sigma-Aldrich) and the beakers were moved to a container containing liquid nitrogen for freezing. Frozen brains were stored at -80°C for up to 4-5 months.

2.6.3 Cryosectioning

Frozen brain samples were cut at 18 μm thickness using a cryostat (NX70 Thermo Fisher) to obtain sagittal brain sections referring to 12-13/21 bregma level from Allen Brain sagittal atlas (*https://mouse.brain-map.org/experiment/thumbnails/100042147?image_type=atlas*). The brain sections were placed on Superfrost Plus glass slides (Thermo scientific). A drop of 1xPBS was placed on a glass slide prior to picking up the brain sections to ensure the brain tissue lays flat. After cutting, brain sections were left to dry in the dark at room temperature overnight and were then stored at -20°C. Brains were sectioned by Beverly Notman and Edita Bulovaite.

2.7 Immunohistochemistry and preparation for imaging

2.7.1 Post-fixation labelling with HaloTag ligands

Brain sections were first washed with 800 μl 1xPBS to remove any remaining OCT and were left to dry in the dark. Hydrophobic marker pen was used to draw around sections to contain the liquid solutions within outlined area of the brain section. 50 μl of 10 μM TMR-Halo solution in 1xPBS was added to each brain section and samples were incubated for 1hr at room temperature in a wet dark chamber. Brain sections were then washed 2 times for 10 minutes with 1xTBS containing 0.2% Triton X detergent to remove any unbound TMR-Halo ligand and once with 1xTBS for 10 minutes.

2.7.2 Mowiol preparation

Mounting medium MOWIOL was prepared by slowly (over a period of an hour) adding 2.4 g MOWIOL (Hoechst) to 4.75 ml (6 g) glycerol and mixing continuously. 6 ml dH_2O was added and the mixture was covered and let to stand at room temperature overnight. 12 ml of 0.2 M Tris (pH 8.5) in dH_2O was heated to 50°C using hot plate and added to the MOWIOL mixture. The solution was incubated at 50°C for 10 min with occasional mixing and then centrifuged at 5000rpm for 15mins at 4°C. Supernatant was collected and 0.5 g (2.5 g/100 ml) DABCO (1,4-diazobicyclo-[2.2.2]-octane) was added to prevent photobleaching. The solution was gently mixed and incubated at 4°C for 15mins. Prepared MOWIOL was aliquoted and stored at -20°C.

2.7.3 Coverslip mounting

Frozen brain sections were placed in a dark chamber and incubated at room temperature for 1-hour prior to mounting the coverslips. Sections were washed with 800 μl of 1xPBS to remove any remaining OCT on or around the brain tissue and let dry. A drop of 12 μl MOWIOL solution was applied on top of the brain section. A glass coverslip (18 mm in diameter, thickness #1.5, VWR) was carefully lowered on top of the sample to avoid any bubbles forming in between the glass slide and the coverslip. The sections were left to dry in the dark at room temperature overnight and were then stored at 4°C for up to 1 week.

2.8 Microscopy

2.8.1 Spinning disc confocal microscope

Imaging for the study was performed using Andor Revolution XDi spinning disc microscope, which was equipped with CSU-X1 (pinhole size: 50 μm) and 2x post-magnification lens. Images of 512 x 512 -pixel size and 16-bit depth were obtained using Andor iXon Ultra back-illuminated EMCCD camera and Olympus UPlanSAPO 100x oil immersion lens (NA 1.4). To cover the whole area of the sagittal brain section, multi-tile single plane image acquisition was arranged with 0% overlap between adjacent tiles. Focus in z-plane was achieved by selecting and recording desired z-position for four points on the brain section which were then used to calculate the intermediate z-positions for in-between image tiles. Resolution of obtained images: pixel resolution 84 nm and optical resolution ~260 nm.

2.8.2 Imaging parameters

High magnification (x100) images at a single synapse resolution covering the whole brain section were obtained using Andor confocal spinning disc microscope. Laser lines, emission filters, laser powers and exposure times used for all fluorescence markers for all studies are summarized in **Table 2.5**. 250 EM Gain, 2-frame averaging and 5000ms acquisition speed were used for all channels to optimize acquired image quality. 'Subtype turnover study', 'PSD93-KO study' and 'SynGAP-KO study' all used $PSD95^{+/HaloTag}$ instead of $PSD95^{HaloTag/HaloTag}$ animals which required slightly higher laser power and exposure time settings to capture the full dynamic range of fluorescence.

Study name	Fluorescent label	Laser line	Laser power	Exposure time	Emission filter
3-month turnover study	SiR-Halo	640 nm	12%	95 ms	QUAD (700/45)
	TMR-Halo	561 nm	13%	110 ms	QUAD (607/34)
Lifespan turnover	SiR-Halo	640 nm	12%	95 ms	QUAD (700/45)
Subtype turnover study	SiR-Halo	640 nm	15%	100 ms	QUAD (700/45)
	PSD95-eGFP	488 nm	30 %	95 ms	QUAD (521/21)
	SAP102-mKO2	561 nm	40 %	100 ms	QUAD (607/34)
PSD93-KO study	SiR-Halo	640 nm	15 %	100 ms	QUAD (700/45)
SynGAP-KO study	SiR-Halo	640 nm	15 %	120 ms	QUAD (700/45)

Table 2.5: Imaging parameters used for different studies and fluorophores.

Imaging for 'PSD93-KO study' was performed by Adrianna Zgraj under the guidance of Edita Bulovaite. Imaging for the rest of the studies was performed by Edita Bulovaite.

2.9 Image analysis

2.9.1 Automated synaptic puncta detection

Synaptic puncta detection from fluorescence images was performed using machine learning-based Ensemble method which was developed in-house by Dr Zhen Qiu (Zhu et al., 2018, Cizeron et al., 2020).

2.9.2 Training of machine learning algorithm

More details on training the machine learning algorithm to detect puncta are available in Melissa Cizeron's PhD thesis and Cizeron et al. (2020). The training of the machine learning algorithm was performed on a set of representative images on which the puncta were already manually localised by three independent individuals with a varying amount of scientific expertise.

Manual puncta detection for SiR-Halo labelling was performed on 249 images of 10.8 x 10.8 μm in size using a 'CellCounter' plugin in Fiji/ImageJ. PSD95-eGFP and SAP102-mKO2 training was performed previously and the details are available in Melissa Cizeron's PhD thesis.

The coordinates of the manually detected puncta were used to train the machine learning algorithm that combines a set of detection methods in order to maximise puncta detection at various degrees of signal-to-noise ratio. The trained ensemble method was used for automated puncta detection in studies presented in **Chapters 3-6**.

2.9.3 Montage stitching

An overview montage of each imaged sagittal brain section was stitched from ~45,000-50,000 image tiles using a custom-written MATLAB script (written by Dr Zhen Qiu). Since image acquisition was set as to not overlap consecutive image tiles, the stitching code was constructed to read the rows and columns for each image from the metadata and put the images in order of the sequence acquired. During stitching, the images were downsized by a factor of 16 to allow easier transfer and manipulation of the resulting montages.

2.9.4 Delineation of brain regions of interest

Quantification of PSD95-HaloTag labelling was performed on anatomical brain regions as defined by the Allen Mouse Brain Atlas. In order to group the detected puncta by brain region of interest (ROI), we first needed to define the boundaries of brain areas. A combination of manual and semi-automated delineation methods was employed for defining 110 anatomical brain regions in each sagittal brain image. The delineations were saved as .roi files and then transformed into binary masks as part of the automated image analysis pipeline.

2.9.4.1 Manual delineations using Fiji/ImageJ

Manual delineations of subcortical brain regions (i.e. subregions of the olfactory areas, cortical subplate, striatum, pallidum, hypothalamus, thalamus, midbrain, cerebellum, pons and medulla) was performed using a polygon

selection tool in Fiji/ImageJ (Schindelin et al., 2012, Schneider et al., 2012). Once drawn, each delineation was added to the ROI manager in Fiji/ImageJ. After all delineations for a given brain image were completed, the resulting .roi files were exported and saved for the 'mapping' step of the analysis pipeline. Manual delineations for data presented in **Chapter 3** and **Chapter 4** were completed by Edita Bulovaite, while delineation performed for datasets in **Chapter 5** were performed by Edita Bulovaite, Theresa Wong, Beverly Notman and Gabor Varga. Delineations performed for datasets in **Chapter 6** were performed by Martyna Marcinkowska and Gabor Varga. Upon completion, all delineations were checked by Edita Bulovaite to ensure consistency within and between datasets.

2.9.4.2 Semi-automated delineations using Delineation Deformer

Delineation Deformer is an in-house custom-built software for semi-automated delineating or brain ROIs, developed by Dr Babis Koniaris. The program provides a user interface for a free-form deformation of a surface on which we map a specially prepared image that contains a multitude of delineated regions (Sederberg and Parry, 1986). The specially prepared images in most cases were delineation templates obtained from the Allen Mouse Brain Atlas resource. The delineation templates mapped on a digital surface get subdivided into a uniform grid, so that each cell contains a subdivision of the delineation template. The software allows the user to manipulate the grid points which results in the deformation of the grid cells and in turn leads to the deformation of the delineation template (Catmull, 1974).

The software superimposes the delineation template on top of the brain image being delineated. We can deform the delineation template to "fit" the underlying montage image of the brain section. In case of any tissue damage observable in the brain image, the software has a function allowing to paint over the damaged areas on the tissue to get them excluded from the finalised delineation. The final delineation is saved as a set of .roi files representing

individual brain regions which then are used in the later steps of the mapping pipeline.

Delineation Deformer was used for outlining the subregions of isocortex and hippocampal formation in datasets presented across **Chapters 3-6**. Delineations for datasets presented in **Chapters 3-5** were performed by Edita Bulovaite and those presented in **Chapter 6** were performed by Adrianna Zgraj and Aidan McConnell-Trevillion.

2.9.5 SynMAP image analysis pipeline

2.9.5.1 Quantification of synapse parameters

Further details on measurement of synaptic parameters can be found in Zhu et al. (2018) and Cizeron et al. (2020). Upon detection and localisation, synaptic puncta are segmented by applying an intensity threshold. The threshold for each detected punctum was set at 10% of the height of its fluorescence intensity profile. A set of punctum characteristics were then quantified for each punctum, including mean pixel intensity, size, skewness, kurtosis, circularity and aspect ratio (Cizeron et al., 2020). Additionally, quantification of puncta density per unit area was performed. For calculations of PSD95-HaloTag turnover, primarily the measurements of puncta density and total fluorescence intensity content (punctum size x punctum mean intensity) were used.

2.9.5.2 Co-localisation analysis

Co-localisation analysis between two fluorescent markers (i.e. SiR-Halo and eGFP) was performed in **Chapter 3** in order to compare the distribution of PSD95-HaloTag labelling in relation to the distribution of well-characterized PSD95-eGFP labelling within individual puncta. Object-based co-localisation method was employed on the already detected synaptic puncta. Distances between nearest neighbours from different channels were measured and a distance threshold of 400 nm was applied to identify markers that co-localised. 400 nm distance is within the range of the previously measured sizes of post-synaptic density as observed by electron microscopy (Harris et al., 1992).

The triple co-localisation between SiR-Halo, eGFP and mKO2 in PSD95$^{eGFP/HaloTag}$;SAP102$^{mKO2/+}$ triple knock-in mice required a more complex algorithm than double co-localisation and the new algorithm was written by adapting multiple hypothesis tracking algorithm to the particle tracking problem. Co-localisation algorithms were developed by Dr Zhen Qiu.

2.9.5.3 Synapse classification

Classification of PSD95$^{+/eGFP}$;SAP102$^{mKO2/+}$ synapses employed a previously developed method (Zhu et al., 2018, Cizeron et al., 2020). Synapse classification is based on the molecular composition of synapses (i.e. PSD95-only, SAP102-only, co-localised PSD95 and SAP102) and on size, shape and fluorescence intensity parameters. Using machine learning algorithm, the synapses were subdivided into 37 subtypes based on their characteristics. A small percentage of puncta (~0.002%) that did not get classified into either of subtype groups were labelled as 'other subtype'.

Synapse classification was performed on PSD95$^{HaloTag/eGFP}$;SAP102$^{mKO2/+}$ brain images in order to assess the co-localisation of different synapse subtypes with PSD95-HaloTag signal at different time points post SiR-Halo injection.

2.10 Data analysis

2.10.1 PSD-95 half-life estimation

PSD95 half-life presented in **Chapter 4** was estimated via two alternative methods: (a) puncta count-based estimation and (b) total punctum intensity-based estimation. Method (a) relies purely on the presence or absence of fluorescent synaptic punctum while method (b) considers the fluorescence content within each punctum. For both methods, the mean at day 0 was considered a reference point to which all the subsequent values were normalised. Single-phase exponential decay function was fitted to fractions of puncta/synapse fluorescence remaining:

$$N(t) = N_0 e^{-\lambda t}$$

where N(t) denotes the puncta density/fluorescence intensity at time t, N_0 = N(0) is quantity at t = 0 and λ is the decay rate constant.

2.10.1.1 Puncta count-based estimation

The detected number of fluorescent puncta per 100 μm^2 (i.e. puncta density) was estimated for each ROI from every brain examined using the SynMAP pipeline. Normalised puncta densities (y-axis) for each animal were plotted against time (x-axis) and an exponential decay function was fitted to estimate half-life and +/- 95% confidence interval.

2.10.1.2 Total puncta intensity-based estimation

For each detected punctum within a ROI, mean fluorescence intensity was multiplied by punctum size to obtain total fluorescence content for each punctum. The resulting fluorescence intensities were summed up to obtain total puncta fluorescence content within a given brain region. Normalised fluorescence intensities (y-axis) for each animal were plotted against time (x-axis) and an exponential decay function was fitted to estimate half-life and +/- 95% confidence interval.

2.10.1.3 PSD95 half-life calculations

PSD95 half-life was defined as the time required for the PSD95-HaloTag puncta density/fluorescence intensity to fall to half its initial value. Half-life was calculated based on the decay constant obtained from exponential curve fitting via the following formula:

$$t_{1/2} = \frac{\ln(2)}{\lambda}$$

2.10.2 PSD95 fraction remaining calculation

The measurement of PSD95 decay in studies presented in Chapters 5 and 6 relies on data from two time points following HaloTag ligand injection: day 0 (reference time point) and day 7 (measurement of decay). In order to compare the decay of puncta number/fluorescence intensity content in these studies, for each ROI we estimated the fraction of puncta/fluorescence intensity

remaining at day 7 compared to day 0. The mean values for fraction remaining were calculated in the following way:

$$f = \frac{A}{B}$$

where A represents the mean of day 7 measurements and B is the mean of day 0 measurements. The error in the measurement of fraction remaining was estimated by following the statistical rules for propagation of uncertainty. The formula used for estimating the standard deviation of a ratio of means was the following:

$$\sigma_f = |f| \sqrt{\left(\frac{\sigma_A}{A}\right)^2 + \left(\frac{\sigma_B}{B}\right)^2}$$

where σ_f is a standard deviation of the function f (i.e. ratio of mean (Day7)/mean (Day0)), σ_A is the standard deviation of A, σ_B is the standard deviation of B.

2.10.3 General statistics

2.10.3.1 Correlations

Covariance of pairs of synaptic parameters (i.e. synapse size, fluorescence intensity, density and half-life) was assessed using Pearson's correlation function in MATLAB. In the results Chapters, the correlation coefficient (R) values are presented alongside p-values (P) which determine the statistical significance of the correlation between the two variables.

2.10.3.2 Bayesian analysis

For statistical evaluation of changes in subtype densities (**Chapter 5**) and genotypes (**Chapter 6**), we employed Bayesian estimation method (Kruschke, 2013). The input data were modelled assuming a t-distribution and Markov chain Monte Carlo algorithm was then performed to estimate the posterior distribution of the changes. P-values were calculated for the resulting distribution. Values for brain regions/subregions were modelled and tested

separately. The results were then corrected for multiple comparisons using the Benjamini-Hochberg procedure. Statistical analyses were performed by Dr Ragini Gokhale and Dr Zhen Qiu.

2.10.4 Cohen's D effect size

The size of a difference in fraction puncta/fluorescence remaining between two groups was measured by calculating a Cohen's D effect size, a measurement that is based on the difference between two means divided by their pooled standard deviation:

$$d = \frac{\bar{x}_1 - \bar{x}_2}{s}$$

The pooled standard deviation was calculated as follows:

$$s = \sqrt{\frac{(n_1 - 1)s_1^2 + (n_2 - 1)s_2^2}{n_1 + n_2}}$$

2.10.5 Similarity matrices

In order to estimate the similarity of regional half-lives between brain subregions, similarity scores were calculated by applying a Gaussian kernel function to differences in PSD95 half-life and plotted as a heatmap. Similarity matrices are presented in **Chapter 5**.

2.10.6 Heatmaps

The heatmaps presented in **Chapters 4-6** were generated via a custom-written python code, kindly provided by Dr Ragini Gokhale. The heatmaps utilized Allen Brain Atlas delineation templates and coloured the brain regions according to the corresponding values provided.

Chapter 3 Optimisation of PSD95-HaloTag labelling with fluorescent ligands in the mouse brain

3.1 Introduction

The majority of published work to date utilising the HaloTag labelling technology in fluorescence microscopy has been done *in vitro* or in single-celled organisms (Los et al., 2008a, England et al., 2015). Applications including visualising protein localisation (Hughes et al., 2014, Lepore et al., 2019), detecting protein trafficking (Svendsen et al., 2008), protein turnover (Merrill et al., 2019, Cohen et al., 2020, Yamaguchi et al., 2009) and inducing labelled protein decay (Buckley et al., 2015) have all been achieved using HaloTag constructs in cell culture. Several groups have investigated protein localisation and turnover in primary neuronal cultures (Kratschke, 2018, Cohen et al., 2020, Merrill et al., 2019), with Kratschke (2018) performing an in-depth characterisation of synaptic PSD95 half-life and its response to pharmacological treatments using primary neurons prepared from the PSD95$^{HaloTag/HaloTag}$ mice used in the current project.

For *in vivo* synaptic protein labelling a number of experimental steps had to be optimised and relevant controls established. We aimed to develop a method that would allow us to fluorescently label and visualise PSD95 with a comparable efficiency across different brain regions, ranging from cortical areas, to thalamic nuclei, olfactory bulb, cerebellum and hindbrain regions. We hypothesized that an intravenous (IV) injection would be most likely to achieve a well-spread efficient level of labelling of our protein of interest compared to more spatially restricted intracortical and intraocular injections or less permeable intraperitoneal injections.

The feasibility of HaloTag labelling in the mouse brain via an IV injection has only recently been demonstrated (Grimm et al., 2017). In this study, the cytosolic HaloTag protein was introduced using a viral vector directly injected into the mouse visual cortex and was successfully labelled after the HaloTag ligand was injected via the tail vein. In a separate study, Masch et al. (2018) used the same mice as in my study (PSD95$^{HaloTag/HaloTag}$) and achieved synaptic labelling with a fluorescent ligand directly injected into the neocortex of anaesthetised mice.

The current chapter presents the steps taken to optimize fluorescence labelling of PSD95-HaloTag protein across the whole brain via an IV injection of HaloTag ligands. More specifically, in Chapter 3 we aimed to:

(1) Examine the ability of a several of fluorescent HaloTag ligands to cross the blood-brain-barrier and label PSD95 protein in brain regions (**Chapter 3.3.1**).
(2) Assess the specificity of labelling by comparing SiR-Halo injected and un-injected PSD95-HaloTag animals as well as injected WT controls (**Chapter 3.3.2**).
(3) Establish an effective dose and concentration of HaloTag dye compound for reliably labelling the PSD95 protein (**Chapter 3.3.3**).
(4) Compare punctate expression obtained with PSD95-HaloTag labelling to the well-established PSD95-eGFP labelling across brain regions and at different stages of life (**Chapter 3.3.4 and 3.3.5**).

3.2 Summary of methods used in this chapter

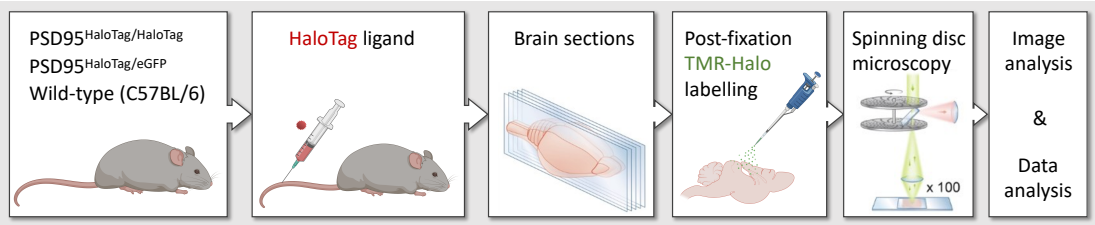

Figure 3.1: A summary of the experimental workflow employed in Chapter 3.

For the optimisation and control experiments, adult (2–6 months old) PSD95$^{HaloTag/HaloTag}$, PSD95$^{HaloTag/eGFP}$, and wild-type C57BL/6 mice were used (**Figure 3.1**; see **Chapter 2.2** for more details). An animal technician (Will Mungall) injected a bolus of 200 µL 1.5 mM SiR-Halo, JF646-Halo or JF549-Halo solution into the tail-vein of mice unless otherwise specified in the results sections. Animals underwent perfusion-fixation at 6-7 hours post-injection and the brain tissue was processed as described in **Chapter 2.6**. For results in **Chapter 3.3.3**, fixed brain tissue sections were incubated in 10 µM TMR-Halo

solution for 1 hour to label any vacant PSD95-HaloTag binding sites (for further details see **Chapter 2.7.1**). Single-synapse resolution images of PSD95 fluorescent labelling were obtained using spinning disc confocal microscopy (**Chapter 2.8.1**). The imaging parameters used for the different mouse lines and fluorophores are outlined in **Table 3.1**. Fluorescent puncta detection and quantification was performed as described in **Chapter 2.9**. Pearson's correlation analyses with Bonferroni correction for multiple comparisons were applied to assess the relationships in puncta density, intensity and animal weight parameters (for details, see **Chapter 2.10.3.1**). Summary data on PSD95-eGFP puncta parameters examined in results **section 3.3.5**, was obtained from Cizeron et al. (2020).

Mouse line imaged	Fluorescent label	Laser line	Laser power	Exposure time	Emission filter
$PSD95^{HaloTag/HaloTag}$ wild-type (C57BL/6)	SiR-Halo	640 nm	12%	95 ms	QUAD (700/45)
	JF646-Halo	640 nm	12%	95 ms	QUAD (700/45)
	TMR-Halo	561 nm	13%	110 ms	QUAD (607/34)
	JF549-Halo	561 nm	13%	110 ms	QUAD (607/34)
$PSD95^{HaloTag/eGFP}$	SiR-Halo	640 nm	15%	100 ms	QUAD (700/45)
	PSD95-eGFP	488 nm	30 %	95 ms	QUAD (521/21)

Table 3.1: Imaging parameters used for visualization of fluorescent markers via spinning disc confocal microscope.

3.3 Results

3.3.1 SiR-Halo as an effective HaloTag ligand for IV injections

In order to compare the efficiency of PSD95-HaloTag labelling by different HaloTag ligands administered via IV injection, adult $PSD95^{HaloTag/HaloTag}$ were injected with 200 μL 1.5 mM JF549-Halo, JF646-Halo or SiR-Halo and brain sections were imaged on the spinning disc confocal microscope. Examples of high-magnification images of synaptic puncta are presented in **Figure 3.2**.

JF549-Halo produced fluorescence puncta in the thalamus, but no punctate staining was observed in hippocampal, cortical or hypothalamic brain regions. In contrast, JF646-Halo produced punctate expression across all brain regions examined, however, labelling in hippocampus was weak. Out of all the HaloTag ligands tested, SiR-Halo produced the strongest fluorescence staining in the hippocampal subregions and additionally, reliably labelled cortical and subcortical brain areas. SiR-Halo was selected as the most promising HaloTag fluorescent ligand for further analyses.

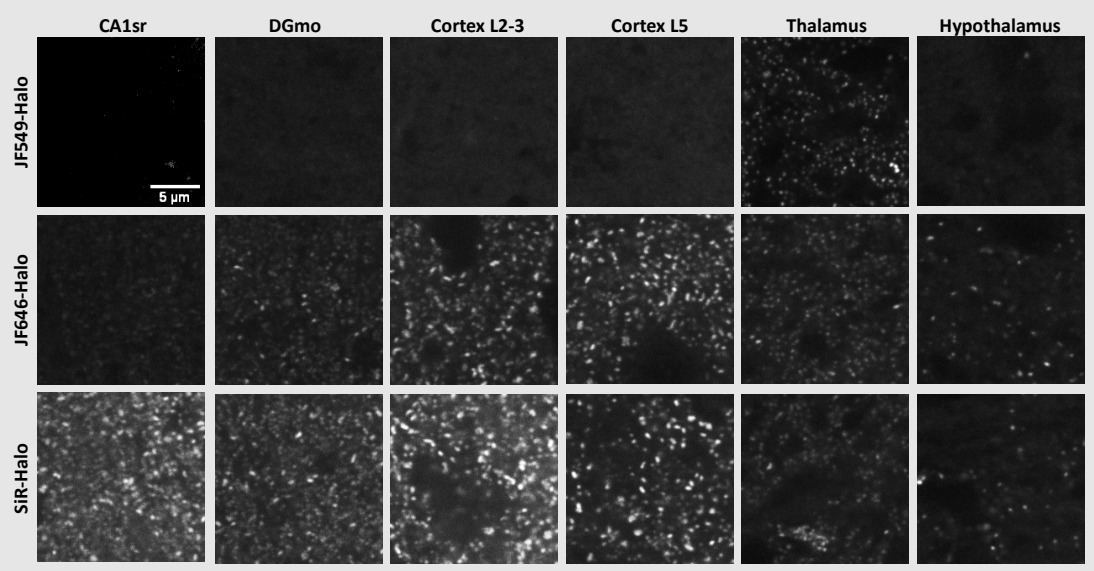

Figure 3.2: Comparison of different HaloTag ligands in labelling efficiency of PSD95-HaloTag fusion protein. *High-magnification representative images of PSD95-HaloTag punctate staining obtained from brain sections of animals IV-injected with 200 µL 1.5 mM JF549-Halo (top row), JF646-Halo (middle row) or SiR-Halo (bottom row) solution. Examples from CA1sr and DGmo of hippocampus, cortical layers 2-3 and 5, as well as subcortical areas of thalamus and hypothalamus are presented. Scale bar: 5 µm.*

3.3.2 Specificity of Labelling

Specificity of SiR-Halo labelling was assessed by comparing images of sagittal brain sections of PSD95$^{HaloTag/HaloTag}$ animal injected with SiR-Halo to the images of un-injected PSD95$^{HaloTag/HaloTag}$ and SiR-Halo injected wild-type brain samples (**Figure 3.3A**). The IV injection of SiR-Halo into PSD95$^{HaloTag/HaloTag}$ mice produced a characteristic fluorescence staining of PSD95, with high fluorescence observed in the mouse isocortex, hippocampus

and striatum. Un-injected PSD95$^{HaloTag/HaloTag}$ mice and injected wild-type negative control mice produced no detectable staining suggesting a high specificity of PSD95-HaloTag labelling with SiR-Halo *in vivo*. A closer look at the high-magnification example images from the injected and un-injected PSD95$^{HaloTag/HaloTag}$ brains (**Figure 3.3B**) confirms that only the injected brain shows punctate fluorescence expression.

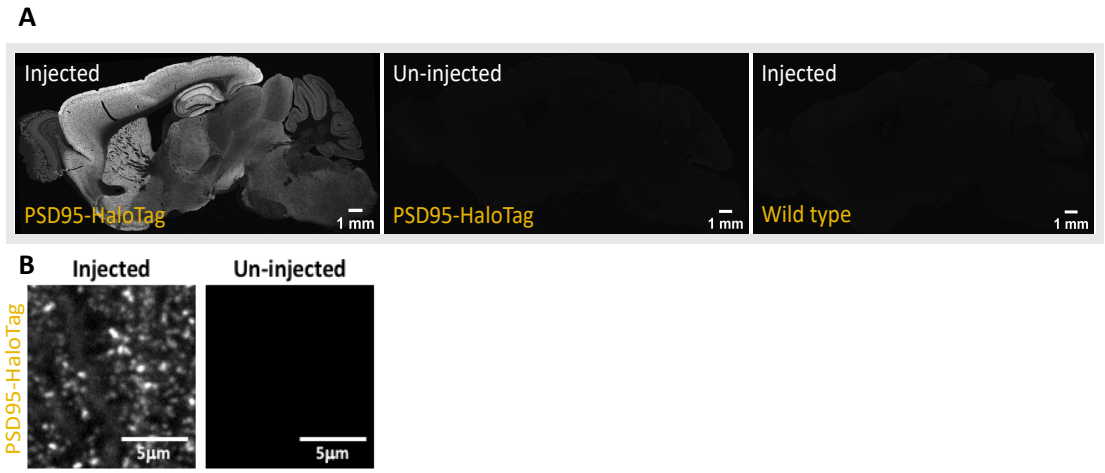

Figure 3.3: Highly specific SiR-Halo labelling of PSD95-HaloTag fusion protein. (A) *High fluorescence levels detected in brain sections from a SiR-Halo injected PSD95$^{HaloTag/HaloTag}$ animal. Un-injected PSD95$^{HaloTag/HaloTag}$ and SiR-Halo injected wild-type brains display no fluorescence signal.* ***(B)*** *Punctate expression of fluorescence is only detected in SiR-Halo injected PSD95$^{HaloTag/HaloTag}$ brain samples and not in un-injected controls. Example puncta images taken from layer 2-3 of isocortex.*

3.3.3 Saturation of labelling via IV injection of HaloTag ligands

In order to establish an optimal dose of SiR-Halo ligand for labelling PSD95 protein *in vivo*, amounts of 100 nmol, 300nmol or 500 nmol of SiR-Halo (as a 200 µl final solution) were injected into the tail vein of a cohort of adult animals and brain sections were visualized using spinning disc confocal microscopy. 100 nmol SiR-Halo injection produced a weak fluorescence signal across the mouse brain, while 300 nmol and 500 nmol showed higher and more saturated labelling of PSD95 (**Figure 3.4**). Injection of 500 nmol SiR-Halo dye solution, however, produced severe seizure-like shaking in the animal immediately post-injection, most likely due to a large concentration of DMSO that was

needed to dissolve the dye, and therefore further testing of optimal doses was carried out on lower amounts of SiR-Halo.

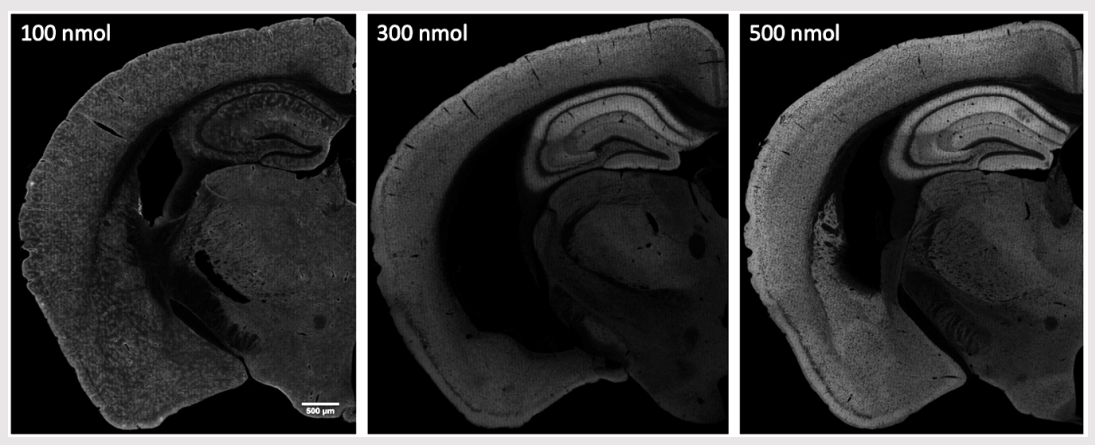

Figure 3.4: Dose-dependent increase in fluorescence labelling of PSD95-HaloTag fusion protein*. Example images of coronal brain sections from PSD95$^{HaloTag/HaloTag}$ animals that received 100 nmol, 300 nmol or 500 nmol SiR-Halo as a 200 µL solution.*

Saturation of labelling by the 300 nmol SiR-Halo injection was assessed by applying TMR-Halo after fixation and sectioning of the tissue and labelling therefore revealed any unoccupied HaloTag protein binding sites (**Figure 3.5A**). As shown in **Figure 3.5B**, IV injection of 300 nmol SiR-Halo prevented any TMR-Halo labelling, whereas TMR-Halo readily labelled un-injected mice. 300 nmol injection of SiR-Halo, therefore, fluorescently labels a vast majority of PSD95 protein.

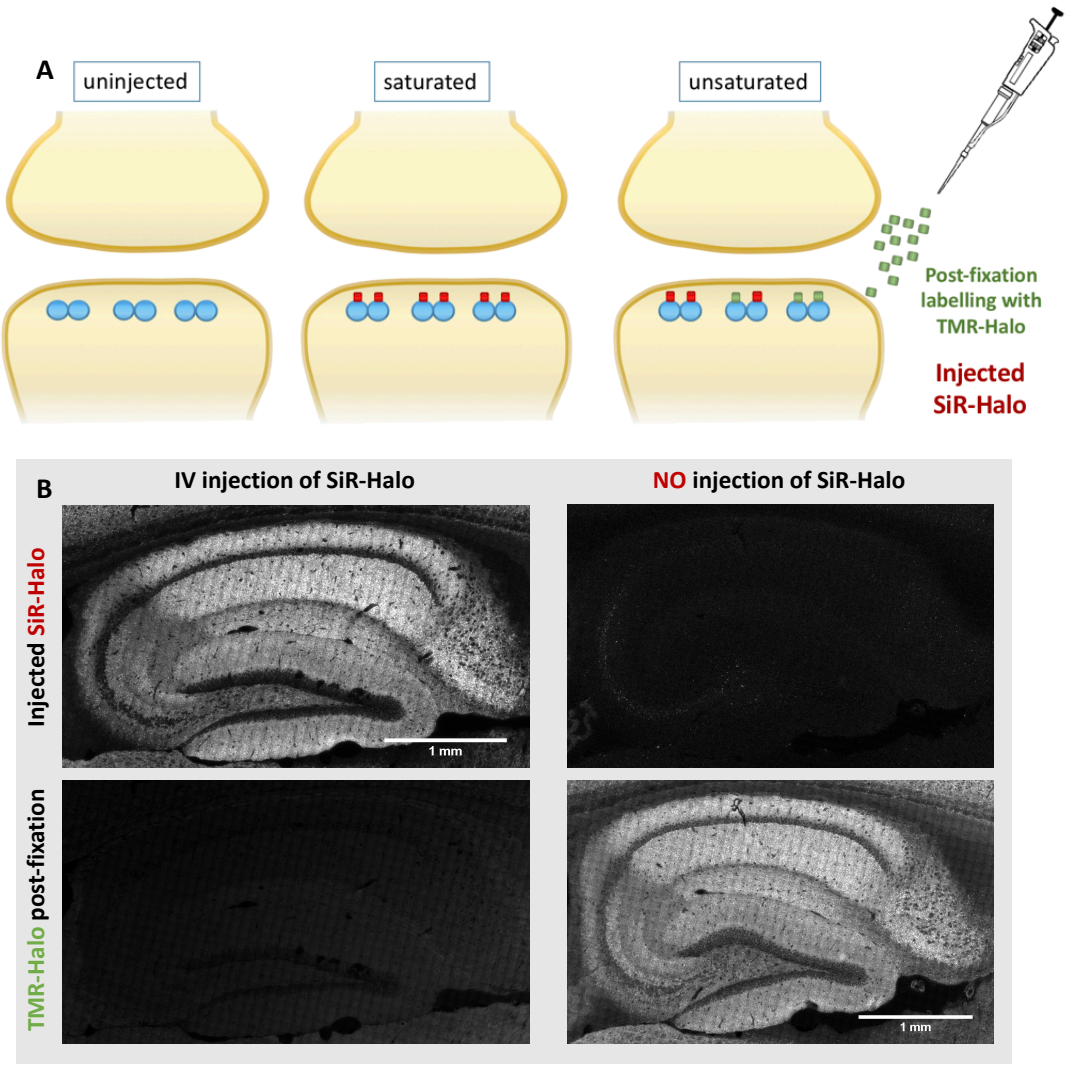

Figure 3.5: Saturation of labelling via IV injection of SiR-Halo. (A) *Schematic representation of the 'un-injected and unlabelled', 'injected and saturated', or 'injected and unsaturated' scenarios in PSD95-HaloTag labelling. Post-fixation labelling with TMR-Halo can be used to distinguish between 'saturated' and 'unsaturated' states.* ***(B)*** *Representative images of hippocampus from an injected (left column) and un-injected (right column) PSD95$^{HaloTag/HaloTag}$ animal with corresponding post-fixation labelling with TMR-Halo.*

3.3.4 Comparison of PSD95-eGFP and PSD95-HaloTag labelling

While the *in vivo* fluorescence labelling of PSD95-HaloTag is target-specific, the efficiency and distribution of labelling across different brain regions still needed to be assessed. PSD95$^{HaloTag/eGFP}$ compound heterozygous animals, in which half of PSD95 protein contained an eGFP fluorescent tag and the other half contained a HaloTag domain, were employed for comparing the

levels of PSD95-HaloTag and PSD95-eGFP fluorescence staining across the brain.

Representative images of a sagittal brain section from 6-month-old PSD95$^{HaloTag/eGFP}$ mouse injected with 300 nmol SiR-Halo displayed comparable staining of PSD95-HaloTag and previously in the lab well-characterised PSD95-eGFP (**Figure 3.6A**). Both fluorescent markers showed higher fluorescence in the cortical, hippocampal and striatal brain regions and lower fluorescence in the thalamic, midbrain and hindbrain areas of the brain. PSD95-HaloTag exhibited a slightly weaker staining across the brain compared to PSD95-eGFP, however, that is likely to be due to different imaging parameters for the two markers or the less stable nature of SiR compared to eGFP fluorophores.

To quantify these results, synaptic puncta of PSD95-HaloTag and PSD95-eGFP were detected across 110 brain regions and puncta densities of respective brain regions were visualized in a scatter plot (**Figure 3.6B**). On average, with PSD95-HaloTag labelling we could detect 50-70% of synaptic puncta detected by PSD95-eGFP. Puncta densities detected in the PSD95-HaloTag channel correlated highly with those detected by quantifying PSD95-eGFP fluorescent puncta (Pearson's correlation: $R = 0.9765$, $P < 0.0001$). Brain subregions, colour-coded by their respective brain area, lay clustered along a diagonal line, with only a few hippocampal subregions (in green) showing mild deviation from the cluster. During titration experiments, of all examined brain regions, the hippocampal subregions were the last to show saturation in labelling by IV injection of SiR-Halo, therefore lower PSD95-HaloTag puncta densities in hippocampal subregions as described above may be explained by a lack of saturation by SiR-Halo injection.

A

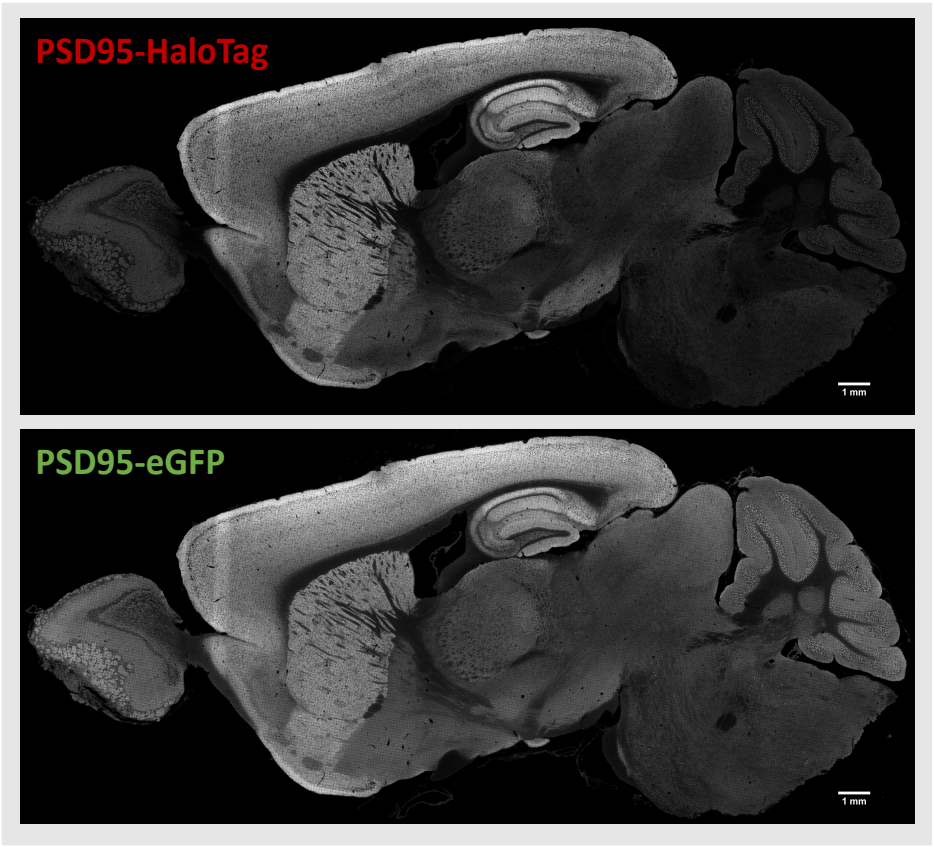
PSD95-HaloTag
1 mm
PSD95-eGFP
1 mm

B

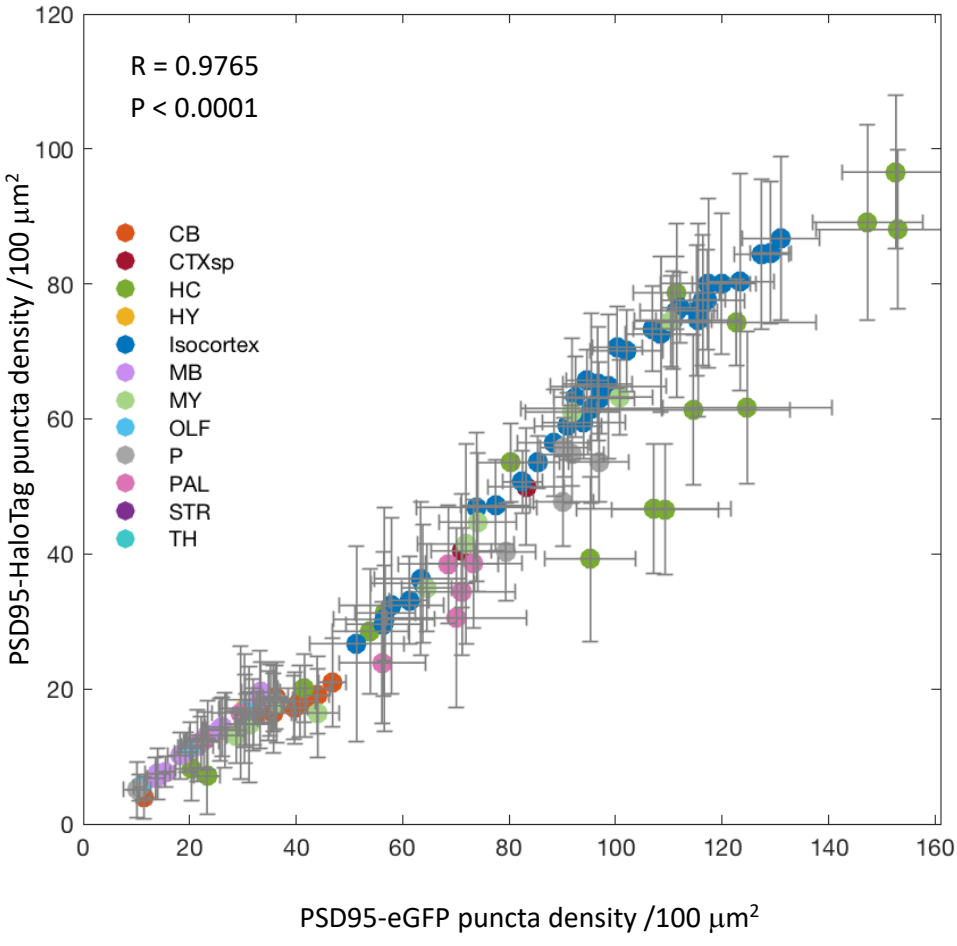
R = 0.9765
P < 0.0001
CB
CTXsp
HC
HY
Isocortex
MB
MY
OLF
P
PAL
STR
TH
PSD95-HaloTag puncta density /100 µm²
PSD95-eGFP puncta density /100 µm²
0
20
40
60
80
100
120
140
160

Figure 3.6: PSD95-HaloTag labelling is comparable to PSD95-eGFP. (A) *Example sagittal brain images from SiR-Halo injected PSD95$^{HaloTag/eGFP}$ mouse.* ***(B)*** *Strong positive correlation between detected synaptic puncta density of PSD95-eGFP (x-axis) and PSD95-HaloTag (y-axis) across 110 brain subregions (+/- SD). Each dot represents a brain subregion, and the colour corresponds to the overarching brain area. R and P values are from the Pearson's correlation test. N = 7 animals.*

We next tested whether SiR-Halo-labelled puncta belong to the same synapses as those containing PSD95-eGFP. Co-localisation analysis was carried out between the two fluorescent markers across the 110 brain subregions and results are summarized in **Figure 3.7**. Around 80% of SiR-Halo positive puncta were found to co-localise with PSD95-eGFP and the co-localisation percentage was consistent across all brain subregions examined (**Figure 3.7A**). Given the stochastic nature of expression of the two genes in individual synapses, 80% is a reasonable value for co-localisation. We also found that out of all PSD95-positive synapses, around 40-50% contained both, PSD95-eGFP and SiR-Halo puncta, another ~40% contained only PSD95-eGFP and the remaining ~10% were positive only for SiR-Halo (**Figure 3.7B**). The lack of saturation by injection of SiR-Halo is likely leading to underestimation in number of synapses containing both, PSD95-eGFP and PSD95-HaloTag, fusion proteins.

With the HaloTag method we are labelling a subpopulation of PSD95-containing synapses. Current analysis does not reveal what subpopulation we are capturing and looking at with HaloTag technology. Are they larger synapses? Synapses more densely packed with protein? Or synapses with a certain molecular composition? Further analysis on synaptic puncta properties of SiR-Halo and PSD95-eGFP in addition to the co-localisation analysis of the two markers, could reveal whether, for example, larger synapses are more likely to contain both, eGFP and SiR-Halo, fluorescent markers.

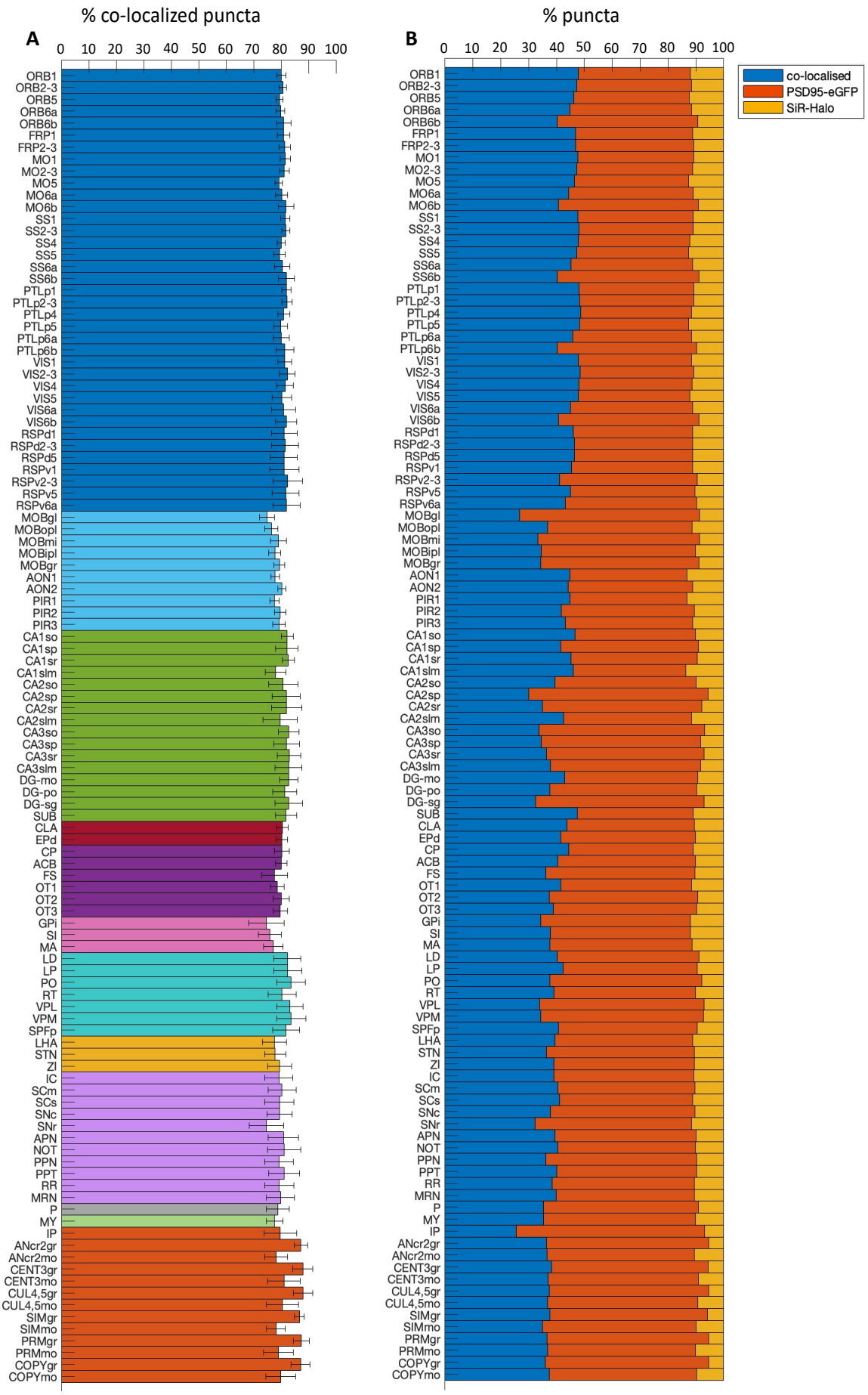
% co-localized puncta
A
0 10 20 30 40 50 60 70 80 90 100
ORB1
ORB2-3
ORB5
ORB6a
ORB6b
FRP1
FRP2-3
MO1
MO2-3
MO5
MO6a
MO6b
SS1
SS2-3
SS4
SS5
SS6a
SS6b
PTLp1
PTLp2-3
PTLp4
PTLp5
PTLp6a
PTLp6b
VIS1
VIS2-3
VIS4
VIS5
VIS6a
VIS6b
RSPd1
RSPd2-3
RSPd5
RSPv1
RSPv2-3
RSPv5
RSPv6a
MOBgl
MOBopl
MOBmi
MOBipl
MOBgr
AON1
AON2
PIR1
PIR2
PIR3
CA1so
CA1sp
CA1sr
CA1slm
CA2so
CA2sp
CA2sr
CA2slm
CA3so
CA3sp
CA3sr
CA3slm
DG-mo
DG-po
DG-sg
SUB
CLA
EPd
CP
ACB
FS
OT1
OT2
OT3
GPi
SI
MA
LD
LP
PO
RT
VPL
VPM
SPFp
LHA
STN
ZI
IC
SCm
SCs
SNc
SNr
APN
NOT
PPN
PPT
RR
MRN
P
MY
IP
ANcr2gr
ANcr2mo
CENT3gr
CENT3mo
CUL4,5gr
CUL4,5mo
SIMgr
SIMmo
PRMgr
PRMmo
COPYgr
COPYmo
% puncta
B
0 10 20 30 40 50 60 70 80 90 100
co-localised
PSD95-eGFP
SiR-Halo

Figure 3.7: Co-localisation between PSD95-HaloTag and PSD95-eGFP synaptic puncta. ***(A)*** *Bar graph showing the percentage of PSD95-HaloTag puncta that co-localise with PSD95-eGFP across 110 brain subregions examined. Error bars: +/- SD.* ***(B)*** *Percentage of synapses that are SiR-Halo positive (yellow), PSD95-eGFP positive (orange) or contain both, PSD95-eGFP and SiR-Halo labelled PSD95-HaloTag (blue). N = 7 animals.*

3.3.5 Puncta labelling comparable to previously published data

The studies described in Chapter 4 and 5 present results of PSD95 lifetime in $PSD95^{HaloTag/HaloTag}$ animals at three different ages in mice: 3-week-old (3W; development), 3-month-old (3M; adulthood) and 18-month-old (18M; ageing). To ensure that labelling efficiency and distribution of PSD95-HaloTag is comparable between ages and corresponds well to the published data on PSD95-eGFP, PSD95-HaloTag puncta densities and mean intensities were compared across brain regions to the puncta parameters published in Cizeron et al. (2020) (**Figure 3.8**). Puncta density measurements of PSD95-HaloTag correlated strongly with puncta densities of PSD95-eGFP at all ages examined (Pearson's correlation; 3W: $R = 0.9344$, $P < 0.0001$; 3M: $R = 0.9230$, $P < 0.0001$; 18M: $R = 0.9635$, $P < 0.0001$). Strong positive correlation was also observed for puncta mean intensities across brain regions (Pearson's correlation; 3W: $R = 0.8812$, $P < 0.0001$; 3M: $R = 0.9129$, $P < 0.0001$; 18M: $R = 0.7993$, $P < 0.0001$). The results suggest that PSD95-HaloTag labelling can reliably represent PSD95 puncta population across brain regions and stages of life.

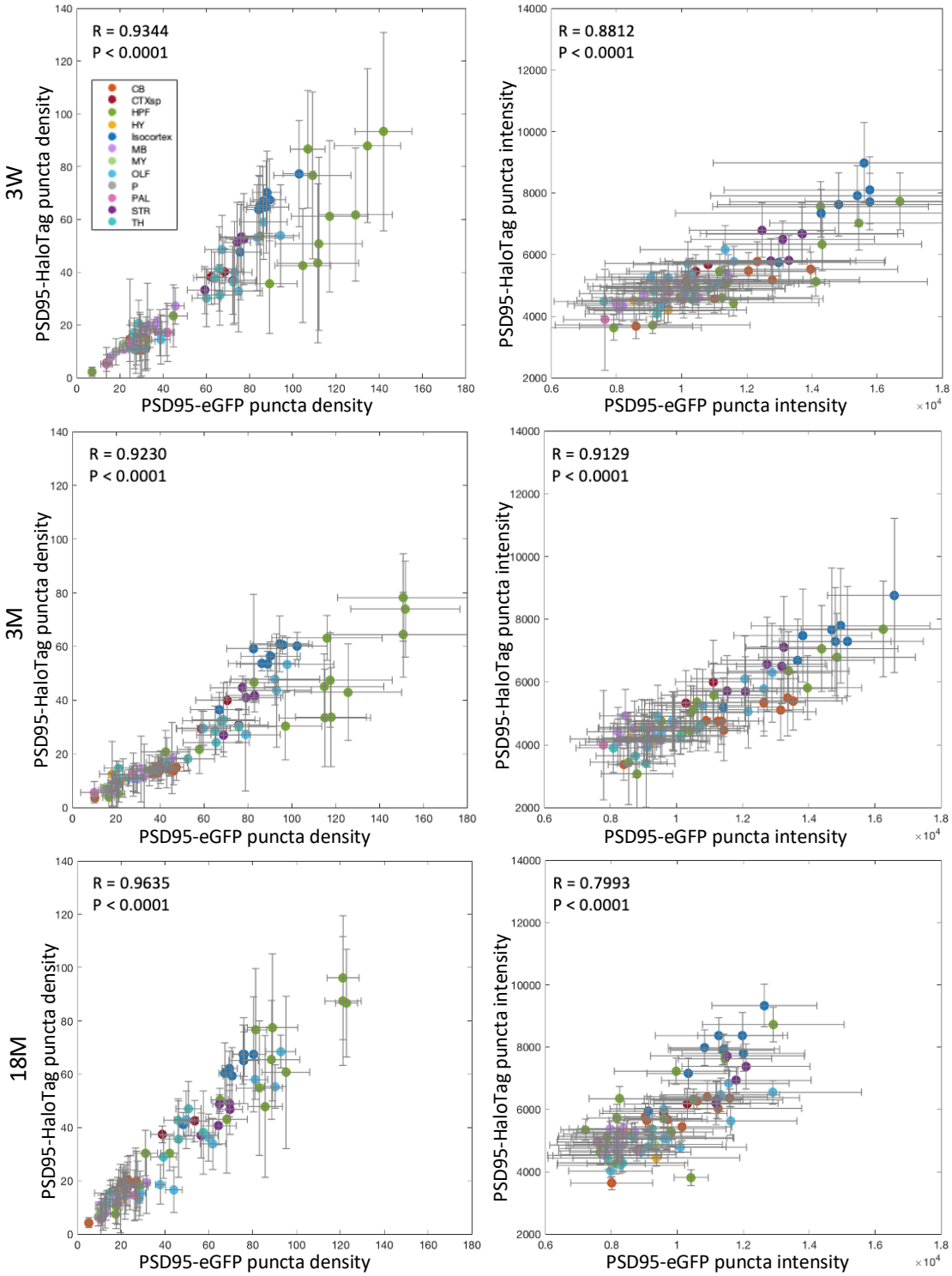

Figure 3.8: PSD95-HaloTag labelling is comparable to the published data on PSD95-eGFP at different stages of life. *Puncta density (left column) and puncta mean intensity (right column) show strong positive correlation between PSD95$^{HaloTag/HaloTag}$ and PSD95$^{eGFP/eGFP}$ in 3-week-old (3W), 3-month-old (3M) and 18-month-old (18M) animals. Each point represents a median density/intensity value for a brain region (+/-SD). N (PSD95$^{HaloTag/HaloTag}$) = 7-10 animals / age group. N (PSD95$^{eGFP/eGFP}$) = 4-5 animals / age group.*

3.4 Discussion

In Chapter 3, we establish the protocols for reliable and efficient *in vivo* HaloTag fluorescence labelling. Out of three HaloTag ligands tested, SiR-Halo proved to be the best at consistently labelling different brain regions and offered high specificity to PSD95-HaloTag fusion protein. An injection of 300 nmol 1.5 mM SiR-Halo solution labelled the vast majority of PSD95 protein and the distribution of labelling was comparable to well-characterized PSD95-eGFP. We observed consistent labelling of PSD95-HaloTag protein in animals of different ages which strongly correlated with PSD95 puncta characteristics described in the published literature.

3.4.1 Capability of HaloTag ligands to cross the blood-brain-barrier

From the three HaloTag ligands tested, we observed a clear superiority of silicon-rhodamine dyes (JF646-Halo and SiR-Halo) compared to tetramethyl-rhodamine (JF549-Halo) in penetrating the brain tissue and labelling PSD95-HaloTag fusion protein. This may be due to unspecific binding interactions that JF549-Halo engages in or, more likely, the differential ability of the HaloTag dyes to cross the blood-brain-barrier (BBB). The BBB is a multicellular vascular barrier that separates the central nervous system from the peripheral blood circulation and controls the passage of molecules and ions into the brain (Obermeier et al., 2013). Endothelial cells of the BBB contain continuous intercellular tight junctions through which only diffusion of hydrophobic molecules and small (under 400-600 Da) lipophilic non-polar molecules is possible (Wong et al., 2013, Siegel, 1999). Large molecules, including the nutrients for brain cells, and immune cells travel through specialised transporters (Obermeier et al., 2013). BBB is unlikely to have specialised transporters for HaloTag ligand constructs, therefore, we would rely on passive forms of transport.

The fluorescent HaloTag ligands tested are relatively small (~ 650-750 Da) but slightly above the threshold for size stated above. Aromatic ring systems and alkyl chains, which compose the large fraction of the three HaloTag-dye

molecules, are known to be lipophilic functional groups which aid the passage of the molecules through the BBB (Harrold and Zavod, 2014). The main difference seen between silicon-rhodamines and tetramethyl-rhodamine is the presence of a silicon atom in the former and an oxygen atom in the latter in one of the aromatic rings of the molecule. Oxygen has a higher polarity than silicon which would contribute to a higher polarity of the JF549-Halo ligand compared to its silicon-rhodamine counterparts and therefore a lower likelihood of it passing through the BBB efficiently.

In the future, finding a second injectable HaloTag ligand with a compatible fluorescence spectrum for 2-colour imaging would be desirable. One of the more promising compounds is JF526-Halo (Grimm et al., 2020) which is fluorogenic and more lipophilic than JF549-Halo and JF646-Halo due to added fluorine atoms. JF526-Halo is excited by 515 nm laser therefore would be spectrally well separated from far-red fluorophores such as SiR-Halo and JF-646.

3.4.2 Effective dose of SiR-Halo for intravenous application

Through titrating the dosage of injected SiR-Halo and analysing the unsaturated PSD95-HaloTag binding sites I concluded that 300 nmol 1.5 mM SiR-Halo solution is an optimal dose for efficient fluorescence labelling of PSD95. Injection of 300 nmol 1.5 mM SiR-Halo solution labelled the vast majority of PSD95-HaloTag as evidenced by lack of fluorescence of post-fixation TMR-Halo label and the comparable SiR-Halo labelling to PSD95-eGFP. Attempts to inject larger doses of SiR-Halo (500 nmol) resulted in mice experiencing severe ataxia and whole-body twisting which lasted for around 1 min with residual effects felt several hours after the injection. Large concentration of DMSO in the injected solution is the most likely cause of the severe adverse effects of injection. Studies assessing the toxicity of different solvent concentrations when applied intravenously suggested that DMSO concentration in the solution should not exceed 40-45% due to the severity of clinical signs caused by higher concentrations (Thackaberry et al., 2014). 500 nmol solution of SiR-Halo had 58% of DMSO which exceeded the

recommended norm and therefore was not used in later experiments. 300 nmol solution has 38% of DMSO which is an acceptable concentration and only produces minor ataxia and whole- or partial-body twisting for ~20s after which animals recover completely within 1min. While further minor optimisations of SiR-Halo dose could be carried out in the future, care should be taken to balance the saturation of fluorescence labelling by injection and the adverse effects that larger doses of SiR-Halo produce.

3.4.3 Tissue penetration of injected SiR-Halo

Intravenous injection of SiR-Halo was found to consistently label all regions of the brain. Interestingly, while titrating the dose of SiR-Halo to be injected, we noticed that hippocampal CA1 subregions were the last ones to get saturated by injection followed by superficial layers of the cortex. This may be due to morphological differences in vasculature of different brain regions. Indeed, in rat brain CA1 region was found to have a low vascular density in contrast to hippocampal CA3 which was rich in micro-vessels (Wilhelm et al., 2016). Lower vascular density could limit the access to the tissue for HaloTag ligands. Low density of capillaries was also observed in superficial layers of the cortex with increased density in deeper layers. At 300 nmol 1.5 mM doses of SiR-Halo, we only occasionally observed unsaturated PSD95-HaloTag binding sites in hippocampal CA1. Unsaturated labelling in this case may lead us to underestimate PSD95 puncta density, intensity and protein lifetimes in hippocampal CA1.

3.4.4 Timing of tissue collection

In the experiments above, brain tissue was collected at 6 hours post-injection to allow sufficient time for the injected SiR-Halo ligand to saturate PSD95 binding sites and for the majority of the unbound ligand to clear from the body. In a different study, (Grimm et al., 2017) injected a HaloTag ligand into the tail-vein and tracked the labelling in the target area in visual cortex and found the fluorescence to peak at 6 hours post-injection. Even though in their study researchers injected a different HaloTag ligand (JF585-Halo) and labelled

cytosolic HaloTag protein, the amount of time it took for the dye to reach its target in the brain after injection could be used to guide my experiments.

Small molecules (< 1 kDa) are known to undergo fast systemic clearance (< 24 hrs) from the body (Li et al., 2017). SiR-Halo is ~0.6 kDa in size and therefore would most likely be cleared from the body rapidly. The presence of residual unbound SiR-Halo at 6 hours post-injection would not cause false positive fluorescence signal since SiR-Halo is fluorogenic and only fluoresces when bound to the HaloTag protein (Lukinavičius et al., 2013). Small size and fluorogenic nature of SiR-Halo both assist in limiting interference of unbound ligand in measurements of synaptic PSD95-HaloTag protein.

To further optimise the timing of tissue collection after injection, future studies could analyse SiR-Halo fluorescence spread and saturation in the first minutes and hours after injection and determine the time at which SiR-Halo labelling peaks across the brain. SiR-Halo injected mice could be subjected to live 2-photon microscopy through a cranial window which would provide high temporal resolution on SiR-Halo labelling across the brain. To provide further confidence on the clearance rates of unbound SiR-Halo ligands, blood samples from mice injected with SiR-Halo could be collected at different time points post-injection and subjected to liquid chromatography - mass spectrometry analysis. Concentrations of SiR-Halo in analysed samples could be plotted against time to estimate half-life of unbound SiR-Halo in the body.

3.4.5 Control labelling with PSD95-eGFP

The efficiency and distribution of injected SiR-Halo labelling was confirmed by using PSD95-eGFP fluorescence as an internal control in a mouse model where one allele of Psd95 gene contained a HaloTag and the other eGFP. SiR-Halo distributed evenly across brain regions as evidenced by a strong positive correlation of regional puncta numbers detected by SiR-Halo and eGFP. With SiR-Halo, however, we could detect 50-70% of puncta detected by PSD95-eGFP which may be due to a number of reasons: less efficient labelling by injected SiR-Halo, different fluorescence properties of the two fluorophores, different imaging or puncta detection settings. SiR-Halo and

eGFP are both bright fluorophores, with SiR possessing a relative brightness of 39,000 $M^{-1}cm^{-1}$ (extinction coefficient = 100,000 $M^{-1}cm^{-1}$ and fluorescence quantum yield of 0.39) and eGFP having 33,000 $M^{-1}cm^{-1}$ (extinction coefficient = 55,000 $M^{-1}cm^{-1}$ and quantum yield = 0.6) (Lukinavičius et al., 2013, Patterson et al., 2001). While SiR-Halo is a brighter fluorophore, eGFP appears to be more photostable and less prone to photobleaching. The relative differences in the fluorescence properties of SiR-Halo and eGFP together with their respective imaging and detection parameters would contribute to differences observed at the level of detected puncta numbers. Since SiR-Halo labelling, on average, distributed evenly across the brain regions, discrepancies in raw numbers of SiR-Halo and eGFP puncta detected are not of major concern for further work on PSD95 protein lifetime estimates.

Chapter 4 The diversity of PSD95 lifetimes in adult mouse brain

4.1 Introduction

The structural stability of post-synaptic structures is thought to be important for long-term information storage and the lifetime of proteins that compose these structures may instruct us on the functional stability of synapses. We measured the lifetime of PSD95, an abundant scaffolding protein that assembles post-synaptic glutamate receptors and signalling proteins into functioning complexes. Absence of PSD95 is known to cause severe learning and memory impairments emphasizing the importance of this molecule in healthy functioning of synapses (Migaud et al., 1998). Mutations in PSD95-interacting proteins have also been associated with >130 psychiatric and neurological diseases in humans (Bayés et al., 2011). Since the lifetimes of proteins that interact within the complexes are known to corelate, measuring the lifetime of PSD95 may provide us information on the lifetime of multi-protein complexes in the synapse (Mathieson et al., 2018, Martin-Perez and Villén, 2017, Price et al., 2010).

PSD95 protein half-life has previously been measured in primary cell cultures (Ehlers, 2003, El-Husseini et al., 2002, Cohen et al., 2013) and *in vivo* (Price et al., 2010, Heo et al., 2018b, Fornasiero et al., 2018), but these measurements relied on bulk protein extracts and thus lacked spatial resolution. Higher spatial and temporal resolution for half-life measurements was achieved by FRAP (fluorescence recovery after photobleaching) studies *in vitro* (Nakagawa et al., 2004, Sharma et al., 2006, Kuriu et al., 2006, Hruska et al., 2015) and *in vivo* (Gray et al., 2006). FRAP measurements, however, are limited to small numbers of synapses and are very sensitive to diffusion and other movement of molecules in addition to protein turnover which may affect the interpretation of half-life measurements.

The mechanisms governing protein lifetime may be different between brain regions, neuron cell types, parts of dendritic tree and individual synapses, and such differences would be important for the specific functions of brain regions. To my knowledge, only one study to date has looked into the regional difference in synaptic protein lifetimes (Fornasiero et al., 2018). In this study,

synaptosome preparations from cerebellum and cortex of heavy isotope-fed mice were subjected to mass spectrometry analysis and results revealed that synaptic proteins located in cerebellum had shorter half-lives compared to those based in the cortex. We aimed to expand on this study and apply single-synapse resolution techniques to examine PSD95 protein lifetime in 110 brain regions and subregions, dendritic arbour of pyramidal cells and visualise the location of synapses with long and short protein lifetimes.

The current chapter presents brain-wide single-synapse resolution visualisation and estimates of PSD95 protein lifetime. More specifically, in Chapter 4 we aimed to:

(1) Visualize synaptic PSD95 lifetime over 14 days in a sagittal plane of the mouse brain (**Chapter 4.3.1** and **4.3.2**).
(2) Confirm that the decayed protein is replaced with newly synthesized PSD95 in stable synapses (**Chapter 4.3.3** and **4.3.4**).
(3) Estimate the half-life of PSD95 in 110 brain subregions using two complementary methods (**Chapter 4.3.5**).
(4) Investigate PSD95 protein lifetime across the dendritic arbour (**Chapter 4.3.6**).
(5) Assess whether PSD95 half-life differs between synapse types and subtypes (**Chapter 4.3.7** and **4.3.8**).

4.2 Summary of methods used in this Chapter

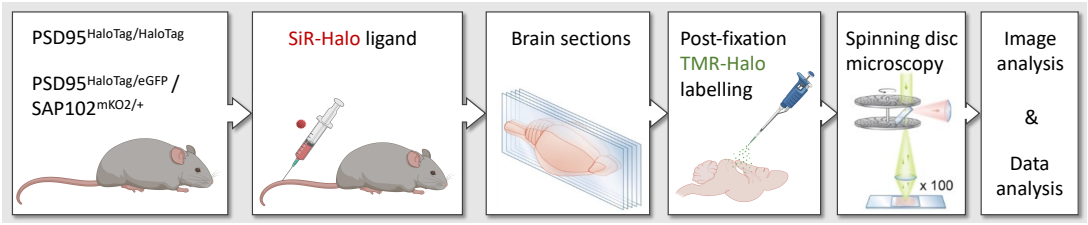

Figure 4.1: A summary of the experimental workflow for Chapter 4.

For results presented in **Chapters 4.3.1 - 4.3.7**, 3-month-old PSD95$^{HaloTag/HaloTag}$ mice were used while the studies presented in **Chapter 4.3.8** used data from 6-month-old PSD95$^{HaloTag/eGFP}$; SAP102$^{mKO2/+}$ animals (**Figure 4.1**; see **Chapter 2.2** for more details). The mice received a bolus injection of 200 µl 1.5 mM SiR-Halo solution and were perfused at different times post-injection (please see **Chapter 2.6** for details). For the study presented in **Chapters 4.3.1 - 4.3.5**, the animals were sacrificed at 5 different, roughly exponentially increasing time points post-injection as shown in **Figure 4.2**. For studies presented in **Chapters 4.3.7 - 4.3.8**, the animals were sacrificed at day 0 or day 7 post-injection. For results presented in **Chapters 4.3.3 - 4.3.4**, fixed brain sections were incubated in 10 µM TMR-Halo solution to label vacant PSD95-HaloTag binding sites (for further details see **Chapter 2.7.1**). Single-synapse resolution images were obtained using spinning disc confocal microscope (**Chapter 2.8**). The imaging parameters used for the studies presented in Chapter 4 are summarized in **Table 4.1**. Fluorescent puncta were detected and quantified as described in **Chapter 2.9**. Density- and intensity-based PSD95 half-life estimations were performed by fitting a single-phase exponential decay on regional puncta densities and puncta fluorescence intensities, respectively (**Chapter 2.10.1**).

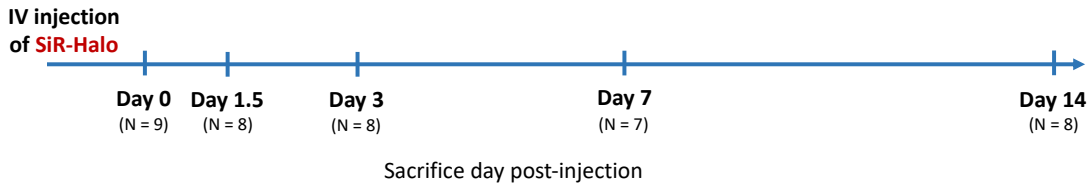

Figure 4.2: The time points and numbers of animals used in the study estimating PSD95 half-life.

Mouse line imaged	Fluorescent label	Laser line	Laser power	Exposure time	Emission filter
PSD95$^{HaloTag/HaloTag}$	SiR-Halo	640 nm	12 %	95 ms	QUAD (700/45)
	TMR-Halo	561 nm	13 %	110 ms	QUAD (607/34)
PSD95$^{HaloTag/eGFP}$ / SAP102$^{mKO2/+}$	SiR-Halo	640 nm	15 %	100 ms	QUAD (700/45)
	PSD95-eGFP	488 nm	30 %	95 ms	QUAD (521/21)
	SAP102-mKO2	561 nm	40 %	100 ms	QUAD (607/34)

Table 4.1: Imaging parameters for visualization of fluorescent markers in Chapter 4.

4.3 Results

4.3.1 Most PSD95 degrades over a two-week period

Images collected from PSD95$^{HaloTag/HaloTag}$ mice injected with SiR-Halo and sacrificed at five different time points post-injection (6 hours, 1.5 days, 3 days, 7 days and 14 days) revealed a loss of labelling across brain regions (**Figure 4.3** and **Appendix 1**). Interestingly, we observed that different brain regions displayed different rates of fluorescence decay. At day 14, subregions of the thalamus, midbrain, olfactory, cerebellar and hindbrain had little or no detectable labelling while isocortex, hippocampus and striatum showed substantially dimmed but still visible fluorescence. Severe reduction in fluorescence over 14 days suggests a degradation of initially fluorescently labelled PSD95 protein.

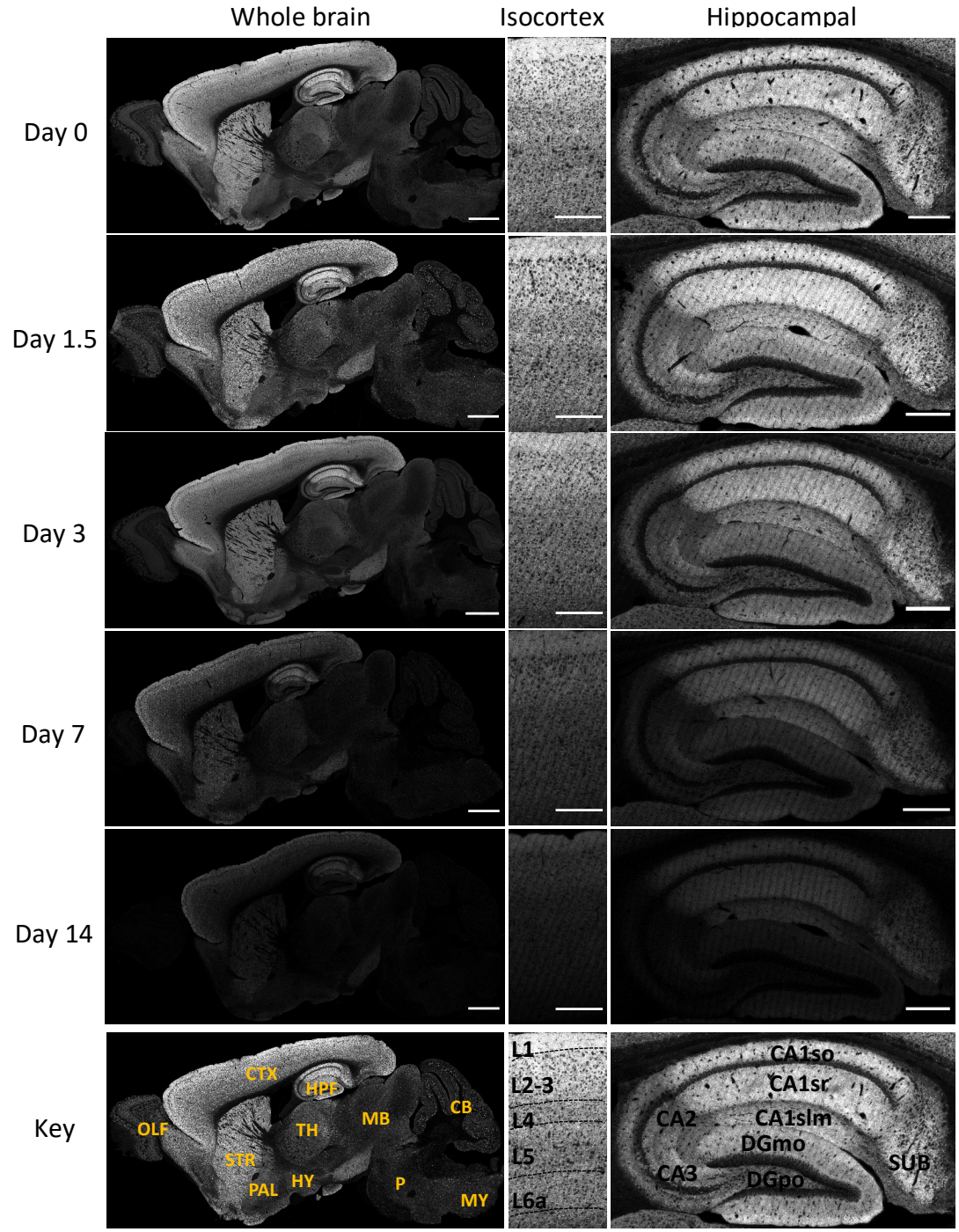

Figure 4.3: SiR-Halo fluorescence labelling at five time points post-injection. *Representative images from whole brain, layers of the isocortex and hippocampal formation. CTX, isocortex; HPF, hippocampal formation; OLF, olfactory areas; STR, striatum; PAL, pallidum; HY, hypothalamus; TH, thalamus; MB, midbrain; CB, cerebellum; P, pons; MY, medulla; CA1so, CA1 stratum oriens; CA1sr, CA1 stratum radiatum; CA1slm, CA1 stratum lacunosum-moleculare; DGmo, dentate gyrus molecular layer; DGpo, dentate gyrus polymorphic layer; SUB, subiculum. Scale bars: 2 mm (whole brain), 500 μm (isocortex and hippocampal formation).*

4.3.2 PSD95 degrades at different rates across brain regions

From the images presented in **section 4.3.1**, it appears that some brain regions and subregions show faster decay of labelled PSD95-HaloTag puncta than others. High-magnification examples of punctate staining reveal a gradient in decay rates in the layers of isocortex, with synapses with the longest PSD95 lifetime located in superficial layers (layer 1) and those with the shortest lifetime located in deep layers (layer 6) of the isocortex (**Figure 4.4A** and **Appendix 2**). In hippocampus, synapses of the CA1 pyramidal cells showed longer PSD95 lifetimes compared to those of CA2 and CA3 pyramidal cells, suggesting that the mechanisms controlling the rates of turnover may be specific to pyramidal cell subtypes (**Figure 4.4B**). While larger synapses are often correlated with higher stability (Berry and Nedivi, 2017), large CA3 thorny excrescence synapses showed shorter lifetimes compared to smaller-sized synapses of the CA1 (**Figure 4.4C**). The observation of differences between brain regions raises an intriguing hypothesis that PSD95 lifetime may be region- or even synapse type-specific.

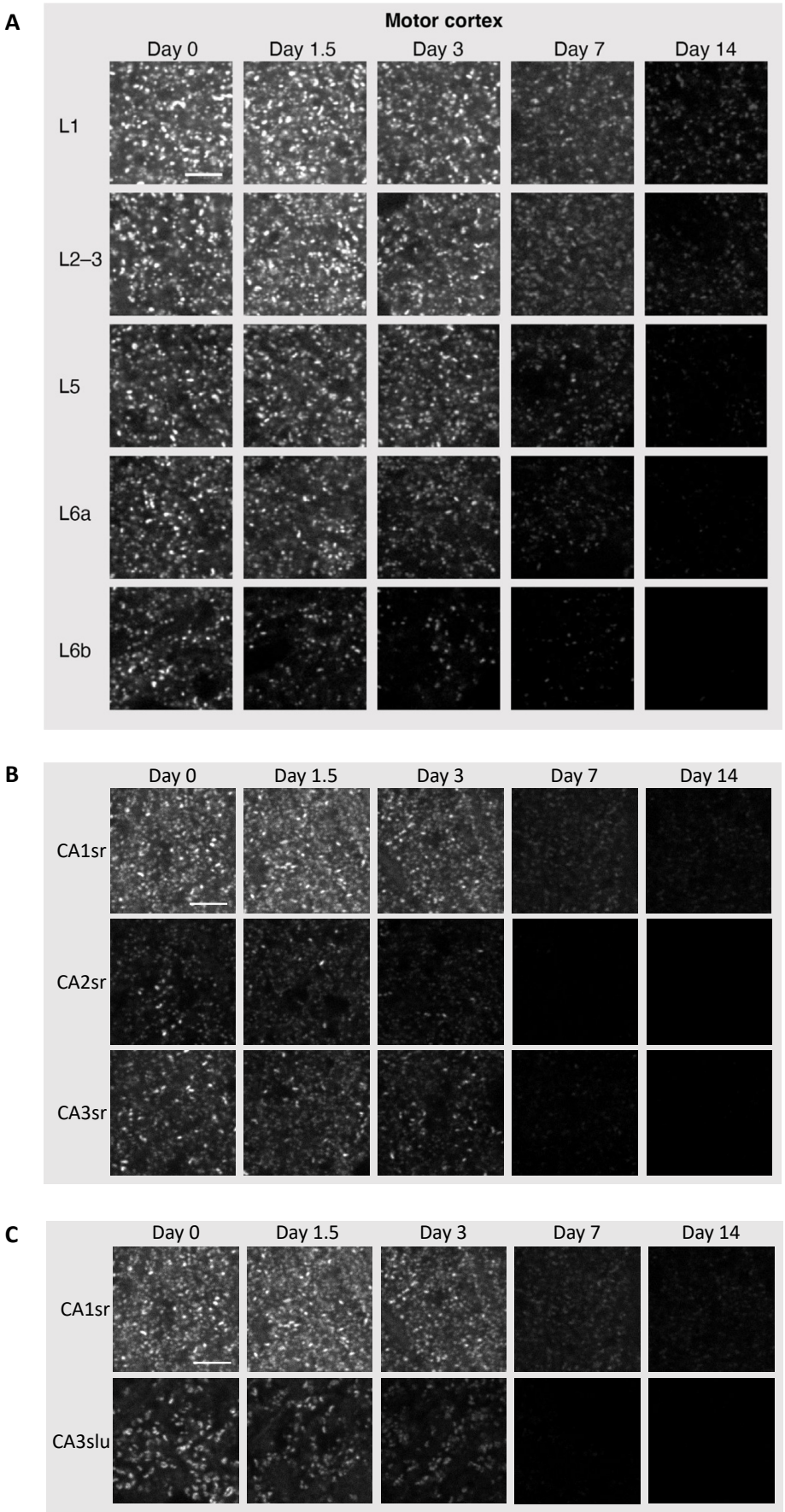
A
Motor cortex
Day 0
Day 1.5
Day 3
Day 7
Day 14
L1
L2–3
L5
L6a
L6b
B
Day 0
Day 1.5
Day 3
Day 7
Day 14
CA1sr
CA2sr
CA3sr
C
Day 0
Day 1.5
Day 3
Day 7
Day 14
CA1sr
CA3slu

Figure 4.4: Fluorescent puncta decay in different brain subregions. *High-magnification single-synapse resolution example images of SiR-Halo puncta decay over a period of 14 days.* ***(A)*** *Representative puncta images from layers of the motor cortex.* ***(B)*** *puncta decay in stratum radiatum area of CA1, CA2 and CA3 pyramidal cells.* ***(C)*** *Examples of large (CA3 stratum lucidum) and small (CA1 stratum radiatum) puncta decay. Scale bar: 5 μm.*

4.3.3 Degraded PSD95 is replaced by newly synthesized protein

In order to confirm whether over the 14-day period the "old" protein is replaced by "new", post-fixation labelling with TMR-Halo was performed to visualize any PSD95-HaloTag proteins unlabelled by SiR-Halo. At day 0, SiR-Halo produced strong punctate staining which was absent or nearly absent in TMR-Halo labelled images (**Figure 4.5A**). Over time, however, SiR-Halo labelling decreased while TMR-Halo increased the labelling of synaptic puncta. Puncta densities of detected SiR-Halo and TMR-Halo at different time points were quantified and examples from isocortex and hippocampal formation are presented in **Figure 4.5B**. TMR-Halo labelling is ~30% at day 0 indicating that even though the initial injection of SiR-Halo was efficient in labelling PSD95-HaloTag binding sites, some of the binding sites were not saturated by injection and were instead occupied through post-fixation labelling with TMR-Halo. Saturation by injection is discussed further in **Chapters 3.3.3** and **3.3.4.** The transition from the majority of puncta having a SiR-Halo label to the majority having TMR-Halo label supports the hypothesis that PSD95 protein initially labelled via the IV injection degrades over time and is replaced by newly synthesized PSD95 that was not labelled by the injected SiR-Halo.

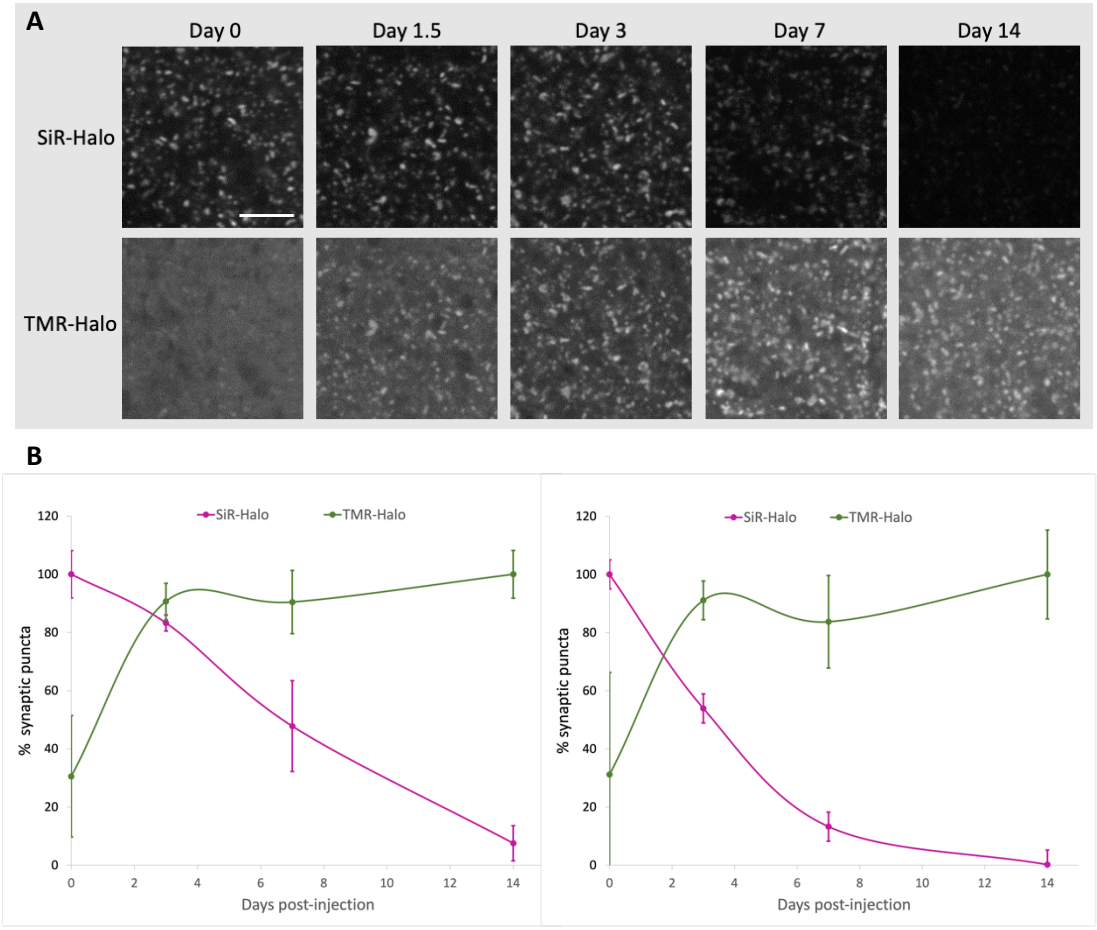

Figure 4.5: Degraded SiR-Halo labelled PSD95-HaloTag is replaced by new protein. (A) *High-magnification representative images of PSD95-HaloTag puncta at different times post-IV injection in layer 2-3 of motor cortex. SiR-Halo labelling (top row) becomes dimmer with time while post-fixation applied TMR-Halo labelling (bottom row) increases with time. Scale bar: 5 μm.* ***(B)*** *Quantified SiR-Halo (magenta) and TMR-Halo (green) puncta numbers at different time points post-injections of SiR-Halo. The values are normalised to the mean of the maximum labelling for SiR-Halo (i.e. at day 0) and TMR-Halo (i.e. day 14). Error bars: +/- SD. N = 3 animals / time point.*

4.3.4 Protein turnover in stable synapses

PSD95 protein decay observed in **sections 4.3.1-4.3.3** may be due to the replacement of old protein with new or the removal of whole synaptic structures (i.e. turnover of dendritic spines). To understand the contribution that spine turnover has to the decay of PSD95, brain sections from day 3 post-injection of SiR-Halo were stained with TMR-Halo and co-localisation of the “old” and “new” protein was examined. Large fractions of co-localised puncta would suggest that protein is being replaced within stable synapses. In contrast, large

fraction of synapses containing only “new” protein would point to a substantial turnover and production of new dendritic spines. **Figure 4.6** presents images of SiR-Halo and TMR-Halo puncta co-localisation in subregions of isocortex and hippocampal formation (for examples from other subregions, see **Appendix 3**). The majority of synaptic puncta across the subregions appear yellow suggesting the presence of both “old” and “new” protein inside them. Co-localisation analysis was carried out between SiR-Halo and TMR-Halo labelled synaptic puncta and results are presented in **Figure 4.7**. Majority, between 50% and 60%, of puncta in layers of the motor (MO) and somatosensory (SS) cortices show co-localisation between SiR-Halo and TMR-Halo. Layer-dependent differences were observed for “SiR-Halo only” and “TMR-Halo only” populations of synaptic puncta, with superficial layers of the cortex containing larger percentages of “SiR-Halo only” compared to “TMR-Halo only” puncta while deeper layers containing more “TMR-Halo only” puncta. Similarly, over 40% of puncta in most of the hippocampal subregions showed co-localisation at day 3 post-injection. CA2 subregions were an exception, with less than 20% of puncta showing co-localisation. The difference in the percentage of co-localised puncta at day 3 post-injection could be related to the turnover rate of protein across the different brain subregions. Interestingly, CA2 appears to have one of the fastest PSD95 turnover rates (**Figure 4.4**) and the co-localisation analysis revealed that more than 70% of the puncta in CA2 were TMR-Halo positive and did not contain any detectable SiR-Halo. These findings suggest that at day 3 post-injection a large proportion of SiR-Halo labelled protein in CA2 had already been replaced with new protein and therefore an earlier time point for co-localisation analysis might be useful to better assess whether protein is turned over in stable synapses. Despite varying rates of turnover in subregions and thus varying relative amounts of SiR-Halo and TMR-Halo labelling, a substantial proportion of synapses contained both “new” and “old” protein supporting the view that protein is turning over in structurally stable synapses.

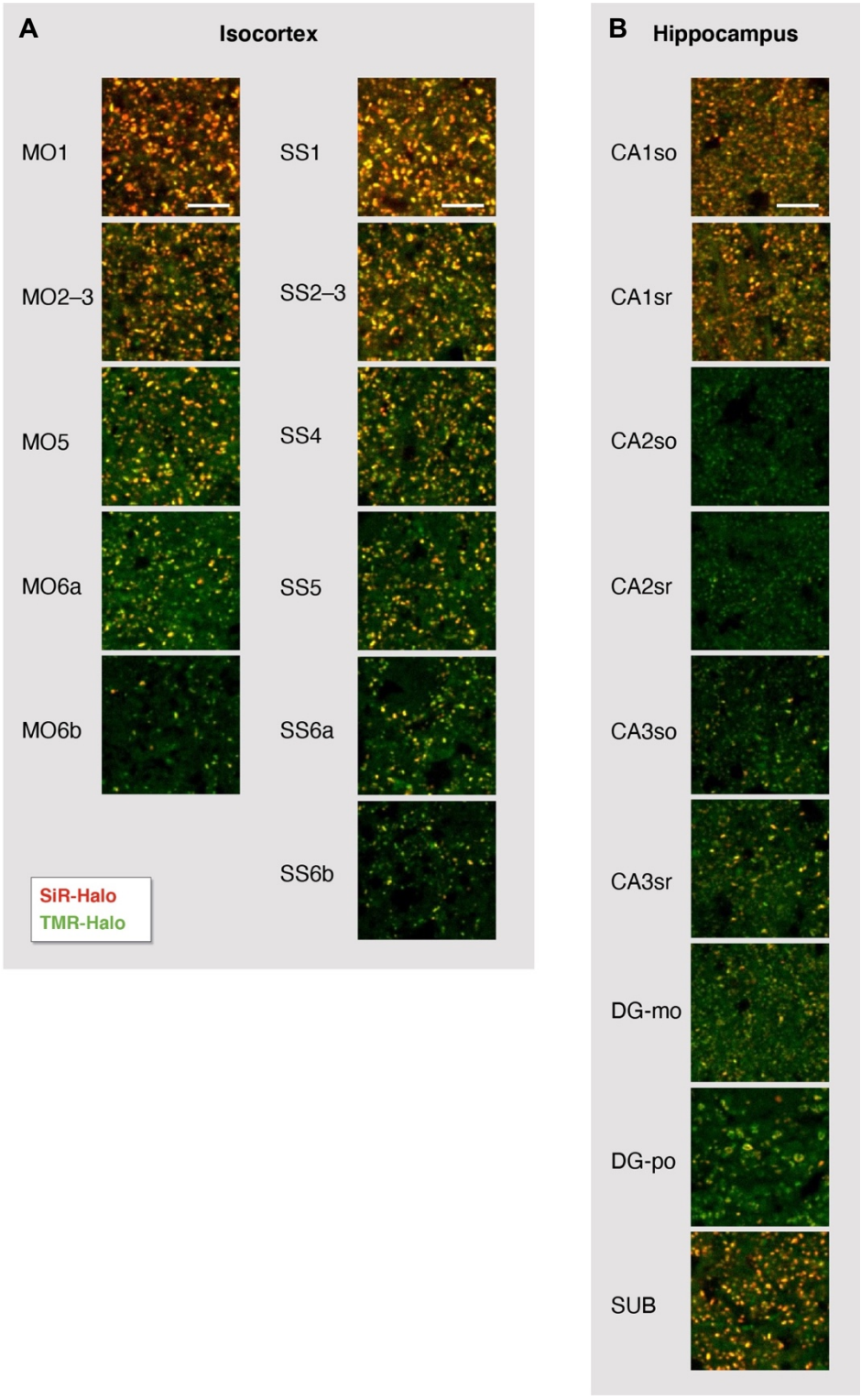

Figure 4.6: PSD95 turns over in stable synapses. *High-resolution puncta images of SiR-Halo (red) injected PSD95-HaloTag mouse brain sections post-fixation stained with TMR-Halo (green) 3 days after injection.* ***(A)*** *Examples from layers of motor cortex (MO) and somatosensory cortex (SS).* ***(B)*** *Puncta examples from subregions of the hippocampal formation. Yellow puncta contain both, SiR-Halo and TMR-Halo labelled PSD95-HaloTag.*

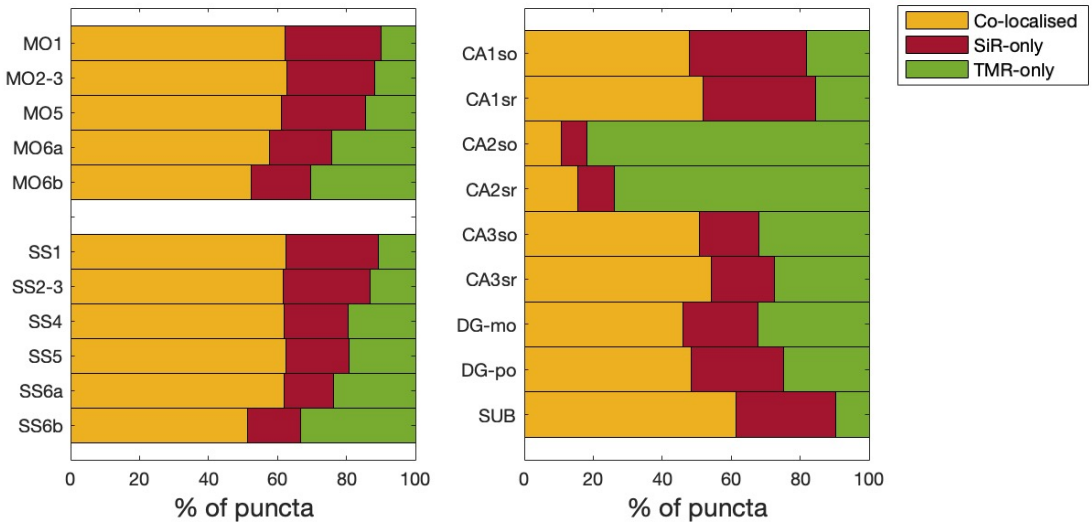

Figure 4.7: Co-localisation between SiR-Halo and TMR-Halo labelling. *Bar graph showing the percentage of fluorescent puncta that are positive for SiR-Halo only, TMR-Halo only or are co-localised in the brain regions presented in* ***Figure 4.6****.*

4.3.5 Half-life estimation

Regional PSD95 half-lives were estimated for 110 brain subregions in adult mouse brain via two different methods: (1) decay of PSD95-containing puncta (i.e. puncta density-based method) and (2) decay of synaptic PSD95 protein (i.e. puncta intensity-based method).

4.3.5.1 Puncta density-based decay

For each brain region examined, fluorescent puncta densities were quantified at different times post-injection of SiR-Halo and a single-phase exponential decay curve was fitted to estimate the half-life of PSD95-positive puncta (**Figure 4.8A**). Surprisingly, the regional half-life estimates were found to range 10-fold, with the longest half-life of 12.1 days found in layer 1 of the motor cortex and the shortest of 1.2 days found in the glomerular layer of the olfactory bulb. At day 14, in the superficial layers of the cortex we could still detect over 30% of synaptic puncta we started with at day 0, however, in olfactory bulb, all fluorescent puncta were already gone by day 7, an observation which signifies the magnitude of a regional difference in lifetime of PSD95-positive puncta.

A summary of PSD95-positive puncta half-life estimates is presented in **Figure 4.8B** (for raw numbers, see **Appendix 4**). Overall, half-life was found to be the longest in cortical and some of the hippocampal subregions and the shortest in the olfactory bulb and the thalamus. Striatum, hypothalamus, midbrain, cerebellum and hindbrain had average half-lives in the range of 3-5 days. Interestingly, within isocortex, all brain regions exhibited a gradient with a ~2.5-fold range in PSD95 half-life from layer 1 ($T_{1/2}$ = 10.6 days) to layer 6b ($T_{1/2}$ = 4.5 days). In hippocampal formation, initial parts of the trisynaptic circuit (dentate gyrus, CA3, and CA2) had shorter half-lives ($T_{1/2}$ = 3.5, 3.0 and 1.9 days, respectively) than the latter part of the circuit, hippocampal CA1 ($T_{1/2}$ = 5.5 days). The ranked half-live estimates (+/- 95% confidence interval) in **Figure 4.8C** reveal a cluster of cortical brain regions with the longest half-lives and a set of subregions of olfactory bulb and hippocampus that have the shortest half-lives out of the regions examined.

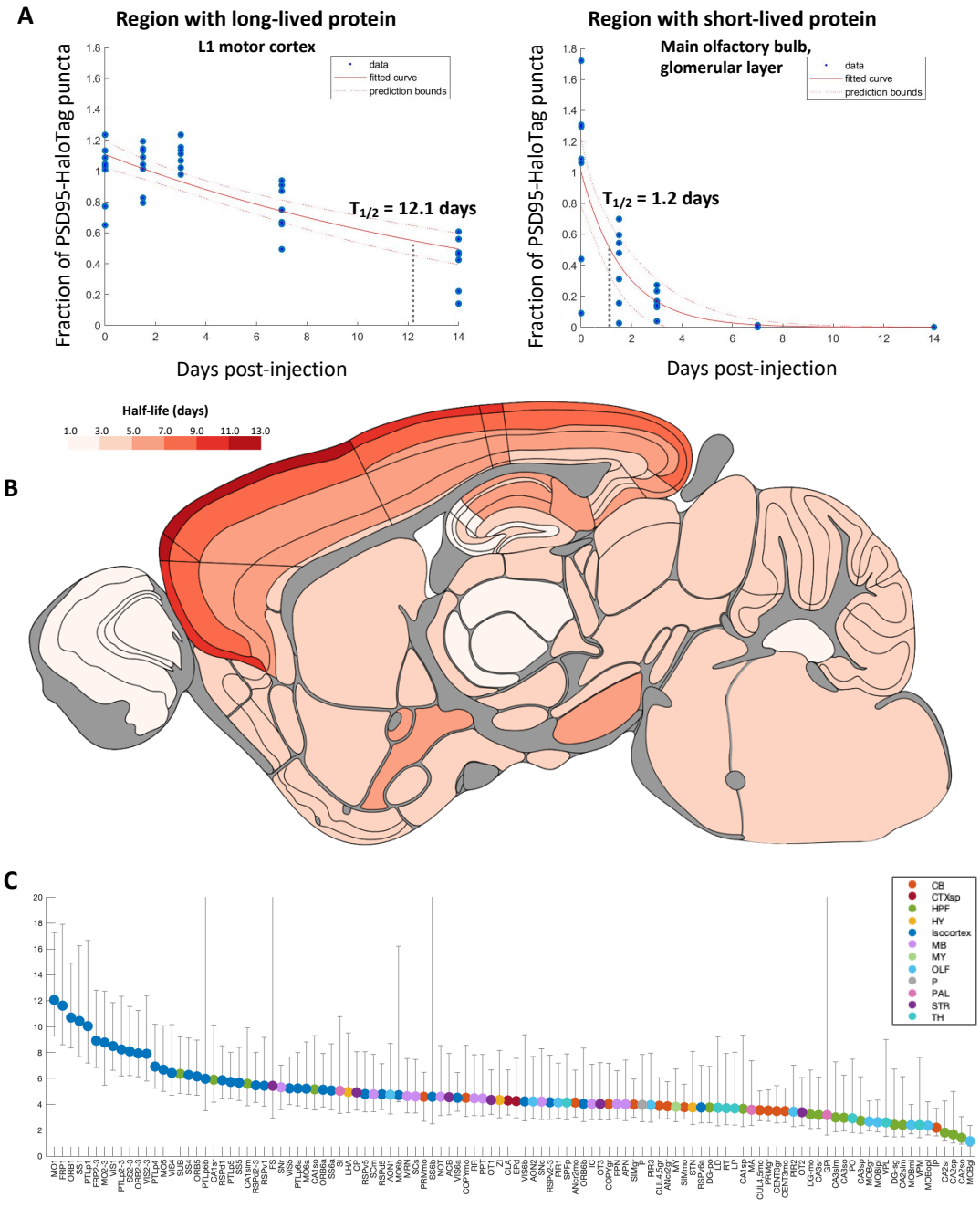

Figure 4.8: PSD95-positive puncta show diverse half-lives across brain regions. (A) *Example fitted single-phase exponential decay curves for the regions with the longest half-life (motor cortex, layer 1) and the shortest half-life (main olfactory bulb, glomerular layer). Each dot represents a normalised puncta density value for the animal. Vertical dashed line represents the estimated half-life.* ***(B)*** *A summary heatmap of PSD95-positive puncta half-lives (in days). Dark red colours highlight brain regions with long half-lives while pale red colours point to regions with short half-lives of PSD95-positive puncta.* ***(C)*** *A rank of brain regions by their half-life (+/- 95% CI) reveals a cluster of cortical subregions (navy blue) sharing long half-lives while several of the hippocampal (green) and olfactory subregions (blue) clustering at the shortest half-lives. N = 7-10 animals / time point.*

4.3.5.2 Puncta intensity-based decay

Fluorescence intensity of detected puncta was summed up for individual brain regions, plotted against time and a single-phase exponential decay was fitted to estimate half-life of synaptic PSD95 protein. The half-life estimates ranged from 1 day in the glomerular layer of the main olfactory bulb to 6.6 days in the layer 1 of the frontal pole cortical region (**Figure 4.9A**; for raw numbers see **Appendix 4**). A summary heatmap of regional PSD95 protein half-lives reveals longer half-lives in cortical, some of the hippocampal, hypothalamic and midbrain regions while the shortest half-lives were detected in olfactory bulb, thalamus, and several subregions of the hippocampus (**Figure 4.9B**). The rank of half-life estimates, similarly to what was observed with the density-based measurement, reveals cortical regions clustering towards the longer half-lives while the subregions of olfactory bulb and thalamus clustering towards the shorter half-lives (**Figure 4.9C**). In contrast to the density-based half-life estimates, the 95% confidence intervals in the intensity-based estimates are wide and largely overlapping suggesting a larger uncertainty in the intensity-based measurements.

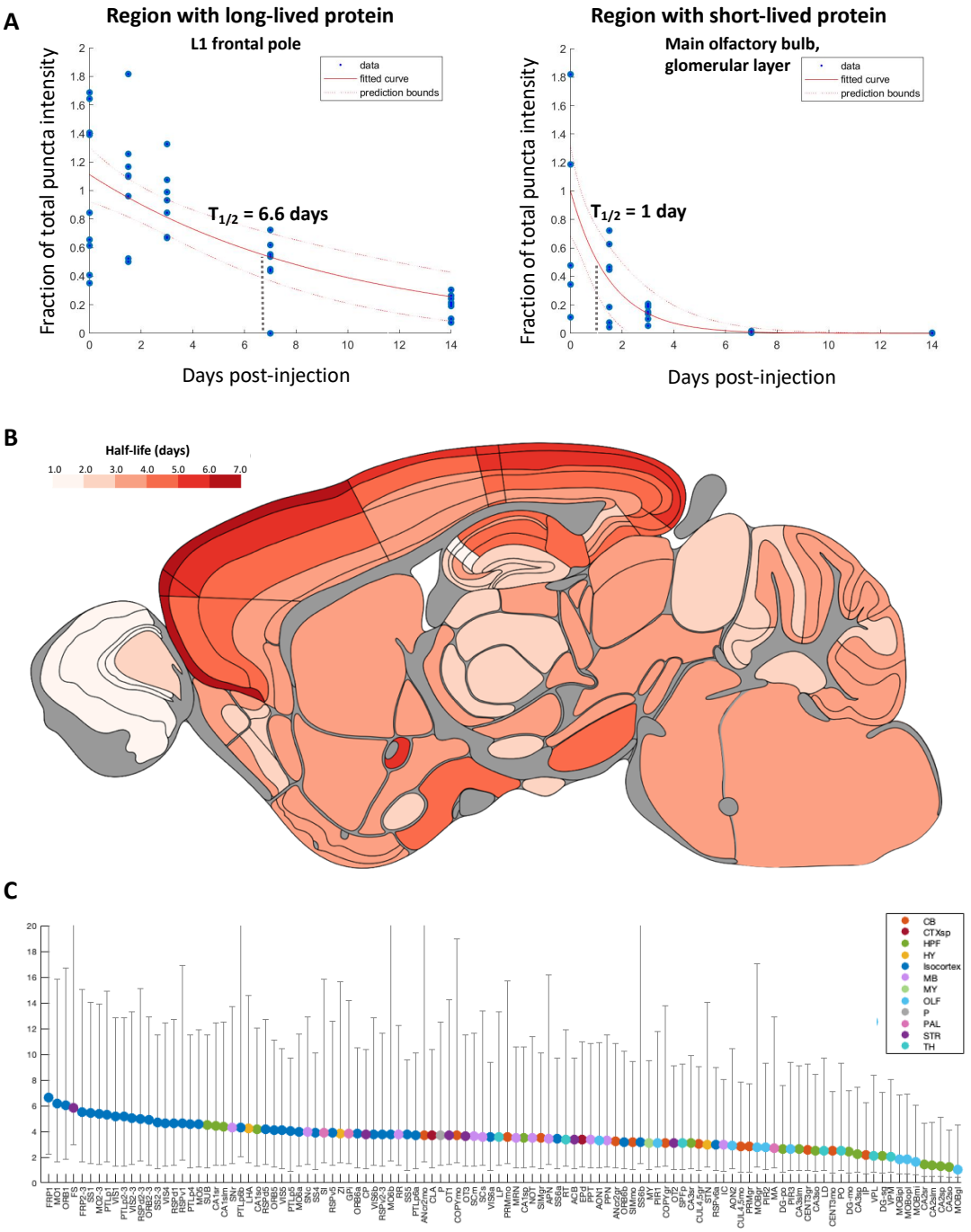

Figure 4.9: Synaptic PSD95 protein half-lives range 6-fold across brain regions. (A) *Example fitted single-phase exponential decay curves for the regions with the longest half-life (frontal pole, layer 1) and the shortest half-life (main olfactory bulb, glomerular layer). Each dot represents a summed puncta intensity value for the animal.* ***(B)*** *A summary heatmap of synaptic PSD95 protein half-lives (in days). Dark red colours highlight brain regions with long half-lives while pale red colours point to regions with short half-lives of synaptic PSD95 protein.* ***(C)*** *A rank of brain regions by their half-life (+/- 95% CI) reveals a cluster of cortical subregions (navy blue) sharing long half-lives while several of the hippocampal (green) and olfactory subregions (light blue) clustering at the shortest half-lives. N = 7-10 animals / time point.*

4.3.5.3 Comparison of the density- and intensity-based half-lives

Puncta intensity-based half-life estimates were found to be on average smaller compared to the density-based estimates. In order to test how comparable the two measurements were across different brain regions, we correlated density- and intensity-based half-life estimates for all 110 brain regions examined (**Figure 4.10**). A strong positive correlation was observed (Pearson's correlation, R = 0.9088, P < 0.0001) suggesting that the two measurements are comparable and show highly similar trends in regional estimates of half-lives.

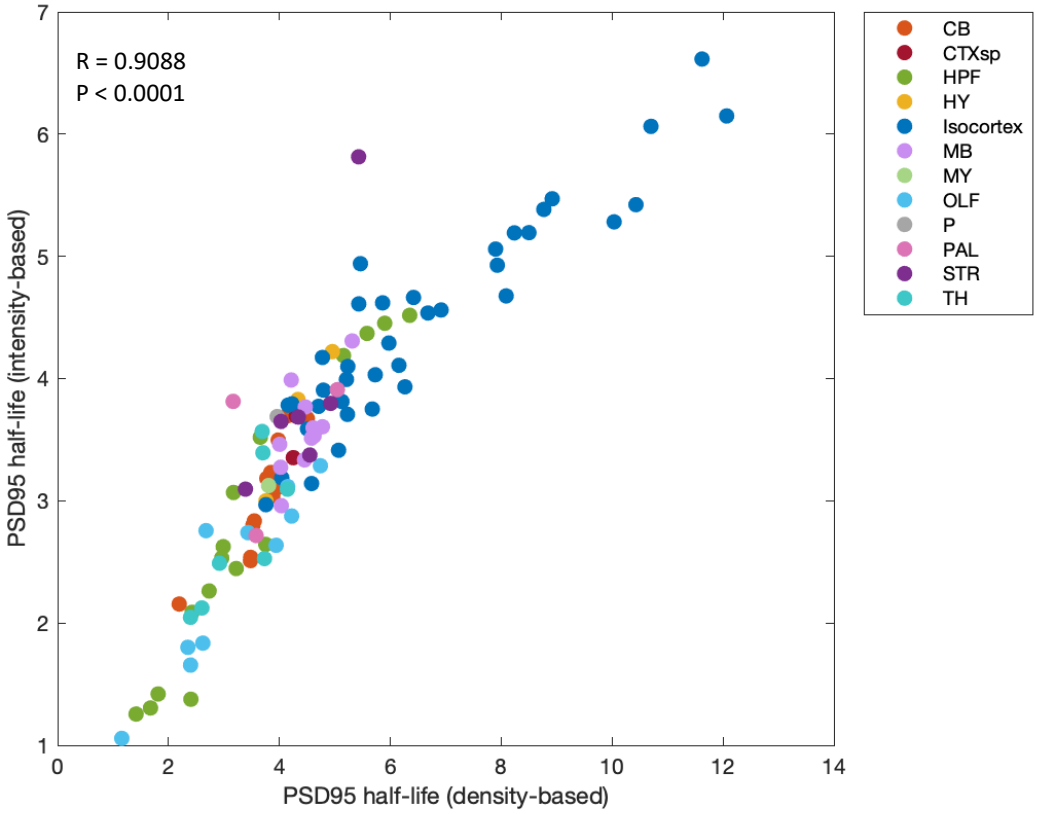

Figure 4.10: Correlation between density- and intensity-based half-life measures. *Puncta density- (x-axis) and intensity-based (y-axis) estimations of half-life (in days) show a strong positive relationship. Each dot represents a brain subregion and colours correspond to the parent brain areas. Pearson's correlation test.*

4.3.6 PSD95 lifetime gradients in CA1 dendrites

The polarized morphology of neurons and longer distances that proteins and molecular machineries need to travel to reach distal synapses raised questions about protein lifetime in different parts of the dendritic tree. PSD95 lifetime was assessed in dendritic layers of the CA1 in brain images from day 0 and day 7 mice (**Figure 4.11** and **Appendix 5**). CA1 region was subdivided into small segments of equal thickness and SiR-Halo-positive puncta were quantified for each of the delineated areas. Mean fraction of puncta at day 7 compared to day 0 (+/- SD) was calculated for each segment. PSD95 protein lifetime was found to increase with distance from the soma in CA1 stratum radiatum before dropping at the boundary with stratum lacunosum. Protein lifetime again increased throughout stratum lacunosum and moleculare. Increase in PSD95 protein lifetimes with distance from the cell body was also observed in the basal dendrites (CA1 stratum oriens). Longer protein lifetimes further away from the soma indicate differences in protein metabolism in proximal and distal dendrites.

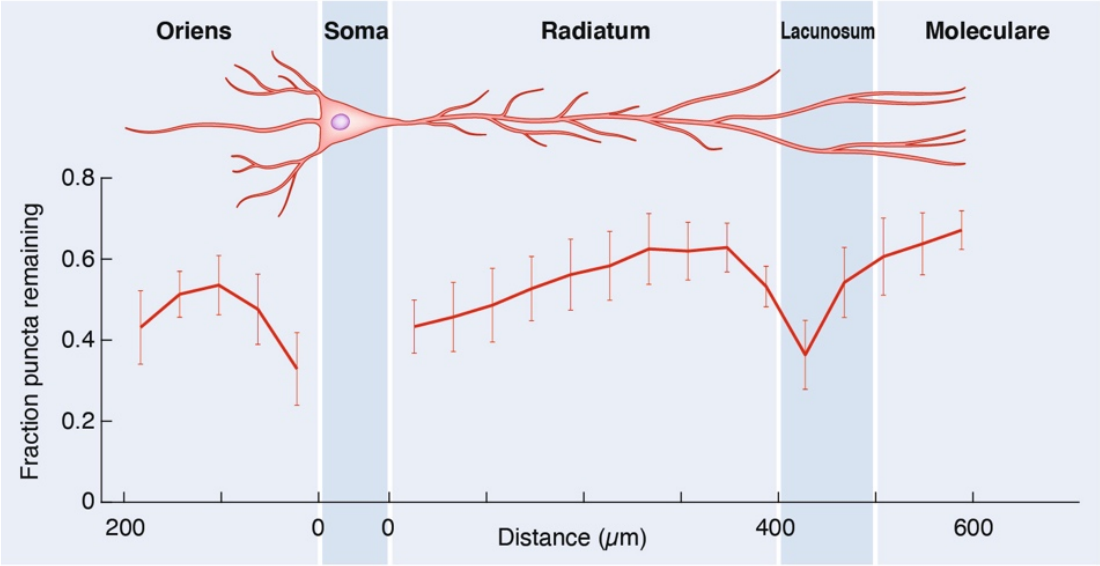

Figure 4.11: Fluorescent puncta decay across apical and basal dendrites of the CA1 pyramidal cells*. Line plot presents mean fraction of puncta remaining at day 7 compared with day 0, +/- SD. Day 0, N = 3; day 7, N = 3 animals.*

4.3.7 PSD95 half-life correlates with synapse parameters

Any relationships between synapse parameters and PSD95 half-life were established by correlating PSD95 density-based half-lives and day 0 puncta density, mean intensity and puncta size (**Figure 4.12**). All three puncta parameters do show a positive correlation with half-life estimates therefore suggesting that brain regions containing higher density of synapses, synapses with higher PSD95 protein content or synapses larger in size tend to have longer PSD95 half-lives. The correlations, however, were based on average synapse intensity and size measurements which provide little information on the behaviour of individual synapses within the diverse puncta population.

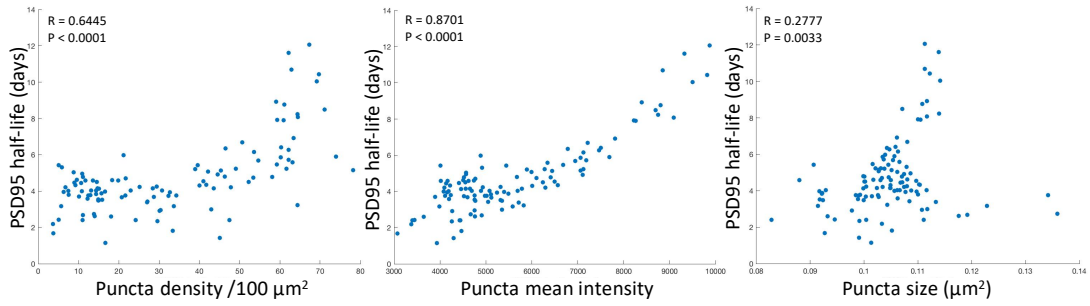

Figure 4.12: PSD95 half-life correlates with synapse parameters. *Puncta density, puncta mean intensity and puncta size all show positive correlation with PSD95 half-life. Each dot represents a brain subregion.*

4.3.8 PSD95 lifetime differs between synapse subtypes

We previously defined 37 synapse subtypes based on their molecular composition and morphology (Zhu et al., 2018, Cizeron et al., 2020). To further investigate whether synapse subtypes have distinct protein half-lives, we mapped PSD95 lifetime in PSD95-HaloTag, PSD95-eGFP and SAP102-mKO2 triple knock-in ($PSD95^{HaloTag/eGFP}$;$SAP102^{mKO2/+}$) mice (for representative images of triple fluorescence from these mice, see **Appendix 6**). 6-month-old mice were injected with SiR-Halo and brain sections collected at day 0 or day 7 post-injection. SiR-Halo positive synapses were categorised into subtypes based on PSD95-eGFP and SAP102-mKO2 characteristics, allowing to estimate the lifetime of 30 out of 37 subtypes (7 subtypes do not contain PSD95 but only SAP102). The rank of subtypes according to their

estimated lifetime reveals that some subtypes show very little decay over 7 days (<20 %) while others display a decay of ~70 % over the same time period (**Figure 4.13A**). On the whole-brain scale, subtype 2 retained the most (96.7 %) and subtype 6 the least (23.3 %) of SiR-Halo label. Similar ranking was observed for 12 main brain areas (**Appendix 7**) and individual brain subregions (**Figure 4.13B**; for raw data see **Appendix 9**). Two of the longest protein lifetime subtypes, subtype 2 and 34, are among the largest synapse subtypes (subtype 2, 7, 27 and 34 are the largest and are defined by their large PSD95-eGFP puncta size) (Zhu et al., 2018), suggesting that bigger synapses may retain their protein for longer. In addition, out of the highest fluorescence intensity subtypes (i.e. subtypes 20, 34, and 35), 34 and 35 are long protein lifetime subtypes, indicating that synapses containing larger amounts of protein may be more stable and have slower turnover of their protein. Interestingly, Type 1 (PSD95-only) and Type 3 (PSD95 + SAP102) synapses both contain long- and short-lived subtypes suggesting that the molecular composition is not playing a major role in determining the lifetime of protein in synapses.

Since long protein lifetime (LPL) synapses show greatest protein stability and therefore may be important for molecular memory storage, we quantified the percentage that LPL synapses occupy in the total population of excitatory synapses across different brain subregions. We grouped together five longest-lived subtypes (subtypes 2, 34, 2, 35 and 5) to represent the LPL synapse population. In the whole brain, LPL synapses represented 6.7% of the total synapse number (**Figure 4.13C** and **Appendix 8**). Interestingly, there was a marked variation in percentage of LPL synapses across brain regions and subregions, with a 15-fold range in the main brain areas: isocortex (11.9%), striatum (5.9%), cortical subplate (4.4%), cerebellum (3.9%), HPF (3.8%), olfactory areas (3.0%), midbrain (2.4%), hypothalamus (2.2%), medulla (2.2%), pons (2.1%), pallidum (1.8%) and thalamus (0.8%). At the level of subregions, the highest percentage of LPL synapses was detected in layer 2/3 of the somatosensory cortex (17.2%) and the lowest in CA2 stratum lacunosum-moleculare (0.2%) (for raw data, see **Appendix 10**). In the

isocortex, superficial layers had 4- to 5- fold more LPL synapses compared to the deep layers, while in the HPF, LPL synapse number ranged 10-fold between subregions. The drastic difference in LPL synapse numbers across the brain points to a varied capacity of brain regions to store information in synapses.

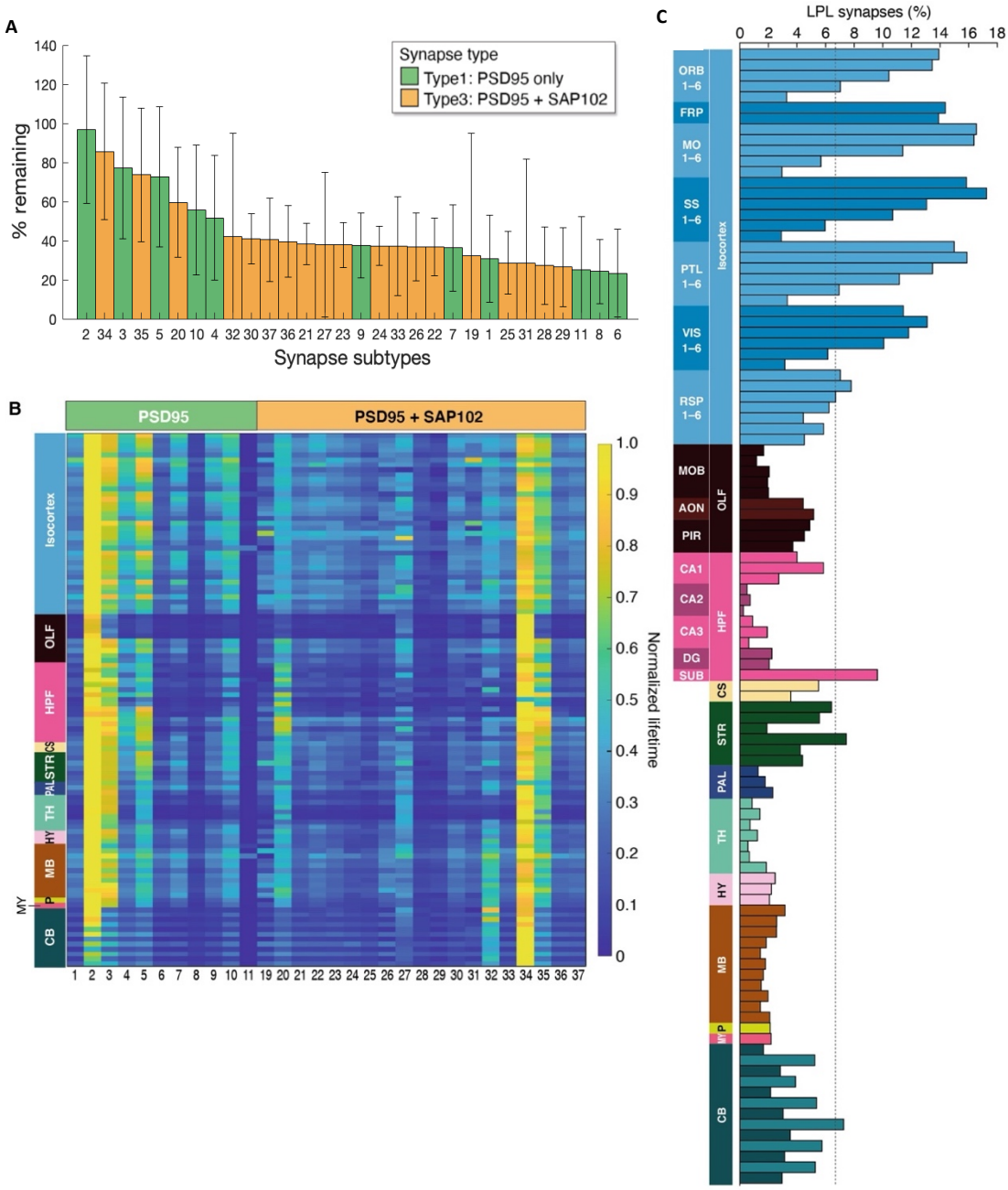

Figure 4.13: PSD95 lifetime differs between synapse subtypes. (A) *Percentage of SiR-Halo-containing subtypes at day 7 compared to day 0 in the whole brain (+/- SD). The bars are ranked according to their associated PSD95 lifetimes. Subtype ID is given at the bottom.*

Colours correspond to synapse type (type 1: PSD95-only and type 3: PSD95 + SAP102). ***(B)*** *A heatmap of subtype lifetimes across brain subregions. Note: scaled rows.* ***(C)*** *Percentage of synapses represented by LPL synapses across brain subregions. Dashed line: average percentage of LPL synapses for the whole brain. Day 0, N = 8; day 7, N = 8 animals.*

4.4 Discussion

In Chapter 4, we visualise and quantify the lifetime of synaptic PSD95 across the brain of adult mice. SiR-Halo labelled PSD95 decayed at different rates across brain regions. Decayed protein was replaced by newly synthesized PSD95, as confirmed by post-fixation staining with TMR-Halo ligand. Half-lives of PSD95-positive puncta and synaptic PSD95 protein were calculated for 110 brain subregions and showed multi-fold differences. Superficial layers of the cortex showed the longest PSD95 lifetimes while olfactory, CA2 and thalamic subregions had the shortest lifetimes. Finally, we identified synapse subtypes which possess long protein lifetimes (LPL synapses), and their numbers were enriched in cortical subregions, areas of the brain known to store long-term memories.

4.4.1 PSD95 half-life estimates in context of previous literature

PSD95 half-life estimated in Chapter 4 is on average slightly shorter than that estimated in *in vivo* studies using SILAC and heavy isotope labelling (Price et al., 2010, Heo et al., 2018b, Fornasiero et al., 2018) but longer than the estimates performed in primary cell cultures (Kratschke, 2018, Ehlers, 2003, El-Husseini et al., 2002). I found PSD95 half-life to range from 1.2 days to 12.1 days in density-based estimate and from 1 day to 6.6 days in intensity-based measurement. Price et al. (2010) estimated PSD95 half-life for the whole brain homogenate to be 15.3 days which is larger than any of the half-life values I found for individual brain regions or subregions. Heo et al. (2018b) performed their measurement on synaptosomes from mouse forebrain and found the half-life to be ~30 days. Fornasiero et al. (2018) found the half-life of PSD95 to be 16.43 days in cortical synaptosomes and 12.73 days in synaptosomes from cerebellum. *In vitro* the half-lives ranged from 8 hours in synaptosomes from rat cortical neurons (Ehlers, 2003) to 36 hours found in rat hippocampal

neurons (El-Husseini et al., 2002) and mouse hippocampal and cortical neurons (Kratschke, 2018). The observation that protein lifetime estimates are smaller *in vitro* compared to *in vivo* is well recognised (Cohen and Ziv, 2019, Alvarez-Castelao and Schuman, 2015). The differences observed between the *in vivo* measurements may be due to a number of factors: (a) efficiency of labelling the existing protein, (b) the number of time points used to estimate half-life, (c) parts of the brain tissue used for measurements and (d) sensitivity of the measurement technique. The labelling whether with heavy isotopes or HaloTag ligands is never 100% saturating and less than saturating labelling will induce bias towards lower half-life value estimates. The number of time points used for estimating half-life should ideally be more than 2 to ensure a reasonable fitting of the exponential decay function to data acquired. In my study we used 5 time points for half-life calculations while Price et al. (2010) used 9 time points and Heo et al. (2018b) as well as Fornasiero et al. (2018) used only 2 time points. Parts of the brain tissue used for measurements were also different between studies, with some using synaptosome preparations others whole-tissue homogenates and some using isolated brain regions while others doing the measurement on whole brain tissue. Considering the multi-fold differences in half-life we observed between brain regions, selection of different brain areas for analysis may result in vastly different estimates of protein lifetime. Finally, different measurement techniques may have their associated limits in sensitivity. In the case of imaging HaloTag-labelled PSD95, puncta of very low intensity, as would happen at later time points after injection, will eventually hide in the background noise of the tissue and will no longer be detected as puncta. Such undetected puncta would skew the half-life estimates towards smaller values. Despite the technical limitations and choice of techniques and protocols that all induce differences in resulting measurements, *in vivo* measurements of lifetime (including the present study) all find the lifetime of PSD95 to be in the order of several days.

4.4.2 Possible factors influencing protein lifetime

More than 6-fold differences in PSD95 lifetime observed between brain regions and subregions raises questions about the possible factors contributing to

differential protein decay. Below I discuss several biological aspects that may play a role in governing protein lifetime.

4.4.2.1 Cell-type

In our study we observe hints of cell-type specific PSD95 protein lifetimes. Lifetime was found to be the longest in isocortex, subiculum and hippocampal CA1, areas populated largely by pyramidal cell types. In contrast, shortest protein lifetime was found in the olfactory bulb composed of mitral cells, tufted relay neurons and granule cells (Nagayama et al., 2014). Cell subtype specific differences in lifetime could be observed in the hippocampal formation, where CA1 pyramidal cells showed longer lifetime compared to CA2 and CA3 pyramidal cells. Our results support previous literature showing that protein lifetimes differ between tissue and cell types (Fornasiero et al., 2018, Dörrbaum et al., 2018, Price et al., 2010, Lajtha et al., 1976, Lajtha, 1959). When heart, muscle, liver and brain tissues were examined, brain tissue was found to have longest protein lifetimes (Lajtha, 1959, Lajtha et al., 1976, Fornasiero et al., 2018, Price et al., 2010). Within the brain, comparisons have been made between neuronal and glial cells, and neurons, on average, displayed longer protein lifetimes (Fornasiero et al., 2018, Dörrbaum et al., 2018). The only published study to date comparing protein lifetimes between neuronal cell types was Fornasiero et al. (2018) which examined protein half-life in cerebellum and cortex which are composed of primarily granular and pyramidal cells, respectively. The study found the lifetime of different classes of proteins to differ between cerebellum and cortex, with histone associated proteins showing longer lifetimes in the cerebellum while cell adhesion molecules, septin and exo-endocytosis factors displaying longer lifetimes in the cortex. PSD95 lifetime in this study was found to be longer in the cortex compared to cerebellum. Our results agree with findings presented in Fornasiero et al. (2018) with cortical areas having longer PSD95 lifetime compared to subregions of the cerebellum.

In order to assess neuron cell-type specific synaptic PSD95 protein lifetimes, future experiments could employ conditional PSD95-HaloTag mouse lines in

which only the protein present in a particular cell type would express the HaloTag construct. Future studies could also further confirm our findings by examining the transciptomic profiles of different neuron types and looking for correlations between the presence and abundance of specific transcripts with the longevity of protein lifetime. Particular attention should be paid to transcripts of proteins that regulate protein synthesis and degradation, such as those that encode ribosomal subunits or E3 ligases specific to proteins of interest as those could give us some insight into the relative presence and abundance of molecular machinery regulating protein turnover.

4.4.2.2 Activity-dependent mechanisms

Increasing brain activity by environmental enrichment *in vivo* or synaptic activity by bicuculline *in vitro* have both been shown to change the lifetime of a number of proteins (Ehlers, 2003, Fornasiero et al., 2018, Heo et al., 2018b, Kratschke, 2018). In these studies, however, only minor or no effects were seen on the lifetime of PSD95. Since previous studies were done on selected forebrain regions, a possibility remains that in the regions not yet examined, such as the olfactory areas, thalamus and cerebellum, activity plays a more substantial role in regulating protein lifetime. The present study did not assess the effects of increased activity on half-life of PSD95. In the future, however, HaloTag ligand-injected PSD95-HaloTag mice could be subjected to environmental enrichment paradigm and careful measurements could be made of changes in protein lifetime in multiple brain regions and subregions.

4.4.2.3 Distance from soma

Our analysis of PSD95 lifetime in synapses from distal and proximal dendrites of CA1 revealed that synapses located further away from the cell body tend to have longer protein lifetimes compared to synapses neighbouring the soma. Similar gradients of PSD95-eGFP puncta intensity and, to a lesser extent, size, have been observed previously (Cizeron et al., 2020). The gradient of protein expression in CA1 dendritic tree is not unique to PSD95. Several published studies have recorded gradients of synaptic AMPA receptors (Andrasfalvy and Magee, 2001, Nicholson et al., 2006, Menon et al., 2013, Walker et al., 2017).

Unique neuronal cell morphology may be the reason for the observed molecular gradients. Neurons are highly polarized cells, and their dendrites can extend hundreds of micrometres away from the cell body. The cell's DNA and majority of protein synthesis and degradation machinery are present in the soma which causes at least a fraction of newly made synaptic proteins or proteins requiring degradation to travel long distances to their target destinations. Synapses in distal neurons would be most likely to get affected and this may impact the lifetime of synaptic proteins. Our observation that distal synapses have longer lifetimes is consistent with the idea that longer time and more complicated logistics are needed to supply protein to these synapses and therefore maintaining slower turnover of distally placed proteins may be more optimal.

To better understand how much of a constraint protein trafficking may be on the supply of PSD95 protein to distal synapses, future experiments could examine the amounts of PSD95 mRNA in the dendrites of CA1 compared to soma in brain tissue. This could be done via high-resolution fluorescence in situ hybridization (Swanger et al., 2011, Moffitt et al., 2016, Cajigas et al., 2012). The larger the fraction of local mRNA supplies, the less of an issue long-distance trafficking would pose as larger fraction of PSD95 protein could be synthesized locally. Antibodies against subunits of the ribosome and proteasome could be used in these same brain sections to assess relative presence of protein synthesis and degradation machinery in distal and proximal dendrites.

4.4.2.4 Dendritic spine dynamics

In our study, PSD95-HaloTag protein was found to turn over in stable synapses as evidenced by most synapses containing both "new" and "old" protein at day 3 post-injection of SiR-Halo. The result is not surprising given that PSD95 preferentially resides in more stable spines (Cane et al., 2014). Stable spines can last for weeks, months or even a lifetime (Zuo et al., 2005, Holtmaat et al., 2005, Yang et al., 2009), therefore their turnover is unlikely to affect the lifetime

of protein that we observe. The measurements of long-lived spines, however, have mainly been performed in the cortical regions due to their easier access via a cranial window. Spines in the hippocampal CA1 have been shown to turn over much faster, with 100% of spines being replaced every 1-2 months (Attardo et al., 2015, Pfeiffer et al., 2018). Our estimated half-life for PSD95-HaloTag puncta in CA1 is 5.5 days and by day 33 post-injection (6^{th} half-life) we would expect to see only around 1.56% PSD95-HaloTag puncta remaining. The puncta half-life measurement in CA1 matches the estimated lifetime for dendritic spines in the region which may suggest that some of the PSD95 puncta decay may be accounted for by the decay of the dendritic spines. A couple of technical issues, however, may be affecting these results: (a) cranial window implantation can cause an artificial increase in spine turnover and (b) CA1 is the last brain area to get saturated by the injection of HaloTag ligands. Cranial window implantation and, even more so, the implantation of a microendoscope to reach the hippocampal formation are both highly invasive procedures that can cause tissue irritation and damage and have been previously been shown to cause the change in dendritic spine dynamics (Xu et al., 2007). In addition, HaloTag labelling of CA1 was not saturating in a fraction of brains examined, which might have led us to underestimate the lifetime of PSD95-HaloTag puncta. Further careful studies of spine and protein lifetime in the CA1 may be needed to confirm current observations.

Dendritic spine dynamics has not yet been explored in a vast majority of brain regions and subregions, and, at this point, we cannot be sure to what extent the lifetime of PSD95 in subcortical brain areas is affected by the turnover of dendritic spines. Future studies examining dendritic spine dynamics in these areas would be needed to assess their impact on protein lifetime.

4.4.2.5 Synapse morphology

Brain regions containing larger PSD95 puncta were found to have longer lifetimes, a result that is consistent with large synapses being more stable (Yang et al., 2009). More detailed analysis into the synapse subtypes revealed subtypes 2 and 34 to be extremely long-lived. These subtypes are defined

primarily by their large size (Zhu et al., 2018) further supporting the hypothesis that large synapses have long protein lifetimes. We did find examples, however, opposing this relationship between puncta size and lifetime. Large excrescence synapses in the CA3 had shorter PSD95 lifetimes compared to small synapses in the CA1. This, however, may be an exception and may be due to cell-subtype specific regulation of protein lifetime.

4.4.2.6 Synapse molecular composition

LPL synapses were identified for both type 1 (PSD95-only) and type 3 (PSD95 + SAP102) puncta suggesting that the molecular composition of synapses may not play a major role in determining the lifetime of synaptic proteins. In synapses, PSD95 and SAP102 assemble into physically distinct complexes (Frank et al., 2016), therefore, the presence of their respective complexes in same synapses may not influence the lifetime of either of the proteins. In contrast, proteins belonging to the same molecular complexes tend to have coordinated lifetimes (Price et al., 2010, Mathieson et al., 2018, Martin-Perez and Villén, 2017). PSD95 forms large ~1.5 MDa multi-protein complexes with PSD93 and NMDA receptor subunit GluN2B (Frank et al., 2016). To test whether the ability to form these complexes affects PSD95 lifetime, mice lacking PSD93 protein or GluN2B subunit could be crossed with PSD95-HaloTag mice and the lifetime of PSD95 examined. PSD95 lifetime in PSD93-KO animals was investigated in a separate study, and the results are presented in **Chapter 6**.

4.4.3 Implications for memory storage

Stability of synaptic connections between neurons is thought to play an important role in long-term memory storage in the brain (Poo et al., 2016, Mongillo et al., 2017). Stable dendritic spines can last for months or even a lifetime (Zuo et al., 2005, Holtmaat et al., 2005, Yang et al., 2009) and learning-associated stabilisation of newly formed dendritic spines has been found to correlate with behavioural performance (Holtmaat et al., 2006, Holtmaat and Svoboda, 2009, Xu et al., 2009, Yang et al., 2009). Majority of studies so far, however, have examined the structural stability and lifetime of the spines but

the lifetime of the synaptic proteins within them would provide important insights into the functional stability of molecular complexes that process neuronal signals.

We find that synapses with longest protein lifetimes are located in isocortex and HPF, areas important for learning and memory storage in the brain (Marr and Brindley, 1971, Willshaw and Buckingham, 1990, Squire and Bayley, 2007). Importantly, regions of isocortex showed longer protein lifetimes and thus more stability of synapses than those of HPF. The findings are consistent with the idea that short-term memory storage in hippocampus is with time transferred to long-term storage facilities in the isocortex (Marr and Brindley, 1971, Bontempi et al., 1999, Frankland and Bontempi, 2005, Squire and Bayley, 2007, Kitamura et al., 2009).

At the level of individual synapses, brain regions were found to be populated by different proportions of LPL and SPL synapses, parallel to the populations of ‘persistent’ and ‘transient’ dendritic spines found in different areas of the brain (Trachtenberg et al., 2002, Holtmaat et al., 2005, Attardo et al., 2015, Pfeiffer et al., 2018). Due to longer protein lifetime, LPL synapses could store molecular memory for longer time periods compared to SPL synapses and thus would be more optimised to ensure ‘persistence’ of memory (Richards and Frankland, 2017). Regional differences in LPL and SPL synapse numbers could point to how specific brain areas balance ‘persistence’ and ‘transience’ of memory as described in Richards and Frankland (2017) which contribute to precise recording of information and flexibility of behaviour, respectively. We find that the LPL synapses are preferentially located in the isocortex while thalamus, pallidum, pons and medulla, subcortical regions important for relaying information and supporting innate behaviours, are composed primarily of SPL synapses. Additionally, larger percentage of LPL synapses is found in the isocortex compared to the HPF which would suggest that HPF is a transient location of information storage. Indeed, more rapid forgetting has been observed of episodic memories (HPF-dependent) compared to slower

forgetting of semantic memories that are isocortex-dependent (Ritchey et al., 2015).

LPL synapses were found to be large in size. Since large spines contain on average more PSD95 (Cane et al., 2014), LPL synapses would likely be located in large dendritic spines. As mentioned above, positive correlation between spine size and its lifetime is well described in the literature (Holtmaat et al., 2005, Zito et al., 2009, Loewenstein et al., 2015). Since learning and memory have been associated with stable dendritic spines, there is an intriguing possibility that LPL synapses are ‘memory’ synapses. Close observation and/or manipulation of LPL synapses during learning and memory tasks would help establish this functional link.

Chapter 5 PSD95 lifetime changes across the lifespan

5.1 Introduction

Tight control of protein synthesis and turnover is important for healthy brain functioning throughout the lifespan. Imbalance in protein homeostasis can cause disease and issues in learning and memory (Cajigas et al., 2010, Park and Kaang, 2019). During development, mutations in components of protein synthesis machinery lead to neurodevelopmental diseases, including autism spectrum disorders and intellectual disability (Louros and Osterweil, 2016). In ageing, dysfunctional proteostasis can cause accumulations of misfolded protein aggregates associated with neurodegenerative diseases, such as Alzheimer's disease, Parkinson's disease and Huntington's disease (Hipp et al., 2019, Jayaraj et al., 2020). Cognitive capacities, including the ability to learn and remember, are largely affected in neurodevelopmental and neurodegenerative diseases and are known to change with age in healthy subjects (Thapar et al., 2017, Hou et al., 2019, Tucker-Drob, 2009).

Changes in protein synthesis and turnover with age have previously been documented in nematodes (Liang et al., 2014, Dhondt et al., 2017), mice (Kruse et al., 2016, Walther and Mann, 2011, Dai et al., 2014) and rats (Dwyer et al., 1980, Fando et al., 1980, Ekstrom et al., 1980) with varied observations. No studies to date, however, have carefully looked into synaptic protein lifetimes at different stages of life or how the lifetime differs between brain regions in developing, mature and old brain. To understand how synaptic protein homeostasis and lifetime changes with age across the mouse brain, we mapped the lifetime of PSD95 in developing (3-week-old, 3W), adult (3-month-old, 3M) and ageing (18-month-old, 18M) mice.

In Chapter 5 I aimed to:

(1) Visualize synaptic PSD95 lifetime over 7 days in 3-week-old (3W), 3-month-old (3M) and 18-month-old (18M) mice, corresponding to childhood, adulthood and old age in mice (**Chapter 5.3.1**).
(2) Estimate the half-life of PSD95 in 110 brain subregions at different stages of life (**Chapter 5.3.2**).

(3) Investigate the changes in protein turnover during development, from 3W to 3M, and ageing, from 3M to 18M (**Chapter 5.3.3**).

(4) Assess the similarity of PSD95 lifetimes between 110 brain subregions within age groups (**Chapter 5.3.4**).

(5) Investigate PSD95 protein lifetime across the dendritic arbour in 3W, 3M and 18M mice (**Chapter 5.3.5**).

(6) Identify changes in LPL synapse numbers at different stages of life (**Chapter 5.3.6**).

5.2 Summary of methods used in this Chapter

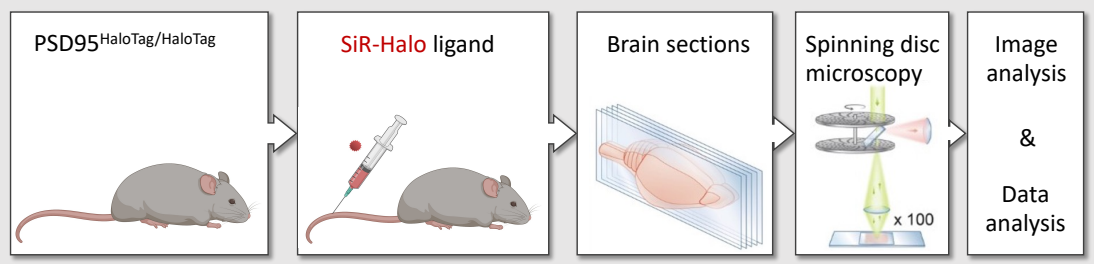

Figure 5.1: A summary of the experimental workflow for Chapter 5.

For results presented in Chapter 5, 3-week-old (3W), 3-month-old (3M) and 18-month-old (18M) PSD95$^{HaloTag/HaloTag}$ mice were used (**Figure 5.1**; see **Chapter 2.2** for more details). The mice received a bolus injection 1.5 mM SiR-Halo solution (injection volume adjusted by average weight of the age group) and were perfused at 6 hours (referred to as day 0) or 7 days 6 hours (referred to as day 7) post-injection (**Figure 5.2**, see **Chapter 2.6**). The n number of mice used for each age group and time point were as follows (m, male; f, female): 3W animals, day 0 n = 8 (5m, 3f), day 7 n = 8 (6m, 2f); 3M animals, day 0 n = 9 (5m, 4f), day 7 n = 7 (2m, 5f); 18M animals, day 0 n = 10 (7m, 3f), day 7 n = 9 (8m, 1f). Single-synapse resolution images were obtained using spinning disc confocal microscope (**Chapter 2.8**). The imaging parameters used for the SiR-Halo image acquisition were the following: 640 nm laser line, 12% laser power, 95 ms exposure time and QUAD (700/45) emission filter.

SiR-Halo puncta were detected and quantified as described in **Chapter 2.9**. Since the study only contained two time points post-injection, one reference and one the measurement of decay, exponential decay function could not be fitted and, instead, fraction of PSD95 puncta or fluorescence intensity at day 7 compared to day 0 was calculated for all regions and subregions within an age group (**Chapter 2.10.2**). The fraction values were then converted into a half-life measure for easier interpretation. Cohen's D values and similarity matrices presented in **Chapter 5.3.3 - 5.3.4** were calculated as per **Chapter 2.10.4** and **Chapter 2.10.5**, respectively.

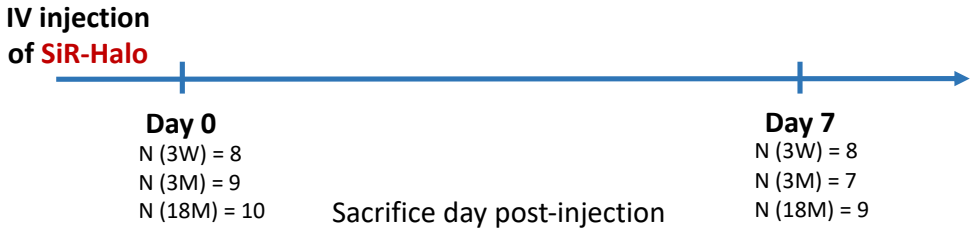

Figure 5.2: The time points and number of animals used in the study.

5.3 Results

5.3.1 Qualitative analysis of PSD95 lifetime across lifespan

We examined the lifetime of PSD95 in development and ageing by injecting 3W, 3M and 18M mice, ages corresponding to mouse childhood, adulthood and old age, respectively. Example sagittal brain section images from 3W, 3M and 18M animals display how SiR-Halo signal decays over a 7-day period at different ages (**Figure 5.3**). At day 0 (upper panel), PSD95-HaloTag labelling is comparable between ages, with highest fluorescence intensity found in isocortex, hippocampal formation and striatum and the lowest found in hindbrain, thalamic, olfactory and midbrain structures. At day 7 (lower panel), we observe a markedly reduced fluorescence across the brain at all ages, with fluorescence in olfactory areas, thalamus, cerebellum and hindbrain dropping to (or nearly to) the level of background noise. Superficial layers of the cortex and hippocampal CA1 stand out at day 7 as regions with the highest remaining SiR-Halo labelling. Interestingly, PSD95-Halo fluorescence appears to overall

decay faster in young animals (3W) compared to adult (3M) and ageing (18M) mice.

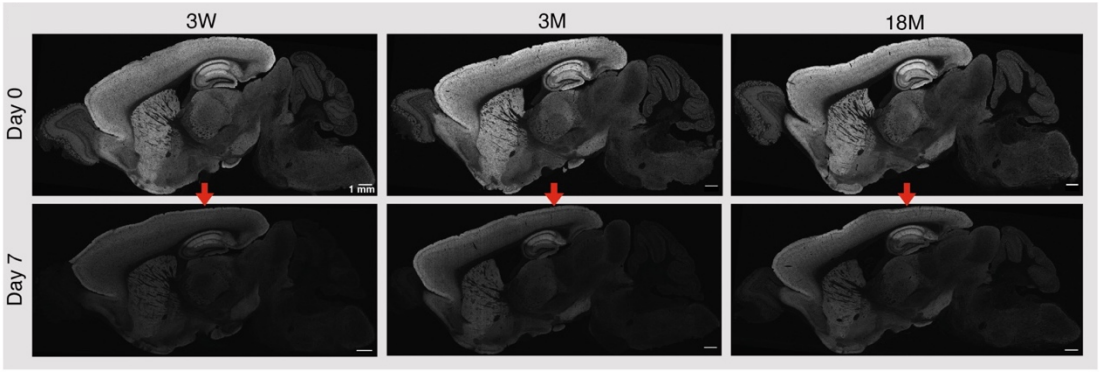

Figure 5.3: The decay of SiR-Halo fluorescence labelling in 3W, 3M and 18M animals over 7 days*. Representative whole brain images of day 0 and day 7 SiR-Halo labelling. Scale bar: 1 mm.*

5.3.2 PSD95 half-life estimates for different stages of life

To quantify the changes in PSD95 lifetime across the lifespan, mean fraction of puncta or fluorescence intensity at day 7 compared to day 0 was calculated followed by a conversion of fraction values to half-life estimates.

5.3.2.1 Puncta density-based decay

The summary of the lifetimes of PSD95-positive puncta in 3W, 3M and 18M age groups is presented in **Figure 5.4** (for raw numbers, see **Appendix 11**). Brain maps reveal that PSD95 puncta lifetime increases with age in majority of brain regions. In young brain (3W), most of the brain regions showed a half-life in the range of 0 to 3 days and only superficial layers of the isocortex (layers 1, 2/3 and 4) together with hippocampal subiculum (SUB) and CA1 stratum lacunosum-moleculare (CA1slm) had half-lives above 3 days. The longest half-life in 3W group was detected in layer 1 of the posterior parietal association area (PTLp1, $T_{1/2}$ = 6.1 days) and the shortest was found in the glomerular layer of the main olfactory bulb (MOBgl, $T_{1/2}$ < 0.5 days) and granule cell layer of the dentate gyrus (DG-sg, $T_{1/2}$ < 0.5 days). In the adult mouse (3M) brain, darker red colours represent higher half-life values compared to those observed in 3W map. The longest half-life detected in 3M

group was found in layer 1 of the somatomotor cortex (MO1, $T_{1/2}$ = 17.3 days) and the shortest in glomerular layer of the main olfactory bulb (MOBgl, $T_{1/2}$ = 1.0 days). PSD95 lifetime values showed an additional increase with ageing. At 18M, the half-life was found to range from 1.3 days in the hippocampal CA2 stratum lacunosum-moleculare (CA2slm) to 18 days in layer 1 of the frontal pole (FRP1).

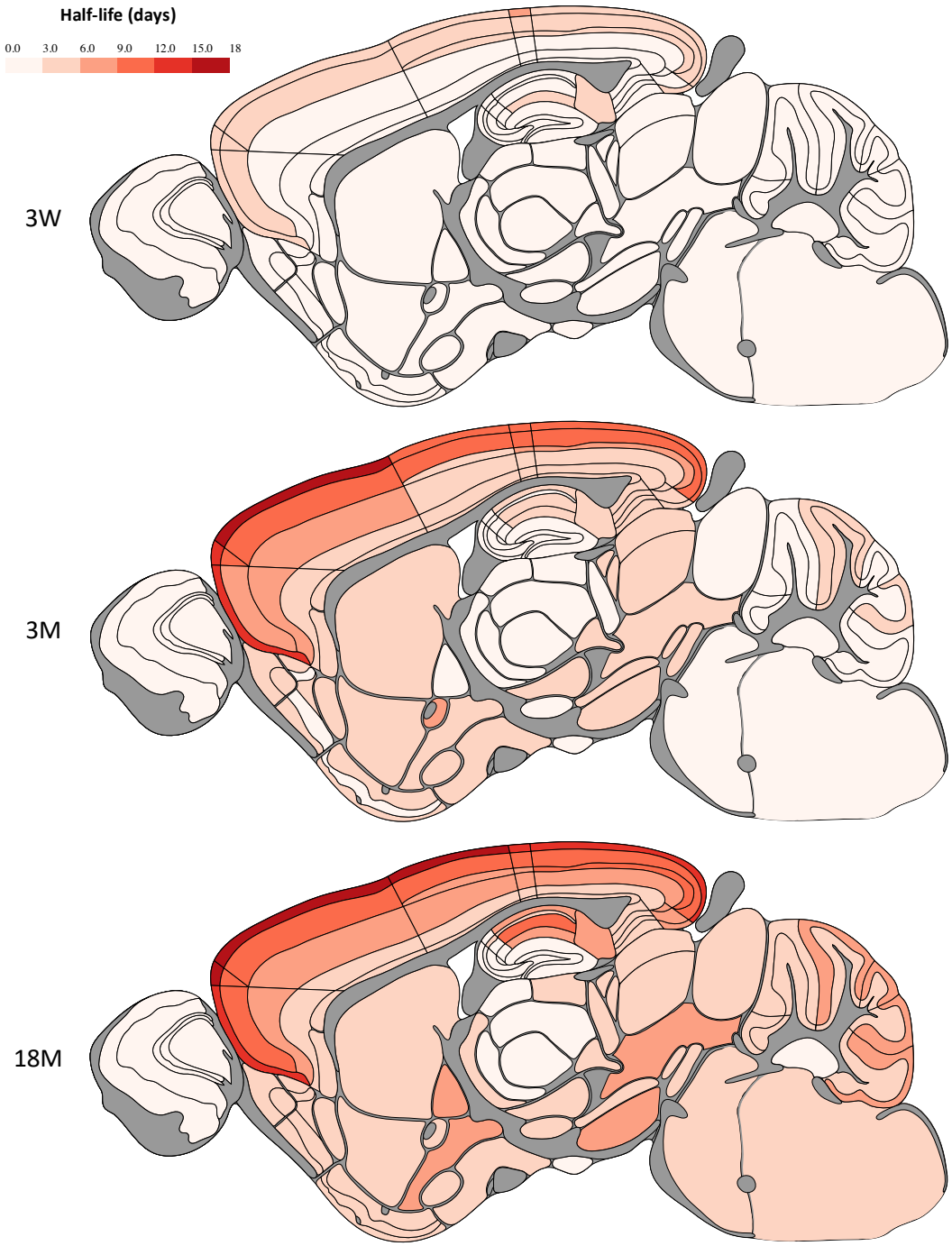

Figure 5.4: Density-based PSD95 lifetime across the lifespan. *Maps of PSD95-positive puncta half-lives (in days) for 110 brain subregions in 3W, 3M and 18M PSD95-HaloTag mice. N = 7-10 animals / group.*

5.3.2.2 Puncta intensity-based decay

Synaptic PSD95 protein lifetimes, estimated for 3W, 3M and 18M age groups, are summarised in **Figure 5.5** (for raw numbers, see **Appendix 11**). The range of half-lives observed in intensity-based decay is 3-fold smaller than that observed in density-based decay. In young mice (3W), PSD95 lifetime ranged from 0.8 days in ventral posteromedial nucleus of the thalamus (VPM) to 3.1 days in layer 1 of somatomotor areas (MO1). 3M animals showed the shortest half-life of 1 day in outer plexiform layer of the main olfactory bulb (MOBopl) and the longest half-life of 6.5 days in layer 1 of the frontal pole (FRP1). In old age (18M), the half-lives ranged from 1.3 days in CA2 stratum lacunosum-moleculare (CA2slm) to 6.2 days in layer 1 of the posterior parietal association areas (PTLp1). Similar to density-based estimates, intensity-based half-lives show an increase with age across most brain subregions. Importantly, superficial layers of the cortex show the longest PSD95 lifetimes across all age groups and the shortest lifetimes are shared between subregions of olfactory bulb, thalamus and hippocampal CA2 which suggests a conserved spatial organisation to protein turnover that is maintained throughout the lifespan.

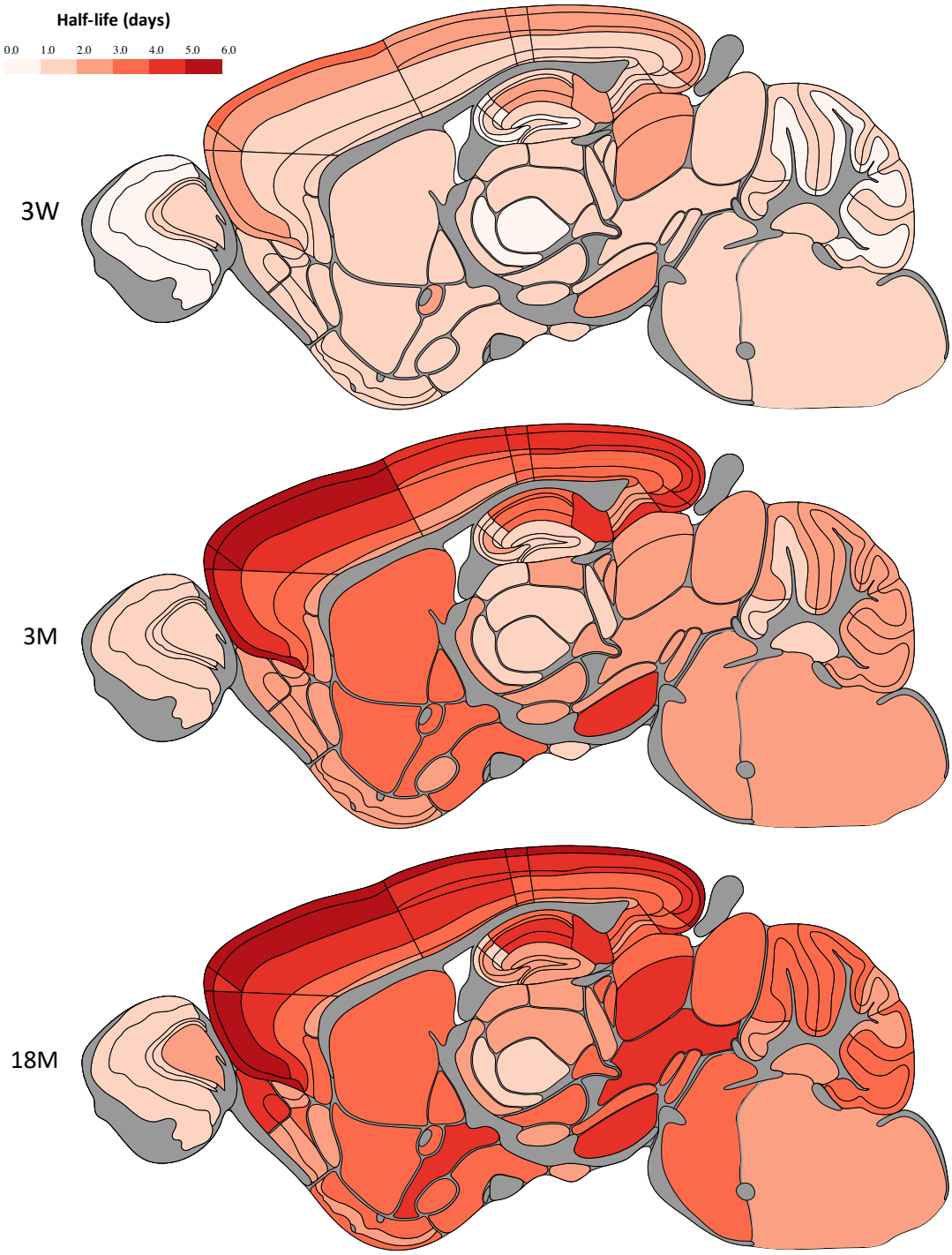

Figure 5.5: Intensity-based PSD95 lifetime across the lifespan. *Maps of synaptic PSD95 protein half-lives (in days) for 110 brain subregions in 3W, 3M and 18M PSD95-HaloTag mice. N = 7-10 animals / group.*

5.3.3 Regional effects on PSD95 lifetime throughout lifespan

To quantify changes in PSD95 lifetime between stages of life, percentage increase in density-based half-life was calculated for changes happening in all brain subregions from childhood to adulthood (3W – 3M) and from adulthood to old age (3M – 18M) (**Figure 5.6A**). During development (3W-3M), most pronounced increases in PSD95 half-life were seen in cortical brain subregions (largest increase of 211.6% detected in FRP2-3) and cerebellum granular layer (largest increase of 230.4% found in SIMgr). In contrast, during ageing, the largest increases in half-life were seen in the molecular layer of cerebellum (148.5% in COPYmo) and only very minor changes were seen in the cortical brain regions.

We assessed the effect size of the changes observed in PSD95 half-life estimates by calculating Cohen's D values for 3W-3M, 3M-18M and 3W-18M age group comparisons (**Figure 5.6B**). Cohen's D effect size >1 is considered large (see horizontal dashed line). A number of brain subregions showed large effect sizes in 3W-3M comparison, with most notable examples being subregions of the isocortex, olfactory bulb, striatum and granular layers of the cerebellum. In the transition from 3M to 18M, fewer subregions showed large Cohen's D values and the largest effect was seen in the olfactory areas and cerebellum. Finally, when comparing the 3W and 18M age groups, large effect sizes were seen across all 110 subregions examined with cerebellum being the most affected.

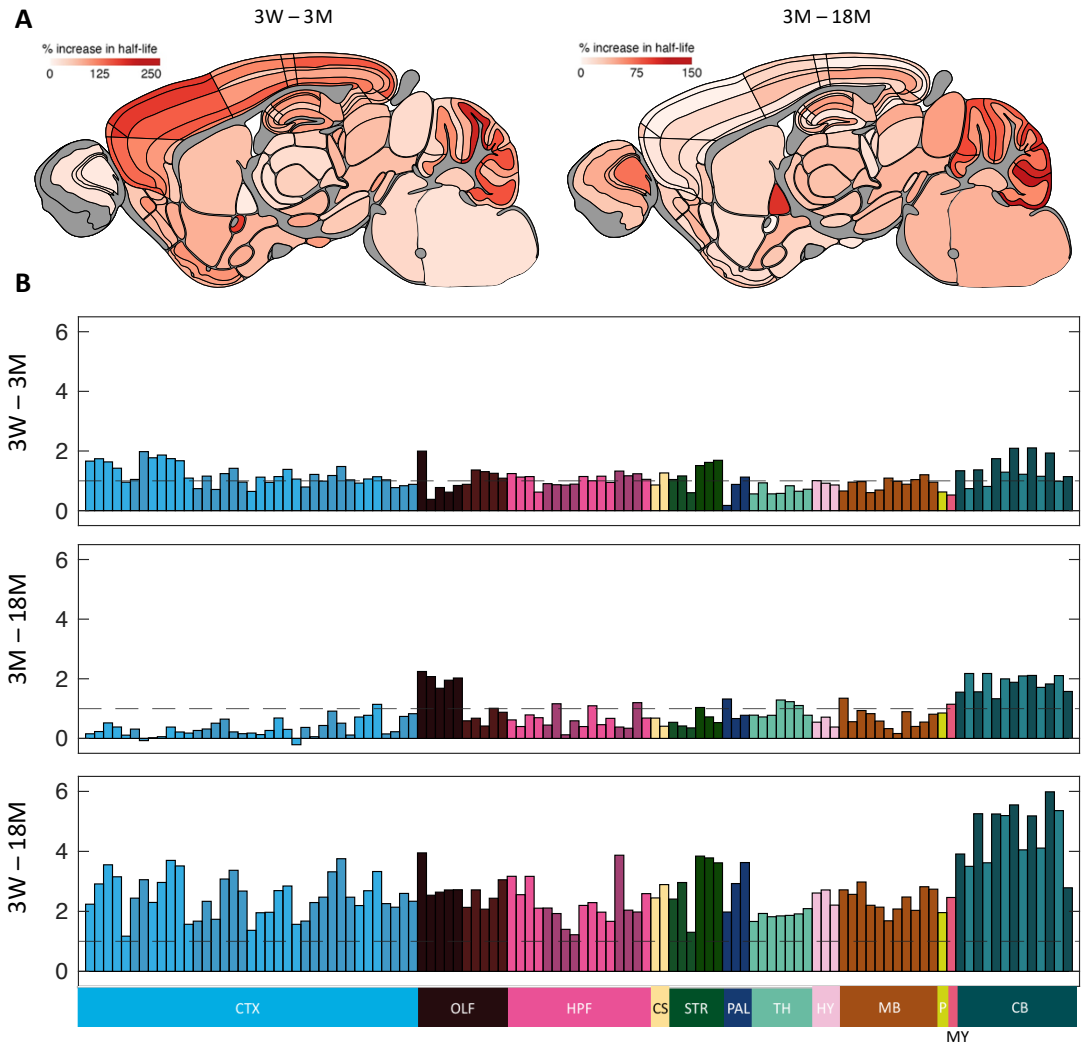

Figure 5.6: Increase in PSD95 lifetime across the lifespan. (A) *Percentage increase in regional PSD95 half-life values between 3W and 3M (on the left) and 3M and 18M (on the right) age groups.* ***(B)*** *Effect size (Cohen's D) estimates for 3W-3M, 3M-18M and 3W-18M age group comparisons. Dashed line marks the Cohen's D = 1. N = 7-10 animals / group.*

5.3.4 Similarity of PSD95 half-lives

To reveal how changes in PSD95 half-lives throughout the lifespan may contribute to half-life differences between brain regions, we plotted similarity matrices for each of age groups (**Figure 5.7**). The similarity scores presented were calculated by applying a Gaussian kernel function to differences in density based PSD95 half-life between pairs of subregions. At 3W, an abundance of red and yellow colours represents a high similarity of PSD95 half-lives between brain subregions which is largely diminished in 3M and 18M

groups suggesting that from childhood to adulthood brain subregions acquire specific protein lifetime signatures that are maintained throughout mature and old age.

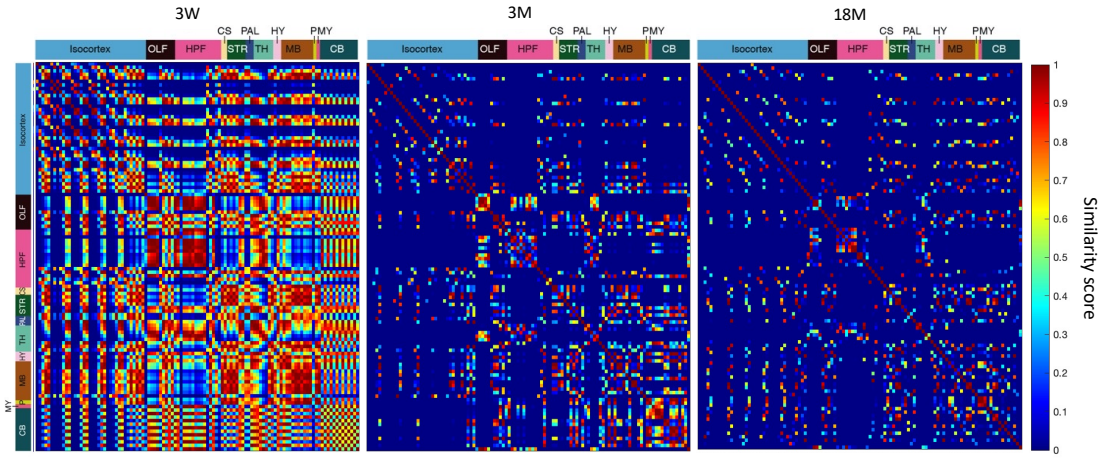

Figure 5.7: Similarity of half-lives across the brain at different ages. *A heatmap of half-life similarity values between pairs of subregions (rows and columns) in 3W, 3M and 18M age groups.*

5.3.5 PSD95 lifetime gradients in hippocampal CA1

We investigated how PSD95 lifetime differs with distance from the soma in apical and basal dendrites of the CA1 and how that changes throughout the lifespan. CA1 dendritic layers in sagittal brain images from day 0 and day 7 mice of 3W, 3M and 18M were subdivided into small segments of equal thickness in a radial direction. SiR-Halo-positive puncta were detected and quantified for each of the delineated areas and mean fraction of SiR-Halo positive puncta at day 7 compared to day 0 (+/- SD) was calculated for each area and age group (**Figure 5.8** and **Appendix 5**). At 3W, PSD95 lifetimes were similar across all segments of CA1 dendritic layers. In 3M group, a gradient of lifetimes was observed across the apical and basal dendrites. PSD95 lifetime in stratum radiatum showed an increase with distance from the soma before dropping at the border with stratum lacunosum and again increasing until the end of stratum moleculare. In stratum oriens, an initial rise in PSD95 lifetime was observed with increasing distance from the soma which then reverted in most distal parts. Interestingly, 3M group showed 4-5-fold

higher lifetimes of PSD95 compared to those seen in 3W age group. At 18M, the gradient of PSD95 lifetimes was similar to that of 3M group with slightly higher lifetime values.

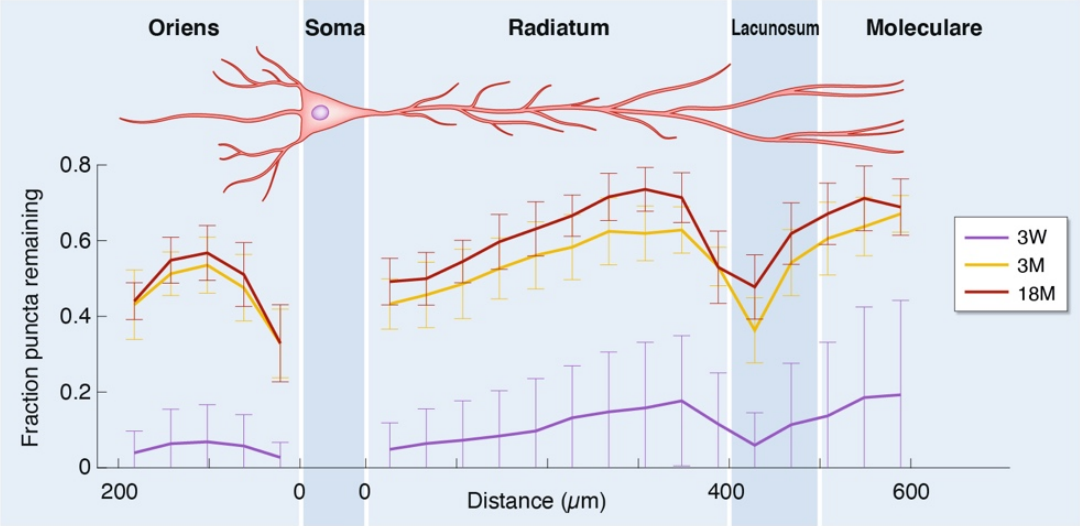

Figure 5.8: PSD95 lifetime gradients across the dendritic tree of CA1 pyramidal cells. *Mean fraction of puncta remaining at day 7 compared to day 0 (+/- SD) in 3W (purple), 3M (yellow) and 18M (maroon) mice. The line plot cover the length of the CA1 dendritic tree, including the apical and basal dendrites. N = 3 for each group.*

5.3.6 LPL synapses accumulate with age

After having discovered in **Chapter 4** that some synapse subtypes are associated with long protein lifetime (LPL) and others with short protein lifetime, we asked how LPL synapse numbers change with age. The PSD95-eGFP and SAP102-mKO2 data used for this analysis was obtained from Cizeron et al. (2020), where synapse subtypes were determined across the sagittal brain sections in 3W, 3M and 18M mice. Differences in subtype densities between developing and adult brain (**Figure 5.9A**) and between adult to ageing brain (**Figure 5.9B**) were calculated as Cohen's D effect size values and plotted in a heatmap with subtypes sorted according to their estimated lifetime. Bayesian analysis was carried out to determine statistically significant differences in subtype densities between ages. Between 3W and 3M, relatively few statistically significant differences are seen, however the majority are detected for subtype 2 (Type 1, PSD95-only synapse), the subtype with the

longest protein lifetime. Interestingly, subtype 34 (Type 3, PSD95+SAP102 synapse), another of the LPL subtypes, does not show differences in this age comparison. The selective effect on Type 1 synapses and not Type 3 synapses would suggest that synapses of different molecular compositions undergo different developmental trajectories. Between 3M and 18M, a number of changes in subtype densities are observed for LPL and SPL synapses. Strikingly, multiple LPL subtypes show increase in density with age. Regions of isocortex showed a preferential accumulation of subtype 2 while other brain areas also saw increases in LPL subtypes 34, 3 and 5.

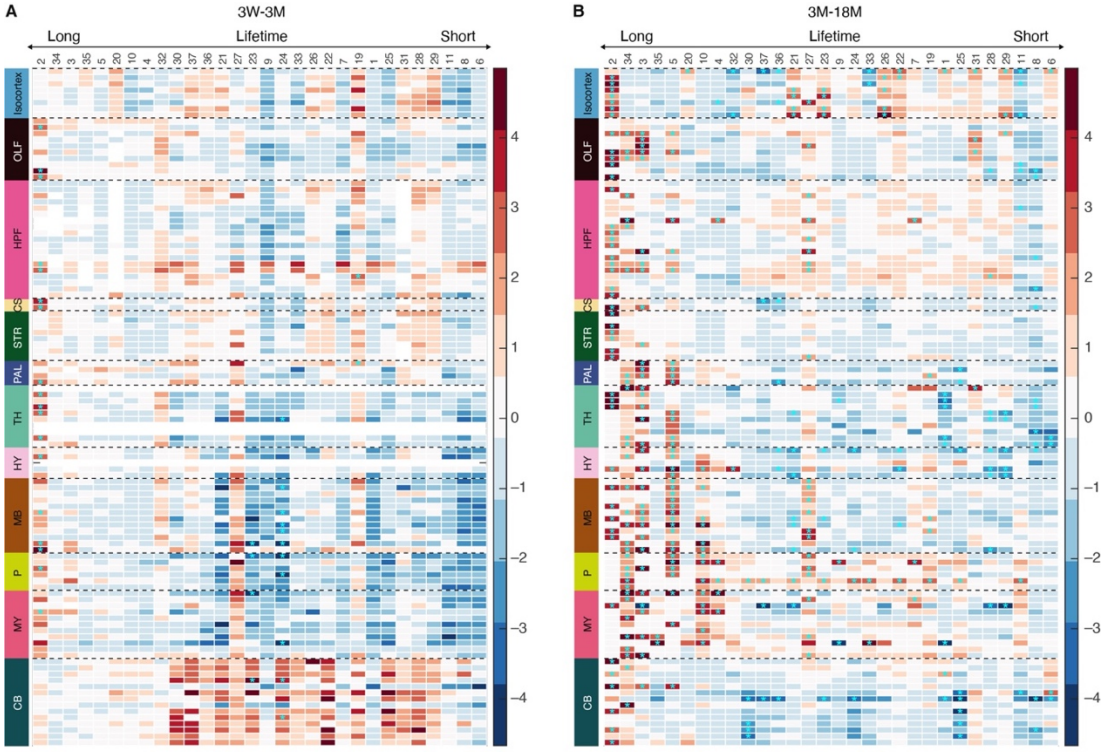

Figure 5.9: Changes (Cohen's D effect size) in LPL and SPL subtype densities in brain subregions with age*. Synapse subtypes sorted according to their associated PSD95 lifetime.* ***(A)*** *Comparison of 3W and 3M age groups.* ***(B)*** *Changes in subtype densities between 3M and 18M. Asterisks indicate significant differences (P<0.05, Benjamini-Hochberg correction).*

5.4 Discussion

In Chapter 5, PSD95 lifetime was visualised and quantified in developing, adult and ageing mouse brain. Protein lifetimes increased with age, with largest increases during development detected in isocortex and granular layer of the

cerebellum and biggest changes in ageing brain seen in the molecular layer of the cerebellum. PSD95 half-lives displayed high similarity between brain subregions in 3W mice but the similarity was substantially reduced in 3M and 18M animals. At the level of dendritic arbour, in 3W only nascent gradients in PSD95 lifetime were observed. In 3M and 18M groups, CA1 gradients became more pronounced suggesting specialisation of different parts of dendritic tree with development. Changes in protein lifetime with age were accompanied with increases in LPL synapse densities across many brain regions and subregions.

5.4.1 Results in context of previous literature

For the first time, the lifetime of a synaptic protein has been mapped and compared across multiple brain regions in development, adulthood and ageing. A global increase in PSD95 lifetime was observed throughout the lifespan which could be caused by an age-dependent decrease in protein synthesis or a slowdown in protein degradation. During development, decreases in protein synthesis have previously been observed in rat forebrain and cerebellum (Fando et al., 1980), the same brain areas that we found most affected in 3W-3M comparison. Slowing of protein synthesis from childhood to adulthood was also found in heart, lung and skeletal muscle tissues in rats (Mays et al., 1991). During ageing, some studies have detected decreases in protein synthesis (Dwyer et al., 1980, Ekstrom et al., 1980, Ingvar et al., 1985, Liang et al., 2014) and turnover (Dhondt et al., 2017) while others saw no change (Mays et al., 1991, Dai et al., 2014) or protein-specific changes in synthesis (Kruse et al., 2016, Walther and Mann, 2011). The changes we observed in 3M-18M comparison were less pronounced than those observed in development but most notable increase in lifetime was observed in the molecular layer of the cerebellum. Dwyer et al. (1980) also detected slowing down in protein synthesis in cerebellum with ageing supporting our findings. None of the previous studies, however, looked specifically into the lifetime of PSD95 or any other synaptic protein, therefore, more detailed analyses into age-dependent changes in the lifetime of other post- or pre-synaptic protein

would be needed to further strengthen the evidence for region-dependent and age-dependent increase in synaptic protein lifetimes.

5.4.2 Structural changes in synapses with age

To better understand the implications of and factors contributing to increasing PSD95 lifetime across the lifespan, we need to take into consideration the dynamic structural changes happening in synapses with age. Fraction of stable dendritic spines is known to increase from developing to mature brain (Holtmaat et al., 2005, Zuo et al., 2005) in mouse isocortex, consistent with our finding of the increasing stability of protein within dendritic spines. Interestingly, with ageing Mostany et al. (2013) and Grillo et al. (2013) find a decrease in dendritic spine and axonal bouton stability in the cortex of >20-month-old mice. While we observe little change in protein lifetime in the isocortex of 18M animals, increasing spine dynamics at this age could start contributing to the turnover of PSD95 puncta that we observe. Spine dynamics in developing and ageing brain has not been assessed in detail in brain regions other than isocortex and a possibility remains that dendritic spine stability is differentially affected with age across the brain. Further studies monitoring dendritic spine dynamics in more easily accessible brain regions such as olfactory areas or cerebellum would be needed to better understand how stability of structural and molecular components of synapses changes with age.

5.4.3 Developmental changes in isocortex

PSD95 lifetime was found to increase more than 200% from developing (3W) to mature brain (3M) in regions of mouse isocortex. Drastic changes in synaptic protein lifetime are not surprising given the well-documented cortical synapse remodelling in the developing brain (Mallya et al., 2019, Farhy-Tselnicker and Allen, 2018, Sakai, 2020, Paolicelli et al., 2011). Critical periods of plasticity, first described by Hubel and Wiesel (1970), occur in the first month of life in mice and may have molecular mechanisms involved in enhancing rates of synaptic protein turnover at this age. To assess the role of developmental critical periods in governing PSD95 lifetime, PSD95-HaloTag mice could be subjected to dark rearing (Mower, 1991, Daw, 1998, Timney et al., 1978) or

monocular deprivation (Zhou et al., 2017, Espinosa and Stryker, 2012, Wiesel and Hubel, 1963), both well-described paradigms for examining effects of critical periods of plasticity on brain structure and function, at birth for several weeks. PSD95 lifetime could be assessed in the visual cortex of these mice and compared to the controls. If critical period of plasticity and associated sensory experiences play a role in governing synaptic protein lifetime, visually deprived mice would likely show changes (possibly an increase) in PSD95 protein lifetime in visual areas of the brain.

5.4.4 Age-dependent changes in cerebellum

Most noticeable changes in PSD95 lifetime throughout the lifespan were observed in the cerebellum. During development, PSD95 lifetime preferentially increased in the granular layer of the cerebellum while with ageing, largest changes in lifetime were observed in the molecular layer. Layer-specific effects with age may be explained by cell-type-specific developmental program and vulnerability to ageing in the cerebellum. Granular layer contains dendrites of highly abundant granule cells (Consalez et al., 2021). Molecular layer, in contrast, contains dendrites of Purkinje cells. Granule cells develop a lot later than Purkinje cells in the postnatal brain and are still proliferating and fine-tuning their connections at ~P14-21 (van Essen et al., 2020, Dhar et al., 2018, Sillitoe and Joyner, 2007), close to the time of PSD95 lifetime assessment for 3W age group. Late postnatal development of granule cells could have associated molecular programs regulating protein lifetime in 3W group, and the silencing of developmental programs in adulthood could lead to the substantial increases in lifetime observed.

Purkinje cells appear to be particularly vulnerable to ageing (Zhang et al., 2010). Thinning of cerebellar molecular layer (Huang et al., 1999, Dlugos and Pentney, 1994), loss of dendrites (Zhang et al., 2006) and regression of distal dendrites of Purkinje cells (Quackenbush et al., 1990) have all been observed in ageing cerebellum. Cerebellar Purkinje cells have shown earlier senescence when compared to hippocampal pyramidal neurons which did not change in numbers in 18-month or 24-month-old mice (Woodruff-Pak et al., 2010). While

our measurements of lifetime are independent of the starting density of synapses and would not be much affected by age-related loss of synapses, underlying metabolic or other intracellular processes may be playing a role in prolonging PSD95 lifetime in the ageing Purkinje cells. From a morphological perspective, Purkinje cells are some of the largest neurons in the brain with intricate dendritic networks and maintaining the health of the dendritic arbours must be a metabolically expensive and complicated task (Lackey et al., 2018). The efficiency of proteostasis is known to decrease with age and thus large cells with extensive dendritic structures would likely be first to get affected (Hipp et al., 2019). Future studies examining the morphology and molecular composition of cerebellar synapses at different ages would be needed to establish clearer picture of factors governing synaptic PSD95 lifetime in cerebellum at different stages of life.

5.4.5 Similarity of regional half-lives

We found PSD95 lifetimes to be similar between brain regions at 3W and become less similar at 3M and 18M. Our result in 3W and 3M groups aligns well with the findings presented in Cizeron et al. (2020). In this study, synapse compositions with age showed a differentiation between brain regions and thus a decreasing similarity from 3W to 3M. Less similar PSD95 lifetimes therefore correspond to less similar synapses in adult brain. 18M group in Cizeron et al. (2020) showed higher similarity compared to 3M group while in current study, 18M group had similar or slightly lower similarity of PSD95 lifetimes. The contrasting results may be due to a number of reasons and firstly, a replication of the two studies would be needed to increase the confidence of the findings presented in both.

5.4.6 CA1 gradients in PSD95 lifetime

PSD95 lifetime formed a gradient in CA1 dendrites in 3M and 18M groups while only a nascent gradient was observed in 3W animals. Gradients detected in mature and ageing animals were similar to those observed for PSD95-eGFP puncta intensity in Cizeron et al. (2020). PSD95 puncta intensity (Zhu et al., 2018), AMPA receptor numbers (Andrasfalvy and Magee, 2001, Menon et al.,

2013, Nicholson et al., 2006), glutamate release probability (Andersen et al., 1980, Jensen et al., 2021) and dendritic EPSP amplitudes (Magee and Cook, 2000) have previously been shown to increase with distance from the soma. Such distance-dependent gradients are thought to be important for overcoming dampening of currents that would otherwise occur due to cable properties of dendritic trees (Andersen et al., 1980). AMPA receptors are anchored to the post-synaptic membrane by PSD95 (Ehrlich and Malinow, 2004, Bats et al., 2007, Chen et al., 2015) therefore higher levels and stability of PSD95 would be required to accommodate for larger numbers of distally located AMPA receptors. Interestingly, in 3W group hippocampal gradient is not yet formed suggesting that the physiological properties of distal synapses in developing brain may not yet be adjusted to compensate for the larger distances that the current needs to travel. To confirm this hypothesis, AMPA receptor expression should be checked at different parts of CA1 dendrites in the developing brain and correlated with protein lifetime results. Additional investigation into release probability and dendritic EPSP amplitudes in 3W brains would provide additional evidence for immature dendritic gradients in the developing brain.

5.4.7 Implications for memory storage

Age-related increase in PSD95 lifetime was found to be accompanied by the increasing numbers of LPL synapses across the brain. At 3W, brain regions are predominantly populated by SPL synapses therefore limiting the long-term information storage capacity of the developing brain. Indeed, infantile amnesia is a well-described phenomenon which manifests in the inability to consolidate or retrieve memories in infants (Alberini and Travaglia, 2017, Donato et al., 2021). With development, capacity to learn and gain new skills increases drastically (Tucker-Drob, 2009), aligning with the increasing numbers of LPL synapses in mature brain. Ageing, on the other hand, has been associated with deteriorating working memory and executive functioning which rely on quick processing and transforming of incoming information (Murman, 2015). Cumulative knowledge and well-developed skills, that are often referred to as crystallized intelligence, are maintained well into the old age (Harada et al.,

2013, Murman, 2015). In our study, with ageing we observe a preferential retention of LPL synapses which are less flexible but better suited for long-term memory storage. While these are only rough parallels between the psychology and the biology of ageing, further studies exploring LPL and SPL synapse role in different types of learning and memory would be useful in establishing any causal links.

Chapter 6 PSD95 lifetime changes in disease

6.1 Introduction

A mutation-induced change in protein interaction landscape and molecular complex assembly may affect the stability and turnover of participating proteins. PSD95 has at least 118 core interacting proteins and mutations in many of them occur in diseases, including schizophrenia, intellectual disability (ID), autism spectrum disorders (ASD), bipolar disorder and others (Fernández et al., 2009). We chose to study synaptic PSD95 lifetime in mutants of two disease-associated PSD95-interacting proteins, PSD93 and SynGAP.

PSD93 (post-synaptic density protein 93) is a PSD scaffolding protein and a paralog to PSD95. Together with PSD95 and NMDAR subunit NR2B, PSD93 is required for the formation of ~1.5 MDa multiprotein signalling complexes in the PSD (Frank et al., 2016). Lack of PSD93 results in deficient synaptic LTP in hippocampus and, interestingly, shows an opposite phenotype to PSD95 mutants which show enhanced LTP (Migaud et al., 1998, Carlisle et al., 2008). Mutations in PSD93 have previously been implicated in schizophrenia (Walsh et al., 2008, Kirov et al., 2012, Fromer et al., 2014, Ingason et al., 2015) and, more recently, in ASD and ID (Reggiani et al., 2017, Ruzzo et al., 2019).

SynGAP (synaptic Ras GTPase-activating protein) is one of the most abundant proteins at the PSD (Cheng et al., 2006) and is best known for its role in stimulating GTPase activity of Ras and Rap molecules in synapses (Kim et al., 1998, Chen et al., 1998, Krapivinsky et al., 2004). Ras and Rap are thought to facilitate NMDAR-dependent addition or removal of AMPARs from the synapse during synaptic plasticity (Zhu et al., 2002). SynGAP can bind all three PDZ domains of PSD95 and studies suggest that by occupying PDZ domains of PSD95, SynGAP regulates the composition of molecular complexes in the PSD (Kim et al., 1998, Walkup et al., 2016). Haploinsufficiency in SynGAP has been linked to premature maturation of structure and function of excitatory neurons early in development (Clement et al., 2012, Aceti et al., 2015, Vazquez et al., 2004). Komiyama et al. (2002) presented the first evidence that SynGAP was involved in synaptic plasticity

and cognitive function in mice. Since then, mutations in SynGAP have been well recognised in ASD and ID (Weldon et al., 2018, Hamdan et al., 2009).

In Chapter 6 I aimed to:

(1) Map the half-lives of PSD95 in mice lacking PSD93 protein (**Chapter 6.3.1**).
(2) Investigate the differences in protein lifetime in heterozygous and homozygous PSD93 mutants compared to healthy controls (**Chapter 6.3.2**).
(3) Map the half-lives of PSD95 in mice lacking SynGAP protein (**Chapter 6.3.3**).
(4) Identify the differences in protein lifetime in heterozygous SynGAP mutants compared to healthy controls (**Chapter 6.3.4**).

6.2 Summary of methods used in this Chapter

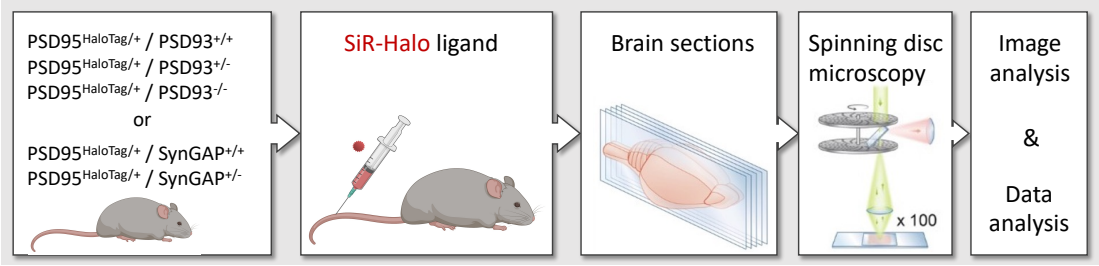

Figure 6.1: A summary of experimental workflow for Chapter 6.

For results presented in Chapter 6, 3-4 months old mice were used of genotypes presented in **Figure 6.1** (see **Chapter 2.2** for more details). The mice received a bolus injection 1.5 mM SiR-Halo solution and were perfused at 6 hours (referred to as day 0) or 7 days 6 hours (referred to as day 7) post-injection (**Figure 6.2A**, see **Chapter 2.6**). The number of mice used for each genotype and time point is summarized in **Figure 6.2B**. Single-synapse resolution images were obtained using spinning disc confocal microscope (**Chapter 2.8**). The imaging parameters used for the SiR-Halo image

acquisition were: 15% laser power, 100 ms exposure time for PSD93-KO study and 120 ms exposure time for SynGAP-KO study (**Chapter 2.8.2**). SiR-Halo puncta were detected and quantified as described in **Chapter 2.9**. Since the study only contained two time points post-injection, one reference and one the measurement of decay, fraction of PSD95 puncta at day 7 compared to day 0 was calculated for all regions and subregions within a genotype group (**Chapter 2.10.2**). The fraction values were then converted into a half-life measure for easier interpretation. Statistical analysis was performed as per **Chapter 2.10.3.2**. Cohen's D values were calculated as per **Chapter 2.10.4**.

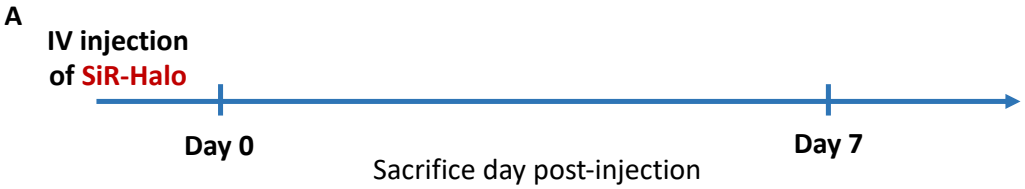

B

PSD93-KO study

	Day 0	Day 7
WT	5	6
HET	8	8
HOM	7	7

SynGAP-KO study

	Day 0	Day 7
WT	6	7
HET	5	7

Figure 6.2: Experimental design used to estimate changes in PSD95 lifetime in disease mutants. (A) *The time points used in estimating changes in PSD95 lifetime in mutants.* ***(B)*** *Number of animals used for each study, time point and genotype.*

6.3 Results

6.3.1 PSD95 half-life estimates for PSD93-KO animals

We examined the lifetime of PSD95 in mice lacking PSD93 protein by injecting 3-4-month-old PSD95$^{HaloTag/+}$/PSD93$^{-/-}$ (referred to as PSD93$^{-/-}$), PSD95$^{HaloTag/+}$/PSD93$^{+/-}$ (referred to as PSD93$^{+/-}$), and PSD95$^{HaloTag/+}$/PSD93$^{+/+}$ (referred to as PSD93$^{+/+}$) mice and obtaining tissue samples at day 0 or day 7 post-injection. Mean fraction of puncta count at day 7 compared to day 0 was calculated and then converted into half-life estimates. The summary of the lifetimes of PSD95-positive puncta in mutant animals is

presented in **Figure 6.3**. Brain maps reveal that PSD95 puncta lifetime is longer in PSD93-KO animals compared to controls in multiple brain regions. In $PSD93^{+/+}$ group, majority of brain regions show half-lives in the range of 0 to 5 days and only some of L1 cortical regions have half-lives >5 days. The longest half-life in $PSD93^{+/+}$ group was detected in layer 1 of motor cortex (MO1, $T_{1/2}$ = 6.8 days). In $PSD93^{+/-}$ group, more brain regions showed half-lives >5 days, including subregions of cortical layers 1, 2-3, 4 and 5, hippocampal CA1 stratum radiatum (CA1sr, $T_{1/2}$ = 6.6 days) and subiculum (SUB, $T_{1/2}$ = 5.2 days). The longest half-life was detected in MO1 ($T_{1/2}$ = 17.5 days) and was more than twice that detected for the region in $PSD93^{+/+}$ group. For $PSD93^{-/-}$ group, a further increase in PSD95 lifetime was observed across multiple brain regions, mostly affecting cortical areas, hippocampal formation and striatum. PSD95 half-life in these animals ranged from 1.3 days in glomerular layer of main olfactory bulb to 27.1 days in MO1, a further 10-day increase from the half-life for the same region in $PSD93^{+/-}$ group.

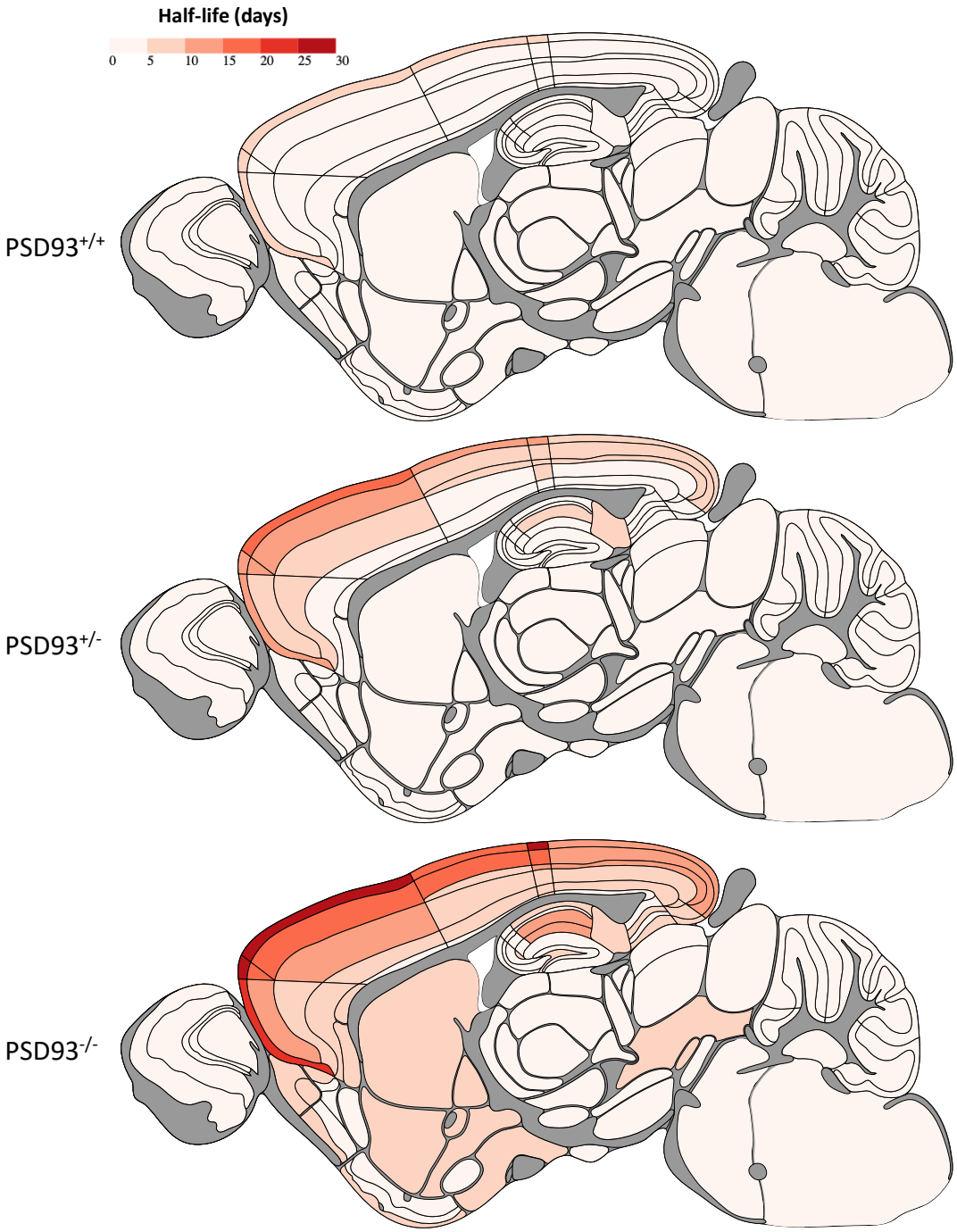

Figure 6.3: PSD95 lifetime in PSD93 mutant animals. *Maps of PSD95-positive puncta half-lives (in days) for 110 brain subregions in PSD95$^{HaloTag/+}$/PSD93$^{+/+}$, PSD95$^{HaloTag/+}$/PSD93$^{+/-}$ and PSD95$^{HaloTag/+}$/PSD93$^{-/-}$ mice. N = 5-7 animals / group.*

6.3.2 PSD95 lifetime changes in PSD93-KO mice

To quantify the magnitude of change in PSD95 lifetime in mutants compared to healthy animals, percentage increase in PSD95 puncta half-life was calculated for all brain subregions for $PSD93^{+/-}$ - $PSD93^{+/+}$ and $PSD93^{-/-}$ - $PSD93^{+/+}$ comparisons (**Figure 6.4A**). In $PSD93^{+/-}$ - $PSD93^{+/+}$, the increase in PSD95 half-life was observed across the brain, with most pronounced increases documented in cortical subregions and hippocampal CA1 (largest increase of 212.2% detected in FRP2-3). In $PSD93^{-/-}$ - $PSD93^{+/+}$ comparison, increases in half-life were, on average, more pronounced than in $PSD93^{+/-}$ - $PSD93^{+/+}$ comparison and largest increase of 381.7% was found in FRP1. Interestingly, only minor differences in half-life between mutant and wild-type animals were observed in subregions of the thalamus and cerebellum, suggesting a region-specific effect of PSD93 mutation on PSD95 lifetime.

Cohen's D effect sizes and results from Bayesian analysis for differences in $PSD93^{+/-}$ - $PSD93^{+/+}$ and $PSD93^{-/-}$ - $PSD93^{+/+}$ comparisons are presented in **Figure 6.4B**. Positive Cohen's D values were observed across all brain subregions suggesting a longer PSD95 lifetime across the brain in mutants compared to healthy controls. A number of brain subregions show statistically significant changes ($p < 0.05$). In $PSD93^{+/-}$ - $PSD93^{+/+}$ comparison, large effect sizes (Cohen's $D > 1$) are detected for multiple brain subregions, including those of isocortex, olfactory areas, hippocampal formation, cortical subplate, striatum, pallidum, hypothalamus and midbrain. Of those, several subregions of the isocortex, olfactory areas, hippocampal formation and cortical subplate show statistically significant differences as revealed by Bayesian inference. Most of the Cohen's D values for $PSD93^{+/-}$ - $PSD93^{+/+}$ comparison lie in the range of 0.5 to 2. In contrast, Cohen's D values for $PSD93^{-/-}$ - $PSD93^{+/+}$ comparison lie mostly in the range of 1.5 to 5.5, confirming larger effect of homozygous knockout mutation on PSD95 lifetime. Largest effect sizes are documented in deeper layers of the isocortex, subregions of olfactory bulb, hippocampal formation and cortical subplate. Majority of brain subregions show statistical significance in $PSD93^{-/-}$ - $PSD93^{+/+}$ comparison.

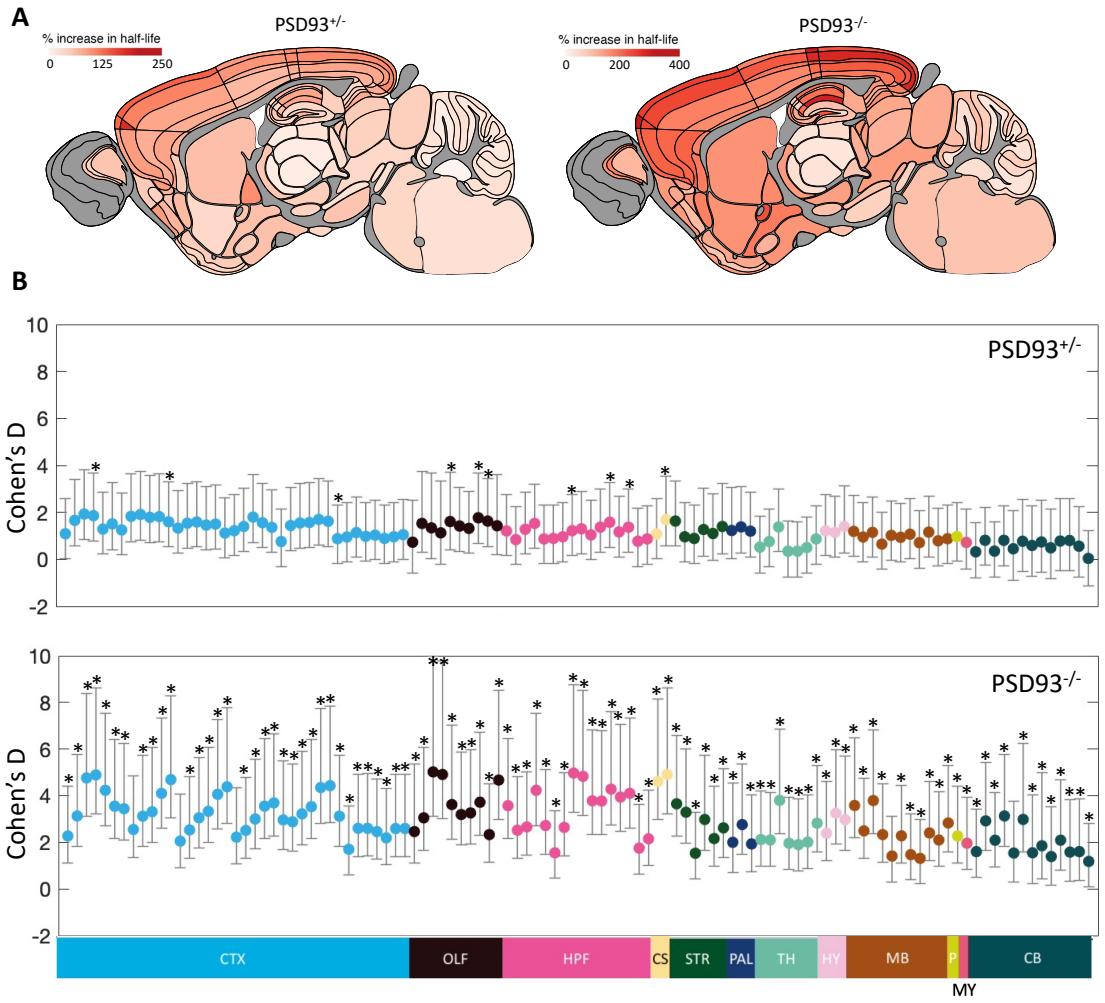

Figure 6.4: Differences in PSD95 lifetime in PSD93 mutants compared to healthy control mice. (A) *Percentage increase in regional PSD95 half-life values between PSD93$^{+/-}$ and PSD93$^{+/+}$ (on the left) and PSD93$^{-/-}$ and PSD93$^{+/+}$ (on the right) groups.* ***(B)*** *Effect size (Cohen's D) estimates with +/- 95% confidence intervals for PSD93$^{+/-}$ - PSD93$^{+/+}$ and PSD93$^{-/-}$ - PSD93$^{+/+}$ comparisons. Asterisks indicate significant differences ($p < 0.05$, Benjamini-Hochberg correction). N = 5-7 animals / group.*

6.3.3 PSD95 half-life estimates for SynGAP-KO animals

PSD95 lifetime in mice lacking SynGAP protein was estimated by injecting 3-4 months old PSD95$^{HaloTag/+}$/SynGAP$^{+/-}$ (referred to as SynGAP$^{+/-}$) and PSD95$^{HaloTag/+}$/ SynGAP$^{+/+}$ (referred to as SynGAP$^{+/+}$) mice and obtaining tissue sections for imaging at day 0 or day 7 post-injection. Similar to the previous studies, fraction of SiR-Halo-positive puncta remaining at day 7 compared to day 0 was calculated for all brain subregions and the values were converted into half-life estimates. A summary of PSD95 half-lives for

SynGAP$^{+/+}$ and SynGAP$^{+/-}$ groups is presented in **Figure 6.5**. In SynGAP$^{+/+}$ group, subcortical brain areas, L6 of the isocortex, and subregions of dentate gyrus, CA3 and CA2 show half-lives in the range of 0 to 5 days. Longer PSD95 puncta lifetimes are observed in hippocampal CA1 and subiculum, and cortical layers L1 to L5. The shortest lifetime was detected in ventral posteromedial nucleus of the thalamus (VPM, $T_{1/2}$ = 1.1 days) and the longest in layer 1 of frontal pole (FRP1, $T_{1/2}$ = 19.6 days).

The brain map of SynGAP$^{+/-}$ group shows an overall similar distribution and range of half-lives to that observed for SynGAP$^{+/+}$ group. The only observable differences are in subregions of striatum, CA1 and frontal pole, which appear to have slightly longer PSD95 puncta lifetimes in mutant animals. The shortest half-life in SynGAP$^{+/-}$ group was detected in VPM ($T_{1/2}$ = 1.1 days) and the longest was found in FRP1 ($T_{1/2}$ = 31.6 days).

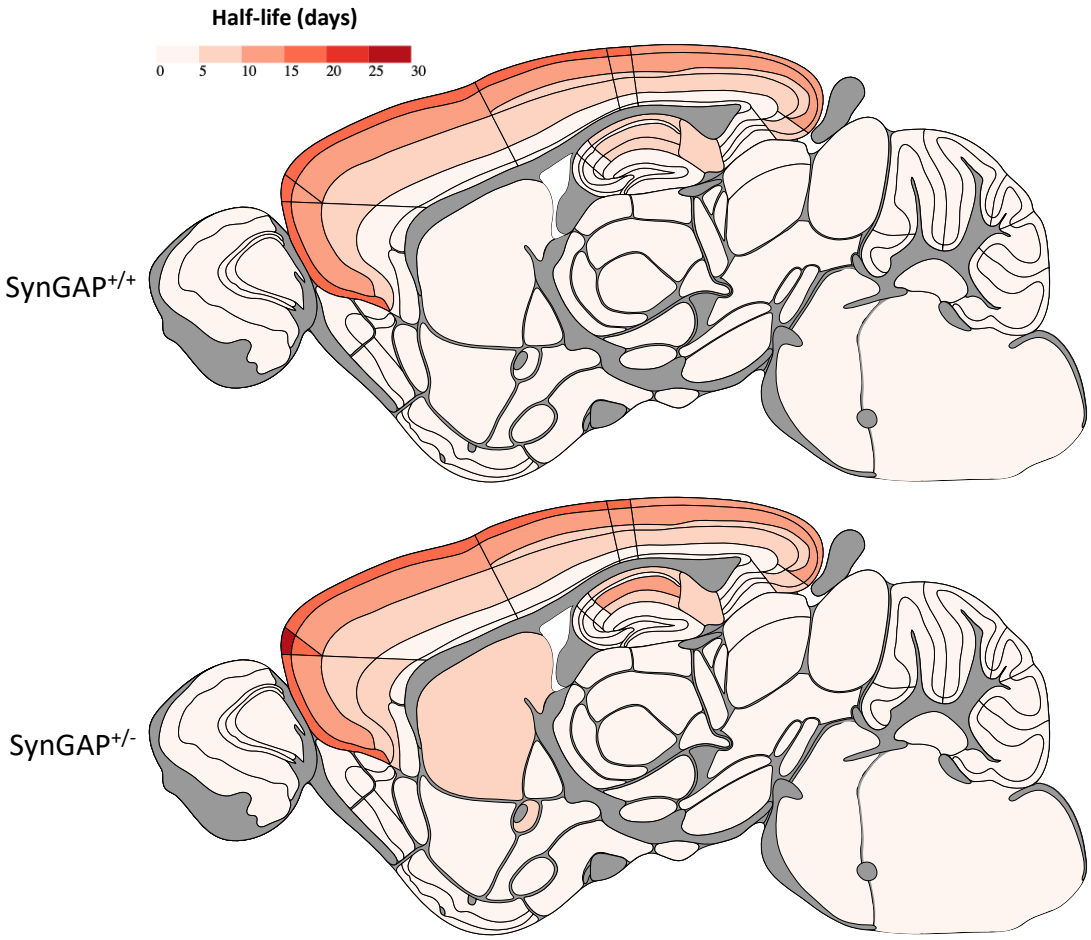

Figure 6.5: PSD95 lifetime in SynGAP mutant animals. *Maps of PSD95-positive puncta half-lives (in days) for 110 brain subregions in PSD95$^{HaloTag/+}$/SynGAP$^{+/+}$ and PSD95$^{HaloTag/+}$/SynGAP$^{+/-}$ mice. N = 5-7 animals / group.*

6.3.4 PSD95 lifetime changes in SynGAP-KO mice

Percentage increase in PSD95 puncta half-life between SynGAP$^{+/+}$ and SynGAP$^{+/-}$ was calculated for all brain subregions to quantify the magnitude of change in PSD95 lifetime in mutants compared to controls (**Figure 6.6A**). PSD95 lifetime was increased in some and slightly decreased in other brain subregions in SynGAP$^{+/-}$ compared to SynGAP$^{+/+}$ groups, however, the changes were minor. The largest percent increase in half-life of 60.8% was observed in FRP1. The effect size measurements also displayed low Cohen's D values (between -1 and 1) and no statistically significant differences following Bayesian analysis ($p > 0.05$) further supporting the conclusion that

heterozygous knockout of SynGAP has little effect on PSD95 lifetime in adult brain (**Figure 6.6B**).

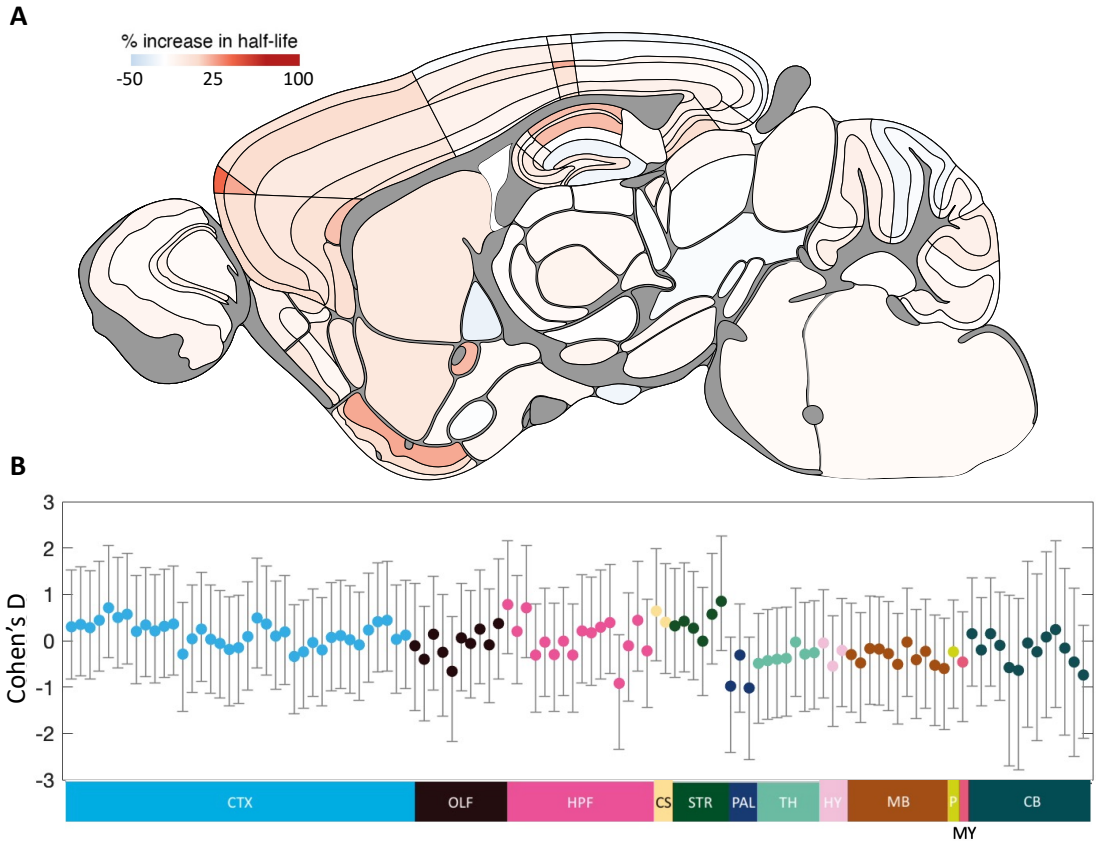

Figure 6.6: Differences in PSD95 lifetime in SynGAP mutant animals compared to healthy controls. (A) *Percentage increase in regional PSD95 half-life values between SynGAP$^{+/-}$ and SynGAP$^{+/+}$.* ***(B)*** *Effect size (Cohen's D) estimates with +/- 95% confidence intervals for SynGAP$^{+/-}$ - SynGAP$^{+/+}$ comparison. N = 5-7 animals / group.*

6.4 Discussion

In Chapter 6, PSD95 lifetime was estimated for PSD93 mutant and SynGAP mutant animals. Protein lifetimes were found to be longer in PSD93 mutants across the whole brain in a gene dose-dependent manner. Biggest differences in lifetime were detected in cortical brain regions and hippocampal CA1. In SynGAP-KO study, minor differences in PSD95 lifetime were detected across the brain. Some brain regions showed a slight increase in protein lifetime while others showed a slight decrease. None of the differences in SynGAP-KO study displayed large effect size or statistical significance. Since the measurement

was carried out at the level of brain subregions, we cannot discount the possibility that mutation-induced changes occur in individual synapse types and subtypes.

6.4.1 Results in context of previous literature

Synaptic protein lifetime, to my knowledge, has not been previously assessed in human disease-relevant PSD93 or SynGAP mutants. Only protein synthesis, one of the factors determining protein lifetime, was investigated in primary cortical neurons of SynGAP knock-out mice and rats revealing an elevation in rate compared to wild-type animals (Wang et al., 2013). *In vitro* results, however, may not be representative of protein metabolism *in vivo* as the extracellular environment can have profound effects on protein turnover (Dörrbaum et al., 2018). Below, I discuss potential mechanisms and explanations for the results we obtained in Chapter 6.

6.4.2 Dramatic increase in PSD95 lifetime in PSD93 mutants

PSD95 half-life was found to increase up to 210% in heterozygous and 380% in homozygous PSD93 mutants, displaying a gene-dosage-dependent effect. Most affected were subregions of isocortex and hippocampal CA1, areas that show dysfunction in PSD93-associated diseases such as Schizophrenia (Bähner and Meyer-Lindenberg, 2017, Heinz et al., 2019) and ID/ASD (Carper and Courchesne, 2005, Weston, 2019, Postema et al., 2019). The least affected were subregions of thalamus and cerebellum despite PSD93 protein being expressed in these brain areas in healthy mice (Roy et al., 2018, Fukaya and Watanabe, 2000). Thalamus and cerebellum, however, express low levels of PSD95 protein which may minimize the effect of the mutation that we can observe (Zhu et al., 2018, Cizeron et al., 2020, Roy et al., 2018). Interestingly, McGee et al. (2001b) have previously documented normal structure and function in cerebellum of mice lacking PSD93 which may suggest additional molecular mechanisms at play in the cerebellum.

In a healthy brain, a subset of PSD95 molecules is involved in PSD93-PSD95-NR2B complex assembly, but in mutants PSD95 would only be assembled into protein complexes that do not require PSD93 (Frank et al., 2016). An average

increase in PSD95 lifetime in mutant animals would suggest that PSD95 complexes that do not involve PSD93 may grant more stability to PSD95 than the PSD93-containing complexes. PSD93-PSD95-NR2B complexes, however, represent only 3% of all multiprotein complexes containing PSD95 and it is currently unknown what percentage of PSD95 molecules is involved in other molecular assemblies containing PSD93 (Frank et al., 2017). Further analysis of endogenous PSD95 complexes using biochemistry techniques would be needed to uncover other types of PSD93-PSD95 multiprotein complexes. We could then use that knowledge to investigate PSD95 protein stability in different types of molecular assemblies which may instruct us on the functional stability of different multiprotein complexes at the PSD.

Increases in PSD95 lifetime in mice lacking PSD93 may be due to molecular reorganisation and compensatory mechanisms at play in mutant mice. Synaptic PSD95 protein levels were previously shown to be elevated in mice lacking PSD93 (Zhu et al., 2018). The density and mean intensity but not size of PSD95-eGFP puncta was higher in PSD93$^{-/-}$ animals compared to controls. Changes in puncta density between wild-type and mutant animals would not affect the measurement of protein lifetime since the calculation only takes into the account the loss of labelling in relation to the amount of labelling detected at day 0. In contrast, elevated fluorescence intensity in PSD93-KO animals may affect the measurement of protein lifetime to some extent as puncta with higher starting fluorescence intensity could be detectable for longer purely because of the set puncta detection threshold. To discount the possibility that the difference in protein turnover in PSD93 mutants compared to controls is a result of a technical limitation, PSD95 lifetime in PSD93 mutants could be assessed using traditional mass-spec based pulse-chase experiments or single-molecule analysis of PSD95-HaloTag labelling.

6.4.3 The effects of SynGAP mutation on PSD95 lifetime

Heterozygous deletion of SynGAP had smaller effect on the lifetime of PSD95 in adult mice compared to PSD93 mutants. This result could be due to a number of reasons, including that (a) SynGAP is expressed in a subset of

synapses and they do not represent a high fraction of PSD95-positive synapses, (b) SynGAP exerts its influence on neuron structure and function at a restricted time window which was not captured in the present analysis and (c) SynGAP and PSD95 interaction simply does not influence the stability and lifetime of PSD95. No studies to date, to my knowledge, have assessed co-localisation of PSD95 and SynGAP proteins at the level of single synapses. Gene expression studies, however, revealed that SynGAP expression is more restricted than that of PSD95 and displays brain region and neuron selectivity (Porter et al., 2005). In the future, antibody staining for SynGAP protein could be completed on SiR-Halo injected PSD95-HaloTag brain sections and sections could be subjected to single-synapse resolution spinning disc microscopy to reveal the fraction of synapses that contain both, SynGAP and PSD95 proteins.

Previous studies have documented that the effects of SynGAP mutation are restricted to early development and many of the phenotypes disappear by P60 (Clement et al., 2012, Aceti et al., 2015). Clement et al. (2012) found that excitatory synaptic transmission and AMPA/NMDA receptor ratio were elevated while spine motility reduced in SynGAP mutants compared to controls at P14-16, but not at P7-9 or >6W. Aceti et al. (2015) documented larger total neurite length and higher complexity of dendritic arbour in mutants compared to wild-type animals at P21 but the differences were no longer detected at P60. A number of studies suggest that SynGAP mutants undergo earlier dendritic spine formation, remodelling and maturation of neuronal structure and function compared to healthy controls, and that only the phenotypes of elevated spine size and behavioural abnormalities in mutants are maintained well into the adulthood (Clement et al., 2012, Vazquez et al., 2004, Aceti et al., 2015). Clement et al. (2012) and Ozkan et al. (2014) further strengthen the support for restricted time window of action by showing that conditional removal of SynGAP only causes pathology when carried out in developing but not mature brain. Future studies examining PSD95 lifetime in SynGAP mutants at different stages of development would be useful to complement the current dataset and

uncover any developmental time window-dependent effects on protein stability and lifetime.

6.4.4 Future disease models

The selection of disease models for the current study was based on two criteria: (1) the presence of the disease-associated protein in the PSD and (2) the close interaction of PSD95 with the disease-associated protein. PSD93 and SynGAP are both proteins of the post-synapse and are close interactors of PSD95. Future studies on PSD95 protein lifetime in mutants could focus on disease-associated proteins that have a direct role in protein synthesis or degradation. For example, a mutation in a translational repressor protein FMRP causes Fragile X syndrome and is one of the leading causes of ASD and ID (Osterweil et al., 2010, Barnes et al., 2016). CYFIP1 is another translational repressor protein which, when mutated, causes ASD, ID and schizophrenia (Louros and Osterweil, 2016, De Rubeis et al., 2013, Haan et al., 2021). Neurodegenerative diseases have links to dysfunctional protein synthesis and degradation machinery, too. Parkin protein, an E3 ubiquitin ligase involved in targeting proteins for degradation, is a risk gene for Parkinson's disease (Arkinson and Walden, 2018, Soukup et al., 2018). Since FMRP, CYFIP1 and Parkin all have known roles in protein synthesis or degradation, understanding how mutations in these proteins affect the turnover and lifetime of an important synaptic organiser PSD95 would be an important goal for future studies.

6.4.5 Implications for memory storage

PSD93 mutations in mice and humans have been linked to impairments in attention, learning and cognitive flexibility in both species (Nithianantharajah et al., 2013). These behavioural abnormalities co-occur with presently described increases in protein lifetime in mice. Longer protein lifetime in synapses would result in longer-term storage of molecular memory but a reduced flexibility to adapt and learn new information which appears to be consistent with behavioural defects in cognitive flexibility and learning in PSD93 mutants. So far these are only rough parallels between molecular

stability and cognitive flexibility and future studies should directly explore the link between behavioural performance and protein lifetime. One way of manipulating the lifetime of PSD95 protein in adult animals without knocking-out other proteins would be the genetic removal of PEST peptide sequence from PSD95, the presence of which selectively targets proteins for degradation and thus is linked to shorter protein lifetimes (Rechsteiner and Rogers, 1996, Colledge et al., 2003). Behavioural paradigms similar to those used in Nithianantharajah et al. (2013) could be employed to directly examine the effects of longer-lived PSD95 on behavioural performance.

Chapter 7 Conclusions and future directions

7.1 Conclusions

PSD95 protein lifetime maps are the first of the kind brain-wide single-synapse resolution maps of protein lifetime. PSD95 half-life was estimated for 110 brain subregions and the study examined on average ~10,000,000 synaptic puncta in each mouse brain. With our method we could detect spatial differences in synaptic protein lifetime at the level of regions, subregions, cell types, dendritic arbour and individual synapses. Single-synapse resolution allowed us for the first time to identify synapses with long protein lifetime and assess their distribution in different brain regions. Analysis of PSD95 lifetime in developing, adult and ageing brain helped us identify brain regions, subregions and synapses most susceptible to changes in protein turnover. We applied the method to map synaptic protein lifetime in mouse models of neurodevelopmental and psychiatric diseases and revealed brain region-, subregion- and mutation-specific changes in protein lifetime. Besides providing novel biological insights, brain-wide maps of synaptic protein lifetime will form a great resource for future research into molecular and synapse biology.

7.2 Future directions

7.2.1 Detecting LPL synapses months after labelling

The longest half-life we detected in adult brain was 12.1 days in L1 of motor cortex. Assuming an exponential nature of decay, 70 days after injection we should still be able to detect >1.5% of synaptic puncta we started with. At the level of synapse subtypes, we showed that subtypes 2 and 34 could retain the large majority of SiR-Halo labelled PSD95 over 7 days. Based on the percentage of SiR-Halo positive subtypes remaining, the half-life of PSD95 for subtypes 2 and 34 would be 153.2 days and 30.7 days, respectively. Assuming an exponential decay of PSD95 in different subtypes, we could still expect to detect SiR-Halo in subtype 2 more than 2 years after SiR-Halo injection and, for subtype 34, more than 6 months after SiR-Halo injection. In our studies, we only tracked the lifetime of PSD95 for up to 2 weeks. Establishing whether at 1-, 2-, 6- or 12- months post-injection we indeed could still detect fluorescently

labelled synaptic puncta would carry important implications for current scientific understanding of structural and functional stability of synapses.

7.2.2 Characterisation of LPL and SPL synapses

In Chapter 4, we classified synapse subtypes into LPL and SPL synapses according to their PSD95 protein lifetime. Synapse subtypes had been previously defined by the molecular and morphological features of PSD95-eGFP and SAP102-mKO2 synaptic markers (Zhu et al., 2018, Cizeron et al., 2020). LPL and SPL synapses could have different functions in the brain and further characterisation of the structure and function of these synapses would be important. In the short-term, immuno-staining for AMPA and NMDA receptors on PSD95-HaloTag brain sections from different time points post-injection could be performed. By analysing co-localisation of SiR-Halo label with immuno-stains, we could investigate the presence and relative abundance of glutamate receptors in LPL synapses and reveal some further functional characteristics of these synapses. Similar immuno-staining approach could be used on $PSD95^{eGFP/+}$;$SAP102^{mKO2/+}$ brain sections. Here, synaptic puncta could be classified into subtypes based on PSD95-eGFP and SAP102-mKO2 markers and co-localisation between different subtypes and the presence as well as abundance of glutamate receptors could be analysed. Subtype 2 and 34 were shown to have the longest protein lifetimes in our study and those subtypes would be of particular interest in the co-localisation analysis.

HaloTag protein can be coupled to moieties like HaloLink^{TM}Resin or HaloTag Biotin that allow the pull down of protein complexes from mammalian cells ((Urh and Rosenberg, 2012, Courtney et al., 2018, Perez-Perri et al., 2016). Using protein pull down assays we could investigate protein composition of SPL and LPL synapses. Brain tissue from PSD95-HaloTag mice could be collected at different times post-injection of SiR-Halo, homogenized and probed with HaloLink^{TM}Resin or HaloTag Biotin to pull down unlabelled PSD95 and its interactors. Biochemical and mass spectrometry analyses could be carried out to assess whether LPL and SPL synapses contain any distinct protein species or preferred PSD95 interactors.

7.2.3 Relationship between spine and protein lifetime

LPL and SPL synapses may coincide with long-lived and short-lived dendritic spines in the brain, respectively. To investigate such possibility, SiR-Halo injected PSD95-HaloTag mice could be sparsely labelled with fluorescent cell-fill constructs and subjected to 2P chronic live imaging through a cranial window. Dendritic spines with their corresponding SiR-Halo content could be visualised and tracked over time, and their lifetime could be determined and compared. Since learning has been shown to induce selective stabilization of newly formed spines (Holtmaat et al., 2006, Yang et al., 2009, Xu et al., 2009, Seaton et al., 2020), we could identify the learning-affected spines and compare their protein lifetime to that in the rest of the dendritic spine population. Any relationship identified between LPL synapses and learning-affected spines would provide crucial insights into molecular mechanisms of learning and memory.

7.2.4 Distribution of pre- and post-synaptic protein lifetimes

Individual synapses are thought to coordinate the size of their pre- and post-synaptic compartments as evidenced by positive correlation between sizes of the PSD, spine head, presynaptic active zone and the number of synaptic vesicles (Harris and Stevens, 1989, Schikorski and Stevens, 1997). Pharmacological silencing of neuronal activity induces increase in the sizes of the PSD, presynaptic active zone and bouton (Murthy et al., 2001). At the level of molecules, changes in the contents of presynaptic scaffolding protein Munc13-1 in a synapse are matched with changes in the amounts of postsynaptic PSD95 so that the stoichiometry is maintained over time (Fisher-Lavie and Ziv, 2013). The coordination of structure and molecular contents of pre- and post-synaptic compartments may be a result of coordinated protein turnover and lifetime at the level of individual synapses. To test this hypothesis, the lifetime of a presynaptic scaffolding protein such as Munc13-1 should be mapped at single-synapse resolution following the experimental setup that was used for PSD95. Endogenous Munc13-1 could be fused to a domain of another self-labelling tag system, such as SNAP or CLIP (Liss et al., 2015, Wilhelm et al., 2021, Hoelzel and Zhang, 2020). Munc13-1 SNAP/CLIP mouse line could

then be crossed with PSD95-HaloTag mouse line and a mixture of fluorescent HaloTag and SNAP/CLIP ligand could be injected into mice and the lifetime of proteins could be estimated. Comparing the lifetime between pre- and post-synaptic protein in individual synapses should be performed to uncover synapse-specific mechanisms of protein lifetime regulation.

7.2.5 Effects of ablating LPL synapses on memory retention

To test whether LPL synapses are important for memory storage, inducing ablation of these synapses after learning should be performed and the effects on behaviour measured. One way of selectively targeting LPL synapses for inactivation or destruction is the use of photosensitizers (Bulina et al., 2006, Jay, 1988, Takemoto et al., 2011, Takemoto et al., 2017). Photosensitizers are molecules that upon irradiation with intense light produce reactive oxygen species, such as singlet oxygen, hydroxyl radicals and superoxide ions (Josefsen and Boyle, 2008, Castano et al., 2004). Reactive oxygen species damage proteins nearby by inducing changes in protein conformation, cross-linking and backbone fragmentation (Yan et al., 2006, Jay, 1988). The effects are locally restricted therefore providing high spatial control (Beck et al., 2002, Linden et al., 1992). HaloTag ligands can be coupled to photosensitizers such as JF570 (Binns et al., 2020) or SeNBD (Benson et al., 2021). HaloTag-coupled photosensitizers could be injected into PSD95-HaloTag mice and after >2 weeks post-injection, at a time when the majority of remaining fluorescence labelling is concentrated in LPL synapses, a strong laser could be used to ablate photosensitizer-containing synapses. Prior to injection of photosensitiser-HaloTag construct, the mice could be subjected to a learning paradigm, such as a motor learning task. Following the ablation of LPL synapses, mice could be retested on the motor task to check if the memory of previous learning is retained.

References

ACETI, M., CRESON, T. K., VAISSIERE, T., ROJAS, C., HUANG, W.-C., WANG, Y.-X., PETRALIA, R. S., PAGE, D. T., MILLER, C. A. & RUMBAUGH, G. 2015. Syngap1 Haploinsufficiency Damages a Postnatal Critical Period of Pyramidal Cell Structural Maturation Linked to Cortical Circuit Assembly. *Biological Psychiatry,* 77**,** 805-815.

ALBERINI, C. M. & TRAVAGLIA, A. 2017. Infantile Amnesia: A Critical Period of Learning to Learn and Remember. *The Journal of neuroscience : the official journal of the Society for Neuroscience,* 37**,** 5783-5795.

ALVAREZ-CASTELAO, B. & SCHUMAN, E. M. 2015. The Regulation of Synaptic Protein Turnover. *Journal of Biological Chemistry,* 290**,** 28623-28630.

ALVAREZ-CASTELAO, B., TOM DIECK, S., FUSCO, C. M., DONLIN-ASP, P., PEREZ, J. D. & SCHUMAN, E. M. 2020. The switch-like expression of heme-regulated kinase 1 mediates neuronal proteostasis following proteasome inhibition. *eLife,* 9**,** e52714.

ANDERSEN, P., SILFVENIUS, H., SUNDBERG, S. H. & SVEEN, O. 1980. A comparison of distal and proximal dendritic synapses on CAi pyramids in guinea-pig hippocampal slices in vitro. *The Journal of physiology,* 307**,** 273-299.

ANDRASFALVY, B. K. & MAGEE, J. C. 2001. Distance-dependent increase in AMPA receptor number in the dendrites of adult hippocampal CA1 pyramidal neurons. *The Journal of neuroscience : the official journal of the Society for Neuroscience,* 21**,** 9151-9159.

ARKINSON, C. & WALDEN, H. 2018. Parkin function in Parkinson's disease. *Science,* 360**,** 267.

ATTARDO, A., FITZGERALD, J. E. & SCHNITZER, M. J. 2015. Impermanence of dendritic spines in live adult CA1 hippocampus. *Nature,* 523**,** 592-596.

BACHMAIR, A., FINLEY, D. & VARSHAVSKY, A. 1986. In vivo half-life of a protein is a function of its amino-terminal residue. *Science,* 234**,** 179.

BÄHNER, F. & MEYER-LINDENBERG, A. 2017. Hippocampal–prefrontal connectivity as a translational phenotype for schizophrenia. *European Neuropsychopharmacology,* 27**,** 93-106.

BAI, F. & WITZMANN, F. A. 2007. Synaptosome proteomics. *Sub-cellular biochemistry,* 43**,** 77-98.

BALLIF, B. A., CAREY, G. R., SUNYAEV, S. R. & GYGI, S. P. 2008. Large-scale identification and evolution indexing of tyrosine phosphorylation sites from murine brain. *Journal of proteome research,* 7**,** 311-318.

BARNES, S. A., THOMSON, S. R., KIND, P. C. & OSTERWEIL, E. K. 2016. Chapter 8 - FMRP and the Pathophysiology of Fragile X Syndrome. *In:* SALA, C. & VERPELLI, C. (eds.) *Neuronal and Synaptic Dysfunction in Autism Spectrum Disorder and Intellectual Disability.* San Diego: Academic Press.

BATS, C., GROC, L. & CHOQUET, D. 2007. The Interaction between Stargazin and PSD-95 Regulates AMPA Receptor Surface Trafficking. *Neuron,* 53**,** 719-734.
BAYÉS, À., VAN DE LAGEMAAT, L. N., COLLINS, M. O., CRONING, M. D. R., WHITTLE, I. R., CHOUDHARY, J. S. & GRANT, S. G. N. 2011. Characterization of the proteome, diseases and evolution of the human postsynaptic density. *Nature Neuroscience,* 14**,** 19-21.
BECK, S., SAKURAI, T., EUSTACE, B. K., BESTE, G., SCHIER, R., RUDERT, F. & JAY, D. G. 2002. Fluorophore-assisted light inactivation: a high-throughput tool for direct target validation of proteins. *Proteomics,* 2**,** 247-55.
BENSON, S., DE MOLINER, F., FERNANDEZ, A., KURU, E., ASIIMWE, N. L., LEE, J.-S., HAMILTON, L., SIEGER, D., BRAVO, I. R., ELLIOT, A. M., FENG, Y. & VENDRELL, M. 2021. Photoactivatable metabolic warheads enable precise and safe ablation of target cells in vivo. *Nature Communications,* 12**,** 2369.
BERLIN, C. M. & SCHIMKE, R. T. 1965. Influence of turnover rates on the responses of enzymes to cortisone. *Mol Pharmacol,* 1**,** 149-56.
BERRY, K. P. & NEDIVI, E. 2017. Spine Dynamics: Are They All the Same? *Neuron,* 96**,** 43-55.
BIANCHETTA, M. J., LAM, T. T., JONES, S. N. & MORABITO, M. A. 2011. Cyclin-Dependent Kinase 5 Regulates PSD-95 Ubiquitination in Neurons. *The Journal of Neuroscience,* 31**,** 12029.
BIER, D. M. 1999. The energy costs of protein metabolism: lean and mean on Uncle Sam's team. *The role of protein and amino acids in sustaining and enhancing performance***,** 109-119.
BIEVER, A., GLOCK, C., TUSHEV, G., CIIRDAEVA, E., DALMAY, T., LANGER, J. D. & SCHUMAN, E. M. 2020. Monosomes actively translate synaptic mRNAs in neuronal processes. *Science,* 367.
BINGOL, B. & SCHUMAN, E. M. 2006. Activity-dependent dynamics and sequestration of proteasomes in dendritic spines. *Nature,* 441**,** 1144-1148.
BINGOL, B., WANG, C.-F., ARNOTT, D., CHENG, D., PENG, J. & SHENG, M. 2010. Autophosphorylated CaMKIIα Acts as a Scaffold to Recruit Proteasomes to Dendritic Spines. *Cell,* 140**,** 567-578.
BINNS, T. C., AYALA, A. X., GRIMM, J. B., TKACHUK, A. N., CASTILLON, G. A., PHAN, S., ZHANG, L., BROWN, T. A., LIU, Z., ADAMS, S. R., ELLISMAN, M. H., KOYAMA, M. & LAVIS, L. D. 2020. Rational Design of Bioavailable Photosensitizers for Manipulation and Imaging of Biological Systems. *Cell Chemical Biology,* 27**,** 1063-1072.e7.
BLEUVEN, C. & LANDRY, C. R. 2016. Molecular and cellular bases of adaptation to a changing environment in microorganisms. *Proceedings of the Royal Society B: Biological Sciences,* 283**,** 20161458.
BODIAN, D. 1965. A SUGGESTIVE RELATIONSHIP OF NERVE CELL RNA WITH SPECIFIC SYNAPTIC SITES. *Proceedings of the National Academy of Sciences,* 53**,** 418.
BOISVERT, F.-M., AHMAD, Y., GIERLIŃSKI, M., CHARRIÈRE, F., LAMONT, D., SCOTT, M., BARTON, G. & LAMOND, A. I. 2012. A Quantitative

Spatial Proteomics Analysis of Proteome Turnover in Human Cells *. *Molecular & Cellular Proteomics,* 11.
BONTEMPI, B., LAURENT-DEMIR, C., DESTRADE, C. & JAFFARD, R. 1999. Time-dependent reorganization of brain circuitry underlying long-term memory storage. *Nature,* 400**,** 671-675.
BROADHEAD, M. J., HORROCKS, M. H., ZHU, F., MURESAN, L., BENAVIDES-PICCIONE, R., DEFELIPE, J., FRICKER, D., KOPANITSA, M. V., DUNCAN, R. R. & KLENERMAN, D. 2016. PSD95 nanoclusters are postsynaptic building blocks in hippocampus circuits. *Scientific reports,* 6**,** 1-14.
BROCKMANN, M. M., DÖNGI, M., EINSFELDER, U., KÖRBER, N., REFOJO, D. & STEIN, V. 2019. Neddylation regulates excitatory synaptic transmission and plasticity. *Scientific reports,* 9**,** 17935-17935.
BUCCIANTINI, M., GIANNONI, E., CHITI, F., BARONI, F., FORMIGLI, L., ZURDO, J., TADDEI, N., RAMPONI, G., DOBSON, C. M. & STEFANI, M. 2002. Inherent toxicity of aggregates implies a common mechanism for protein misfolding diseases. *nature,* 416**,** 507-511.
BUCHLER, N. E., GERLAND, U. & HWA, T. 2005. Nonlinear protein degradation and the function of genetic circuits. *Proceedings of the National Academy of Sciences of the United States of America,* 102**,** 9559.
BUCKLEY, D. L., RAINA, K., DARRICARRERE, N., HINES, J., GUSTAFSON, J. L., SMITH, I. E., MIAH, A. H., HARLING, J. D. & CREWS, C. M. 2015. HaloPROTACS: Use of Small Molecule PROTACs to Induce Degradation of HaloTag Fusion Proteins. *ACS Chemical Biology,* 10**,** 1831-1837.
BULINA, M. E., CHUDAKOV, D. M., BRITANOVA, O. V., YANUSHEVICH, Y. G., STAROVEROV, D. B., CHEPURNYKH, T. V., MERZLYAK, E. M., SHKROB, M. A., LUKYANOV, S. & LUKYANOV, K. A. 2006. A genetically encoded photosensitizer. *Nature Biotechnology,* 24**,** 95-99.
BUTKEVICH, A. N., BELOV, V. N., KOLMAKOV, K., SOKOLOV, V. V., SHOJAEI, H., SIDENSTEIN, S. C., KAMIN, D., MATTHIAS, J., VLIJM, R., ENGELHARDT, J. & HELL, S. W. 2017. Hydroxylated Fluorescent Dyes for Live-Cell Labeling: Synthesis, Spectra and Super-Resolution STED. *Chemistry (Weinheim an der Bergstrasse, Germany),* 23**,** 12114-12119.
BUTKO, M. T., YANG, J., GENG, Y., KIM, H. J., JEON, N. L., SHU, X., MACKEY, M. R., ELLISMAN, M. H., TSIEN, R. Y. & LIN, M. Z. 2012. Fluorescent and photo-oxidizing TimeSTAMP tags track protein fates in light and electron microscopy. *Nature Neuroscience,* 15**,** 1742-1751.
CAI, C., LI, H., RIVERA, C. & KEINÄNEN, K. 2006. Interaction between SAP97 and PSD-95, two Maguk proteins involved in synaptic trafficking of AMPA receptors. *J Biol Chem,* 281**,** 4267-73.
CAJIGAS, IVÁN J., TUSHEV, G., WILL, TRISTAN J., TOM DIECK, S., FUERST, N. & SCHUMAN, ERIN M. 2012. The Local Transcriptome in the Synaptic Neuropil Revealed by Deep Sequencing and High-Resolution Imaging. *Neuron,* 74**,** 453-466.

CAJIGAS, I. J., WILL, T. & SCHUMAN, E. M. 2010. Protein homeostasis and synaptic plasticity. *The EMBO Journal,* 29**,** 2746-2752.
CANE, M., MACO, B., KNOTT, G. & HOLTMAAT, A. 2014. The Relationship between PSD-95 Clustering and Spine Stability In Vivo. *The Journal of Neuroscience,* 34**,** 2075-2086.
CARLISLE, H. J., FINK, A. E., GRANT, S. G. N. & O'DELL, T. J. 2008. Opposing effects of PSD-93 and PSD-95 on long-term potentiation and spike timing-dependent plasticity. *The Journal of Physiology,* 586**,** 5885-5900.
CARPER, R. A. & COURCHESNE, E. 2005. Localized enlargement of the frontal cortex in early autism. *Biological Psychiatry,* 57**,** 126-133.
CASTANO, A. P., DEMIDOVA, T. N. & HAMBLIN, M. R. 2004. Mechanisms in photodynamic therapy: part one-photosensitizers, photochemistry and cellular localization. *Photodiagnosis Photodyn Ther,* 1**,** 279-93.
CATMULL, E. E. 1974. *A subdivision algorithm for computer display of curved surfaces*, The University of Utah.
CATTS, V. S., DERMINIO, D. S., HAHN, C.-G. & WEICKERT, C. S. 2015. Postsynaptic density levels of the NMDA receptor NR1 subunit and PSD-95 protein in prefrontal cortex from people with schizophrenia. *npj Schizophrenia,* 1**,** 15037.
CHEN, H.-J., ROJAS-SOTO, M., OGUNI, A. & KENNEDY, M. B. 1998. A Synaptic Ras-GTPase Activating Protein (p135 SynGAP) Inhibited by CaM Kinase II. *Neuron,* 20**,** 895-904.
CHEN, L., CHETKOVICH, D. M., PETRALIA, R. S., SWEENEY, N. T., KAWASAKI, Y., WENTHOLD, R. J., BREDT, D. S. & NICOLL, R. A. 2000. Stargazin regulates synaptic targeting of AMPA receptors by two distinct mechanisms. *Nature,* 408**,** 936-943.
CHEN, X., LEVY, J. M., HOU, A., WINTERS, C., AZZAM, R., SOUSA, A. A., LEAPMAN, R. D., NICOLL, R. A. & REESE, T. S. 2015. PSD-95 family MAGUKs are essential for anchoring AMPA and NMDA receptor complexes at the postsynaptic density. *Proceedings of the National Academy of Sciences,* 112**,** E6983.
CHEN, X., VINADE, L., LEAPMAN, R. D., PETERSEN, J. D., NAKAGAWA, T., PHILLIPS, T. M., SHENG, M. & REESE, T. S. 2005. Mass of the postsynaptic density and enumeration of three key molecules. *Proceedings of the National Academy of Sciences,* 102**,** 11551-11556.
CHENG, D., HOOGENRAAD, C. C., RUSH, J., RAMM, E., SCHLAGER, M. A., DUONG, D. M., XU, P., WIJAYAWARDANA, S. R., HANFELT, J., NAKAGAWA, T., SHENG, M. & PENG, J. 2006. Relative and absolute quantification of postsynaptic density proteome isolated from rat forebrain and cerebellum. *Mol Cell Proteomics,* 5**,** 1158-70.
CIZERON, M., QIU, Z., KONIARIS, B., GOKHALE, R., KOMIYAMA, N. H., FRANSÉN, E. & GRANT, S. G. N. 2020. A brainwide atlas of synapses across the mouse life span. *Science,* 369**,** 270-275.
CLEMENT, JAMES P., ACETI, M., CRESON, THOMAS K., OZKAN, EMIN D., SHI, Y., REISH, NICHOLAS J., ALMONTE, ANTOINE G., MILLER, BROOKE H., WILTGEN, BRIAN J., MILLER, COURTNEY A., XU, X. & RUMBAUGH, G. 2012. Pathogenic SYNGAP1 Mutations

Impair Cognitive Development by Disrupting Maturation of Dendritic Spine Synapses. *Cell,* 151**,** 709-723.
COHEN, L. D., BOULOS, A. & ZIV, N. E. 2020. A non-fluorescent HaloTag blocker for improved measurement and visualization of protein synthesis in living cells. *F1000Res,* 9.
COHEN, L. D. & ZIV, N. E. 2019. Neuronal and synaptic protein lifetimes. *Current Opinion in Neurobiology,* 57**,** 9-16.
COHEN, L. D., ZUCHMAN, R., SOROKINA, O., MÜLLER, A., DIETERICH, D. C., ARMSTRONG, J. D., ZIV, T. & ZIV, N. E. 2013. Metabolic Turnover of Synaptic Proteins: Kinetics, Interdependencies and Implications for Synaptic Maintenance. *PLOS ONE,* 8**,** e63191.
COLEY, A. A. & GAO, W.-J. 2018. PSD95: A synaptic protein implicated in schizophrenia or autism? *Progress in Neuro-Psychopharmacology and Biological Psychiatry,* 82**,** 187-194.
COLLEDGE, M., DEAN, R. A., SCOTT, G. K., LANGEBERG, L. K., HUGANIR, R. L. & SCOTT, J. D. 2000. Targeting of PKA to glutamate receptors through a MAGUK-AKAP complex. *Neuron,* 27**,** 107-119.
COLLEDGE, M., SNYDER, E. M., CROZIER, R. A., SODERLING, J. A., JIN, Y., LANGEBERG, L. K., LU, H., BEAR, M. F. & SCOTT, J. D. 2003. Ubiquitination Regulates PSD-95 Degradation and AMPA Receptor Surface Expression. *Neuron,* 40**,** 595-607.
CONSALEZ, G. G., GOLDOWITZ, D., CASONI, F. & HAWKES, R. 2021. Origins, Development, and Compartmentation of the Granule Cells of the Cerebellum. *Frontiers in Neural Circuits,* 14.
COURTNEY, N. A., BRIGUGLIO, J. S., BRADBERRY, M. M., GREER, C. & CHAPMAN, E. R. 2018. Excitatory and Inhibitory Neurons Utilize Different Ca²⁺ Sensors and Sources to Regulate Spontaneous Release. *Neuron,* 98**,** 977-991.e5.
CRAVEN, S. E., EL-HUSSEINI, A. E. & BREDT, D. S. 1999. Synaptic Targeting of the Postsynaptic Density Protein PSD-95 Mediated by Lipid and Protein Motifs. *Neuron,* 22**,** 497-509.
CRUZ-MARTÍN, A., CRESPO, M. & PORTERA-CAILLIAU, C. 2010. Delayed Stabilization of Dendritic Spines in Fragile X Mice. *The Journal of Neuroscience,* 30**,** 7793.
CURRAN, O. E. 2018. *Synaptome mapping of the postsynaptic density 95 protein in the human brain.* University of Edinburgh.
DAI, D.-F., KARUNADHARMA, P. P., CHIAO, Y. A., BASISTY, N., CRISPIN, D., HSIEH, E. J., CHEN, T., GU, H., DJUKOVIC, D., RAFTERY, D., BEYER, R. P., MACCOSS, M. J. & RABINOVITCH, P. S. 2014. Altered proteome turnover and remodeling by short-term caloric restriction or rapamycin rejuvenate the aging heart. *Aging Cell,* 13**,** 529-539.
DAKOJI, S., TOMITA, S., KARIMZADEGAN, S., NICOLL, R. A. & BREDT, D. S. 2003. Interaction of transmembrane AMPA receptor regulatory proteins with multiple membrane associated guanylate kinases. *Neuropharmacology,* 45**,** 849-856.
DAW, N. W. 1998. Critical Periods and Amblyopia. *Archives of Ophthalmology,* 116**,** 502-505.

DE ARCE, K. P., VARELA-NALLAR, L., FARIAS, O., CIFUENTES, A., BULL, P., COUCH, B. A., KOLESKE, A. J., INESTROSA, N. C. & ALVAREZ, A. R. 2010. Synaptic Clustering of PSD-95 Is Regulated by c-Abl through Tyrosine Phosphorylation. *The Journal of Neuroscience,* 30**,** 3728.

DE CAMILLI, P., HARRIS, S. M., JR., HUTTNER, W. B. & GREENGARD, P. 1983. Synapsin I (Protein I), a nerve terminal-specific phosphoprotein. II. Its specific association with synaptic vesicles demonstrated by immunocytochemistry in agarose-embedded synaptosomes. *Journal of Cell Biology,* 96**,** 1355-1373.

DE PAOLA, V., HOLTMAAT, A., KNOTT, G., SONG, S., WILBRECHT, L., CARONI, P. & SVOBODA, K. 2006. Cell Type-Specific Structural Plasticity of Axonal Branches and Boutons in the Adult Neocortex. *Neuron,* 49**,** 861-875.

DE RUBEIS, S., PASCIUTO, E., LI, K. W., FERNÁNDEZ, E., DI MARINO, D., BUZZI, A., OSTROFF, L. E., KLANN, E., ZWARTKRUIS, F. J. T., KOMIYAMA, N. H., GRANT, S. G. N., POUJOL, C., CHOQUET, D., ACHSEL, T., POSTHUMA, D., SMIT, A. B. & BAGNI, C. 2013. CYFIP1 coordinates mRNA translation and cytoskeleton remodeling to ensure proper dendritic spine formation. *Neuron,* 79**,** 1169-1182.

DELLA SALA, G., PUTIGNANO, E., CHELINI, G., MELANI, R., CALCAGNO, E., MICHELE RATTO, G., AMENDOLA, E., GROSS, C. T., GIUSTETTO, M. & PIZZORUSSO, T. 2016. Dendritic Spine Instability in a Mouse Model of CDKL5 Disorder Is Rescued by Insulin-like Growth Factor 1. *Biological Psychiatry,* 80**,** 302-311.

DHAR, M., HANTMAN, A. W. & NISHIYAMA, H. 2018. Developmental pattern and structural factors of dendritic survival in cerebellar granule cells in vivo. *Scientific Reports,* 8**,** 17561.

DHONDT, I., PETYUK, V. A., BAUER, S., BREWER, H. M., SMITH, R. D., DEPUYDT, G. & BRAECKMAN, B. P. 2017. Changes of Protein Turnover in Aging Caenorhabditis elegans*. *Molecular & Cellular Proteomics,* 16**,** 1621-1633.

DLUGOS, C. A. & PENTNEY, R. J. 1994. Morphometric analyses of purkinje and granule cells in aging F344 rats. *Neurobiology of Aging,* 15**,** 435-440.

DONATO, F., ALBERINI, C. M., AMSO, D., DRAGOI, G., DRANOVSKY, A. & NEWCOMBE, N. S. 2021. The Ontogeny of Hippocampus-Dependent Memories. *J Neurosci,* 41**,** 920-926.

DONLIN-ASP, P. G., POLISSENI, C., KLIMEK, R., HECKEL, A. & SCHUMAN, E. M. 2021. Differential regulation of local mRNA dynamics and translation following long-term potentiation and depression. *Proceedings of the National Academy of Sciences,* 118**,** e2017578118.

DÖRRBAUM, A. R., ALVAREZ-CASTELAO, B., NASSIM-ASSIR, B., LANGER, J. D. & SCHUMAN, E. M. 2020. Proteome dynamics during homeostatic scaling in cultured neurons. *eLife,* 9**,** e52939.

DÖRRBAUM, A. R., KOCHEN, L., LANGER, J. D. & SCHUMAN, E. M. 2018. Local and global influences on protein turnover in neurons and glia. *eLife,* 7**,** e34202.

DRUMMOND, D. A. & WILKE, C. O. 2008. Mistranslation-Induced Protein Misfolding as a Dominant Constraint on Coding-Sequence Evolution. *Cell,* 134**,** 341-352.

DWYER, B. E., FANDO, J. L. & WASTERLAIN, C. G. 1980. Rat Brain Protein Synthesis Declines During Postdevelopmental Aging. *Journal of Neurochemistry,* 35**,** 746-749.

EHLERS, M. D. 2003. Activity level controls postsynaptic composition and signaling via the ubiquitin-proteasome system. *Nature Neuroscience,* 6**,** 231-242.

EHRLICH, I., KLEIN, M., RUMPEL, S. & MALINOW, R. 2007. PSD-95 is required for activity-driven synapse stabilization. *Proceedings of the National Academy of Sciences,* 104**,** 4176-4181.

EHRLICH, I. & MALINOW, R. 2004. Postsynaptic Density 95 controls AMPA Receptor Incorporation during Long-Term Potentiation and Experience-Driven Synaptic Plasticity. *The Journal of Neuroscience,* 24**,** 916.

EKSTROM, R., LIU, D. S. H. & RICHARDSON, A. 1980. Changes in Brain Protein Synthesis during the Life Span of Male Fischer Rats. *Gerontology,* 26**,** 121-128.

EL-HUSSEINI, A. E.-D., SCHNELL, E., CHETKOVICH, D. M., NICOLL, R. A. & BREDT, D. S. 2000. PSD-95 Involvement in Maturation of Excitatory Synapses. *Science,* 290**,** 1364.

EL-HUSSEINI, D., SCHNELL, E., DAKOJI, S., SWEENEY, N., ZHOU, Q., PRANGE, O., GAUTHIER-CAMPBELL, C., AGUILERA-MORENO, A., NICOLL, R. A. & BREDT, D. S. 2002. Synaptic strength regulated by palmitate cycling on PSD-95. *Cell,* 108**,** 849-63.

ELIAS, G. M., ELIAS, L. A. B., APOSTOLIDES, P. F., KRIEGSTEIN, A. R. & NICOLL, R. A. 2008. Differential trafficking of AMPA and NMDA receptors by SAP102 and PSD-95 underlies synapse development. *Proceedings of the National Academy of Sciences,* 105**,** 20953.

ELKOBI, A., EHRLICH, I., BELELOVSKY, K., BARKI-HARRINGTON, L. & ROSENBLUM, K. 2008. ERK-dependent PSD-95 induction in the gustatory cortex is necessary for taste learning, but not retrieval. *Nature Neuroscience,* 11**,** 1149-1151.

ENGLAND, C. G., LUO, H. & CAI, W. 2015. HaloTag Technology: A Versatile Platform for Biomedical Applications. *Bioconjugate Chemistry,* 26**,** 975-986.

ESPINOSA, J. S. & STRYKER, MICHAEL P. 2012. Development and Plasticity of the Primary Visual Cortex. *Neuron,* 75**,** 230-249.

FANDO, J. L., SALINAS, M. & WASTERLAIN, C. G. 1980. Age-dependent changes in brain protein synthesis in the rat. *Neurochemical Research,* 5**,** 373-383.

FARHY-TSELNICKER, I. & ALLEN, N. J. 2018. Astrocytes, neurons, synapses: a tripartite view on cortical circuit development. *Neural Development,* 13**,** 7.

FELIG, P., OWEN, O. E., WAHREN, J. & CAHILL, G. F., JR. 1969. Amino acid metabolism during prolonged starvation. *J Clin Invest,* 48**,** 584-94.

FERNÁNDEZ, E., COLLINS, M. O., UREN, R. T., KOPANITSA, M. V., KOMIYAMA, N. H., CRONING, M. D., ZOGRAFOS, L., ARMSTRONG,

J. D., CHOUDHARY, J. S. & GRANT, S. G. 2009. Targeted tandem affinity purification of PSD-95 recovers core postsynaptic complexes and schizophrenia susceptibility proteins. *Mol Syst Biol,* 5**,** 269.

FISHBAIN, S., INOBE, T., ISRAELI, E., CHAVALI, S., YU, H., KAGO, G., BABU, M. M. & MATOUSCHEK, A. 2015. Sequence composition of disordered regions fine-tunes protein half-life. *Nature Structural & Molecular Biology,* 22**,** 214-221.

FISHER-LAVIE, A. & ZIV, N. E. 2013. Matching Dynamics of Presynaptic and Postsynaptic Scaffolds. *The Journal of Neuroscience,* 33**,** 13094.

FITZGERALD, P. J., PINARD, C. R., CAMP, M. C., FEYDER, M., SAH, A., BERGSTROM, H. C., GRAYBEAL, C., LIU, Y., SCHLÜTER, O. M., GRANT, S. G., SINGEWALD, N., XU, W. & HOLMES, A. 2015. Durable fear memories require PSD-95. *Molecular Psychiatry,* 20**,** 901-912.

FORNASIERO, E. F., MANDAD, S., WILDHAGEN, H., ALEVRA, M., RAMMNER, B., KEIHANI, S., OPAZO, F., URBAN, I., ISCHEBECK, T., SAKIB, M. S., FARD, M. K., KIRLI, K., CENTENO, T. P., VIDAL, R. O., RAHMAN, R.-U., BENITO, E., FISCHER, A., DENNERLEIN, S., REHLING, P., FEUSSNER, I., BONN, S., SIMONS, M., URLAUB, H. & RIZZOLI, S. O. 2018. Precisely measured protein lifetimes in the mouse brain reveal differences across tissues and subcellular fractions. *Nature Communications,* 9**,** 4230.

FRANK, R. A. W. & GRANT, S. G. N. 2017. Supramolecular organization of NMDA receptors and the postsynaptic density. *Current Opinion in Neurobiology,* 45**,** 139-147.

FRANK, R. A. W., KOMIYAMA, N. H., RYAN, T. J., ZHU, F., O'DELL, T. J. & GRANT, S. G. N. 2016. NMDA receptors are selectively partitioned into complexes and supercomplexes during synapse maturation. *Nature Communications,* 7**,** 11264.

FRANK, R. A. W., ZHU, F., KOMIYAMA, N. H. & GRANT, S. G. N. 2017. Hierarchical organization and genetically separable subfamilies of PSD95 postsynaptic supercomplexes. *Journal of Neurochemistry,* 142**,** 504-511.

FRANKLAND, P. W. & BONTEMPI, B. 2005. The organization of recent and remote memories. *Nat Rev Neurosci,* 6**,** 119-30.

FRANKLIN, J. L. & JOHNSON, E. M., JR. 1998. Control of Neuronal Size Homeostasis by Trophic Factor–mediated Coupling of Protein Degradation to Protein Synthesis. *Journal of Cell Biology,* 142**,** 1313-1324.

FROMER, M., POCKLINGTON, A. J., KAVANAGH, D. H., WILLIAMS, H. J., DWYER, S., GORMLEY, P., GEORGIEVA, L., REES, E., PALTA, P., RUDERFER, D. M., CARRERA, N., HUMPHREYS, I., JOHNSON, J. S., ROUSSOS, P., BARKER, D. D., BANKS, E., MILANOVA, V., GRANT, S. G., HANNON, E., ROSE, S. A., CHAMBERT, K., MAHAJAN, M., SCOLNICK, E. M., MORAN, J. L., KIROV, G., PALOTIE, A., MCCARROLL, S. A., HOLMANS, P., SKLAR, P., OWEN, M. J., PURCELL, S. M. & O'DONOVAN, M. C. 2014. De novo mutations in schizophrenia implicate synaptic networks. *Nature,* 506**,** 179-184.

FUKAYA, M. & WATANABE, M. 2000. Improved immunohistochemical detection of postsynaptically located PSD-95/SAP90 protein family by protease section pretreatment: a study in the adult mouse brain. *J Comp Neurol,* 426**,** 572-86.
GAMACHE, T. R., ARAKI, Y. & HUGANIR, R. L. 2020. Twenty Years of SynGAP Research: From Synapses to Cognition. *The Journal of Neuroscience,* 40**,** 1596.
GARCIA, E. P., MEHTA, S., BLAIR, L. A., WELLS, D. G., SHANG, J., FUKUSHIMA, T., FALLON, J. R., GARNER, C. C. & MARSHALL, J. 1998. SAP90 binds and clusters kainate receptors causing incomplete desensitization. *Neuron,* 21**,** 727-739.
GAWRON, D., NDAH, E., GEVAERT, K. & VAN DAMME, P. 2016. Positional proteomics reveals differences in N-terminal proteoform stability. *Molecular Systems Biology,* 12**,** 858.
GHODA, L., VAN DAALEN WETTERS, T., MACRAE, M., ASCHERMAN, D. & COFFINO, P. 1989. Prevention of rapid intracellular degradation of ODC by a carboxyl-terminal truncation. *Science,* 243**,** 1493.
GIBBS, D. J., BACARDIT, J., BACHMAIR, A. & HOLDSWORTH, M. J. 2014. The eukaryotic N-end rule pathway: conserved mechanisms and diverse functions. *Trends in Cell Biology,* 24**,** 603-611.
GILMAN, SARAH R., IOSSIFOV, I., LEVY, D., RONEMUS, M., WIGLER, M. & VITKUP, D. 2011. Rare De Novo Variants Associated with Autism Implicate a Large Functional Network of Genes Involved in Formation and Function of Synapses. *Neuron,* 70**,** 898-907.
GLESSNER, J. T., WANG, K., CAI, G., KORVATSKA, O., KIM, C. E., WOOD, S., ZHANG, H., ESTES, A., BRUNE, C. W. & BRADFIELD, J. P. 2009. Autism genome-wide copy number variation reveals ubiquitin and neuronal genes. *Nature,* 459**,** 569-573.
GOLDBERG, A. L. 1972. Degradation of Abnormal Proteins in <em>Escherichia coli</em&gt. *Proceedings of the National Academy of Sciences,* 69**,** 422.
GOLDBERG, A. L. 2003. Protein degradation and protection against misfolded or damaged proteins. *Nature,* 426**,** 895-899.
GOLDBERG, A. L. & DICE, J. F. 1974. Intracellular Protein Degradation in Mammalian and Bacterial Cells. *Annual Review of Biochemistry,* 43**,** 835-869.
GRAY, N. W., WEIMER, R. M., BUREAU, I. & SVOBODA, K. 2006. Rapid Redistribution of Synaptic PSD-95 in the Neocortex In Vivo. *PLOS Biology,* 4**,** e370.
GREER, P. L., HANAYAMA, R., BLOODGOOD, B. L., MARDINLY, A. R., LIPTON, D. M., FLAVELL, S. W., KIM, T.-K., GRIFFITH, E. C., WALDON, Z. & MAEHR, R. 2010. The Angelman Syndrome protein Ube3A regulates synapse development by ubiquitinating arc. *Cell,* 140**,** 704-716.
GRILLO, F. W., SONG, S., TELES-GRILO RUIVO, L. M., HUANG, L., GAO, G., KNOTT, G. W., MACO, B., FERRETTI, V., THOMPSON, D., LITTLE, G. E. & DE PAOLA, V. 2013. Increased axonal bouton

dynamics in the aging mouse cortex. *Proceedings of the National Academy of Sciences,* 110**,** E1514-E1523.
GRIMM, J. B., ENGLISH, B. P., CHEN, J., SLAUGHTER, J. P., ZHANG, Z., REVYAKIN, A., PATEL, R., MACKLIN, J. J., NORMANNO, D., SINGER, R. H., LIONNET, T. & LAVIS, L. D. 2015. A general method to improve fluorophores for live-cell and single-molecule microscopy. *Nat Methods,* 12**,** 244-50, 3 p following 250.
GRIMM, J. B., MUTHUSAMY, A. K., LIANG, Y., BROWN, T. A., LEMON, W. C., PATEL, R., LU, R., MACKLIN, J. J., KELLER, P. J., JI, N. & LAVIS, L. D. 2017. A general method to fine-tune fluorophores for live-cell and in vivo imaging. *Nature Methods,* 14**,** 987-994.
GRIMM, J. B., TKACHUK, A. N., XIE, L., CHOI, H., MOHAR, B., FALCO, N., SCHAEFER, K., PATEL, R., ZHENG, Q., LIU, Z., LIPPINCOTT-SCHWARTZ, J., BROWN, T. A. & LAVIS, L. D. 2020. A general method to optimize and functionalize red-shifted rhodamine dyes. *Nature Methods,* 17**,** 815-821.
GRUTZENDLER, J., KASTHURI, N. & GAN, W.-B. 2002. Long-term dendritic spine stability in the adult cortex. *Nature,* 420**,** 812-816.
HAAN, N., WESTACOTT, L. J., CARTER, J., OWEN, M. J., GRAY, W. P., HALL, J. & WILKINSON, L. S. 2021. Haploinsufficiency of the schizophrenia and autism risk gene Cyfip1 causes abnormal postnatal hippocampal neurogenesis through microglial and Arp2/3 mediated actin dependent mechanisms. *Translational Psychiatry,* 11**,** 313.
HAFNER, A.-S., DONLIN-ASP, P. G., LEITCH, B., HERZOG, E. & SCHUMAN, E. M. 2019. Local protein synthesis is a ubiquitous feature of neuronal pre- and postsynaptic compartments. *Science,* 364**,** eaau3644.
HAMDAN, F. F., GAUTHIER, J., SPIEGELMAN, D., NOREAU, A., YANG, Y., PELLERIN, S., DOBRZENIECKA, S., CÔTÉ, M., PERREAU-LINCK, E., CARMANT, L., D'ANJOU, G., FOMBONNE, É., ADDINGTON, A. M., RAPOPORT, J. L., DELISI, L. E., KREBS, M.-O., MOUAFFAK, F., JOOBER, R., MOTTRON, L., DRAPEAU, P., MARINEAU, C., LAFRENIÈRE, R. G., LACAILLE, J. C., ROULEAU, G. A. & MICHAUD, J. L. 2009. Mutations in SYNGAP1 in Autosomal Nonsyndromic Mental Retardation. *New England Journal of Medicine,* 360**,** 599-605.
HANNA, J., GUERRA-MORENO, A., ANG, J. & MICOOGULLARI, Y. 2019. Protein Degradation and the Pathologic Basis of Disease. *The American Journal of Pathology,* 189**,** 94-103.
HARADA, C. N., NATELSON LOVE, M. C. & TRIEBEL, K. L. 2013. Normal cognitive aging. *Clinics in geriatric medicine,* 29**,** 737-752.
HARRIS, K. M., JENSEN, F. E. & TSAO, B. 1992. Three-dimensional structure of dendritic spines and synapses in rat hippocampus (CA1) at postnatal day 15 and adult ages: implications for the maturation of synaptic physiology and long-term potentiation. *J Neurosci,* 12**,** 2685-705.
HARRIS, K. M. & STEVENS, J. K. 1989. Dendritic spines of CA 1 pyramidal cells in the rat hippocampus: serial electron microscopy with reference to their biophysical characteristics. *J Neurosci,* 9**,** 2982-97.
HARROLD, M. W. & ZAVOD, R. M. 2014. Basic concepts in medicinal chemistry. Taylor & Francis.

HARTL, F. U. 2017. Protein Misfolding Diseases. *Annual Review of Biochemistry,* 86**,** 21-26.
HAWKINS, A. J. S. 1991. Protein Turnover: A Functional Appraisal. *Functional Ecology,* 5**,** 222-233.
HAYAMIZU, K. 2017. 21 - Amino Acids and Energy Metabolism: An Overview. *In:* BAGCHI, D. (ed.) *Sustained Energy for Enhanced Human Functions and Activity.* Academic Press.
HEINZ, A., MURRAY, G. K., SCHLAGENHAUF, F., STERZER, P., GRACE, A. A. & WALTZ, J. A. 2019. Towards a Unifying Cognitive, Neurophysiological, and Computational Neuroscience Account of Schizophrenia. *Schizophrenia Bulletin,* 45**,** 1092-1100.
HEO, S., DIERING, G. H., NA, C. H., NIRUJOGI, R. S., BACHMAN, J. L., PANDEY, A. & HUGANIR, R. L. 2018a. Identification of long-lived synaptic proteins by proteomic analysis of synaptosome protein turnover. *Proceedings of the National Academy of Sciences of the United States of America,* 115**,** E3827-E3836.
HEO, S., DIERING, G. H., NA, C. H., NIRUJOGI, R. S., BACHMAN, J. L., PANDEY, A. & HUGANIR, R. L. 2018b. Identification of long-lived synaptic proteins by proteomic analysis of synaptosome protein turnover. *Proceedings of the National Academy of Sciences,* 115**,** E3827-E3836.
HESS, D. T., MATSUMOTO, A., KIM, S.-O., MARSHALL, H. E. & STAMLER, J. S. 2005. Protein S-nitrosylation: purview and parameters. *Nature Reviews Molecular Cell Biology,* 6**,** 150-166.
HINKSON, I. V. & ELIAS, J. E. 2011. The dynamic state of protein turnover: It's about time. *Trends in Cell Biology,* 21**,** 293-303.
HIPP, M. S., KASTURI, P. & HARTL, F. U. 2019. The proteostasis network and its decline in ageing. *Nature Reviews Molecular Cell Biology,* 20**,** 421-435.
HO, G. P., SELVAKUMAR, B., MUKAI, J., HESTER, L. D., WANG, Y., GOGOS, J. A. & SNYDER, S. H. 2011. S-nitrosylation and S-palmitoylation reciprocally regulate synaptic targeting of PSD-95. *Neuron,* 71**,** 131-41.
HOELZEL, C. A. & ZHANG, X. 2020. Visualizing and Manipulating Biological Processes by Using HaloTag and SNAP-Tag Technologies. *Chembiochem : a European journal of chemical biology,* 21**,** 1935-1946.
HOLTMAAT, A. & SVOBODA, K. 2009. Experience-dependent structural synaptic plasticity in the mammalian brain. *Nature Reviews Neuroscience,* 10**,** 647-658.
HOLTMAAT, A., WILBRECHT, L., KNOTT, G. W., WELKER, E. & SVOBODA, K. 2006. Experience-dependent and cell-type-specific spine growth in the neocortex. *Nature,* 441**,** 979-983.
HOLTMAAT, A. J. G. D., TRACHTENBERG, J. T., WILBRECHT, L., SHEPHERD, G. M., ZHANG, X., KNOTT, G. W. & SVOBODA, K. 2005. Transient and Persistent Dendritic Spines in the Neocortex In Vivo. *Neuron,* 45**,** 279-291.

HOU, Y., DAN, X., BABBAR, M., WEI, Y., HASSELBALCH, S. G., CROTEAU, D. L. & BOHR, V. A. 2019. Ageing as a risk factor for neurodegenerative disease. *Nature Reviews Neurology,* 15**,** 565-581.

HRUSKA, M., HENDERSON, N. T., XIA, N. L., LE MARCHAND, S. J. & DALVA, M. B. 2015. Anchoring and synaptic stability of PSD-95 is driven by ephrin-B3. *Nature Neuroscience,* 18**,** 1594-1605.

HUANG, C.-M., BROWN, N. & HUANG, R. H. 1999. Age-related changes in the cerebellum: parallel fibers. *Brain Research,* 840**,** 148-152.

HUBEL, D. H. & WIESEL, T. N. 1970. The period of susceptibility to the physiological effects of unilateral eye closure in kittens. *The Journal of Physiology,* 206**,** 419-436.

HUGHES, B. G., FAN, X., CHO, W. J. & SCHULZ, R. 2014. MMP-2 is localized to the mitochondria-associated membrane of the heart. *American Journal of Physiology-Heart and Circulatory Physiology,* 306**,** H764-H770.

HUSI, H., WARD, M. A., CHOUDHARY, J. S., BLACKSTOCK, W. P. & GRANT, S. G. N. 2000. Proteomic analysis of NMDA receptor–adhesion protein signaling complexes. *Nature Neuroscience,* 3**,** 661-669.

IFRIM, M. F., WILLIAMS, K. R. & BASSELL, G. J. 2015. Single-Molecule Imaging of PSD-95 mRNA Translation in Dendrites and Its Dysregulation in a Mouse Model of Fragile X Syndrome. *The Journal of Neuroscience,* 35**,** 7116-7130.

INGASON, A., GIEGLING, I., HARTMANN, A. M., GENIUS, J., KONTE, B., FRIEDL, M., RIPKE, S., SULLIVAN, P. F., ST. CLAIR, D., COLLIER, D. A., O'DONOVAN, M. C., MIRNICS, K., RUJESCU, D. & SCHIZOPHRENIA WORKING GROUP OF THE PSYCHIATRIC GENOMICS, C. 2015. Expression analysis in a rat psychosis model identifies novel candidate genes validated in a large case–control sample of schizophrenia. *Translational Psychiatry,* 5**,** e656-e656.

INGVAR, M. C., MAEDER, P., SOKOLOFF, L. & SMITH, C. B. 1985. EFFECTS OF AGEING ON LOCAL RATES OF CEREBRAL PROTEIN SYNTHESIS IN SPRAGUE-DAWLEY RATS. *Brain,* 108**,** 155-170.

ISSHIKI, M., TANAKA, S., KURIU, T., TABUCHI, K., TAKUMI, T. & OKABE, S. 2014. Enhanced synapse remodelling as a common phenotype in mouse models of autism. *Nature Communications,* 5**,** 4742.

JACKSON, J. S., WITTON, J., JOHNSON, J. D., AHMED, Z., WARD, M., RANDALL, A. D., HUTTON, M. L., ISAAC, J. T., O'NEILL, M. J. & ASHBY, M. C. 2017. Altered Synapse Stability in the Early Stages of Tauopathy. *Cell Reports,* 18**,** 3063-3068.

JÄHNE, S., MIKULASCH, F., HEUER, H. G. H., TRUCKENBRODT, S., AGÜI-GONZALEZ, P., GREWE, K., VOGTS, A., RIZZOLI, S. O. & PRIESEMANN, V. 2021. Presynaptic activity and protein turnover are correlated at the single-synapse level. *Cell Reports,* 34**,** 108841.

JAY, D. G. 1988. Selective destruction of protein function by chromophore-assisted laser inactivation. *Proceedings of the National Academy of Sciences,* 85**,** 5454-5458.

JAYARAJ, G. G., HIPP, M. S. & HARTL, F. U. 2020. Functional Modules of the Proteostasis Network. *Cold Spring Harb Perspect Biol,* 12.

JENSEN, T. P., KOPACH, O., REYNOLDS, J. P., SAVTCHENKO, L. P. & RUSAKOV, D. A. 2021. Release probability increases towards distal dendrites boosting high-frequency signal transfer in the rodent hippocampus. *eLife,* 10**,** e62588.

JEYIFOUS, O., LIN, E. I., CHEN, X., ANTINONE, S. E., MASTRO, R., DRISDEL, R., REESE, T. S. & GREEN, W. N. 2016. Palmitoylation regulates glutamate receptor distributions in postsynaptic densities through control of PSD95 conformation and orientation. *Proceedings of the National Academy of Sciences,* 113**,** E8482.

JIANG, M., ASH, R. T., BAKER, S. A., SUTER, B., FERGUSON, A., PARK, J., RUDY, J., TORSKY, S. P., CHAO, H.-T., ZOGHBI, H. Y. & SMIRNAKIS, S. M. 2013. Dendritic Arborization and Spine Dynamics Are Abnormal in the Mouse Model of MECP2 Duplication Syndrome. *The Journal of Neuroscience,* 33**,** 19518.

JIANG, Y.-H., ARMSTRONG, D., ALBRECHT, U., ATKINS, C. M., NOEBELS, J. L., EICHELE, G., SWEATT, J. D. & BEAUDET, A. L. 1998. Mutation of the Angelman Ubiquitin Ligase in Mice Causes Increased Cytoplasmic p53 and Deficits of Contextual Learning and Long-Term Potentiation. *Neuron,* 21**,** 799-811.

JOHNSTON, C. A., WHITNEY, D. S., VOLKMAN, B. F., DOE, C. Q. & PREHODA, K. E. 2011. Conversion of the enzyme guanylate kinase into a mitotic-spindle orienting protein by a single mutation that inhibits GMP-induced closing. *Proceedings of the National Academy of Sciences,* 108**,** E973.

JOSEFSEN, L. B. & BOYLE, R. W. 2008. Photodynamic therapy and the development of metal-based photosensitisers. *Metal-based drugs,* 2008.

KIM, E., NAISBITT, S., HSUEH, Y.-P., RAO, A., ROTHSCHILD, A., CRAIG, A. M. & SHENG, M. 1997. GKAP, a novel synaptic protein that interacts with the guanylate kinase-like domain of the PSD-95/SAP90 family of channel clustering molecules. *The Journal of cell biology,* 136**,** 669-678.

KIM, E. & SHENG, M. 2004. PDZ domain proteins of synapses. *Nature Reviews Neuroscience,* 5**,** 771-781.

KIM, J. H., LIAO, D., LAU, L.-F. & HUGANIR, R. L. 1998. SynGAP: a Synaptic RasGAP that Associates with the PSD-95/SAP90 Protein Family. *Neuron,* 20**,** 683-691.

KIM, M. J., FUTAI, K., JO, J., HAYASHI, Y., CHO, K. & SHENG, M. 2007. Synaptic Accumulation of PSD-95 and Synaptic Function Regulated by Phosphorylation of Serine-295 of PSD-95. *Neuron,* 56**,** 488-502.

KIROV, G., POCKLINGTON, A. J., HOLMANS, P., IVANOV, D., IKEDA, M., RUDERFER, D., MORAN, J., CHAMBERT, K., TONCHEVA, D., GEORGIEVA, L., GROZEVA, D., FJODOROVA, M., WOLLERTON, R., REES, E., NIKOLOV, I., VAN DE LAGEMAAT, L. N., BAYÉS, À., FERNANDEZ, E., OLASON, P. I., BÖTTCHER, Y., KOMIYAMA, N. H., COLLINS, M. O., CHOUDHARY, J., STEFANSSON, K., STEFANSSON, H., GRANT, S. G. N., PURCELL, S., SKLAR, P.,

O'DONOVAN, M. C. & OWEN, M. J. 2012. De novo CNV analysis implicates specific abnormalities of postsynaptic signalling complexes in the pathogenesis of schizophrenia. *Molecular Psychiatry,* 17**,** 142-153.

KITAMURA, T., SAITOH, Y., TAKASHIMA, N., MURAYAMA, A., NIIBORI, Y., AGETA, H., SEKIGUCHI, M., SUGIYAMA, H. & INOKUCHI, K. 2009. Adult neurogenesis modulates the hippocampus-dependent period of associative fear memory. *Cell,* 139**,** 814-27.

KOMIYAMA, N. H., WATABE, A. M., CARLISLE, H. J., PORTER, K., CHARLESWORTH, P., MONTI, J., STRATHDEE, D. J., O'CARROLL, C. M., MARTIN, S. J., MORRIS, R. G., O'DELL, T. J. & GRANT, S. G. 2002. SynGAP regulates ERK/MAPK signaling, synaptic plasticity, and learning in the complex with postsynaptic density 95 and NMDA receptor. *J Neurosci,* 22**,** 9721-32.

KORNAU, H. C., SCHENKER, L. T., KENNEDY, M. B. & SEEBURG, P. H. 1995. Domain interaction between NMDA receptor subunits and the postsynaptic density protein PSD-95. *Science,* 269**,** 1737.

KRAPIVINSKY, G., MEDINA, I., KRAPIVINSKY, L., GAPON, S. & CLAPHAM, D. E. 2004. SynGAP-MUPP1-CaMKII Synaptic Complexes Regulate p38 MAP Kinase Activity and NMDA Receptor- Dependent Synaptic AMPA Receptor Potentiation. *Neuron,* 43**,** 563-574.

KRATSCHKE, M. M. Investigating PSD-95 turnover at the synapse using the HaloTag technology. 2018.

KRUSCHKE, J. K. 2013. Bayesian estimation supersedes the t test. *J Exp Psychol Gen,* 142**,** 573-603.

KRUSE, S. E., KARUNADHARMA, P. P., BASISTY, N., JOHNSON, R., BEYER, R. P., MACCOSS, M. J., RABINOVITCH, P. S. & MARCINEK, D. J. 2016. Age modifies respiratory complex I and protein homeostasis in a muscle type-specific manner. *Aging Cell,* 15**,** 89-99.

KUHLENDAHL, S., SPANGENBERG, O., KONRAD, M., KIM, E. & GARNER, C. C. 1998. Functional analysis of the guanylate kinase-like domain in the synapse-associated protein SAP97. *European Journal of Biochemistry,* 252**,** 305-313.

KURIU, T., INOUE, A., BITO, H., SOBUE, K. & OKABE, S. 2006. Differential Control of Postsynaptic Density Scaffolds via Actin-Dependent and -Independent Mechanisms. *The Journal of Neuroscience,* 26**,** 7693-7706.

LACKEY, E. P., HECK, D. H. & SILLITOE, R. V. 2018. Recent advances in understanding the mechanisms of cerebellar granule cell development and function and their contribution to behavior. *F1000Research,* 7**,** F1000 Faculty Rev-1142.

LAI, C. S. W., FRANKE, T. F. & GAN, W.-B. 2012. Opposite effects of fear conditioning and extinction on dendritic spine remodelling. *Nature,* 483**,** 87-91.

LAJTHA, A. 1959. AMINO ACID AND PROTEIN METABOLISM OF THE BRAIN—V. *Journal of Neurochemistry,* 3**,** 358-365.

LAJTHA, A., LATZKOVITS, L. & TOTH, J. 1976. Comparison of turnover rates of proteins of the brain, liver and kidney in mouse in vivo following long

term labeling. *Biochimica et Biophysica Acta (BBA) - Nucleic Acids and Protein Synthesis,* 425**,** 511-520.
LAMBERT, J. T., HILL, T. C., PARK, D. K., CULP, J. H. & ZITO, K. 2017. Protracted and asynchronous accumulation of PSD95-family MAGUKs during maturation of nascent dendritic spines. *Developmental neurobiology,* 77**,** 1161-1174.
LANG, C., SCHULZE, J., MENDEL, R.-R. & HÄNSCH, R. 2006. HaloTag™: a new versatile reporter gene system in plant cells. *Journal of Experimental Botany,* 57**,** 2985-2992.
LELIEVELD, S. H., REIJNDERS, M. R. F., PFUNDT, R., YNTEMA, H. G., KAMSTEEG, E.-J., DE VRIES, P., DE VRIES, B. B. A., WILLEMSEN, M. H., KLEEFSTRA, T., LÖHNER, K., VREEBURG, M., STEVENS, S. J. C., VAN DER BURGT, I., BONGERS, E. M. H. F., STEGMANN, A. P. A., RUMP, P., RINNE, T., NELEN, M. R., VELTMAN, J. A., VISSERS, L. E. L. M., BRUNNER, H. G. & GILISSEN, C. 2016. Meta-analysis of 2,104 trios provides support for 10 new genes for intellectual disability. *Nature Neuroscience,* 19**,** 1194-1196.
LENDVAI, B., STERN, E. A., CHEN, B. & SVOBODA, K. 2000. Experience-dependent plasticity of dendritic spines in the developing rat barrel cortex in vivo. *Nature,* 404**,** 876-881.
LEPORE, A., TAYLOR, H., LANDGRAF, D., OKUMUS, B., JARAMILLO-RIVERI, S., MCLAREN, L., BAKSHI, S., PAULSSON, J. & KAROUI, M. E. 2019. Quantification of very low-abundant proteins in bacteria using the HaloTag and epi-fluorescence microscopy. *Scientific Reports,* 9**,** 7902.
LI, Z., KRIPPENDORFF, B.-F. & SHAH, D. K. 2017. Influence of Molecular size on the clearance of antibody fragments. *Pharmaceutical research,* 34**,** 2131-2141.
LIANG, V., ULLRICH, M., LAM, H., CHEW, Y. L., BANISTER, S., SONG, X., ZAW, T., KASSIOU, M., GÖTZ, J. & NICHOLAS, H. R. 2014. Altered proteostasis in aging and heat shock response in C. elegans revealed by analysis of the global and de novo synthesized proteome. *Cellular and Molecular Life Sciences,* 71**,** 3339-3361.
LINDEN, K. G., LIAO, J. C. & JAY, D. G. 1992. Spatial specificity of chromophore assisted laser inactivation of protein function. *Biophys J,* 61**,** 956-62.
LISS, V., BARLAG, B., NIETSCHKE, M. & HENSEL, M. 2015. Self-labelling enzymes as universal tags for fluorescence microscopy, super-resolution microscopy and electron microscopy. *Scientific Reports,* 5**,** 17740.
LOEWENSTEIN, Y., YANOVER, U. & RUMPEL, S. 2015. Predicting the Dynamics of Network Connectivity in the Neocortex. *The Journal of Neuroscience,* 35**,** 12535.
LOS, G. V., ENCELL, L. P., MCDOUGALL, M. G., HARTZELL, D. D., KARASSINA, N., ZIMPRICH, C., WOOD, M. G., LEARISH, R., OHANA, R. F., URH, M., SIMPSON, D., MENDEZ, J., ZIMMERMAN, K., OTTO, P., VIDUGIRIS, G., ZHU, J., DARZINS, A., KLAUBERT, D. H., BULLEIT, R. F. & WOOD, K. V. 2008a. HaloTag: a novel protein

labeling technology for cell imaging and protein analysis. *ACS Chem Biol,* 3**,** 373-82.
LOS, G. V., ENCELL, L. P., MCDOUGALL, M. G., HARTZELL, D. D., KARASSINA, N., ZIMPRICH, C., WOOD, M. G., LEARISH, R., OHANA, R. F., URH, M., SIMPSON, D., MENDEZ, J., ZIMMERMAN, K., OTTO, P., VIDUGIRIS, G., ZHU, J., DARZINS, A., KLAUBERT, D. H., BULLEIT, R. F. & WOOD, K. V. 2008b. HaloTag: A Novel Protein Labeling Technology for Cell Imaging and Protein Analysis. *ACS Chemical Biology,* 3**,** 373-382.
LOUROS, S. R. & OSTERWEIL, E. K. 2016. Perturbed proteostasis in autism spectrum disorders. *Journal of Neurochemistry,* 139**,** 1081-1092.
LUKINAVIČIUS, G., UMEZAWA, K., OLIVIER, N., HONIGMANN, A., YANG, G., PLASS, T., MUELLER, V., REYMOND, L., CORRÊA, I. R., JR., LUO, Z. G., SCHULTZ, C., LEMKE, E. A., HEPPENSTALL, P., EGGELING, C., MANLEY, S. & JOHNSSON, K. 2013. A near-infrared fluorophore for live-cell super-resolution microscopy of cellular proteins. *Nat Chem,* 5**,** 132-9.
MA, L., QIAO, Q., TSAI, J.-W., YANG, G., LI, W. & GAN, W.-B. 2016. Experience-dependent plasticity of dendritic spines of layer 2/3 pyramidal neurons in the mouse cortex. *Developmental Neurobiology,* 76**,** 277-286.
MA, Q., RUAN, H., PENG, L., ZHANG, M., GACK, M. U. & YAO, W.-D. 2017. Proteasome-independent polyubiquitin linkage regulates synapse scaffolding, efficacy, and plasticity. *Proceedings of the National Academy of Sciences,* 114**,** E8760.
MACGILLAVRY, HAROLD D., SONG, Y., RAGHAVACHARI, S. & BLANPIED, THOMAS A. 2013. Nanoscale Scaffolding Domains within the Postsynaptic Density Concentrate Synaptic AMPA Receptors. *Neuron,* 78**,** 615-622.
MAGEE, J. C. & COOK, E. P. 2000. Somatic EPSP amplitude is independent of synapse location in hippocampal pyramidal neurons. *Nat Neurosci,* 3**,** 895-903.
MALLYA, A. P., WANG, H.-D., LEE, H. N. R. & DEUTCH, A. Y. 2019. Microglial Pruning of Synapses in the Prefrontal Cortex During Adolescence. *Cerebral Cortex,* 29**,** 1634-1643.
MARR, D. & BRINDLEY, G. S. 1971. Simple memory: a theory for archicortex. *Philosophical Transactions of the Royal Society of London. B, Biological Sciences,* 262**,** 23-81.
MARTIN-PEREZ, M. & VILLÉN, J. 2017. Determinants and Regulation of Protein Turnover in Yeast. *Cell Systems,* 5**,** 283-294.e5.
MASCH, J.-M., STEFFENS, H., FISCHER, J., ENGELHARDT, J., HUBRICH, J., KELLER-FINDEISEN, J., D'ESTE, E., URBAN, N. T., GRANT, S. G. N., SAHL, S. J., KAMIN, D. & HELL, S. W. 2018. Robust nanoscopy of a synaptic protein in living mice by organic-fluorophore labeling. *Proceedings of the National Academy of Sciences,* 115**,** E8047.
MATHIESON, T., FRANKEN, H., KOSINSKI, J., KURZAWA, N., ZINN, N., SWEETMAN, G., POECKEL, D., RATNU, V. S., SCHRAMM, M., BECHER, I., STEIDEL, M., NOH, K.-M., BERGAMINI, G., BECK, M.,

BANTSCHEFF, M. & SAVITSKI, M. M. 2018. Systematic analysis of protein turnover in primary cells. *Nature Communications,* 9**,** 689.
MAYS, P. K., MCANULTY, R. J. & LAURENT, G. J. 1991. Age-related changes in rates of protein synthesis and degradation in rat tissues. *Mechanisms of Ageing and Development,* 59**,** 229-241.
MCGEE, A. W., DAKOJI, S. R., OLSEN, O., BREDT, D. S., LIM, W. A. & PREHODA, K. E. 2001a. Structure of the SH3-Guanylate Kinase Module from PSD-95 Suggests a Mechanism for Regulated Assembly of MAGUK Scaffolding Proteins. *Molecular Cell,* 8**,** 1291-1301.
MCGEE, A. W., TOPINKA, J. R., HASHIMOTO, K., PETRALIA, R. S., KAKIZAWA, S., KAUER, F. W., AGUILERA-MORENO, A., WENTHOLD, R. J., KANO, M. & BREDT, D. S. 2001b. PSD-93 knock-out mice reveal that neuronal MAGUKs are not required for development or function of parallel fiber synapses in cerebellum. *The Journal of neuroscience : the official journal of the Society for Neuroscience,* 21**,** 3085-3091.
MENON, V., MUSIAL, TIMOTHY F., LIU, A., KATZ, Y., KATH, WILLIAM L., SPRUSTON, N. & NICHOLSON, DANIEL A. 2013. Balanced Synaptic Impact via Distance-Dependent Synapse Distribution and Complementary Expression of AMPARs and NMDARs in Hippocampal Dendrites. *Neuron,* 80**,** 1451-1463.
MERRILL, R. A., SONG, J., KEPHART, R. A., KLOMP, A. J., NOACK, C. E. & STRACK, S. 2019. A robust and economical pulse-chase protocol to measure the turnover of HaloTag fusion proteins. *Journal of Biological Chemistry,* 294**,** 16164-16171.
MIGAUD, M., CHARLESWORTH, P., DEMPSTER, M., WEBSTER, L. C., WATABE, A. M., MAKHINSON, M., HE, Y., RAMSAY, M. F., MORRIS, R. G., MORRISON, J. H., O'DELL, T. J. & GRANT, S. G. 1998. Enhanced long-term potentiation and impaired learning in mice with mutant postsynaptic density-95 protein. *Nature,* 396**,** 433-9.
MILLER, S., LESK, A. M., JANIN, J. & CHOTHIA, C. 1987. The accessible surface area and stability of oligomeric proteins. *Nature,* 328**,** 834-836.
MISHRA, A. & JANA, N. R. 2008. Regulation of turnover of tumor suppressor p53 and cell growth by E6-AP, a ubiquitin protein ligase mutated in Angelman mental retardation syndrome. *Cell Mol Life Sci,* 65**,** 656-66.
MOCZULSKA, K. E., TINTER-THIEDE, J., PETER, M., USHAKOVA, L., WERNLE, T., BATHELLIER, B. & RUMPEL, S. 2013. Dynamics of dendritic spines in the mouse auditory cortex during memory formation and memory recall. *Proceedings of the National Academy of Sciences,* 110**,** 18315.
MOFFITT, J. R., HAO, J., BAMBAH-MUKKU, D., LU, T., DULAC, C. & ZHUANG, X. 2016. High-performance multiplexed fluorescence in situ hybridization in culture and tissue with matrix imprinting and clearing. *Proceedings of the National Academy of Sciences,* 113**,** 14456.
MONGILLO, G., RUMPEL, S. & LOEWENSTEIN, Y. 2017. Intrinsic volatility of synaptic connections — a challenge to the synaptic trace theory of memory. *Current Opinion in Neurobiology,* 46**,** 7-13.

MORABITO, M. A., SHENG, M. & TSAI, L.-H. 2004. Cyclin-Dependent Kinase 5 Phosphorylates the N-Terminal Domain of the Postsynaptic Density Protein PSD-95 in Neurons. *The Journal of Neuroscience,* 24**,** 865.

MOSTANY, R., ANSTEY, J. E., CRUMP, K. L., MACO, B., KNOTT, G. & PORTERA-CAILLIAU, C. 2013. Altered Synaptic Dynamics during Normal Brain Aging. *The Journal of Neuroscience,* 33**,** 4094.

MOWER, G. D. 1991. The effect of dark rearing on the time course of the critical period in cat visual cortex. *Brain Res Dev Brain Res,* 58**,** 151-8.

MUDDASHETTY, R. S., KELIĆ, S., GROSS, C., XU, M. & BASSELL, G. J. 2007. Dysregulated Metabotropic Glutamate Receptor-Dependent Translation of AMPA Receptor and Postsynaptic Density-95 mRNAs at Synapses in a Mouse Model of Fragile X Syndrome. *The Journal of Neuroscience,* 27**,** 5338.

MUMBY, S. M. 1997. Reversible palmitoylation of signaling proteins. *Current Opinion in Cell Biology,* 9**,** 148-154.

MURMAN, D. L. 2015. The Impact of Age on Cognition. *Seminars in hearing,* 36**,** 111-121.

MURMU, R. P., LI, W., HOLTMAAT, A. & LI, J.-Y. 2013. Dendritic Spine Instability Leads to Progressive Neocortical Spine Loss in a Mouse Model of Huntington's Disease. *The Journal of Neuroscience,* 33**,** 12997.

MURTHY, V. N., SCHIKORSKI, T., STEVENS, C. F. & ZHU, Y. 2001. Inactivity produces increases in neurotransmitter release and synapse size. *Neuron,* 32**,** 673-82.

NAGAYAMA, S., HOMMA, R. & IMAMURA, F. 2014. Neuronal organization of olfactory bulb circuits. *Frontiers in Neural Circuits,* 8.

NAIR, D., HOSY, E., PETERSEN, J. D., CONSTALS, A., GIANNONE, G., CHOQUET, D. & SIBARITA, J.-B. 2013. Super-Resolution Imaging Reveals That AMPA Receptors Inside Synapses Are Dynamically Organized in Nanodomains Regulated by PSD95. *The Journal of Neuroscience,* 33**,** 13204.

NAKAGAWA, T., ENGLER, J. A. & SHENG, M. 2004. The dynamic turnover and functional roles of α-actinin in dendritic spines. *Neuropharmacology,* 47**,** 734-745.

NEEDHAM, P. G., GUERRIERO, C. J. & BRODSKY, J. L. 2019. Chaperoning Endoplasmic Reticulum-Associated Degradation (ERAD) and Protein Conformational Diseases. *Cold Spring Harb Perspect Biol,* 11.

NELSON, C. D., KIM, M. J., HSIN, H., CHEN, Y. & SHENG, M. 2013. Phosphorylation of threonine-19 of PSD-95 by GSK-3β is required for PSD-95 mobilization and long-term depression. *The Journal of neuroscience : the official journal of the Society for Neuroscience,* 33**,** 12122-12135.

NICHOLSON, D. A., TRANA, R., KATZ, Y., KATH, W. L., SPRUSTON, N. & GEINISMAN, Y. 2006. Distance-dependent differences in synapse number and AMPA receptor expression in hippocampal CA1 pyramidal neurons. *Neuron,* 50**,** 431-42.

NIETHAMMER, M., KIM, E. & SHENG, M. 1996. Interaction between the C terminus of NMDA receptor subunits and multiple members of the PSD-

95 family of membrane-associated guanylate kinases. *The Journal of Neuroscience,* 16**,** 2157.
NITHIANANTHARAJAH, J., KOMIYAMA, N. H., MCKECHANIE, A., JOHNSTONE, M., BLACKWOOD, D. H., ST CLAIR, D., EMES, R. D., VAN DE LAGEMAAT, L. N., SAKSIDA, L. M. & BUSSEY, T. J. 2013. Synaptic scaffold evolution generated components of vertebrate cognitive complexity. *Nature neuroscience,* 16**,** 16-24.
NOWACKA, A., BORCZYK, M., SALAMIAN, A., WÓJTOWICZ, T., WŁODARCZYK, J. & RADWANSKA, K. 2020. PSD-95 Serine 73 phosphorylation is not required for induction of NMDA-LTD. *Scientific Reports,* 10**,** 2054.
OBERMEIER, B., DANEMAN, R. & RANSOHOFF, R. M. 2013. Development, maintenance and disruption of the blood-brain barrier. *Nature Medicine,* 19**,** 1584-1596.
OGLE, J. M. & RAMAKRISHNAN, V. 2005. Structural insights into translational fidelity. *Annu. Rev. Biochem.,* 74**,** 129-177.
OSTERWEIL, E. K., KRUEGER, D. D., REINHOLD, K. & BEAR, M. F. 2010. Hypersensitivity to mGluR5 and ERK1/2 leads to excessive protein synthesis in the hippocampus of a mouse model of fragile X syndrome. *Journal of Neuroscience,* 30**,** 15616-15627.
OSTROFF, L. E., FIALA, J. C., ALLWARDT, B. & HARRIS, K. M. 2002. Polyribosomes Redistribute from Dendritic Shafts into Spines with Enlarged Synapses during LTP in Developing Rat Hippocampal Slices. *Neuron,* 35**,** 535-545.
OSTROFF, L. E., WATSON, D. J., CAO, G., PARKER, P. H., SMITH, H. & HARRIS, K. M. 2018. Shifting patterns of polyribosome accumulation at synapses over the course of hippocampal long-term potentiation. *Hippocampus,* 28**,** 416-430.
OZKAN, EMIN D., CRESON, THOMAS K., KRAMÁR, ENIKÖ A., ROJAS, C., SEESE, RON R., BABYAN, ALEX H., SHI, Y., LUCERO, R., XU, X., NOEBELS, JEFFREY L., MILLER, COURTNEY A., LYNCH, G. & RUMBAUGH, G. 2014. Reduced Cognition in Syngap1 Mutants Is Caused by Isolated Damage within Developing Forebrain Excitatory Neurons. *Neuron,* 82**,** 1317-1333.
PADMASHRI, R., REINER, B. C., SURESH, A., SPARTZ, E. & DUNAEVSKY, A. 2013. Altered Structural and Functional Synaptic Plasticity with Motor Skill Learning in a Mouse Model of Fragile X Syndrome. *The Journal of Neuroscience,* 33**,** 19715.
PAN, F., ALDRIDGE, G. M., GREENOUGH, W. T. & GAN, W.-B. 2010. Dendritic spine instability and insensitivity to modulation by sensory experience in a mouse model of fragile X syndrome. *Proceedings of the National Academy of Sciences,* 107**,** 17768.
PANDEY, K., YU, X.-W., STEINMETZ, A. & ALBERINI, C. M. 2021. Autophagy coupled to translation is required for long-term memory. *Autophagy,* 17**,** 1614-1635.
PAOLICELLI, R. C., BOLASCO, G., PAGANI, F., MAGGI, L., SCIANNI, M., PANZANELLI, P., GIUSTETTO, M., FERREIRA, T. A., GUIDUCCI, E., DUMAS, L., RAGOZZINO, D. & GROSS, C. T. 2011. Synaptic Pruning

by Microglia Is Necessary for Normal Brain Development. *Science,* 333**,** 1456.
PARK, H. & KAANG, B. K. 2019. Balanced actions of protein synthesis and degradation in memory formation. *Learn Mem,* 26**,** 299-306.
PATTERSON, G., DAY, R. N. & PISTON, D. 2001. Fluorescent protein spectra. *Journal of Cell Science,* 114**,** 837-838.
PEDERSEN, S. W., ALBERTSEN, L., MORAN, G. E., LEVESQUE, B., PEDERSEN, S. B., BARTELS, L., WAPENAAR, H., YE, F., ZHANG, M., BOWEN, M. E. & STRØMGAARD, K. 2017. Site-Specific Phosphorylation of PSD-95 PDZ Domains Reveals Fine-Tuned Regulation of Protein–Protein Interactions. *ACS Chemical Biology,* 12**,** 2313-2323.
PEREZ-PERRI, J. I., DENGLER, V. L., AUDETAT, K. A., PANDEY, A., BONNER, E. A., URH, M., MENDEZ, J., DANIELS, D. L., WAPPNER, P., GALBRAITH, M. D. & ESPINOSA, J. M. 2016. The TIP60 Complex Is a Conserved Coactivator of HIF1A. *Cell Reports,* 16**,** 37-47.
PFEIFFER, T., POLL, S., BANCELIN, S., ANGIBAUD, J., INAVALLI, V. V. G. K., KEPPLER, K., MITTAG, M., FUHRMANN, M. & NÄGERL, U. V. 2018. Chronic 2P-STED imaging reveals high turnover of dendritic spines in the hippocampus in vivo. *eLife,* 7**,** e34700.
POO, M.-M., PIGNATELLI, M., RYAN, T. J., TONEGAWA, S., BONHOEFFER, T., MARTIN, K. C., RUDENKO, A., TSAI, L.-H., TSIEN, R. W., FISHELL, G., MULLINS, C., GONÇALVES, J. T., SHTRAHMAN, M., JOHNSTON, S. T., GAGE, F. H., DAN, Y., LONG, J., BUZSÁKI, G. & STEVENS, C. 2016. What is memory? The present state of the engram. *BMC Biology,* 14**,** 40.
PORTER, K., KOMIYAMA, N. H., VITALIS, T., KIND, P. C. & GRANT, S. G. N. 2005. Differential expression of two NMDA receptor interacting proteins, PSD-95 and SynGAP during mouse development. *European Journal of Neuroscience,* 21**,** 351-362.
POSTEMA, M. C., VAN ROOIJ, D., ANAGNOSTOU, E., ARANGO, C., AUZIAS, G., BEHRMANN, M., FILHO, G. B., CALDERONI, S., CALVO, R., DALY, E., DERUELLE, C., DI MARTINO, A., DINSTEIN, I., DURAN, F. L. S., DURSTON, S., ECKER, C., EHRLICH, S., FAIR, D., FEDOR, J., FENG, X., FITZGERALD, J., FLORIS, D. L., FREITAG, C. M., GALLAGHER, L., GLAHN, D. C., GORI, I., HAAR, S., HOEKSTRA, L., JAHANSHAD, N., JALBRZIKOWSKI, M., JANSSEN, J., KING, J. A., KONG, X. Z., LAZARO, L., LERCH, J. P., LUNA, B., MARTINHO, M. M., MCGRATH, J., MEDLAND, S. E., MURATORI, F., MURPHY, C. M., MURPHY, D. G. M., O'HEARN, K., ORANJE, B., PARELLADA, M., PUIG, O., RETICO, A., ROSA, P., RUBIA, K., SHOOK, D., TAYLOR, M. J., TOSETTI, M., WALLACE, G. L., ZHOU, F., THOMPSON, P. M., FISHER, S. E., BUITELAAR, J. K. & FRANCKS, C. 2019. Altered structural brain asymmetry in autism spectrum disorder in a study of 54 datasets. *Nature Communications,* 10**,** 4958.
PRICE, J. C., GUAN, S., BURLINGAME, A., PRUSINER, S. B. & GHAEMMAGHAMI, S. 2010. Analysis of proteome dynamics in the

mouse brain. *Proceedings of the National Academy of Sciences,* 107**,** 14508-14513.

PURCELL, S. M., MORAN, J. L., FROMER, M., RUDERFER, D., SOLOVIEFF, N., ROUSSOS, P., O'DUSHLAINE, C., CHAMBERT, K., BERGEN, S. E., KÄHLER, A., DUNCAN, L., STAHL, E., GENOVESE, G., FERNÁNDEZ, E., COLLINS, M. O., KOMIYAMA, N. H., CHOUDHARY, J. S., MAGNUSSON, P. K., BANKS, E., SHAKIR, K., GARIMELLA, K., FENNELL, T., DEPRISTO, M., GRANT, S. G., HAGGARTY, S. J., GABRIEL, S., SCOLNICK, E. M., LANDER, E. S., HULTMAN, C. M., SULLIVAN, P. F., MCCARROLL, S. A. & SKLAR, P. 2014. A polygenic burden of rare disruptive mutations in schizophrenia. *Nature,* 506**,** 185-90.

QIN, M., KANG, J., BURLIN, T. V., JIANG, C. & SMITH, C. B. 2005. Postadolescent changes in regional cerebral protein synthesis: an in vivo study in the FMR1 null mouse. *Journal of Neuroscience,* 25**,** 5087-5095.

QUACKENBUSH, L. J., NGO, H. & PENTNEY, R. J. 1990. Evidence for nonrandom regression of dendrites of Purkinje neurons during aging. *Neurobiology of aging,* 11**,** 111-115.

RADEMACHER, N., KUROPKA, B., KUNDE, S.-A., WAHL, M. C., FREUND, C. & SHOICHET, S. A. 2019. Intramolecular domain dynamics regulate synaptic MAGUK protein interactions. *eLife,* 8**,** e41299.

RANGARAJU, V., TOM DIECK, S. & SCHUMAN, E. M. 2017. Local translation in neuronal compartments: how local is local? *EMBO reports,* 18**,** 693-711.

RATNER, S., RITTENBERG, D., KESTON, A. S. & SCHOENHEIMER, R. 1940. Studies in protein metabolism. 14. The chemical interaction of dietary glycine and body proteins in rats. *Journal of Biological Chemistry,* 134**,** 665-676.

RECHSTEINER, M. & ROGERS, S. W. 1996. PEST sequences and regulation by proteolysis. *Trends in Biochemical Sciences,* 21**,** 267-271.

REGGIANI, C., COPPENS, S., SEKHARA, T., DIMOV, I., PICHON, B., LUFIN, N., ADDOR, M.-C., BELLIGNI, E. F., DIGILIO, M. C., FALETRA, F., FERRERO, G. B., GERARD, M., ISIDOR, B., JOSS, S., NIEL-BÜTSCHI, F., PERRONE, M. D., PETIT, F., RENIERI, A., ROMANA, S., TOPA, A., VERMEESCH, J. R., LENAERTS, T., CASIMIR, G., ABRAMOWICZ, M., BONTEMPI, G., VILAIN, C., DECONINCK, N. & SMITS, G. 2017. Novel promoters and coding first exons in DLG2 linked to developmental disorders and intellectual disability. *Genome Medicine,* 9**,** 67.

RICHARDS, B. A. & FRANKLAND, P. W. 2017. The Persistence and Transience of Memory. *Neuron,* 94**,** 1071-1084.

RITCHEY, M., MONTCHAL, M. E., YONELINAS, A. P. & RANGANATH, C. 2015. Delay-dependent contributions of medial temporal lobe regions to episodic memory retrieval. *eLife,* 4**,** e05025.

RITTENBERG, D. & SCHOENHEIMER, R. 1937. Deuterium as an indicator in the study of intermediary metabolism. 11. Further studies on the biological uptake of deuterium into organic substances, with special

reference to fat and cholesterol formation. *Journal of Biological Chemistry,* 121**,** 235-253.
ROSS, A. B., LANGER, J. D. & JOVANOVIC, M. 2021. Proteome Turnover in the Spotlight: Approaches, Applications, and Perspectives. *Molecular & Cellular Proteomics,* 20**,** 100016.
ROY, M., SOROKINA, O., MCLEAN, C., TAPIA-GONZÁLEZ, S., DEFELIPE, J., ARMSTRONG, J. D. & GRANT, S. G. N. 2018. Regional Diversity in the Postsynaptic Proteome of the Mouse Brain. *Proteomes,* 6.
RUZZO, E. K., PÉREZ-CANO, L., JUNG, J.-Y., WANG, L.-K., KASHEF-HAGHIGHI, D., HARTL, C., SINGH, C., XU, J., HOEKSTRA, J. N., LEVENTHAL, O., LEPPÄ, V. M., GANDAL, M. J., PASKOV, K., STOCKHAM, N., POLIOUDAKIS, D., LOWE, J. K., PROBER, D. A., GESCHWIND, D. H. & WALL, D. P. 2019. Inherited and De Novo Genetic Risk for Autism Impacts Shared Networks. *Cell,* 178**,** 850-866.e26.
SAKAI, J. 2020. Core Concept: How synaptic pruning shapes neural wiring during development and, possibly, in disease. *Proceedings of the National Academy of Sciences,* 117**,** 16096.
SANS, N., PETRALIA, R. S., WANG, Y. X., BLAHOS, J., 2ND, HELL, J. W. & WENTHOLD, R. J. 2000. A developmental change in NMDA receptor-associated proteins at hippocampal synapses. *J Neurosci,* 20**,** 1260-71.
SANTRA, M., DILL, K. A. & DE GRAFF, A. M. R. 2019. Proteostasis collapse is a driver of cell aging and death. *Proceedings of the National Academy of Sciences,* 116**,** 22173.
SCHANZENBÄCHER, C. T., LANGER, J. D. & SCHUMAN, E. M. 2018. Time- and polarity-dependent proteomic changes associated with homeostatic scaling at central synapses. *eLife,* 7**,** e33322.
SCHANZENBÄCHER, CHRISTOPH T., SAMBANDAN, S., LANGER, JULIAN D. & SCHUMAN, ERIN M. 2016. Nascent Proteome Remodeling following Homeostatic Scaling at Hippocampal Synapses. *Neuron,* 92**,** 358-371.
SCHIKORSKI, T. & STEVENS, C. F. 1997. Quantitative ultrastructural analysis of hippocampal excitatory synapses. *J Neurosci,* 17**,** 5858-67.
SCHIMKE, R. T. & DOYLE, D. 1970. Control of Enzyme Levels in Animal Tissues. *Annual Review of Biochemistry,* 39**,** 929-976.
SCHINDELIN, J., ARGANDA-CARRERAS, I., FRISE, E., KAYNIG, V., LONGAIR, M., PIETZSCH, T., PREIBISCH, S., RUEDEN, C., SAALFELD, S., SCHMID, B., TINEVEZ, J.-Y., WHITE, D. J., HARTENSTEIN, V., ELICEIRI, K., TOMANCAK, P. & CARDONA, A. 2012. Fiji: an open-source platform for biological-image analysis. *Nature Methods,* 9**,** 676-682.
SCHNEIDER, C. A., RASBAND, W. S. & ELICEIRI, K. W. 2012. NIH Image to ImageJ: 25 years of image analysis. *Nature Methods,* 9**,** 671-675.
SCHNELL, E., SIZEMORE, M., KARIMZADEGAN, S., CHEN, L., BREDT, D. S. & NICOLL, R. A. 2002. Direct interactions between PSD-95 and stargazin control synaptic AMPA receptor number. *Proceedings of the National Academy of Sciences,* 99**,** 13902.

SCHOENHEIMER, R. 1942. The dynamic state of body constituents. *The Dynamic State of Body Constituents.*

SCHUBERT, U., ANTON, L. C., GIBBS, J., NORBURY, C. C., YEWDELL, J. W. & BENNINK, J. R. 2000. Rapid degradation of a large fraction of newly synthesized proteins by proteasomes. *Nature,* 404**,** 770-774.

SEATON, G., HODGES, G., DE HAAN, A., GREWAL, A., PANDEY, A., KASAI, H. & FOX, K. 2020. Dual-Component Structural Plasticity Mediated by αCaMKII Autophosphorylation on Basal Dendrites of Cortical Layer 2/3 Neurones. *The Journal of Neuroscience,* 40**,** 2228-2245.

SEDERBERG, T. W. & PARRY, S. R. 1986. Free-form deformation of solid geometric models. *SIGGRAPH Comput. Graph.,* 20**,** 151–160.

SHA, Z., BRILL, L. M., CABRERA, R., KLEIFELD, O., SCHELIGA, J. S., GLICKMAN, M. H., CHANG, E. C. & WOLF, D. A. 2009. The eIF3 Interactome Reveals the Translasome, a Supercomplex Linking Protein Synthesis and Degradation Machineries. *Molecular Cell,* 36**,** 141-152.

SHARMA, K., FONG, D. K. & CRAIG, A. M. 2006. Postsynaptic protein mobility in dendritic spines: Long-term regulation by synaptic NMDA receptor activation. *Molecular and Cellular Neuroscience,* 31**,** 702-712.

SIEGEL, G. J. 1999. Basic neurochemistry: molecular, cellular and medical aspects.

SILLITOE, R. V. & JOYNER, A. L. 2007. Morphology, Molecular Codes, and Circuitry Produce the Three-Dimensional Complexity of the Cerebellum. *Annual Review of Cell and Developmental Biology,* 23**,** 549-577.

SOTO, C. & PRITZKOW, S. 2018. Protein misfolding, aggregation, and conformational strains in neurodegenerative diseases. *Nature Neuroscience,* 21**,** 1332-1340.

SOUKUP, S.-F., VANHAUWAERT, R. & VERSTREKEN, P. 2018. Parkinson's disease: convergence on synaptic homeostasis. *The EMBO Journal,* 37**,** e98960.

SPIRES-JONES, T. L., MEYER-LUEHMANN, M., OSETEK, J. D., JONES, P. B., STERN, E. A., BACSKAI, B. J. & HYMAN, B. T. 2007. Impaired Spine Stability Underlies Plaque-Related Spine Loss in an Alzheimer's Disease Mouse Model. *The American Journal of Pathology,* 171**,** 1304-1311.

SQUIRE, L. R. & BAYLEY, P. J. 2007. The neuroscience of remote memory. *Curr Opin Neurobiol,* 17**,** 185-96.

STEINER, P., HIGLEY, M. J., XU, W., CZERVIONKE, B. L., MALENKA, R. C. & SABATINI, B. L. 2008. Destabilization of the postsynaptic density by PSD-95 serine 73 phosphorylation inhibits spine growth and synaptic plasticity. *Neuron,* 60**,** 788-802.

STESSMAN, H. A., XIONG, B., COE, B. P., WANG, T., HOEKZEMA, K., FENCKOVA, M., KVARNUNG, M., GERDTS, J., TRINH, S. & COSEMANS, N. 2017. Targeted sequencing identifies 91 neurodevelopmental-disorder risk genes with autism and developmental-disability biases. *Nature genetics,* 49**,** 515-526.

STEWARD, O. & FASS, B. 1983. Polyribosomes associated with dendritic spines in the denervated dentate gyrus: evidence for local regulation of protein synthesis during reinnervation. *Prog Brain Res,* 58**,** 131-6.
SUBRAMANIAN, M., RAGE, F., TABET, R., FLATTER, E., MANDEL, J.-L. & MOINE, H. 2011. G-quadruplex RNA structure as a signal for neurite mRNA targeting. *EMBO reports,* 12**,** 697-704.
SVENDSEN, S., ZIMPRICH, C., MCDOUGALL, M. G., KLAUBERT, D. H. & LOS, G. V. 2008. Spatial separation and bidirectional trafficking of proteins using a multi-functional reporter. *BMC Cell Biology,* 9**,** 17.
SWANGER, S. A., BASSELL, G. J. & GROSS, C. 2011. High-Resolution Fluorescence In Situ Hybridization to Detect mRNAs in Neuronal Compartments In Vitro and In Vivo. *In:* GERST, J. E. (ed.) *RNA Detection and Visualization: Methods and Protocols.* Totowa, NJ: Humana Press.
TAKAMORI, S., RHEE, J. S., ROSENMUND, C. & JAHN, R. 2000. Identification of a vesicular glutamate transporter that defines a glutamatergic phenotype in neurons. *Nature,* 407**,** 189-194.
TAKEMOTO, K., IWANARI, H., TADA, H., SUYAMA, K., SANO, A., NAGAI, T., HAMAKUBO, T. & TAKAHASHI, T. 2017. Optical inactivation of synaptic AMPA receptors erases fear memory. *Nature Biotechnology,* 35**,** 38-47.
TAKEMOTO, K., MATSUDA, T., MCDOUGALL, M., KLAUBERT, D. H., HASEGAWA, A., LOS, G. V., WOOD, K. V., MIYAWAKI, A. & NAGAI, T. 2011. Chromophore-Assisted Light Inactivation of HaloTag Fusion Proteins Labeled with Eosin in Living Cells. *ACS Chemical Biology,* 6**,** 401-406.
TAKEUCHI, M., HATA, Y., HIRAO, K., TOYODA, A., IRIE, M. & TAKAI, Y. 1997. SAPAPs: a family of PSD-95/SAP90-associated proteins localized at postsynaptic density. *Journal of Biological Chemistry,* 272**,** 11943-11951.
TEYRA, J., HUANG, H., JAIN, S., GUAN, X., DONG, A., LIU, Y., TEMPEL, W., MIN, J., TONG, Y., KIM, P. M., BADER, G. D. & SIDHU, S. S. 2017. Comprehensive Analysis of the Human SH3 Domain Family Reveals a Wide Variety of Non-canonical Specificities. *Structure,* 25**,** 1598-1610.e3.
THACKABERRY, E. A., WANG, X., SCHWEIGER, M., MESSICK, K., VALLE, N., DEAN, B., SAMBRONE, A., BOWMAN, T. & XIE, M. 2014. Solvent-based formulations for intravenous mouse pharmacokinetic studies: tolerability and recommended solvent dose limits. *Xenobiotica,* 44**,** 235-241.
THAPAR, A., COOPER, M. & RUTTER, M. 2017. Neurodevelopmental disorders. *The Lancet Psychiatry,* 4**,** 339-346.
TIMNEY, B., MITCHELL, D. E. & GIFFIN, F. 1978. The development of vision in cats after extended periods of dark-rearing. *Experimental Brain Research,* 31**,** 547-560.
TOPINKA, J. R. & BREDT, D. S. 1998. N-Terminal Palmitoylation of PSD-95 Regulates Association with Cell Membranes and Interaction with K+ Channel Kv1.4. *Neuron,* 20**,** 125-134.

TRACHTENBERG, J. T., CHEN, B. E., KNOTT, G. W., FENG, G., SANES, J. R., WELKER, E. & SVOBODA, K. 2002. Long-term in vivo imaging of experience-dependent synaptic plasticity in adult cortex. *Nature,* 420**,** 788-794.

TSAI, N. P., WILKERSON, J. R., GUO, W., MAKSIMOVA, M. A., DEMARTINO, G. N., COWAN, C. W. & HUBER, K. M. 2012. Multiple autism-linked genes mediate synapse elimination via proteasomal degradation of a synaptic scaffold PSD-95. *Cell,* 151**,** 1581-94.

TSUI, J. & MALENKA, R. C. 2006. Substrate Localization Creates Specificity in Calcium/Calmodulin-dependent Protein Kinase II Signaling at Synapses*. *Journal of Biological Chemistry,* 281**,** 13794-13804.

TSURUMI, C., ISHIDA, N., TAMURA, T., KAKIZUKA, A., NISHIDA, E., OKUMURA, E., KISHIMOTO, T., INAGAKI, M., OKAZAKI, K. & SAGATA, N. 1995. Degradation of c-Fos by the 26S proteasome is accelerated by c-Jun and multiple protein kinases. *Molecular and Cellular Biology,* 15**,** 5682-5687.

TUCKER-DROB, E. M. 2009. Differentiation of cognitive abilities across the life span. *Dev Psychol,* 45**,** 1097-118.

URH, M. & ROSENBERG, M. 2012. HaloTag, a Platform Technology for Protein Analysis. *Current chemical genomics,* 6**,** 72-78.

VALLEJO, D., CODOCEDO, J. F. & INESTROSA, N. C. 2017. Posttranslational Modifications Regulate the Postsynaptic Localization of PSD-95. *Molecular Neurobiology,* 54**,** 1759-1776.

VAN DER LEE, R., LANG, B., KRUSE, K., GSPONER, J., SÁNCHEZ DE GROOT, N., HUYNEN, MARTIJN A., MATOUSCHEK, A., FUXREITER, M. & BABU, M. M. 2014. Intrinsically Disordered Segments Affect Protein Half-Life in the Cell and during Evolution. *Cell Reports,* 8**,** 1832-1844.

VAN ESSEN, M. J., NAYLER, S., BECKER, E. B. E. & JACOB, J. 2020. Deconstructing cerebellar development cell by cell. *PLOS Genetics,* 16**,** e1008630.

VAZQUEZ, L. E., CHEN, H.-J., SOKOLOVA, I., KNUESEL, I. & KENNEDY, M. B. 2004. SynGAP Regulates Spine Formation. *The Journal of Neuroscience,* 24**,** 8862.

VILLASANA, L. E., KLANN, E. & TEJADA-SIMON, M. V. 2006. Rapid isolation of synaptoneurosomes and postsynaptic densities from adult mouse hippocampus. *Journal of neuroscience methods,* 158**,** 30-36.

VOGL, A. M., BROCKMANN, M. M., GIUSTI, S. A., MACCARRONE, G., VERCELLI, C. A., BAUDER, C. A., RICHTER, J. S., ROSELLI, F., HAFNER, A. S., DEDIC, N., WOTJAK, C. T., VOGT-WEISENHORN, D. M., CHOQUET, D., TURCK, C. W., STEIN, V., DEUSSING, J. M. & REFOJO, D. 2015. Neddylation inhibition impairs spine development, destabilizes synapses and deteriorates cognition. *Nat Neurosci,* 18**,** 239-51.

VOGLEWEDE, R. L., VANDEMARK, K. M., DAVIDSON, A. M., DEWITT, A. R., HEFFLER, M. D., TRIMMER, E. H. & MOSTANY, R. 2019. Reduced sensory-evoked structural plasticity in the aging barrel cortex. *Neurobiology of aging,* 81**,** 222-233.

WALKER, A. S., NEVES, G., GRILLO, F., JACKSON, R. E., RIGBY, M., O'DONNELL, C., LOWE, A. S., VIZCAY-BARRENA, G., FLECK, R. A. & BURRONE, J. 2017. Distance-dependent gradient in NMDAR-driven spine calcium signals along tapering dendrites. *Proceedings of the National Academy of Sciences,* 114**,** E1986.

WALKUP, W. G. I. V., MASTRO, T. L., SCHENKER, L. T., VIELMETTER, J., HU, R., IANCU, A., REGHUNATHAN, M., BANNON, B. D. & KENNEDY, M. B. 2016. A model for regulation by SynGAP-α1 of binding of synaptic proteins to PDZ-domain 'Slots' in the postsynaptic density. *eLife,* 5**,** e16813.

WALSH, T., MCCLELLAN, J. M., MCCARTHY, S. E., ADDINGTON, A. M., PIERCE, S. B., COOPER, G. M., NORD, A. S., KUSENDA, M., MALHOTRA, D., BHANDARI, A., STRAY, S. M., RIPPEY, C. F., ROCCANOVA, P., MAKAROV, V., LAKSHMI, B., FINDLING, R. L., SIKICH, L., STROMBERG, T., MERRIMAN, B., GOGTAY, N., BUTLER, P., ECKSTRAND, K., NOORY, L., GOCHMAN, P., LONG, R., CHEN, Z., DAVIS, S., BAKER, C., EICHLER, E. E., MELTZER, P. S., NELSON, S. F., SINGLETON, A. B., LEE, M. K., RAPOPORT, J. L., KING, M. C. & SEBAT, J. 2008. Rare structural variants disrupt multiple genes in neurodevelopmental pathways in schizophrenia. *Science,* 320**,** 539-43.

WALTHER, D. M. & MANN, M. 2011. Accurate Quantification of More Than 4000 Mouse Tissue Proteins Reveals Minimal Proteome Changes During Aging. *Molecular & Cellular Proteomics,* 10**,** M110.004523.

WANG, C. C., HELD, R. G. & HALL, B. J. 2013. SynGAP regulates protein synthesis and homeostatic synaptic plasticity in developing cortical networks. *PLoS One,* 8**,** e83941.

WELDON, M., KILINC, M., LLOYD HOLDER, J. & RUMBAUGH, G. 2018. The first international conference on SYNGAP1-related brain disorders: a stakeholder meeting of families, researchers, clinicians, and regulators. *Journal of Neurodevelopmental Disorders,* 10**,** 6.

WESTON, C. S. E. 2019. Four Social Brain Regions, Their Dysfunctions, and Sequelae, Extensively Explain Autism Spectrum Disorder Symptomatology. *Brain sciences,* 9**,** 130.

WIESEL, T. N. & HUBEL, D. H. 1963. SINGLE-CELL RESPONSES IN STRIATE CORTEX OF KITTENS DEPRIVED OF VISION IN ONE EYE. *Journal of Neurophysiology,* 26**,** 1003-1017.

WILHELM, I., NYÚL-TÓTH, Á., SUCIU, M., HERMENEAN, A. & KRIZBAI, I. A. 2016. Heterogeneity of the blood-brain barrier. *Tissue barriers,* 4**,** e1143544-e1143544.

WILHELM, J., KÜHN, S., TARNAWSKI, M., GOTTHARD, G., TÜNNERMANN, J., TÄNZER, T., KARPENKO, J., MERTES, N., XUE, L., UHRIG, U., REINSTEIN, J., HIBLOT, J. & JOHNSSON, K. 2021. Kinetic and Structural Characterization of the Self-Labeling Protein Tags HaloTag7, SNAP-tag, and CLIP-tag. *Biochemistry,* 60**,** 2560-2575.

WILLSHAW, D. J. & BUCKINGHAM, J. 1990. An assessment of Marr's theory of the hippocampus as a temporary memory store. *Philosophical*

Transactions of the Royal Society of London. Series B: Biological Sciences, 329**,** 205-215.

WOJCIK, S. M., RHEE, J. S., HERZOG, E., SIGLER, A., JAHN, R., TAKAMORI, S., BROSE, N. & ROSENMUND, C. 2004. An essential role for vesicular glutamate transporter 1 (VGLUT1) in postnatal development and control of quantal size. *Proceedings of the National Academy of Sciences of the United States of America,* 101**,** 7158.

WONG, A. D., YE, M., LEVY, A. F., ROTHSTEIN, J. D., BERGLES, D. E. & SEARSON, P. C. 2013. The blood-brain barrier: an engineering perspective. *Front Neuroeng,* 6**,** 7.

WOODRUFF-PAK, D. S., FOY, M. R., AKOPIAN, G. G., LEE, K. H., ZACH, J., NGUYEN, K. P. T., COMALLI, D. M., KENNARD, J. A., AGELAN, A. & THOMPSON, R. F. 2010. Differential effects and rates of normal aging in cerebellum and hippocampus. *Proceedings of the National Academy of Sciences,* 107**,** 1624.

WU, Q., SUN, M., BERNARD, L. P. & ZHANG, H. 2017. Postsynaptic density 95 (PSD-95) serine 561 phosphorylation regulates a conformational switch and bidirectional dendritic spine structural plasticity. *Journal of Biological Chemistry,* 292**,** 16150-16160.

XU, H.-T., PAN, F., YANG, G. & GAN, W.-B. 2007. Choice of cranial window type for in vivo imaging affects dendritic spine turnover in the cortex. *Nature Neuroscience,* 10**,** 549-551.

XU, T., YU, X., PERLIK, A. J., TOBIN, W. F., ZWEIG, J. A., TENNANT, K., JONES, T. & ZUO, Y. 2009. Rapid formation and selective stabilization of synapses for enduring motor memories. *Nature,* 462**,** 915-919.

YAMAGUCHI, K., INOUE, S., OHARA, O. & NAGASE, T. 2009. Pulse-chase experiment for the analysis of protein stability in cultured mammalian cells by covalent fluorescent labeling of fusion proteins. *Methods Mol Biol,* 577**,** 121-31.

YAN, P., XIONG, Y., CHEN, B., NEGASH, S., SQUIER, T. C. & MAYER, M. U. 2006. Fluorophore-assisted light inactivation of calmodulin involves singlet-oxygen mediated cross-linking and methionine oxidation. *Biochemistry,* 45**,** 4736-48.

YANG, G., PAN, F. & GAN, W.-B. 2009. Stably maintained dendritic spines are associated with lifelong memories. *Nature,* 462**,** 920-924.

YANG, Y., LIU, D.-Q., HUANG, W., DENG, J., SUN, Y., ZUO, Y. & POO, M.-M. 2016. Selective synaptic remodeling of amygdalocortical connections associated with fear memory. *Nature neuroscience,* 19**,** 1348-1355.

YI, J. J. & EHLERS, M. D. 2005. Ubiquitin and Protein Turnover in Synapse Function. *Neuron,* 47**,** 629-632.

YUKI, D., SUGIURA, Y., ZAIMA, N., AKATSU, H., TAKEI, S., YAO, I., MAESAKO, M., KINOSHITA, A., YAMAMOTO, T., KON, R., SUGIYAMA, K. & SETOU, M. 2014. DHA-PC and PSD-95 decrease after loss of synaptophysin and before neuronal loss in patients with Alzheimer's disease. *Scientific Reports,* 4**,** 7130.

ZALFA, F., ELEUTERI, B., DICKSON, K. S., MERCALDO, V., DE RUBEIS, S., DI PENTA, A., TABOLACCI, E., CHIURAZZI, P., NERI, G., GRANT,

S. G. N. & BAGNI, C. 2007. A new function for the fragile X mental retardation protein in regulation of PSD-95 mRNA stability. *Nature Neuroscience,* 10**,** 578-587.
ZHANG, C., HUA, T., ZHU, Z. & LUO, X. 2006. Age-related changes of structures in cerebellar cortex of cat. *Journal of biosciences,* 31**,** 55-60.
ZHANG, C., ZHU, Q. & HUA, T. 2010. Aging of cerebellar Purkinje cells. *Cell and Tissue Research,* 341**,** 341-347.
ZHOU, Y., LAI, B. & GAN, W.-B. 2017. Monocular deprivation induces dendritic spine elimination in the developing mouse visual cortex. *Scientific Reports,* 7**,** 4977.
ZHU, F., CIZERON, M., QIU, Z., BENAVIDES-PICCIONE, R., KOPANITSA, M. V., SKENE, N. G., KONIARIS, B., DEFELIPE, J., FRANSÉN, E., KOMIYAMA, N. H. & GRANT, S. G. N. 2018. Architecture of the Mouse Brain Synaptome. *Neuron,* 99**,** 781-799.e10.
ZHU, J. J., QIN, Y., ZHAO, M., VAN AELST, L. & MALINOW, R. 2002. Ras and Rap Control AMPA Receptor Trafficking during Synaptic Plasticity. *Cell,* 110**,** 443-455.
ZITO, K., SCHEUSS, V., KNOTT, G., HILL, T. & SVOBODA, K. 2009. Rapid Functional Maturation of Nascent Dendritic Spines. *Neuron,* 61**,** 247-258.
ZUO, Y., LIN, A., CHANG, P. & GAN, W.-B. 2005. Development of Long-Term Dendritic Spine Stability in Diverse Regions of Cerebral Cortex. *Neuron,* 46**,** 181-189.

Appendices

Appendix 1: Representative images of SiR-Halo fluorescence labelling at five time points post-injection.

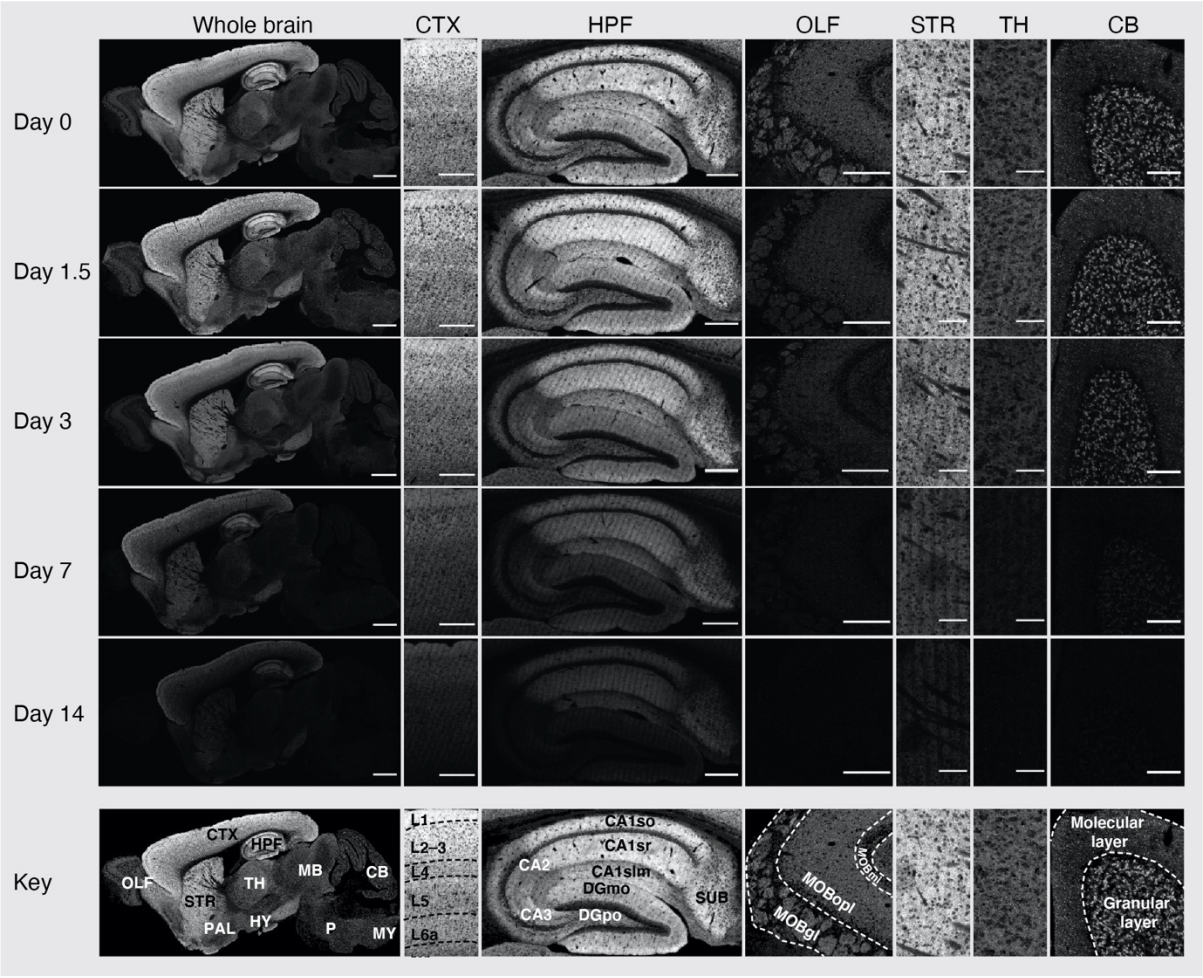

Appendix. Figure 1: Representative images of SiR-Halo fluorescence labelling in different brain regions across time. *Images from whole brain, layers of the isocortex, subregions of hippocampal formation, olfactory areas, striatum, thalamus and cerebellum. CTX, isocortex; HPF, hippocampal formation; OLF, olfactory areas; STR, striatum; TH, thalamus; CB, cerebellum; PAL, pallidum; HY, hypothalamus; MB, midbrain; P, pons; MY, medulla; CA1so, CA1 stratum oriens; CA1sr, stratum radiatum; CA1slm, stratum lacunosum-moleculare; DGmo, dentate gyrus molecular layer; DGpo, dentate gyrus polymorphic layer; SUB, subiculum; MOBmi, mitral layer of the main olfactory bulb; MOBopl, outer plexiform layer of the main olfactory bulb; MOBgl, glomerular layer of the main olfactory bulb. Scale bars: 2 mm (whole brain), 500 µm (CTX, HPF, OLF), 200 µm (STR, TH, CB).*

Appendix 2: Fluorescent puncta decay in different brain subregions.

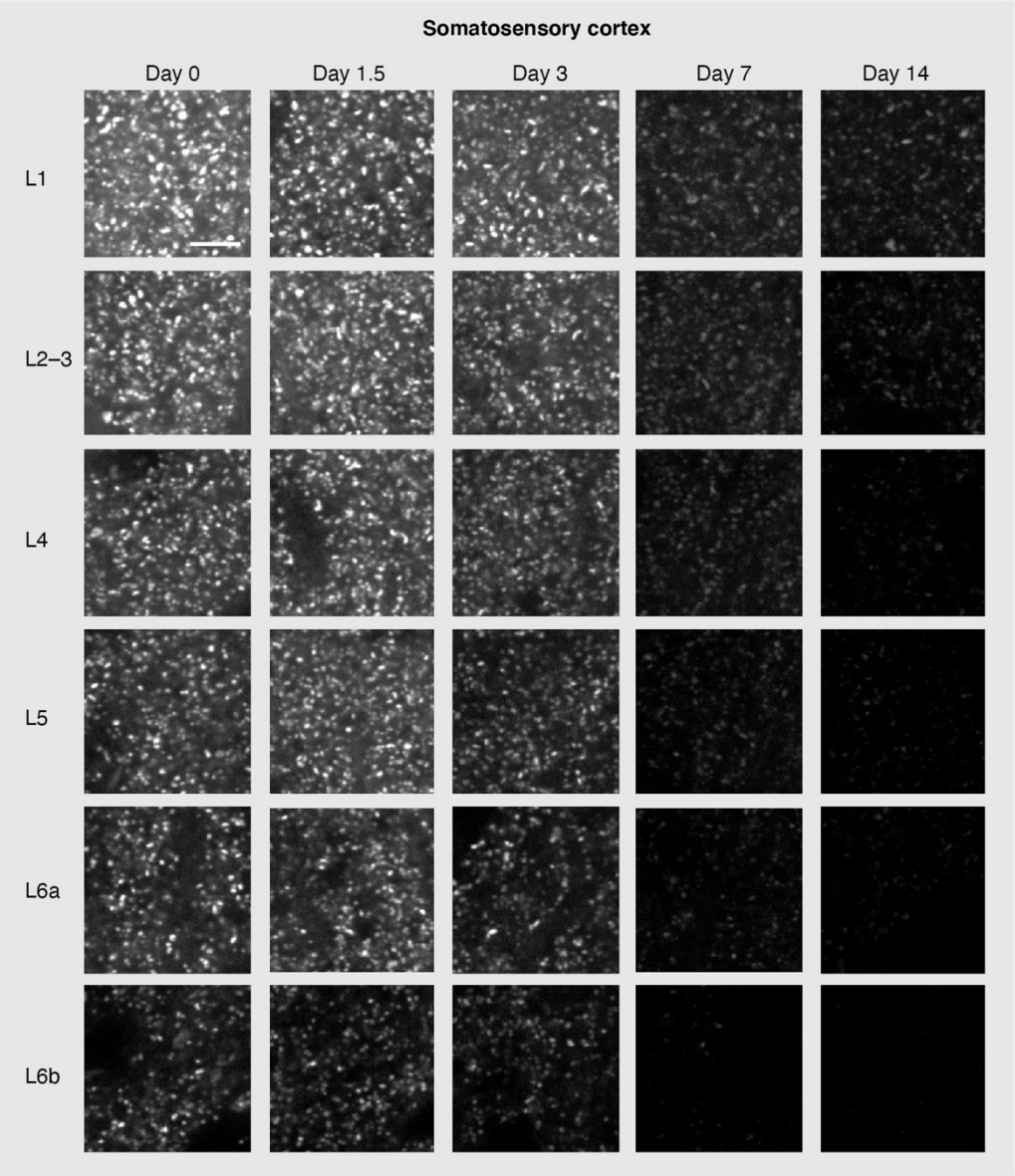

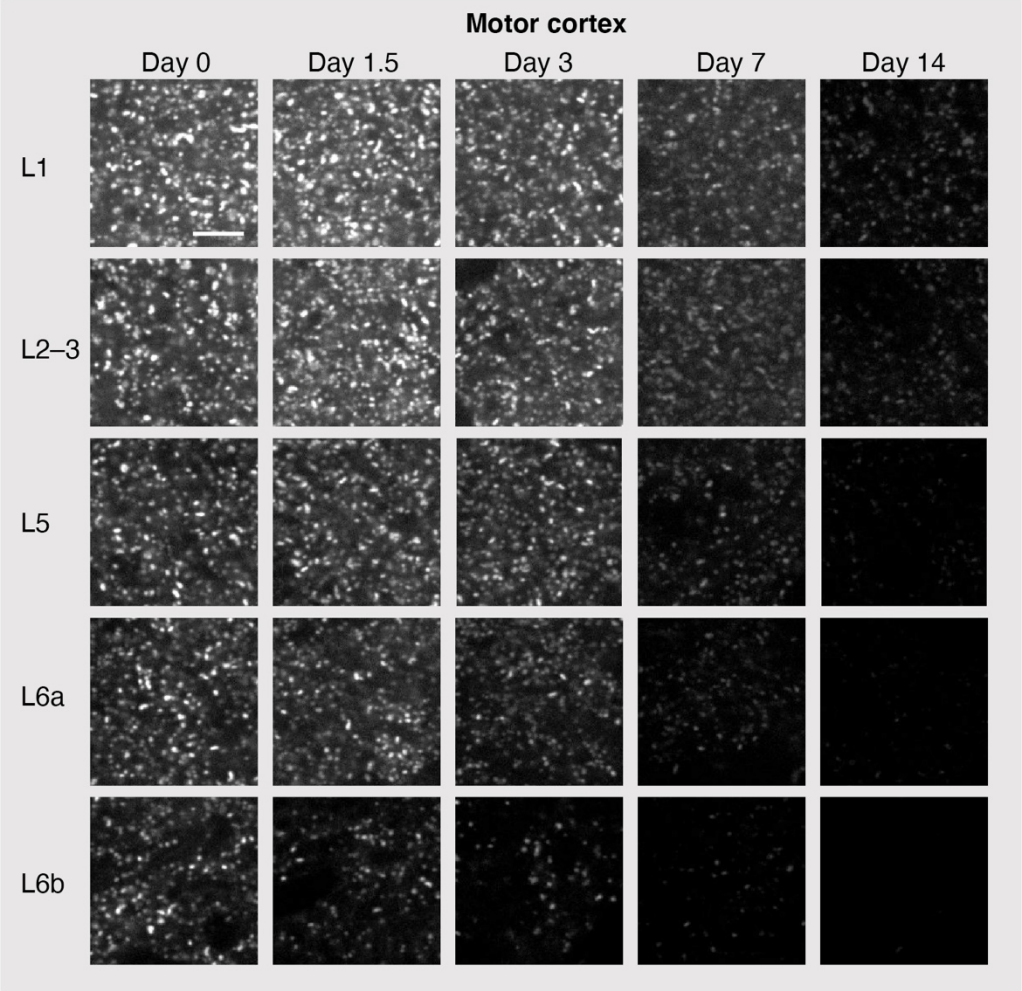
Motor cortex
Day 0
Day 1.5
Day 3
Day 7
Day 14
L1
L2–3
L5
L6a
L6b

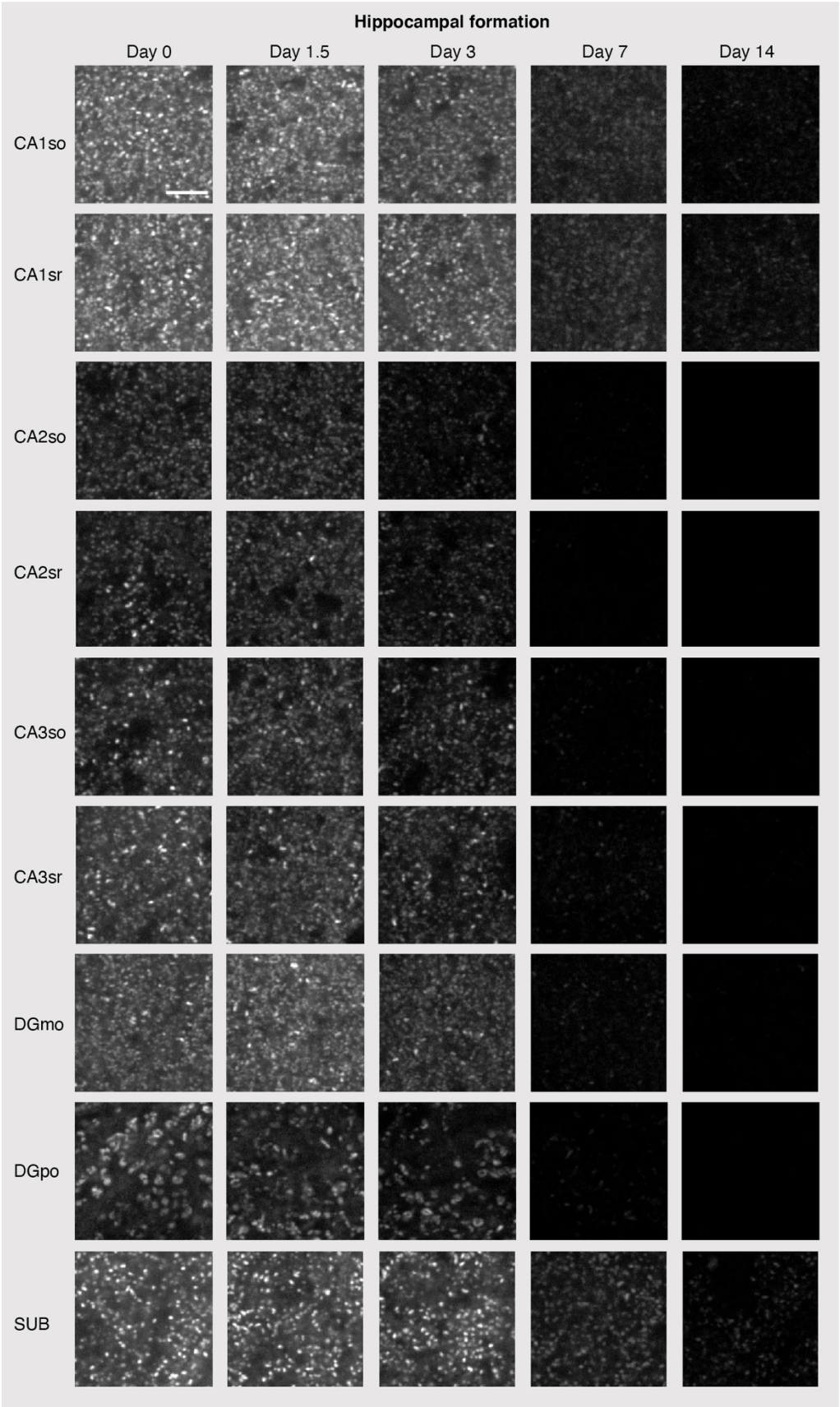
Hippocampal formation
Day 0
Day 1.5
Day 3
Day 7
Day 14
CA1so
CA1sr
CA2so
CA2sr
CA3so
CA3sr
DGmo
DGpo
SUB

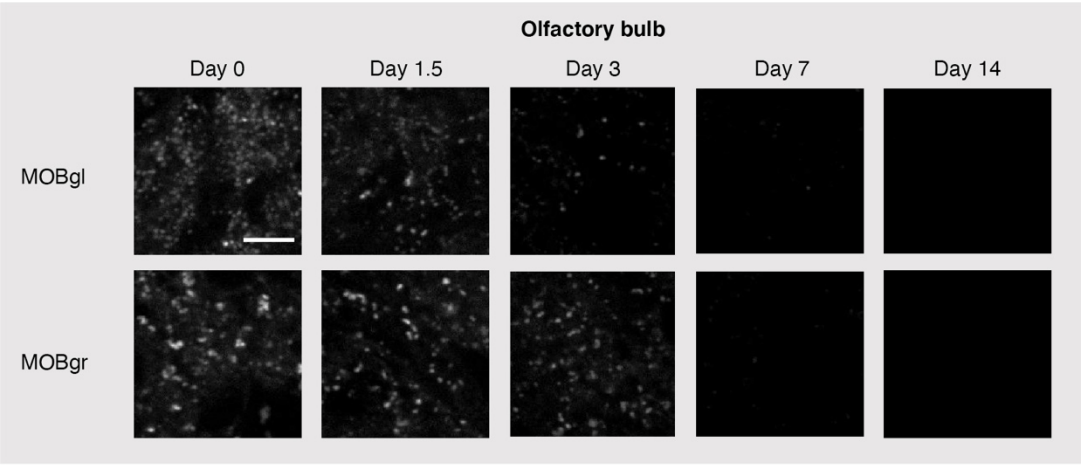
Olfactory bulb
Day 0
Day 1.5
Day 3
Day 7
Day 14
MOBgl
MOBgr

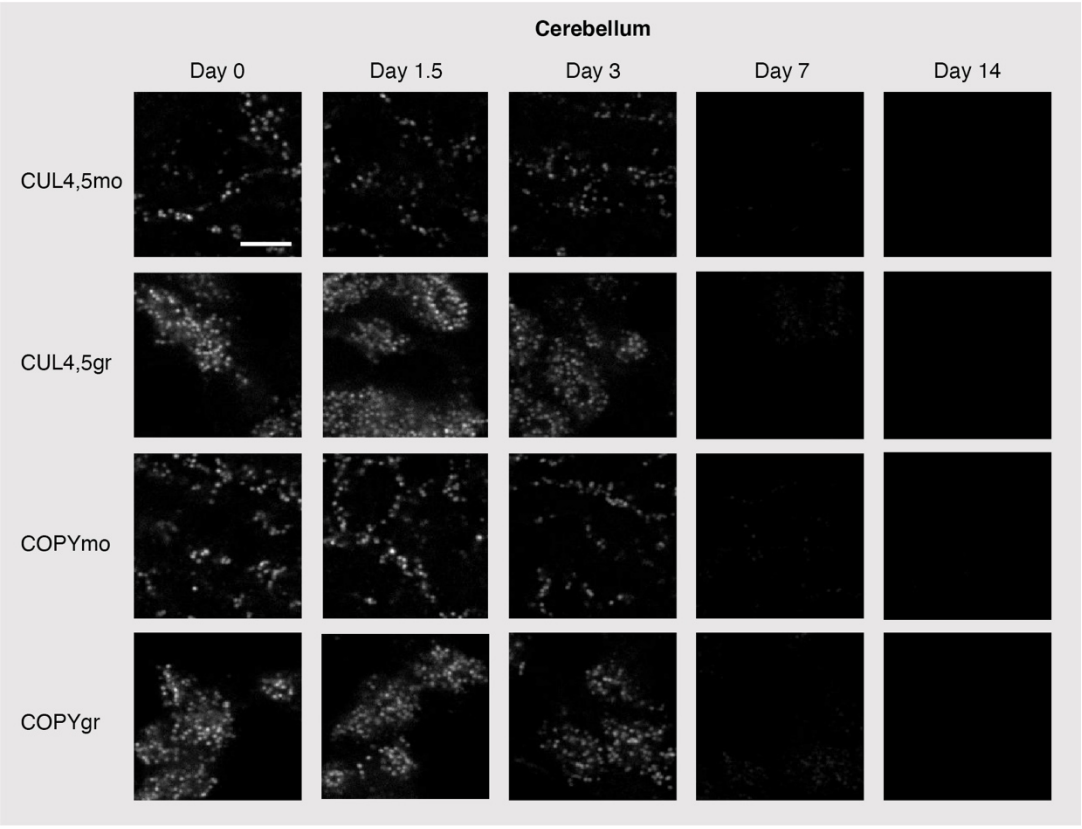
Cerebellum
Day 0
Day 1.5
Day 3
Day 7
Day 14
CUL4,5mo
CUL4,5gr
COPYmo
COPYgr

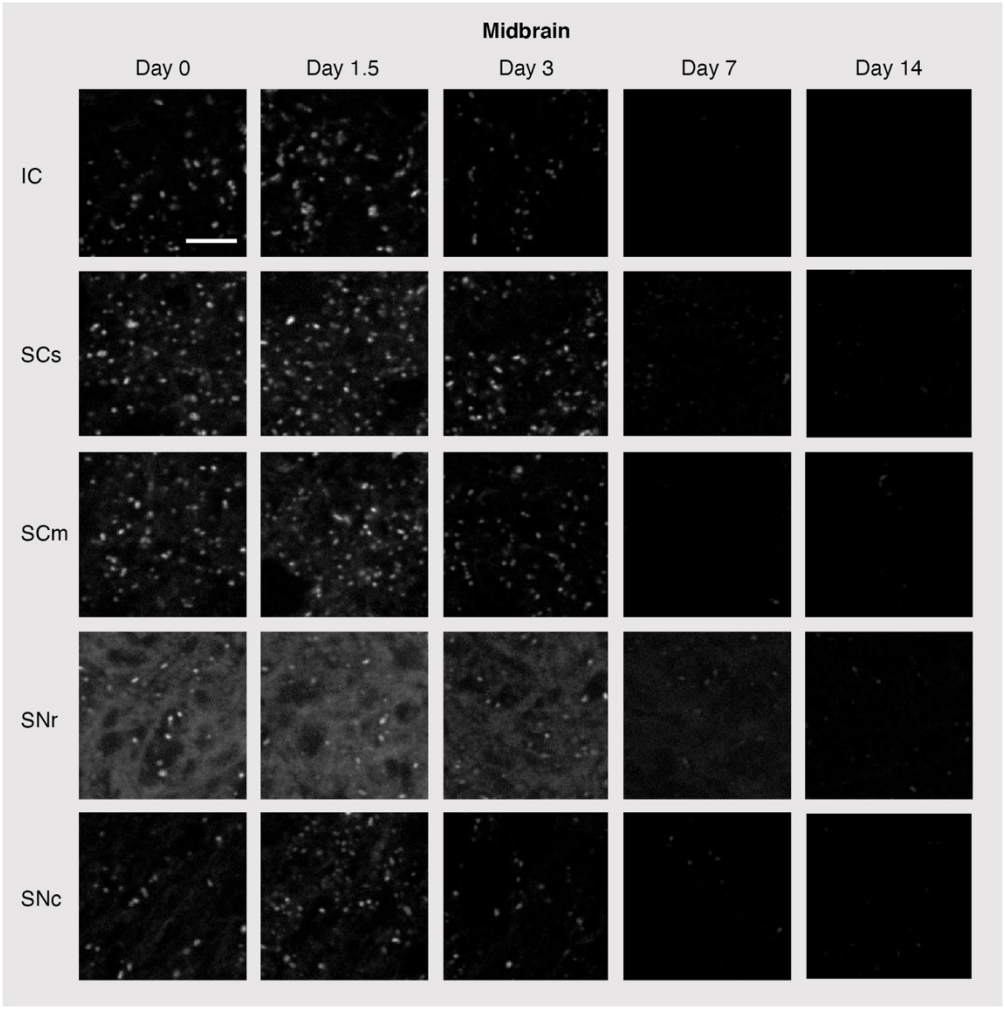
Midbrain
Day 0
Day 1.5
Day 3
Day 7
Day 14
IC
SCs
SCm
SNr
SNc

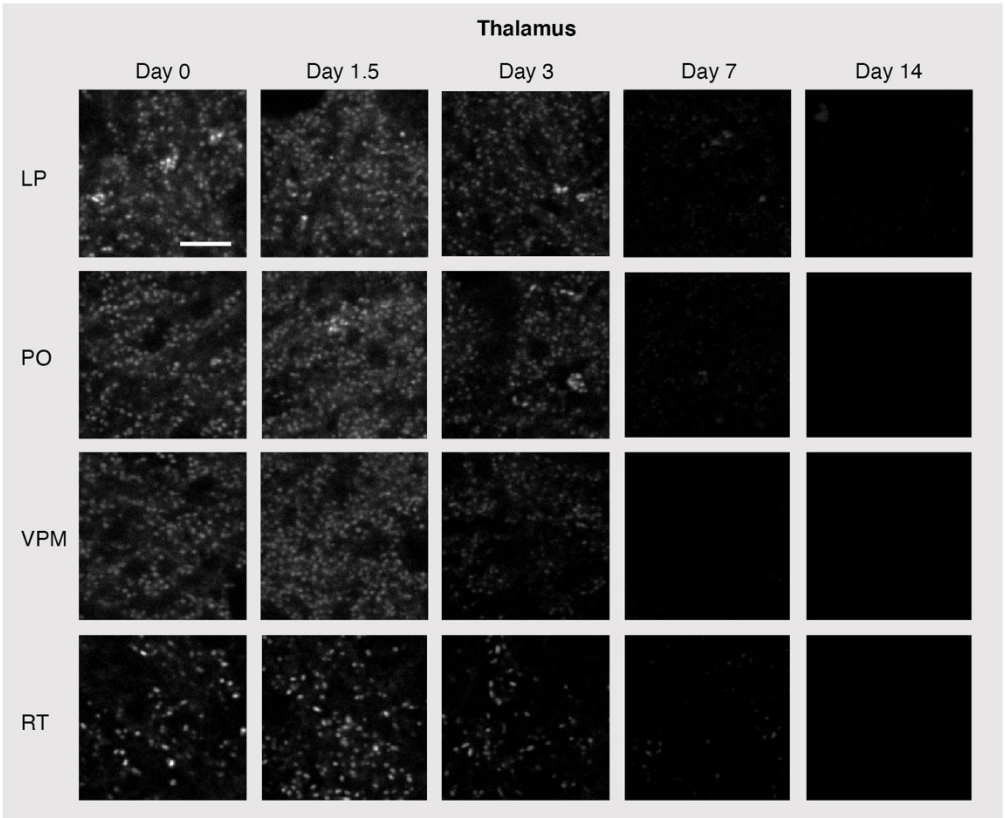
Thalamus
Day 0
Day 1.5
Day 3
Day 7
Day 14
LP
PO
VPM
RT

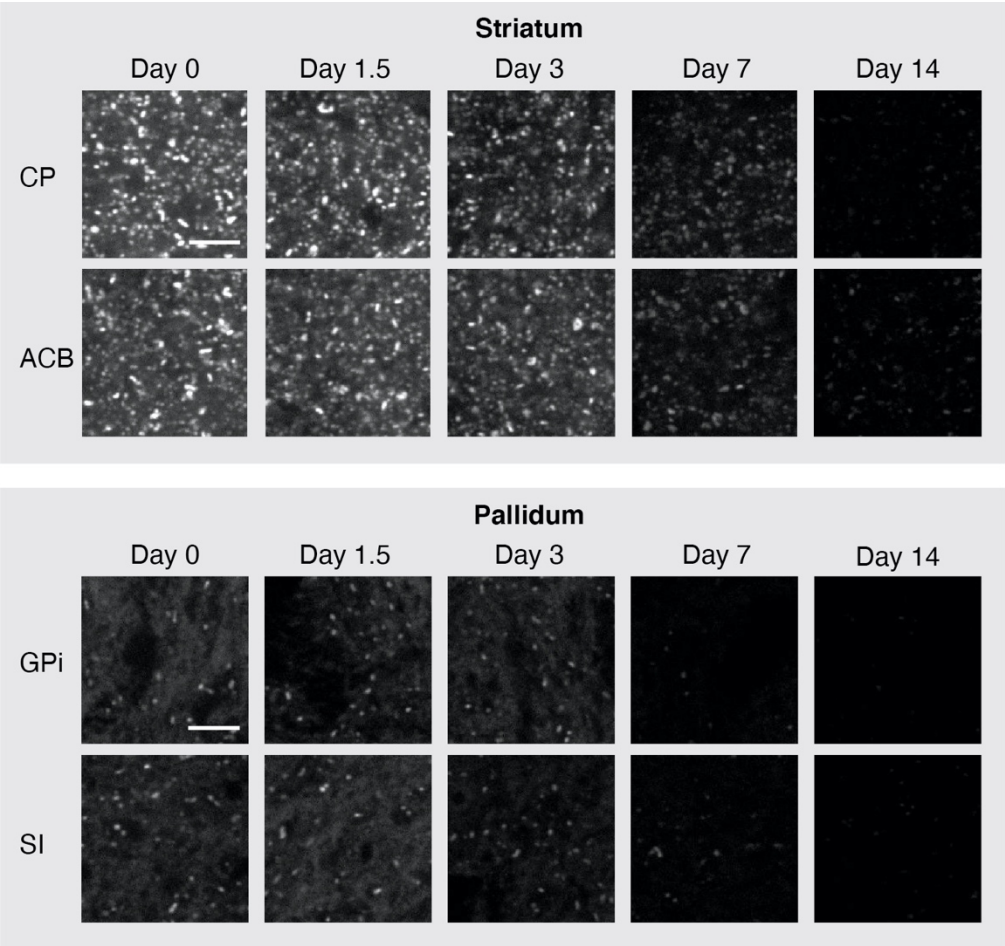

Appendix. Figure 2: Fluorescent puncta decay in different brain subregions. *Example high-magnification single-synapse resolution images of SiR-Halo puncta decay over 2 weeks. Images from subregions of isocortex, hippocampal formation, olfactory areas, cerebellum, midbrain, thalamus, striatum and pallidum. CA1so, CA1 stratum oriens; CA1sr, CA1 stratum radiatum; CA2so, CA2 stratum oriens; CA2sr, CA2 stratum radiatum; CA3so, CA3 stratum oriens; CA3sr, CA3 stratum radiatum; DGmo, dentate gyrus molecular layer; DGpo, dentate gyrus polymorphic layer; SUB, subiculum; MOBgl, glomerular layer of the main olfactory bulb; MOBgr, granular layer of the main olfactory bulb; CUL4,5mo, lobules IV-V molecular layer; CUL4,5gr, lobules IV-V granular layer; COPYmo, copula pyramidis molecular layer; COPYgr, copula pyramidis granular layer; IC, inferior colliculus; SCs, superior colliculus, sensory related; SCm, superior colliculus, motor related; SNr, substantia nigra, reticular part; SNc, substantia nigra, compact part; LP, lateral posterior nucleus of the thalamus; PO, posterior complex of the thalamus; VPM, ventral posteromedial nucleus of the thalamus; RT, reticular nucleus of the thalamus; CP, caudoputamen; ACB, nucleus accumbens; GPi, globus pallidus, internal segment; SI, substantia innominate. Scale bars: 5 µm*

Appendix 3: Co-localisation of SiR-Halo and TMR-Halo labelling at day 3 post-injection.

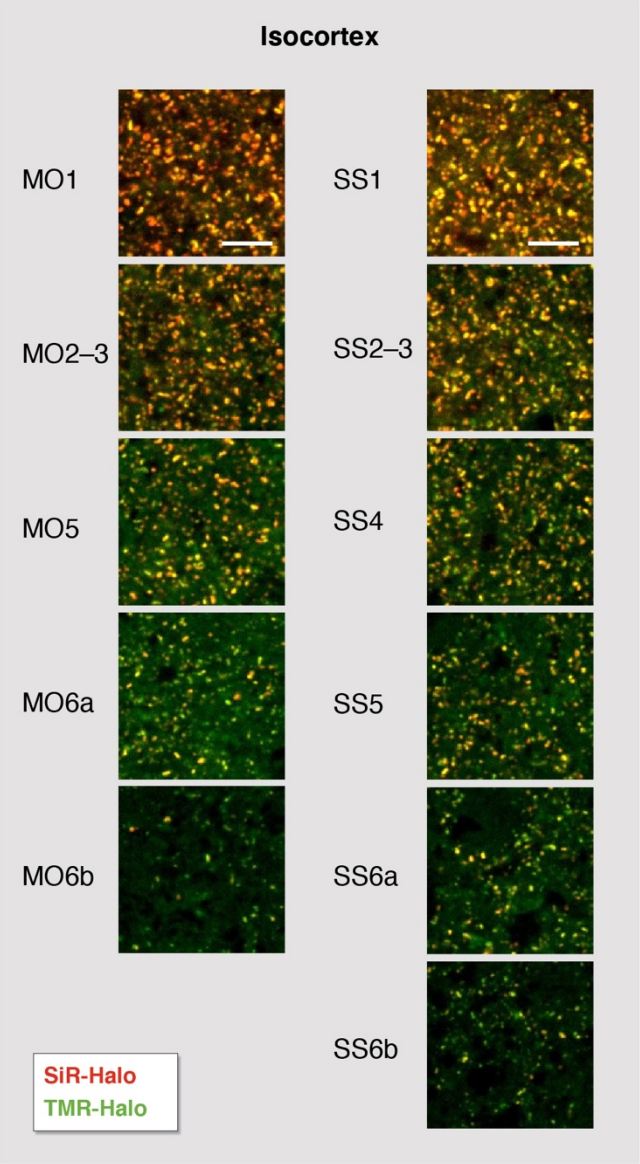

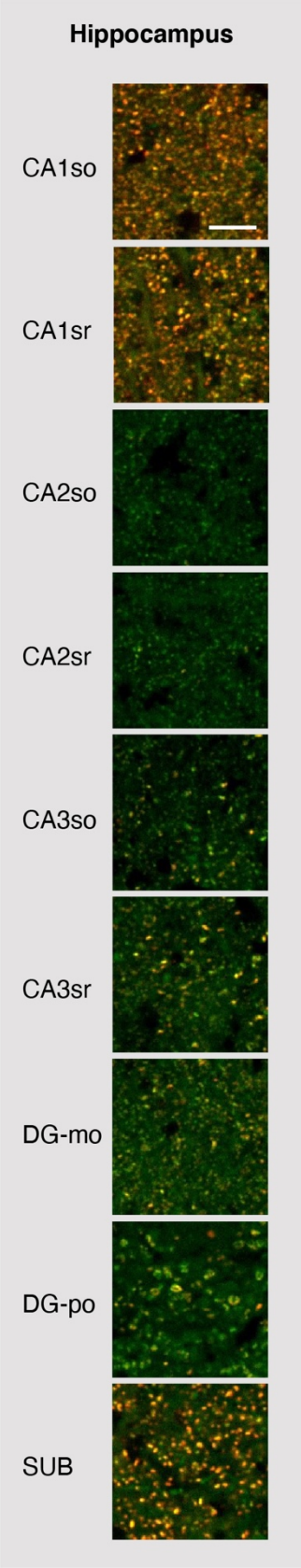

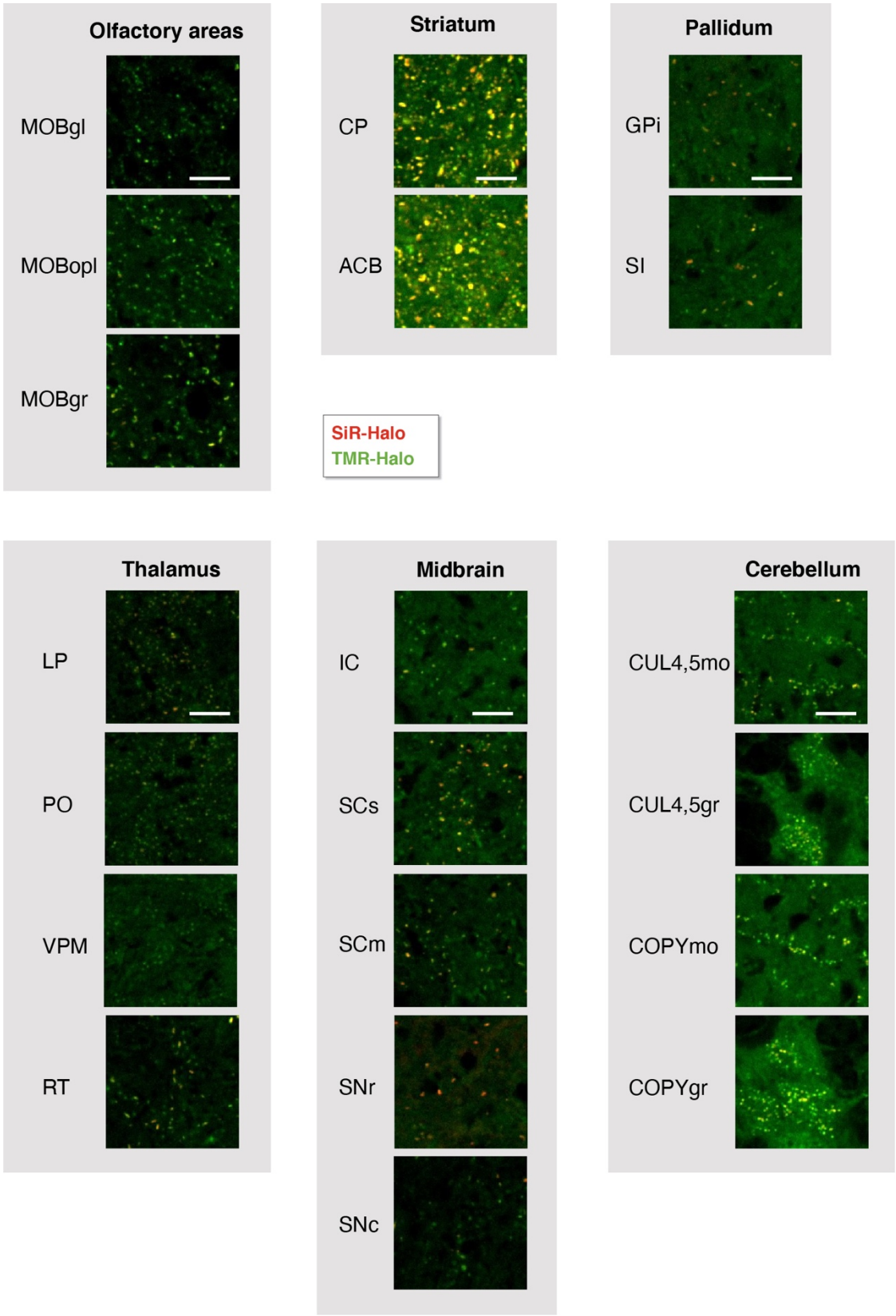

Appendix. Figure 3: Co-localisation of SiR-Halo and TMR-Halo. *Representative high-magnification images from subregions of isocortex, hippocampal formation, olfactory areas, striatum, pallidum, thalamus, midbrain and cerebellum. Scale bars: 5 µm.*

Appendix 4: Raw numbers for PSD95 half-life estimation. Density- and intensity-based PSD95 half-life estimates (+/- 95% CI) for 12 main brain areas and 110 brain subregions in 3-month-old mice. Mean (+/- SD) are provided for 5 time points used to fit an exponential decay function and estimate half-life.

		PSD95 puncta density (/ 100um2)			PSD95 puncta intensity (AU)		
		Half-life (days)			Half-life (days)		
Abbreviation	**Region name**	**MEAN**	95%CI_lower	95%CI_upper	**MEAN**	95%CI_lower	95%CI_upper
Isocortex	Isocortex	6.5391	5.0011	9.4460	4.7310	3.5167	7.2263
OLF	Olfactory areas	2.9038	1.8902	6.2558	2.5827	1.6701	5.6939
HPF	Hippocampal Formation	3.8465	2.6216	7.2195	3.6075	2.5078	6.4247
CTXsp	Cortical subplate	4.2813	3.1027	6.9039	3.6050	2.4079	7.1692
STR	Striatum	4.9688	3.3213	7.6735	3.7890	2.5835	7.1043
PAL	Pallidum	4.8710	3.1027	11.3370	3.6005	2.1639	10.7105
TH	Thalamus	2.7693	1.7294	7.5498	2.5620	1.5906	6.5819
HY	Hypothalamus	4.5722	3.1209	8.5405	4.0153	2.4547	11.0229
MB	Midbrain	4.3594	3.1393	7.1238	3.3877	2.2920	6.4907
P	Pons	3.9608	2.6486	7.8544	3.6891	2.3307	8.8431
MY	Medulla	3.8064	2.6537	6.7296	3.1247	2.0689	6.3812
CB	Cerebellum	3.8106	2.8893	5.5944	3.0346	2.1325	5.2592

	PSD95 puncta density (/ 100um2)									
	Day 0		Day 1.5		Day 3		Day 7		Day 14	
Brain region	**MEAN**	SD	**MEAN**	SD	**MEAN**	SD	**MEAN**	SD	**MEAN**	SD
Isocortex	15.1645	0.6938	15.0644	0.7950	14.7378	0.3342	15.9532	0.8630	16.3327	0.3744
OLF	14.9284	1.0758	14.8974	1.0429	14.7253	0.5868	11.7565	5.9721	1.9776	5.5935
HPF	14.9287	0.6246	15.0738	0.8026	14.6295	0.3944	15.3009	0.4362	10.1604	6.3463
CTXsp	15.0630	0.9752	14.8332	0.7377	14.8834	0.6241	15.7874	0.6114	9.2213	7.6719
STR	15.3306	1.0415	15.4682	1.5510	15.0059	0.7015	17.0247	1.2322	14.8464	6.5554
PAL	14.9702	0.4965	15.0580	0.9827	14.7189	0.5404	15.1496	0.6099	8.2500	7.7473
TH	13.7250	0.3613	13.7981	0.5954	13.5430	0.3627	7.4052	6.9883	0.0000	0.0000
HY	15.3722	0.6980	15.4806	1.1527	15.0037	0.4768	15.4828	0.4955	7.5052	8.0726
MB	15.1146	0.2893	15.2103	0.6524	14.8229	0.3005	12.9684	5.7262	8.8731	7.3730
P	15.5528	0.2879	15.7148	0.6525	15.4672	0.4176	12.3181	6.0633	5.2143	6.5311
MY	15.5915	0.5906	15.4343	0.5928	15.1404	0.1655	12.3645	6.0930	1.6667	4.0825
CB	13.7103	0.3435	13.7790	0.4172	13.2934	0.2425	9.3974	6.4220	0.0000	0.0000

	PSD95 puncta intensity (AU)									
	Day 0		Day 1.5		Day 3		Day 7		Day 14	
Brain region	**MEAN**	SD	**MEAN**	SD	**MEAN**	SD	**MEAN**	SD	**MEAN**	SD
Isocortex	5.9E+11	2.1E+11	5.0E+11	1.6E+11	4.6E+11	6.3E+10	1.9E+11	9.1E+10	5.4E+10	2.9E+10
OLF	8.1E+10	5.0E+10	4.9E+10	3.0E+10	4.2E+10	1.5E+10	8.6E+09	6.7E+09	8.3E+08	8.7E+08
HPF	8.5E+10	3.8E+10	6.3E+10	3.1E+10	5.8E+10	1.3E+10	1.6E+10	1.1E+10	2.9E+09	2.0E+09
CTXsp	1.0E+10	5.3E+09	9.1E+09	4.0E+09	6.8E+09	2.2E+09	1.8E+09	1.2E+09	1.7E+08	1.8E+08
STR	2.0E+11	1.0E+11	1.7E+11	7.7E+10	1.4E+11	2.4E+10	4.2E+10	2.8E+10	6.4E+09	4.4E+09
PAL	8.0E+09	4.8E+09	6.2E+09	5.0E+09	4.9E+09	2.4E+09	1.9E+09	1.5E+09	2.1E+08	1.8E+08
TH	4.4E+10	2.8E+10	2.8E+10	2.3E+10	2.4E+10	1.2E+10	2.3E+09	2.1E+09	1.7E+08	1.7E+08
HY	1.5E+10	8.3E+09	1.2E+10	8.5E+09	1.1E+10	6.3E+09	3.1E+09	2.7E+09	4.4E+08	4.8E+08
MB	5.4E+10	2.7E+10	3.6E+10	1.8E+10	3.7E+10	1.2E+10	8.5E+09	6.2E+09	1.3E+09	1.0E+09
P	1.6E+10	9.1E+09	1.3E+10	7.9E+09	1.2E+10	3.8E+09	2.6E+09	2.4E+09	2.6E+08	2.5E+08
MY	3.5E+10	1.5E+10	2.7E+10	1.5E+10	2.2E+10	6.1E+09	4.3E+09	4.0E+09	3.2E+08	2.9E+08
CB	3.6E+10	1.4E+10	2.5E+10	1.3E+10	2.2E+10	6.9E+09	3.7E+09	3.3E+09	8.2E+07	6.1E+07

		PSD95 puncta density (/ 100um2)			PSD95 puncta intensity (AU)		
		Half-life (days)			Half-life (days)		
Abbreviation	**Brain_area**	**MEAN**	95%CI_lower	95%CI_upper	**MEAN**	95%CI_lower	95%CI_upper
ORB1	Isocortex	10.7033	8.3512	14.8968	6.0634	4.2427	10.6213
ORB2-3	Isocortex	7.9317	6.1286	11.2396	4.9274	3.5591	8.0050
ORB5	Isocortex	6.1558	4.6898	8.9623	4.1084	2.9032	7.0247
ORB6a	Isocortex	5.1268	3.7898	7.9326	3.8119	2.6646	6.6944
ORB6b	Isocortex	4.0440	2.6690	8.3421	3.1870	2.0591	7.0471
FRP1	Isocortex	11.6241	8.6052	17.9062	6.6143	4.3782	13.5186
FRP2-3	Isocortex	8.9208	6.8425	12.8052	5.4708	3.8366	9.5307
MO1	Isocortex	12.0694	9.2766	17.2639	6.1486	4.5067	9.6725
MO2-3	Isocortex	8.7707	6.6906	12.7323	5.3839	3.9391	8.5027
MO5	Isocortex	6.6777	4.9975	10.0704	4.5363	3.2758	7.3738
MO6a	Isocortex	5.2116	3.6968	8.8209	3.9931	2.7089	7.5924
MO6b	Isocortex	4.7057	2.7528	16.2102	3.7728	2.0947	18.9735
SS1	Isocortex	10.4311	7.6820	16.2482	5.4226	3.9536	8.6289
SS2-3	Isocortex	8.0909	6.2221	11.5582	4.6762	3.5480	6.8566
SS4	Isocortex	6.2672	4.7705	9.1276	3.9323	2.8921	6.1412
SS5	Isocortex	5.6769	4.2866	8.3977	3.7503	2.7677	5.8150
SS6a	Isocortex	5.0669	3.5785	8.6763	3.4134	2.3393	6.3112
SS6b	Isocortex	4.5813	2.4871	28.9777	3.1410	1.6267	45.4511
PTLp1	Isocortex	10.0383	7.1844	16.6542	5.2821	3.6431	9.6019
PTLp2-3	Isocortex	8.2390	6.1833	12.3446	5.1919	3.9235	7.6724
PTLp4	Isocortex	6.9176	5.2392	10.1844	4.5611	3.4025	6.9164
PTLp5	Isocortex	5.7285	4.4575	8.0207	4.0312	3.1192	5.6966
PTLp6a	Isocortex	5.2274	3.8832	8.0012	3.7074	2.6137	6.3748
PTLp6b	Isocortex	5.9754	3.5096	20.1204	4.2904	2.2759	37.3630
VIS1	Isocortex	8.5007	6.6266	11.8588	5.1940	3.9262	7.6709
VIS2-3	Isocortex	7.9009	5.7955	12.4042	5.0592	3.6465	8.2588
VIS4	Isocortex	6.4180	4.6929	10.1560	4.6636	3.3363	7.7448
VIS5	Isocortex	5.2353	3.9767	7.6582	4.0991	3.0296	6.3360
VIS6a	Isocortex	4.5068	3.4605	6.4659	3.5889	2.6055	5.7645
VIS6b	Isocortex	4.2265	2.7279	9.3732	3.7933	2.3994	9.0507
RSPd1	Isocortex	5.8642	4.4662	8.5300	4.6195	3.2380	8.0568
RSPd2-3	Isocortex	5.4622	4.1456	8.0068	4.9398	3.2613	10.1781
RSPd5	Isocortex	4.7770	3.5896	7.1378	4.1727	2.7641	8.5089
RSPv1	Isocortex	5.4322	3.8594	9.1698	4.6109	2.8387	12.2728
RSPv2-3	Isocortex	4.1605	2.8361	7.7943	3.7829	2.4939	7.8300
RSPv5	Isocortex	4.7935	3.4112	8.0627	3.9054	2.5187	8.6891
RSPv6a	Isocortex	3.7569	2.5672	7.0079	2.9682	1.9696	6.0208
MOBgl	Olfactory areas	1.1581	0.7659	2.3738	1.0561	0.6231	3.4618
MOBopl	Olfactory areas	2.3504	1.6332	4.1882	1.8013	1.0938	5.0990
MOBmi	Olfactory areas	2.3984	1.7161	3.9813	1.6560	1.0203	4.3944
MOBipl	Olfactory areas	2.6196	1.8784	4.3268	1.8356	1.1231	5.0210
MOBgr	Olfactory areas	2.6773	1.9520	4.2603	2.7559	1.5250	14.2868
AON1	Olfactory areas	4.7411	3.2573	8.7013	3.2868	2.0967	7.6004
AON2	Olfactory areas	4.2214	2.9087	7.6956	2.8752	1.7740	7.5817
PIR1	Olfactory areas	4.1506	2.9185	7.1814	3.1162	1.8995	8.6697
PIR2	Olfactory areas	3.4331	2.2711	7.0270	2.7396	1.7306	6.5697
PIR3	Olfactory areas	3.9428	2.6206	7.9535	2.6362	1.6408	6.7027
CA1so	Hippocampal formation	5.1573	3.5674	9.3040	4.1882	2.8550	7.8573
CA1sp	Hippocampal formation	3.6578	2.2726	9.3492	3.5202	2.3465	7.0430
CA1sr	Hippocampal formation	5.8991	4.1630	10.1308	4.4526	3.0862	7.9901
CA1slm	Hippocampal formation	5.5809	3.8854	9.9092	4.3693	2.9892	8.1161
CA2so	Hippocampal formation	1.4157	0.9220	3.0481	1.2555	0.8031	2.8753

CA2sp	Hippocampal formation	1.6763	1.0070	4.9975	1.3050	0.7871	3.8159
CA2sr	Hippocampal formation	1.8131	1.1516	4.2603	1.4194	0.9110	3.2120
CA2slm	Hippocampal formation	2.4051	1.4951	6.1395	1.3764	0.8672	3.3329
CA3so	Hippocampal formation	2.9596	1.9394	6.2446	2.5317	1.6131	5.8808
CA3sp	Hippocampal formation	2.7332	1.7588	6.1286	2.2621	1.4463	5.1890
CA3sr	Hippocampal formation	3.1738	2.1433	6.1070	3.0680	1.9787	6.8261
CA3slm	Hippocampal formation	2.9877	1.8795	7.2779	2.6247	1.6451	6.4889
DG-mo	Hippocampal formation	3.2209	2.1262	6.6457	2.4457	1.6525	4.7034
DG-po	Hippocampal formation	3.7549	2.5739	6.9329	2.6436	1.8073	4.9201
DG-sg	Hippocampal formation	2.4270	1.4808	6.7231	2.0878	1.3250	4.9208
SUB	Hippocampal formation	6.3533	4.8438	9.2174	4.5177	3.3459	6.9523
CLA	Cortical subplate	4.3026	3.1767	6.6649	3.6938	2.5524	6.6819
EPd	Cortical subplate	4.2524	2.9584	7.5531	3.3528	2.1485	7.6295
CP	Striatum	4.9264	3.5455	8.0636	3.7970	2.6656	6.5976
ACB	Striatum	4.5482	3.1883	7.9389	3.3748	2.2994	6.3400
FS	Striatum	5.4279	2.9124	40.0200	5.8143	2.8428	128.5200
OT1	Striatum	4.3403	3.2194	6.6585	3.6854	2.2315	10.5756
OT2	Striatum	3.3895	2.3512	6.0696	3.0953	2.0884	5.9767
OT3	Striatum	4.0299	2.7949	7.2210	3.6495	2.3744	7.8822
GPi	Pallidum	3.1665	1.6279	57.7142	3.8131	2.3352	10.3859
SI	Pallidum	5.0447	3.2944	10.7732	3.9093	2.3378	11.9262
MA	Pallidum	3.5803	2.3641	7.3708	2.7159	1.5674	10.1613
LD	Thalamus	3.7326	2.3393	9.2272	2.5273	1.5328	7.1969
LP	Thalamus	3.6889	2.3959	8.0244	3.5671	2.1843	9.7216
PO	Thalamus	2.9210	1.8140	7.4902	2.4893	1.5218	6.8338
RT	Thalamus	3.7027	2.4160	7.9298	3.3927	2.1198	8.4923
VPL	Thalamus	2.6029	1.5211	9.0066	2.1231	1.2801	6.2171
VPM	Thalamus	2.3976	1.4224	7.6195	2.0469	1.2341	5.9953
SPFp	Thalamus	4.1456	2.8097	7.8946	3.0950	2.0686	6.1431
LHA	Hypothalamus	4.9546	3.3502	9.5121	4.2206	2.6517	10.3356
STN	Hypothalamus	3.7589	2.4484	8.0881	2.9997	1.7360	11.0260
ZI	Hypothalamus	4.3349	2.9533	8.1547	3.8292	2.2851	11.8095
IC	Midbrain	4.0346	2.8200	7.0910	2.9600	2.0926	5.0554
SCm	Midbrain	4.7770	3.4297	7.8686	3.6057	2.3255	8.0217
SCs	Midbrain	4.6087	3.3308	7.4725	3.5963	2.2046	9.7532
SNc	Midbrain	4.2137	2.8246	8.2902	3.9882	2.5692	8.9081
SNr	Midbrain	5.3155	3.5933	10.1948	4.3076	2.7955	9.3822
APN	Midbrain	4.0066	2.7430	7.4189	3.4625	2.0040	12.7210
NOT	Midbrain	4.5813	3.1293	8.5405	3.5129	2.2634	7.8423
PPN	Midbrain	4.0229	2.8929	6.6014	3.2743	2.0430	8.2418
PPT	Midbrain	4.4547	3.1083	7.8499	3.3345	2.1454	7.4805
RR	Midbrain	4.4662	3.1251	7.8277	3.7673	2.4221	8.4728
MRN	Midbrain	4.6272	3.3356	7.5416	3.5316	2.3604	7.0095
P	Pons	3.9608	2.6486	7.8544	3.6891	2.3307	8.8431
MY	Medulla	3.8064	2.6537	6.7296	3.1247	2.0689	6.3812
IP	Cerebellum	2.1935	1.5604	3.6909	2.1555	1.4649	4.0776
ANcr2gr	Cerebellum	3.8465	2.8905	5.7475	3.2314	2.0541	7.5712
ANcr2mo	Cerebellum	4.1431	3.0098	6.6393	3.6958	2.0621	17.7875
CENT3gr	Cerebellum	3.4832	2.5615	5.4407	2.5374	1.5649	6.7030
CENT3mo	Cerebellum	3.4797	2.5990	5.2591	2.5109	1.7268	4.5997
CUL4,5gr	Cerebellum	3.8810	2.8572	6.0484	3.0372	2.0374	5.9634
CUL4,5mo	Cerebellum	3.5491	2.7397	5.0337	2.8348	1.9767	5.0096
SIMgr	Cerebellum	3.9813	2.9916	5.9498	3.4967	2.3779	6.6039
SIMmo	Cerebellum	3.7733	2.8583	5.5541	3.1831	2.1346	6.2561
PRMgr	Cerebellum	3.5239	2.6887	5.1155	2.8028	1.9675	4.8708
PRMmo	Cerebellum	4.5813	2.6918	15.4033	3.5457	2.0751	12.1729
COPYgr	Cerebellum	4.0276	2.8006	7.1665	3.1157	1.8238	10.6818
COPYmo	Cerebellum	4.5039	3.0562	8.5563	3.6726	2.0867	15.2999

	PSD95 puncta density (/ 100um2)									
	Day 0		Day 1.5		Day 3		Day 7		Day 14	
Brain subregion	**MEAN**	SD	**MEAN**	SD	**MEAN**	SD	**MEAN**	SD	**MEAN**	SD
ORB1	62.8687	11.4417	65.6859	10.4541	66.2266	4.6247	43.7134	10.1226	24.0173	9.1668
ORB2-3	59.3126	13.8279	58.2794	11.7704	59.5634	4.7418	33.9976	11.1842	14.4212	7.4156
ORB5	53.5819	14.6930	51.3053	12.3307	51.1972	5.8436	24.3127	10.3227	6.9741	4.2135
ORB6a	45.3404	14.9908	41.3984	12.7191	40.5198	5.9146	16.0179	8.9564	2.9059	2.2706
ORB6b	23.0066	12.1634	14.8942	6.3028	17.3811	6.2472	5.9005	4.5664	0.6623	0.7041
FRP1	62.1839	11.9902	64.9020	10.9018	65.8945	4.9560	42.7557	19.7491	27.1394	8.0717
FRP2-3	59.0363	14.7934	61.2123	11.3051	59.9959	5.2302	38.3689	10.6226	17.0027	7.6832
MO1	67.2778	12.1222	69.2405	9.8815	73.3358	5.6865	50.7879	10.8619	28.1936	10.7256
MO2-3	61.1267	14.6468	61.9421	10.8651	64.6317	5.9441	39.5738	11.9611	16.3134	8.4269
MO5	50.6986	15.8797	50.5214	10.8230	51.1161	6.0704	25.6720	10.3920	7.5688	4.8452
MO6a	38.9490	15.8529	36.8030	12.0468	36.5463	7.0140	14.2262	8.0768	1.8111	1.7181
MO6b	21.7451	15.3823	15.4078	9.9708	20.2734	9.8383	6.2713	4.9863	0.4460	0.4851
SS1	69.6685	13.4310	71.9572	9.4151	75.8227	5.3447	46.3238	25.0742	26.2473	11.6406
SS2-3	64.4906	9.8576	64.0776	9.7314	67.1186	4.3725	37.6429	19.2467	15.8673	9.1418
SS4	62.1959	12.6550	59.4552	12.6867	62.5909	5.4017	27.6182	17.2005	8.5013	5.9417
SS5	54.6272	14.2378	51.8459	12.6358	52.6704	4.3000	21.9648	13.4972	5.0278	3.9415
SS6a	42.2048	16.2173	38.6547	14.9451	39.1548	5.1221	14.5505	10.6408	1.7570	1.7661
SS6b	19.9070	16.6429	11.2855	9.4419	19.2598	9.4262	5.0201	4.5660	0.3244	0.3834
PTLp1	69.1760	21.4804	73.0114	7.7650	74.6333	7.9864	45.8913	25.4664	24.7471	11.4766
PTLp2-3	64.4065	14.0416	64.9155	10.4137	68.6729	4.9933	37.9828	20.0892	16.3404	9.5498
PTLp4	63.4093	11.2112	63.6180	13.3662	65.5238	4.6843	32.9009	20.0404	10.4746	6.9194
PTLp5	62.1599	10.2356	58.5227	12.1266	59.2120	5.6583	25.5329	15.7972	6.1091	5.1932
PTLp6a	49.0647	12.8816	45.4666	14.2247	45.9396	4.9223	17.6707	12.5484	2.7842	2.5336
PTLp6b	21.1925	15.8660	16.6242	8.4331	26.6934	5.0184	8.1094	6.8836	0.7569	0.8335
VIS1	71.0622	12.7020	71.5652	7.3562	71.7950	5.3347	42.1224	20.1843	20.2194	8.9707
VIS2-3	60.9104	20.8680	64.5506	9.0891	62.7801	6.3803	36.6853	18.2710	13.8265	7.7615
VIS4	60.3217	21.9105	61.6583	9.8433	58.6984	10.9444	29.3019	17.0043	8.6230	5.6004
VIS5	61.6313	10.2049	56.8873	11.9048	50.7917	18.6537	24.2200	15.0627	5.1089	4.2501
VIS6a	52.2604	8.9228	44.6421	14.7350	41.3038	8.4902	16.0488	12.0092	1.8652	1.9546
VIS6b	25.1451	13.2869	17.3946	8.1644	18.9759	7.9470	7.4143	7.7335	0.5677	0.7025
RSPd1	60.2256	12.7867	56.4277	16.2005	56.6440	6.3615	24.8224	13.9231	7.4471	5.1156
RSPd2-3	59.2044	11.7267	54.6031	16.3184	55.2924	7.2486	22.4282	14.0816	5.1089	4.3291
RSPd5	58.1232	13.7759	46.0072	15.4438	50.1024	8.9229	17.4699	11.9389	3.6898	3.6211
RSPv1	39.6098	10.6863	34.3567	13.5016	38.4790	10.0775	14.8286	10.1971	2.6085	2.3650
RSPv2-3	28.4609	11.0648	21.9629	11.3662	23.5577	7.3639	6.3794	6.2579	0.5406	0.5780
RSPv5	46.3496	16.3436	36.6138	12.6089	41.2632	10.2358	13.8554	10.9998	2.3923	2.0454
RSPv6a	34.3357	15.0227	26.2068	12.4444	23.9632	9.5385	7.4143	6.6439	0.8380	1.0040
MOBgl	16.7130	9.2859	6.7038	4.1050	2.9039	1.3264	0.1622	0.1081	0.0000	0.0000
MOBopl	29.5954	12.3101	20.7600	10.5918	13.8400	4.7608	0.4685	0.4621	0.0000	0.0000
MOBmi	11.0596	4.0576	7.7232	3.4706	5.2981	1.5681	0.2883	0.3256	0.0000	0.0000
MOBipl	14.0563	4.5172	11.2630	4.7557	7.1980	2.5487	0.4685	0.4621	0.0000	0.0000
MOBgr	11.1214	3.5966	8.0630	3.3934	6.4875	1.6327	0.3398	0.4972	0.0000	0.0000
AON1	53.3732	21.3477	48.5346	20.7952	45.3179	9.8979	16.4710	10.4424	1.7300	1.9180
AON2	47.7913	20.1546	41.2497	18.2382	38.0465	9.5123	11.6054	8.8156	0.8920	1.0106
PIR1	43.6149	15.7735	37.6680	15.3527	35.2796	9.4047	10.4521	6.5858	0.3244	0.3655
PIR2	27.1123	13.0034	20.6113	9.9788	19.4007	7.9707	3.5501	2.8430	0.0811	0.1609
PIR3	32.6943	14.3397	28.8018	13.7452	25.6689	6.7790	7.4967	5.6832	0.1352	0.1981
CA1so	78.1984	29.9527	68.4296	29.4221	76.6201	15.3265	25.3321	18.7213	4.2439	3.6143
CA1sp	20.7480	11.1490	14.1779	10.4647	15.2727	7.7849	3.8616	3.8833	0.2433	0.2695
CA1sr	73.9815	24.8801	69.2270	24.2705	74.9982	17.5769	30.8311	18.9683	7.2038	5.5462
CA1slm	63.1810	25.1845	62.0232	19.6284	66.7537	8.4565	24.0810	19.6760	3.4059	3.9568
CA2so	45.0521	27.2038	20.2059	18.7568	11.8127	6.8567	0.9113	1.0628	0.0000	0.0000
CA2sp	3.7964	2.8234	1.6895	1.8709	1.3516	0.6715	0.2317	0.3085	0.0811	0.1119
CA2sr	33.3866	20.7457	18.6921	17.0026	11.0152	4.3124	1.6682	1.7467	0.0541	0.1001
CA2slm	47.4789	28.1930	32.9916	27.9523	23.4361	11.7519	0.6024	0.7059	0.0000	0.0000
CA3so	30.3591	16.6347	23.5848	14.3929	17.4487	5.7062	3.1202	3.1059	0.0270	0.0765

CA3sp	13.8160	7.9804	9.5961	6.0701	7.8661	3.8161	0.8496	0.9800	0.0541	0.1001
CA3sr	33.6389	16.0682	27.1934	14.7615	21.2601	7.1222	3.6454	3.5515	0.0270	0.0765
CA3slm	42.9857	24.5085	34.0594	24.8798	27.0313	10.5876	2.2088	2.2193	0.1757	0.2448
DG-mo	64.4065	33.2548	49.0752	28.4526	42.6283	16.2249	7.1208	6.0300	0.1892	0.3152
DG-po	21.6490	10.0536	18.8678	8.3801	16.8405	4.2697	3.1974	3.0119	0.0676	0.1284
DG-sg	5.1059	3.2955	3.2573	2.8352	2.5950	1.4803	0.2163	0.2163	0.0000	0.0000
SUB	46.5418	11.0010	42.7364	9.8807	44.1555	5.5048	20.1421	10.8034	8.0959	5.7874
CLA	40.0333	14.2867	37.0405	9.9676	32.2348	6.3723	10.3337	8.1685	1.1894	1.3331
EPd	29.4370	11.3110	27.1394	12.4559	23.3955	4.3250	7.5688	5.2776	0.2163	0.2312
CP	44.5956	14.7478	40.9253	15.2258	42.3309	6.6097	13.5002	8.4530	1.7570	1.7278
ACB	40.9794	15.8279	37.8438	15.6534	32.8295	8.0158	11.9555	8.2068	2.0698	1.5130
FS	5.1089	4.2363	4.1628	2.5685	6.0009	3.9211	1.5138	1.5189	0.2703	0.3419
OT1	41.7603	12.9649	38.2763	8.2949	31.8042	7.5410	11.4613	5.9788	0.7569	0.8837
OT2	27.0177	12.1266	21.6559	7.6164	16.5740	6.0139	5.0458	2.9923	0.2163	0.2792
OT3	30.7616	13.3741	28.9621	9.5315	22.3973	7.0636	7.4426	3.9665	0.2780	0.3686
GPi	5.6766	6.3583	3.3982	1.9571	3.5321	1.0204	1.0813	1.1027	0.1622	0.2519
SI	8.8392	4.1668	7.9858	4.2157	8.0630	2.0237	3.0893	2.3614	0.4325	0.4325
MA	12.2722	4.8060	10.2178	5.8287	7.8931	3.8265	2.6722	2.2618	0.1545	0.2057
LD	32.3294	17.6326	26.1663	17.1490	27.3016	11.2401	3.3055	3.9751	0.1081	0.1156
LP	28.7252	15.1844	22.6522	13.6273	23.1658	6.8398	3.5218	2.9853	0.1622	0.1917
PO	30.1549	17.2848	21.1655	16.6837	19.4084	9.5771	1.5138	1.7613	0.0000	0.0000
RT	10.1638	4.7991	8.5284	5.2423	7.9472	2.9076	1.3902	1.4870	0.0270	0.0765
VPL	18.1410	12.2551	12.3668	11.6268	10.3259	7.2017	0.3089	0.4299	0.0000	0.0000
VPM	24.2440	15.1153	15.8133	15.1297	12.4884	10.2164	0.2471	0.3625	0.0000	0.0000
SPFp	14.6930	6.3266	12.5966	6.4718	12.0559	3.4869	3.1820	2.6857	0.2433	0.2933
LHA	10.9326	4.4359	10.5963	5.2730	10.0093	1.7994	3.6145	2.8077	0.5406	0.6116
STN	12.4344	5.8493	10.9052	6.5650	9.3451	3.5533	2.1934	2.3280	0.1622	0.2238
ZI	9.2507	3.3182	7.7039	4.3756	7.9202	2.0932	2.2243	1.9965	0.1892	0.2695
IC	14.3686	5.3542	10.7044	4.0867	12.2857	4.0892	2.6568	2.0881	0.1352	0.1609
SCm	11.1489	3.9949	9.9610	3.7857	9.7583	1.5993	3.4291	2.4352	0.4866	0.4439
SCs	18.3813	6.5939	16.0430	5.6568	15.9755	2.6747	5.0201	3.7236	0.8109	0.7288
SNc	6.7278	2.9620	5.5955	3.0307	5.7036	1.6180	1.3902	1.2785	0.2163	0.2585
SNr	5.9108	2.4609	5.0548	2.6332	5.2981	0.9740	2.1625	1.6563	0.5136	0.5772
APN	10.8005	4.6237	8.9203	4.3462	9.1230	2.1855	1.8999	1.6157	0.0541	0.1001
NOT	11.7256	4.9307	11.2315	4.9321	10.6773	2.3737	3.0121	2.8989	0.2433	0.2435
PPN	7.5207	2.4698	5.8928	2.6997	5.5684	1.3014	1.8845	1.5429	0.1352	0.2568
PPT	10.6203	4.0191	9.4474	4.3184	9.2582	1.7925	2.6722	2.2721	0.2433	0.1805
RR	9.0224	2.6994	7.0281	3.9263	7.1363	2.0087	2.7649	1.9955	0.2973	0.3257
MRN	9.5871	3.2311	8.0013	3.3261	7.9472	1.3616	2.9039	2.0737	0.4325	0.4325
P	6.3674	2.6510	5.1630	2.7070	5.0008	1.4035	1.1173	1.1395	0.0927	0.1156
MY	7.5928	2.3921	6.5184	2.9451	5.8748	0.9517	1.2615	1.1719	0.0360	0.0883
IP	3.6763	1.4222	2.1895	1.4411	1.6759	0.4870	0.1236	0.1156	0.0000	0.0000
ANcr2gr	14.3961	2.7921	12.2614	3.6520	11.5910	1.0212	2.5301	1.5474	0.0000	0.0000
ANcr2mo	15.1015	3.2865	13.8833	3.3585	12.3695	1.2921	2.7392	2.3820	0.0360	0.0883
CENT3gr	14.8942	4.4170	10.7449	4.3346	11.1639	2.6026	1.9463	1.7657	0.0000	0.0000
CENT3mo	15.0294	4.5287	11.6775	4.6004	10.7314	1.6788	2.1934	1.7982	0.0000	0.0000
CUL4,5gr	15.7262	4.4276	13.0561	4.6824	13.1777	2.6551	2.3479	2.1604	0.0000	0.0000
CUL4,5mo	14.8852	3.7048	11.4477	3.6855	10.7314	1.6907	2.3479	1.8537	0.0000	0.0000
SIMgr	16.5895	2.4899	13.3210	4.8659	13.0183	1.0856	3.8493	2.9548	0.0360	0.0883
SIMmo	12.9930	1.5838	10.3800	3.4431	9.5691	0.6211	2.9194	2.1589	0.0000	0.0000
PRMgr	15.8583	2.1783	11.4396	3.4059	12.2722	1.6786	2.7248	1.7000	0.0000	0.0000
PRMmo	13.5697	7.3976	13.1048	3.2206	13.6238	1.0813	3.1717	3.0378	0.0360	0.0883
COPYgr	13.1604	4.0580	10.9855	3.8301	11.1153	0.9743	2.2706	1.5544	0.0000	0.0000
COPYmo	14.5505	4.0605	12.8236	3.9325	12.7588	0.8784	2.8113	3.9757	0.0000	0.0000

	PSD95 puncta intensity (AU)									
	Day 0		Day 1.5		Day 3		Day 7		Day 14	
Brain subregion	MEAN	SD	MEAN	SD	MEAN	SD	MEAN	SD	MEAN	SD
ORB1	2.0E+10	7.9E+09	1.9E+10	8.4E+09	1.7E+10	3.1E+09	8.3E+09	3.4E+09	3.4E+09	1.4E+09
ORB2-3	3.5E+10	1.4E+10	2.9E+10	1.1E+10	2.6E+10	4.7E+09	1.2E+10	4.4E+09	3.8E+09	1.9E+09
ORB5	2.6E+10	1.2E+10	2.1E+10	8.9E+09	1.8E+10	3.7E+09	7.2E+09	3.6E+09	1.5E+09	9.1E+08
ORB6a	1.8E+10	8.2E+09	1.5E+10	6.6E+09	1.2E+10	2.4E+09	4.0E+09	2.5E+09	6.2E+08	4.7E+08
ORB6b	1.7E+09	9.9E+08	1.1E+09	5.6E+08	1.0E+09	4.5E+08	2.9E+08	2.3E+08	3.4E+07	4.0E+07
FRP1	3.6E+09	1.9E+09	3.8E+09	1.5E+09	3.3E+09	8.3E+08	1.7E+09	8.3E+08	7.2E+08	2.8E+08
FRP2-3	4.5E+09	2.1E+09	4.1E+09	1.4E+09	3.6E+09	9.6E+08	1.8E+09	8.3E+08	5.8E+08	2.9E+08
MO1	3.8E+10	1.4E+10	3.4E+10	1.0E+10	3.2E+10	7.8E+09	1.7E+10	7.0E+09	7.0E+09	3.0E+09
MO2-3	8.4E+10	3.3E+10	7.3E+10	2.2E+10	6.9E+10	1.2E+10	3.2E+10	1.4E+10	1.0E+10	5.3E+09
MO5	6.6E+10	2.8E+10	5.5E+10	1.9E+10	5.1E+10	7.7E+09	2.0E+10	1.0E+10	4.3E+09	2.7E+09
MO6a	1.4E+10	7.2E+09	1.1E+10	4.9E+09	1.0E+10	2.4E+09	3.1E+09	2.0E+09	3.4E+08	3.1E+08
MO6b	1.5E+09	1.2E+09	9.8E+08	7.9E+08	1.1E+09	6.9E+08	2.9E+08	2.4E+08	1.8E+07	1.9E+07
SS1	2.1E+10	7.9E+09	1.8E+10	5.4E+09	1.8E+10	3.7E+09	7.5E+09	4.7E+09	3.2E+09	1.7E+09
SS2-3	4.4E+10	1.4E+10	3.7E+10	1.0E+10	3.3E+10	3.4E+09	1.3E+10	7.6E+09	4.5E+09	2.8E+09
SS4	1.3E+10	4.8E+09	1.0E+10	3.8E+09	9.3E+09	1.2E+09	3.0E+09	2.0E+09	7.5E+08	5.6E+08
SS5	3.6E+10	1.3E+10	2.7E+10	9.8E+09	2.5E+10	3.0E+09	7.6E+09	4.9E+09	1.4E+09	1.1E+09
SS6a	1.3E+10	6.4E+09	9.1E+09	4.4E+09	8.1E+09	1.4E+09	2.2E+09	1.7E+09	2.5E+08	2.2E+08
SS6b	9.7E+08	9.4E+08	5.2E+08	4.8E+08	6.8E+08	5.4E+08	1.2E+08	1.1E+08	1.0E+07	1.0E+07
PTLp1	3.7E+09	1.8E+09	3.3E+09	1.2E+09	2.9E+09	6.3E+08	1.3E+09	8.1E+08	5.3E+08	3.2E+08
PTLp2-3	5.6E+09	1.6E+09	4.9E+09	1.4E+09	4.7E+09	7.6E+08	1.9E+09	1.1E+09	6.3E+08	3.9E+08
PTLp4	1.5E+09	4.0E+08	1.3E+09	5.0E+08	1.2E+09	2.1E+08	4.2E+08	2.8E+08	1.1E+08	7.3E+07
PTLp5	3.7E+09	8.6E+08	3.0E+09	1.0E+09	2.7E+09	4.2E+08	8.8E+08	5.8E+08	1.6E+08	1.3E+08
PTLp6a	1.4E+09	6.4E+08	1.1E+09	4.7E+08	1.0E+09	1.6E+08	3.0E+08	2.3E+08	3.6E+07	3.2E+07
PTLp6b	1.1E+08	9.7E+07	8.6E+07	8.1E+07	9.9E+07	5.5E+07	2.0E+07	1.9E+07	2.4E+06	2.3E+06
VIS1	2.6E+10	6.7E+09	2.2E+10	7.2E+09	2.1E+10	4.8E+09	8.6E+09	4.2E+09	3.3E+09	1.6E+09
VIS2-3	4.0E+10	1.7E+10	3.6E+10	1.1E+10	3.1E+10	7.7E+09	1.5E+10	7.4E+09	4.0E+09	2.7E+09
VIS4	1.4E+10	5.7E+09	1.2E+10	4.2E+09	1.1E+10	2.7E+09	4.4E+09	2.7E+09	8.8E+08	6.5E+08
VIS5	2.9E+10	8.4E+09	2.4E+10	8.8E+09	2.0E+10	6.7E+09	7.6E+09	4.8E+09	1.1E+09	1.0E+09
VIS6a	1.2E+10	3.4E+09	9.6E+09	4.8E+09	7.8E+09	2.2E+09	2.5E+09	1.9E+09	2.2E+08	2.3E+08
VIS6b	1.4E+09	7.6E+08	1.1E+09	7.2E+08	9.9E+08	4.5E+08	3.2E+08	3.2E+08	2.4E+07	2.6E+07
RSPd1	1.4E+09	6.1E+08	1.2E+09	5.1E+08	1.2E+09	2.1E+08	4.4E+08	2.9E+08	8.0E+07	6.0E+07
RSPd2-3	3.4E+09	1.5E+09	3.2E+09	1.7E+09	3.2E+09	1.0E+09	1.0E+09	6.6E+08	1.7E+08	1.5E+08
RSPd5	7.8E+08	3.4E+08	5.2E+08	3.1E+08	6.6E+08	2.1E+08	1.7E+08	1.1E+08	2.1E+07	2.5E+07
RSPv1	2.1E+09	8.9E+08	1.7E+09	1.4E+09	1.8E+09	7.9E+08	6.4E+08	5.6E+08	7.4E+07	6.8E+07
RSPv2-3	1.2E+09	5.5E+08	8.6E+08	5.5E+08	8.9E+08	2.7E+08	2.3E+08	2.4E+08	2.0E+07	1.7E+07
RSPv5	2.4E+09	1.2E+09	1.5E+09	7.2E+08	2.0E+09	9.3E+08	4.7E+08	4.2E+08	5.8E+07	4.9E+07
RSPv6a	2.1E+09	1.1E+09	1.2E+09	6.8E+08	1.3E+09	5.5E+08	3.1E+08	2.9E+08	2.9E+07	3.3E+07
MOBgl	5.7E+09	4.7E+09	2.1E+09	1.5E+09	8.5E+08	3.2E+08	6.2E+07	3.8E+07	1.2E+07	9.6E+06
MOBopl	1.6E+10	1.3E+10	8.3E+09	5.5E+09	5.9E+09	2.2E+09	1.4E+08	1.1E+08	1.1E+07	7.0E+06
MOBmi	1.5E+09	1.1E+09	7.5E+08	4.8E+08	5.0E+08	2.3E+08	2.0E+07	1.9E+07	4.7E+06	3.6E+06
MOBipl	2.1E+09	1.5E+09	1.0E+09	4.9E+08	7.9E+08	4.4E+08	2.5E+07	2.4E+07	2.0E+06	1.6E+06
MOBgr	5.3E+09	2.6E+09	3.0E+09	2.5E+09	3.7E+09	3.8E+09	9.1E+07	1.6E+08	1.8E+07	1.7E+07
AON1	2.5E+10	1.4E+10	1.5E+10	9.4E+09	1.5E+10	5.1E+09	4.7E+09	3.7E+09	4.8E+08	4.9E+08
AON2	1.7E+10	9.4E+09	9.5E+09	6.9E+09	1.0E+10	6.3E+09	1.9E+09	1.7E+09	2.6E+08	3.4E+08
PIR1	6.6E+09	4.2E+09	5.4E+09	3.7E+09	3.8E+09	1.5E+09	9.5E+08	6.2E+08	7.2E+07	7.6E+07
PIR2	4.1E+09	2.6E+09	3.0E+09	1.7E+09	2.1E+09	8.6E+08	3.9E+08	2.8E+08	3.2E+07	3.9E+07
PIR3	2.8E+09	1.8E+09	2.0E+09	1.1E+09	1.4E+09	5.7E+08	3.3E+08	2.4E+08	1.7E+07	2.0E+07
CA1so	1.2E+10	5.1E+09	9.1E+09	4.9E+09	9.6E+09	2.1E+09	2.7E+09	2.0E+09	3.5E+08	2.8E+08
CA1sp	1.8E+09	8.9E+08	1.3E+09	7.6E+08	1.2E+09	4.3E+08	3.7E+08	2.7E+08	4.5E+07	4.2E+07
CA1sr	2.0E+10	8.5E+09	1.6E+10	7.3E+09	1.7E+10	4.7E+09	5.5E+09	3.5E+09	9.9E+08	7.2E+08
CA1slm	7.9E+09	3.7E+09	6.9E+09	3.0E+09	6.6E+09	1.5E+09	2.0E+09	1.6E+09	2.5E+08	2.7E+08
CA2so	5.9E+08	3.8E+08	2.5E+08	2.5E+08	1.3E+08	6.7E+07	1.2E+07	1.2E+07	5.5E+05	7.4E+05
CA2sp	7.7E+07	6.2E+07	3.0E+07	2.9E+07	2.0E+07	8.9E+06	3.9E+06	4.2E+06	1.1E+06	1.2E+06
CA2sr	6.5E+08	4.3E+08	2.8E+08	2.5E+08	1.7E+08	8.3E+07	3.2E+07	3.5E+07	1.0E+06	1.3E+06
CA2slm	9.0E+08	6.2E+08	3.8E+08	3.4E+08	2.4E+08	1.7E+08	1.3E+07	1.5E+07	2.6E+05	3.6E+05
CA3so	1.7E+09	1.0E+09	1.2E+09	9.2E+08	8.4E+08	2.7E+08	1.3E+08	1.2E+08	1.4E+06	2.4E+06

CA3sp	1.1E+09	7.1E+08	6.5E+08	3.9E+08	4.9E+08	2.2E+08	6.1E+07	6.5E+07	7.7E+06	8.9E+06
CA3sr	2.1E+09	1.1E+09	1.8E+09	1.2E+09	1.3E+09	4.1E+08	2.1E+08	2.1E+08	4.6E+06	6.7E+06
CA3slm	4.2E+08	2.4E+08	3.2E+08	2.6E+08	2.0E+08	6.6E+07	3.3E+07	3.8E+07	1.3E+06	1.7E+06
DG-mo	2.1E+10	1.1E+10	1.4E+10	8.5E+09	1.1E+10	3.4E+09	1.4E+09	1.1E+09	6.2E+07	6.8E+07
DG-po	1.1E+09	5.8E+08	7.9E+08	4.1E+08	6.0E+08	1.9E+08	8.8E+07	8.4E+07	3.8E+06	3.8E+06
DG-sg	1.0E+09	6.5E+08	5.9E+08	4.4E+08	4.2E+08	2.1E+08	4.4E+07	3.9E+07	2.4E+06	2.7E+06
SUB	1.2E+10	4.4E+09	9.7E+09	3.1E+09	8.3E+09	1.3E+09	3.7E+09	2.0E+09	1.1E+09	6.5E+08
CLA	5.1E+09	2.5E+09	4.8E+09	2.0E+09	3.7E+09	1.2E+09	9.1E+08	6.5E+08	1.4E+08	1.5E+08
EPd	5.0E+09	2.8E+09	3.9E+09	2.4E+09	3.1E+09	9.9E+08	8.2E+08	5.4E+08	3.1E+07	3.1E+07
CP	1.3E+11	5.8E+10	1.0E+11	4.6E+10	9.0E+10	1.2E+10	2.7E+10	1.7E+10	3.6E+09	2.9E+09
ACB	6.2E+10	3.3E+10	5.1E+10	2.3E+10	3.6E+10	1.0E+10	1.3E+10	9.4E+09	2.2E+09	1.4E+09
FS	2.7E+08	1.9E+08	3.4E+08	3.6E+08	4.0E+08	2.8E+08	8.1E+07	7.5E+07	2.4E+07	2.9E+07
OT1	7.8E+09	5.9E+09	8.0E+09	2.8E+09	5.0E+09	1.4E+09	1.4E+09	8.9E+08	1.4E+08	1.5E+08
OT2	5.5E+09	2.9E+09	4.7E+09	2.0E+09	2.9E+09	7.9E+08	8.7E+08	5.2E+08	4.4E+07	4.1E+07
OT3	6.6E+09	3.7E+09	6.2E+09	2.7E+09	4.5E+09	1.5E+09	1.2E+09	6.4E+08	7.7E+07	7.8E+07
GPi	7.3E+08	4.3E+08	6.1E+08	3.9E+08	5.4E+08	2.9E+08	1.5E+08	1.6E+08	2.5E+07	3.5E+07
SI	6.0E+09	3.8E+09	5.2E+09	3.8E+09	4.0E+09	2.0E+09	1.6E+09	1.3E+09	1.7E+08	1.5E+08
MA	1.2E+09	7.3E+08	1.0E+09	8.7E+08	5.1E+08	3.1E+08	1.6E+08	1.4E+08	6.4E+06	6.2E+06
LD	4.9E+09	3.5E+09	2.9E+09	2.0E+09	2.7E+09	1.7E+09	2.6E+08	2.7E+08	1.5E+07	1.5E+07
LP	4.3E+09	2.8E+09	3.4E+09	2.2E+09	3.3E+09	1.6E+09	5.7E+08	4.9E+08	4.6E+07	4.6E+07
PO	1.5E+10	9.8E+09	9.2E+09	7.9E+09	8.2E+09	4.4E+09	6.2E+08	6.6E+08	2.7E+07	2.6E+07
RT	2.6E+09	1.6E+09	2.0E+09	1.3E+09	1.9E+09	9.2E+08	2.8E+08	2.9E+08	1.2E+07	1.5E+07
VPL	5.1E+09	3.8E+09	3.0E+09	2.7E+09	2.3E+09	1.4E+09	1.5E+08	1.6E+08	1.6E+07	1.9E+07
VPM	1.1E+10	7.1E+09	6.7E+09	6.5E+09	4.2E+09	3.1E+09	1.5E+08	2.0E+08	2.7E+07	3.6E+07
SPFp	1.8E+09	8.8E+08	1.4E+09	8.1E+08	1.0E+09	4.0E+08	2.6E+08	2.1E+08	2.4E+07	2.5E+07
LHA	8.3E+09	4.1E+09	7.4E+09	5.1E+09	6.3E+09	2.4E+09	2.3E+09	1.9E+09	3.0E+08	3.4E+08
STN	1.2E+09	8.2E+08	9.5E+08	7.5E+08	7.1E+08	5.4E+08	1.0E+08	1.0E+08	9.4E+06	1.1E+07
ZI	3.9E+09	2.7E+09	3.0E+09	2.1E+09	3.0E+09	1.6E+09	7.3E+08	7.3E+08	6.3E+07	7.2E+07
IC	2.0E+10	8.5E+09	1.2E+10	5.8E+09	1.2E+10	2.9E+09	2.6E+09	1.9E+09	2.7E+08	2.6E+08
SCm	7.8E+09	4.5E+09	5.5E+09	3.1E+09	5.7E+09	2.2E+09	1.3E+09	9.8E+08	2.1E+08	1.8E+08
SCs	8.5E+09	4.9E+09	5.5E+09	2.9E+09	6.7E+09	4.4E+09	1.1E+09	9.1E+08	2.3E+08	1.9E+08
SNc	9.0E+08	4.4E+08	6.7E+08	4.3E+08	7.4E+08	2.9E+08	1.6E+08	1.4E+08	3.5E+07	4.1E+07
SNr	3.2E+09	1.6E+09	2.6E+09	1.7E+09	2.2E+09	6.3E+08	9.8E+08	7.7E+08	2.1E+08	1.9E+08
APN	1.8E+09	1.4E+09	1.1E+09	7.4E+08	1.5E+09	7.4E+08	1.4E+08	1.2E+08	1.2E+07	1.2E+07
NOT	3.2E+08	1.8E+08	2.8E+08	1.4E+08	2.3E+08	1.3E+08	4.2E+07	4.0E+07	7.4E+06	7.7E+06
PPN	7.3E+08	5.0E+08	4.4E+08	2.3E+08	5.0E+08	1.7E+08	1.1E+08	9.3E+07	9.3E+06	9.4E+06
PPT	3.8E+08	2.0E+08	3.3E+08	2.1E+08	2.4E+08	9.7E+07	5.2E+07	4.5E+07	7.8E+06	6.2E+06
RR	5.1E+08	2.6E+08	3.3E+08	2.3E+08	3.9E+08	1.3E+08	9.3E+07	6.7E+07	1.5E+07	1.5E+07
MRN	9.6E+09	5.3E+09	7.2E+09	3.5E+09	6.4E+09	2.0E+09	1.8E+09	1.4E+09	3.0E+08	2.3E+08
P	1.6E+10	9.1E+09	1.3E+10	7.9E+09	1.2E+10	3.8E+09	2.6E+09	2.4E+09	2.6E+08	2.5E+08
MY	3.5E+10	1.5E+10	2.7E+10	1.5E+10	2.2E+10	6.1E+09	4.3E+09	4.0E+09	3.2E+08	2.9E+08
IP	7.0E+08	3.4E+08	4.2E+08	3.0E+08	3.0E+08	1.0E+08	3.0E+07	2.1E+07	2.7E+06	2.7E+06
ANcr2gr	1.1E+09	3.3E+08	9.0E+08	6.9E+08	7.6E+08	2.0E+08	1.1E+08	7.1E+07	1.5E+06	1.3E+06
ANcr2mo	1.3E+09	4.9E+08	1.3E+09	1.1E+09	9.3E+08	2.6E+08	1.7E+08	1.7E+08	2.3E+06	2.2E+06
CENT3gr	1.5E+09	9.9E+08	8.2E+08	5.7E+08	9.0E+08	6.0E+08	8.5E+07	9.8E+07	1.9E+06	2.0E+06
CENT3mo	1.7E+09	8.4E+08	8.9E+08	4.3E+08	9.8E+08	3.7E+08	1.2E+08	1.0E+08	1.8E+06	1.8E+06
CUL4,5gr	4.3E+09	2.2E+09	2.5E+09	1.1E+09	3.0E+09	1.0E+09	3.2E+08	3.0E+08	8.0E+06	6.9E+06
CUL4,5mo	4.1E+09	1.9E+09	2.3E+09	9.4E+08	2.6E+09	7.2E+08	3.6E+08	3.1E+08	8.3E+06	7.2E+06
SIMgr	4.4E+09	1.5E+09	3.6E+09	1.9E+09	3.1E+09	1.4E+08	7.4E+08	5.7E+08	1.0E+07	1.1E+07
SIMmo	4.8E+09	1.2E+09	3.7E+09	2.2E+09	3.0E+09	2.4E+08	7.5E+08	6.0E+08	1.2E+07	1.5E+07
PRMgr	2.1E+09	3.8E+08	1.4E+09	8.3E+08	1.3E+09	3.0E+08	2.0E+08	1.3E+08	4.0E+06	3.1E+06
PRMmo	2.4E+09	1.0E+09	2.1E+09	1.3E+09	1.7E+09	2.8E+08	3.4E+08	3.3E+08	5.9E+06	4.8E+06
COPYgr	3.9E+09	2.7E+09	2.5E+09	1.0E+09	2.6E+09	5.0E+08	4.4E+08	3.2E+08	8.2E+06	3.7E+06
COPYmo	3.8E+09	2.3E+09	3.1E+09	1.5E+09	2.6E+09	6.0E+08	6.0E+08	8.5E+08	8.0E+06	8.5E+06

Appendix 5: Raw numbers for CA1 gradient analysis. Mean fraction of puncta remaining (+/- SD) at day 7 compared to day 0 in different parts of the CA1 apical and basal dendrites in 3-week, 3-month, and 18-month-old animals. Puncta density values (/100 μm^2) provided. Mean (+/- SD) provided for day 0 and day 7 measurements.

		Ratio of means = mean (Day7)/mean (Day0)					
		3W		3M		18M	
Abbreviation	**Subregion**	**MEAN**	SD	**MEAN**	SD	**MEAN**	SD
CA1so_1	CA1so	0.0400	0.0575	0.4314	0.0916	0.4407	0.0486
CA1so_2	CA1so	0.0641	0.0911	0.5132	0.0576	0.5488	0.0605
CA1so_3	CA1so	0.0690	0.0981	0.5357	0.0740	0.5682	0.0724
CA1so_4	CA1so	0.0581	0.0827	0.4762	0.0877	0.5111	0.0843
CA1so_5	CA1so	0.0278	0.0397	0.3289	0.0905	0.3294	0.1018
CA1sr_1	CA1sr	0.0492	0.0700	0.4333	0.0664	0.4923	0.0614
CA1sr_2	CA1sr	0.0645	0.0917	0.4571	0.0862	0.5000	0.0696
CA1sr_3	CA1sr	0.0732	0.1040	0.4863	0.0917	0.5455	0.0560
CA1sr_4	CA1sr	0.0843	0.1197	0.5270	0.0802	0.5974	0.0723
CA1sr_5	CA1sr	0.0976	0.1384	0.5616	0.0885	0.6316	0.0716
CA1sr_6	CA1sr	0.1325	0.1373	0.5833	0.0859	0.6667	0.0544
CA1sr_7	CA1sr	0.1481	0.1580	0.6250	0.0883	0.7162	0.0622
CA1sr_8	CA1sr	0.1585	0.1734	0.6197	0.0722	0.7361	0.0577
CA1sr_9	CA1sr	0.1772	0.1720	0.6286	0.0611	0.7143	0.0657
CA1sr_10	CA1sr	0.1159	0.1352	0.5323	0.0509	0.5303	0.0955
CA1slm_1	CA1slm	0.0600	0.0857	0.3636	0.0858	0.4783	0.0851
CA1slm_2	CA1slm	0.1143	0.1623	0.5424	0.0874	0.6190	0.0814
CA1slm_3	CA1slm	0.1375	0.1947	0.6061	0.0961	0.6714	0.0812
CA1slm_4	CA1slm	0.1860	0.2392	0.6377	0.0773	0.7123	0.0857
CA1slm_5	CA1slm	0.1932	0.2497	0.6714	0.0487	0.6892	0.0744

	PSD95 puncta density (3W)				PSD95 puncta density (3M)				PSD95 puncta density (18M)			
	Day 0		Day 7		Day 0		Day 7		Day 0		Day 7	
area	MEAN	SD	MEAN	SD	MEAN	SD	MEAN	SD	MEAN	SD	MEAN	SD
CA1so_1	57.6667	14.4972	2.3067	3.2621	58.8200	7.4745	25.3733	4.3154	68.0467	6.5242	29.9867	1.6311
CA1so_2	89.9600	12.9461	5.7667	8.1553	87.6533	8.1553	44.9800	2.8251	94.5733	1.6311	51.9000	5.6502
CA1so_3	100.3400	14.9489	6.9200	9.7864	96.8800	9.7864	51.9000	4.8932	101.4933	3.2621	57.6667	7.1096
CA1so_4	99.1867	14.4972	5.7667	8.1553	96.8800	9.7864	46.1333	7.1096	103.8000	2.8251	53.0533	8.6308
CA1so_5	83.0400	17.6426	2.3067	3.2621	87.6533	10.6956	28.8333	7.1096	98.0333	3.2621	32.2933	9.9213
CA1sr_1	70.3533	10.6956	3.4600	4.8932	69.2000	7.4745	29.9867	3.2621	74.9667	3.2621	36.9067	4.3154
CA1sr_2	89.3833	12.3412	5.7667	8.1553	80.7333	8.1553	36.9067	5.8809	85.3467	1.6311	42.6733	5.8809
CA1sr_3	94.5733	13.3508	6.9200	9.7864	84.1933	10.6956	40.9433	5.7087	88.8067	1.6311	48.4400	4.8932
CA1sr_4	95.7267	11.7617	8.0733	11.4174	85.3467	9.0814	44.9800	4.8932	88.8067	4.3154	53.0533	5.8809
CA1sr_5	94.5733	10.6956	9.2267	13.0485	84.1933	8.1553	47.2867	5.8809	87.6533	4.3154	55.3600	5.6502
CA1sr_6	95.7267	11.7617	12.6867	13.0485	83.0400	7.4745	48.4400	5.6502	86.5000	2.8251	57.6667	4.3154
CA1sr_7	93.4200	10.1860	13.8400	14.6795	83.0400	7.4745	51.9000	5.6502	85.3467	4.3154	61.1267	4.3154
CA1sr_8	94.5733	10.6956	14.9933	16.3106	81.8867	6.5242	50.7467	4.3154	83.0400	2.8251	61.1267	4.3154
CA1sr_9	91.1133	10.6956	16.1467	15.5593	80.7333	5.8809	50.7467	3.2621	80.7333	4.3154	57.6667	4.3154
CA1sr_10	79.5800	9.7864	9.2267	10.6956	71.5067	4.3154	38.0600	2.8251	76.1200	2.8251	40.3667	7.1096
CA1slm_1	57.6667	11.4174	3.4600	4.8932	50.7467	1.6311	18.4533	4.3154	53.0533	6.5242	25.3733	3.2621
CA1slm_2	80.7333	10.6956	9.2267	13.0485	68.0467	1.6311	36.9067	5.8809	72.6600	2.8251	44.9800	5.6502
CA1slm_3	92.2667	6.5242	12.6867	17.9417	76.1200	2.8251	46.1333	7.1096	80.7333	4.3154	54.2067	5.8809
CA1slm_4	99.1867	6.5242	18.4533	23.6925	79.5800	2.8251	50.7467	5.8809	84.1933	4.3154	59.9733	6.5242
CA1slm_5	101.4933	5.8809	19.6067	25.3209	80.7333	3.2621	54.2067	3.2621	85.3467	5.8809	58.8200	4.8932

Appendix 6: Triple co-localisation of puncta in PSD95$^{HaloTag/eGFP}$; SAP102$^{mKO2/+}$ knock-in mice.

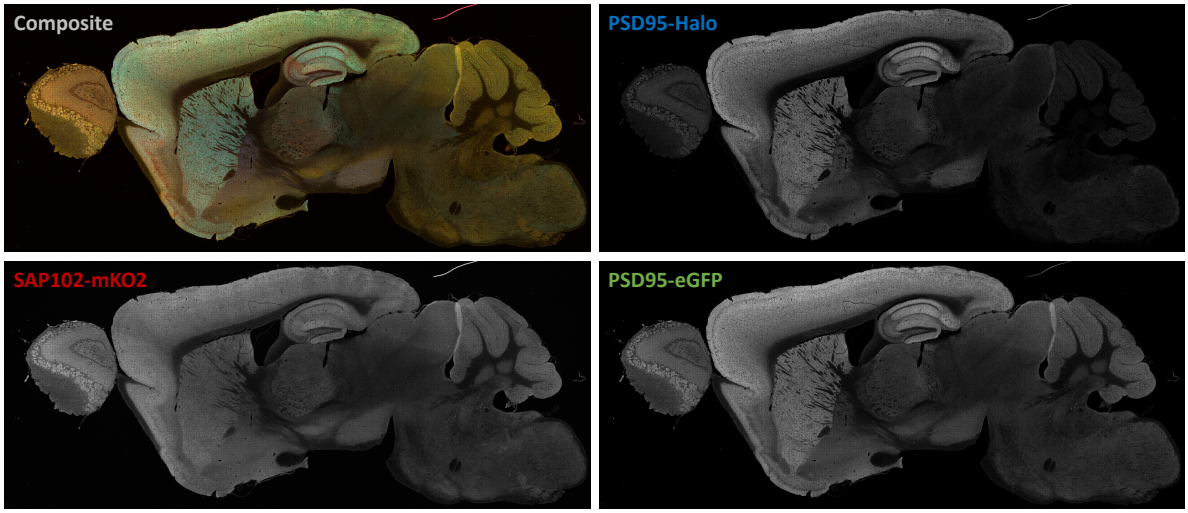

Appendix. Figure 4: Representative images of fluorescence from SiR-Halo injected PSD95$^{HaloTag/eGFP}$;SAP102^{mKO2} mouse. *Composite image shows PSD95-HaloTag (in blue), PSD95-eGFP (in green) and SAP102-mKO2 (in red).*

Appendix 7: PSD95 lifetime differs between synapse subtypes.

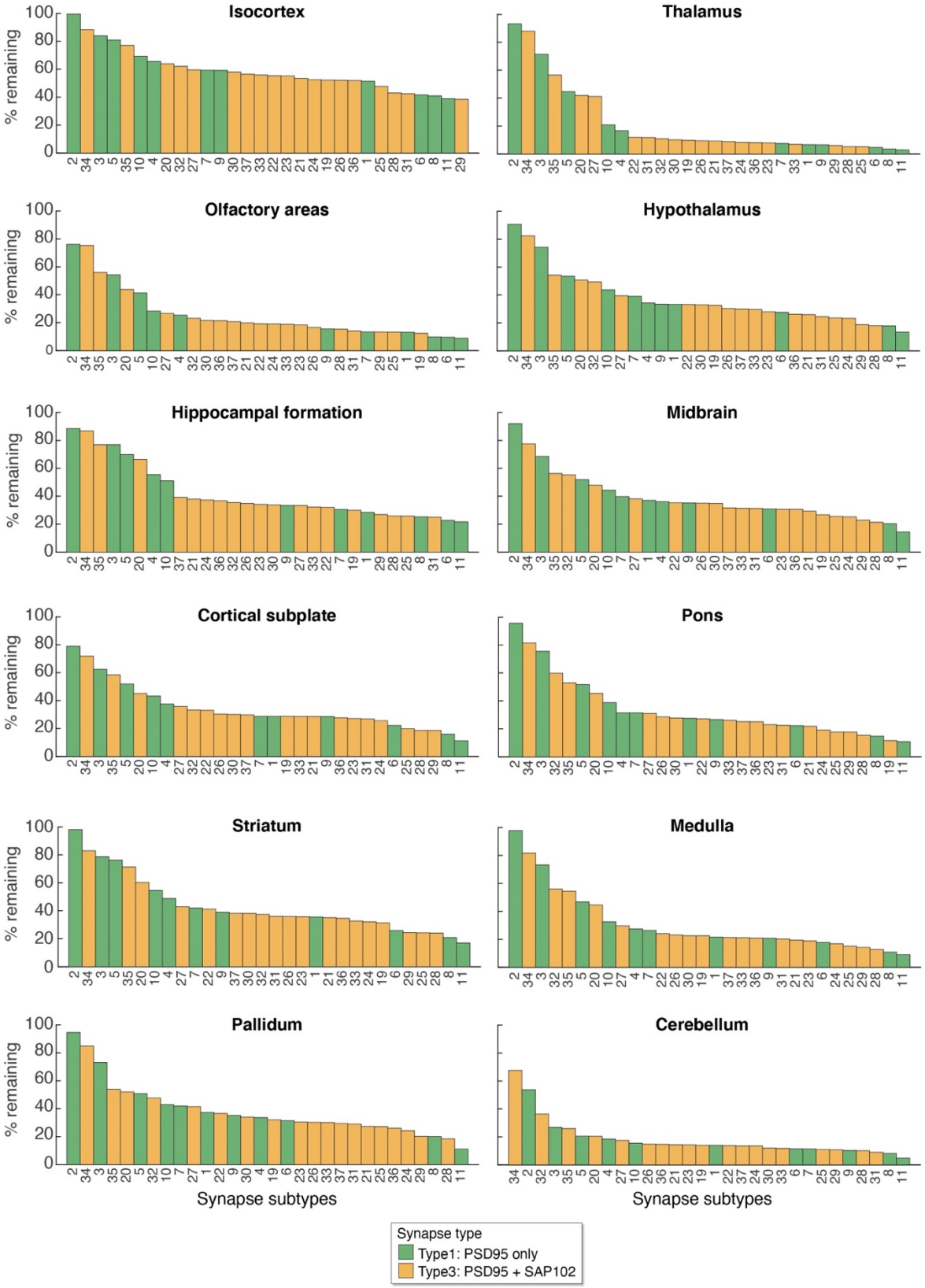

Appendix. Figure 5: Percentage of SiR-Halo positive subtypes at day 7 compared to day 0 in different brain regions. *The bars are ranked according to their associated PSD95 lifetimes. The bars are ranked according to their associated PSD95 lifetimes. Subtype ID is provided at the bottom. Colours correspond to synapse type (type 1: PSD95-only and type 3: PSD95 + SAP102).*

Appendix 8: LPL synapse composition across brain subregions.

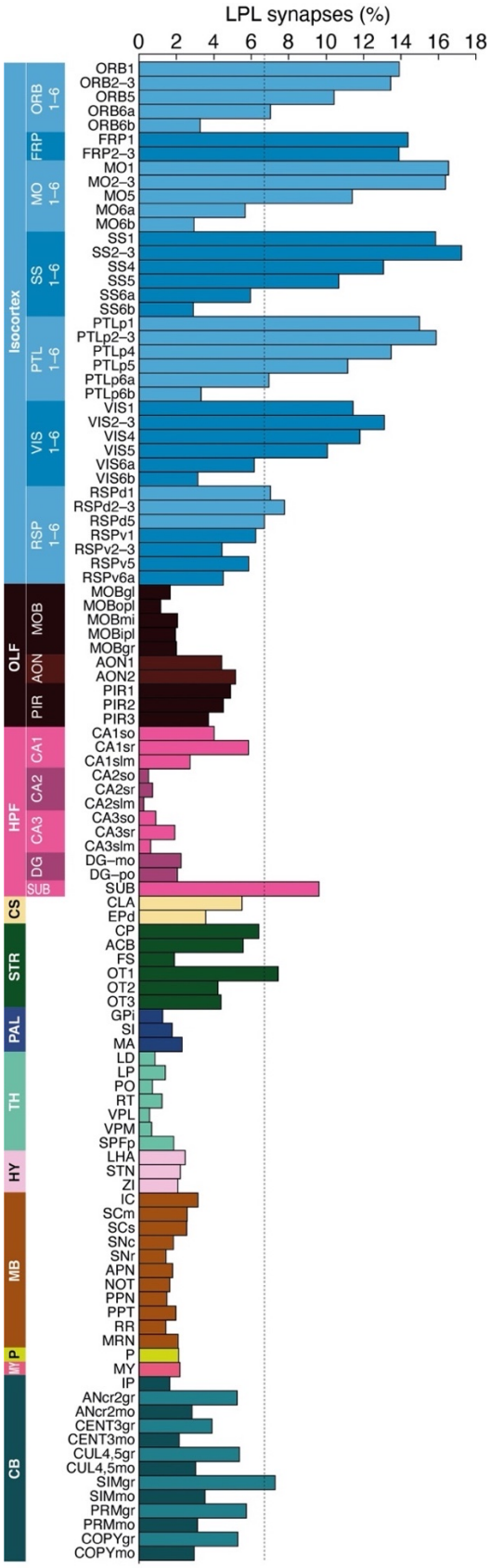

Appendix. Figure 6: Percentage of LPL synapses in brain subergions. *Dotted line indicates the average for whole brain (6.7%).*

Appendix 9: Data for percentage of SiR-Halo positive subtypes remaining 7 days post-injection. Percentage of SiR-Halo-positive subtypes remaining at day 7 compared to day 0 in 12 main brain areas and 110 brain subregions. Data presented for PSD95-positive subtypes (i.e. subtypes 1-11 and 19-37).

Type 1 (PSD95-only) subtypes: main brain areas

	% remaining at day 7 compared to day 0										
Abbreviation	**subtype1**	**subtype2**	**subtype3**	**subtype4**	**subtype5**	**subtype6**	**subtype7**	**subtype8**	**subtype9**	**subtype10**	**subtype11**
Isocortex	51.4389	99.5975	83.9671	65.6363	80.9840	41.6562	59.2636	40.9073	59.1278	69.3359	38.8619
OLF	13.2030	76.0929	54.3190	25.4794	41.3070	9.6098	13.4577	9.8303	15.5942	28.3359	8.9538
HPF	28.5115	88.4715	76.8545	55.4827	69.9111	22.6874	30.5979	25.3138	33.4456	51.0846	21.6521
CTXsp	28.6938	78.8294	62.4935	37.5840	51.9274	22.1313	28.7164	16.0405	28.5462	43.1482	11.2676
STR	35.5998	98.0859	78.7209	48.7417	76.3497	25.8484	41.9893	20.7888	38.9695	54.6488	17.0011
PAL	37.3645	94.5488	73.0816	33.7144	50.8380	31.4628	41.9386	20.0805	35.2475	42.9462	11.1774
TH	6.5772	93.2668	71.3643	16.7080	44.6427	4.7175	7.4917	3.5700	6.4972	20.8924	2.9367
HY	33.3027	90.5727	74.1698	34.3170	53.4355	27.5972	39.0448	17.8632	33.4364	43.7713	13.4564
MB	37.0789	91.9866	68.5715	36.1535	51.9262	30.9608	39.7741	20.3649	35.1792	44.3257	14.5139
P	27.6264	95.5530	75.4458	31.5148	51.7333	22.2672	31.4827	14.8019	26.6871	38.8823	10.8604
MY	21.5714	97.8596	73.3158	27.4394	46.8258	17.7105	26.3928	10.8154	20.7853	32.6362	9.0202
CB	14.0129	53.8349	26.8427	18.4966	20.5240	11.4994	11.4790	8.1456	10.2743	15.5527	4.8609
whole brain	30.7165	96.7573	77.2253	51.6097	72.8028	23.3667	36.2556	24.2085	37.6962	55.7335	25.2535

Type 3 (PSD95 + SAP102) subtypes: main brain areas

	% remaining at day 7 compared to day 0																		
Abbreviation	**subtype 19**	**subtype 20**	**subtype 21**	**subtype 22**	**subtype 23**	**subtype 24**	**subtype 25**	**subtype 26**	**subtype 27**	**subtype 28**	**subtype 29**	**subtype 30**	**subtype 31**	**subtype 32**	**subtype 33**	**subtype 34**	**subtype 35**	**subtype 36**	**subtype 37**
Isocortex	52.2269	63.9014	53.5071	55.2957	55.1456	52.4949	47.7355	52.0690	59.5317	42.9647	38.5103	57.9339	42.3450	62.0341	55.9038	88.3248	77.0784	51.9059	56.4640
OLF	12.3816	43.9088	19.9057	19.1444	18.4267	19.0968	13.3240	16.6728	26.6755	15.3353	13.3448	21.6283	14.1775	23.1292	18.9149	75.2798	56.0234	21.4243	20.7812
HPF	30.0088	66.3685	37.9810	32.0340	34.1385	37.3125	25.8377	34.8344	33.3882	25.8931	26.9719	33.8320	25.0728	35.4576	32.2436	86.7367	76.8572	36.8221	39.2089
CTXsp	28.6806	45.1494	28.5714	33.0318	27.1972	25.6704	19.8600	30.3488	35.8588	18.6024	18.5918	30.0983	26.9161	33.2377	28.6489	71.7581	58.3703	27.7249	29.7946
STR	31.3672	60.3195	35.1720	41.1809	35.7416	32.2330	24.1811	35.9434	42.9628	24.0790	24.3092	38.1447	36.0401	37.4213	32.6870	82.9472	71.3675	34.6610	38.2549
PAL	32.1140	52.0532	27.2774	36.6180	30.5720	24.2351	27.1917	30.3122	41.4182	18.4806	20.1750	34.0412	29.0899	47.6434	30.1546	84.9453	53.8857	26.0906	29.4390
TH	9.8595	41.9136	9.3097	11.9362	7.9146	8.3102	5.0941	9.4711	41.1682	5.1719	5.9972	10.1985	11.7985	10.9733	6.8568	87.9301	56.5027	8.0696	8.9096
HY	32.6046	50.7655	25.9926	33.2145	27.9796	23.2109	23.6281	30.3096	39.4483	18.0334	18.7358	33.0269	24.5904	49.4142	29.7349	82.4135	54.2646	26.3380	29.9182
MB	26.8515	47.9142	29.3206	35.3900	30.7443	25.3890	25.5429	35.0996	38.2378	21.3238	22.9428	34.8088	31.2976	55.3034	31.3850	77.5328	56.2775	30.7127	31.6840
P	11.6545	45.4517	21.8149	27.2760	23.0731	19.1856	17.7897	28.6431	31.0353	15.5014	17.6663	27.8528	22.5407	59.8043	26.1678	81.5698	52.9168	25.0468	25.1069
MY	22.6121	44.6151	19.4789	24.1059	18.8663	16.9296	15.2038	23.1269	29.6104	12.7578	14.3363	22.6608	20.2604	56.0054	21.1542	81.7741	54.5081	20.9064	21.2128
CB	14.0603	20.4509	14.4268	13.7823	14.2899	13.5763	11.0068	14.8548	17.4748	10.0974	10.7772	12.0727	8.9396	36.3484	11.8092	67.5956	25.9533	14.6941	13.5766
wholebrain	32.4175	59.5570	38.3517	36.6414	37.8073	37.2119	28.6295	36.8176	37.9255	27.2009	26.4874	40.8691	28.6170	41.9455	37.1877	85.5575	73.6713	39.6210	40.4174

Type 1 (PSD95-only) subtypes: subregions

	% remaining at day 7compared to day 0										
Abbreviation	**subtype1**	**subtype2**	**subtype3**	**subtype4**	**subtype5**	**subtype6**	**subtype7**	**subtype8**	**subtype9**	**subtype10**	**subtype11**
ORB1	83.2301	109.7985	98.4620	85.8957	102.2128	71.6211	89.1007	62.0651	84.6706	90.3223	56.5585
ORB2-3	61.1892	96.6050	84.5725	69.5175	82.2138	51.9636	69.3155	46.1178	65.6832	72.2231	40.9790
ORB5	51.4235	91.1082	77.8905	58.8974	72.3309	42.2719	55.4907	34.2094	52.6017	62.6725	27.7864
ORB6a	44.1054	90.2425	74.0018	51.7050	65.3741	34.1710	48.1080	26.3900	42.7912	56.2587	20.2786
ORB6b	36.7551	91.6079	63.0381	39.9582	58.0085	28.5821	41.0098	18.0546	34.0177	47.9809	13.4614
FRP1	94.1133	116.6963	109.4422	91.8139	109.2814	77.8742	89.2704	65.7164	87.0032	96.6148	53.0049
FRP2-3	70.4038	98.0136	91.7174	76.5103	90.6890	61.2358	78.5220	52.6512	69.9603	77.8832	48.4899
MO1	78.0917	113.0024	102.7795	90.2711	104.4486	70.2709	85.5525	69.7368	87.2560	91.2990	65.9206
MO2-3	64.5286	102.8144	91.4428	76.9828	90.2518	55.3502	72.6380	53.5799	72.4939	78.9631	49.9381
MO5	56.5535	98.4737	83.6484	65.0241	78.3198	46.7244	62.0334	39.0102	58.8093	68.6521	33.6805
MO6a	42.3717	89.5290	68.7064	49.0815	60.8034	32.9911	43.5976	24.8389	39.6976	52.7514	18.9295
MO6b	30.4841	83.7135	54.2294	34.9502	47.8517	23.3370	27.0149	15.7987	26.6214	38.7691	11.3126
SS1	71.7726	112.8158	97.9824	85.8842	100.0294	66.1019	80.9048	65.6917	84.1038	85.9682	61.5199
SS2-3	63.3810	96.3970	88.1964	75.2841	86.5012	54.9679	73.6193	53.3831	71.1838	76.0503	47.7180
SS4	46.4172	89.2885	74.2100	57.2124	68.5842	38.9642	54.3646	35.5692	51.4826	58.5286	28.5251
SS5	47.4821	92.0005	74.5625	56.5600	67.5929	39.5898	50.0770	33.0327	49.0297	59.2624	26.5324
SS6a	38.1124	86.7946	63.8249	46.0610	56.9620	29.5092	38.1000	23.2570	36.3129	49.5783	16.8418
SS6b	26.4493	87.2219	60.0122	31.9207	44.9398	20.5056	24.3123	13.4460	21.9842	37.2789	7.4843
PTLp1	63.3438	102.5365	97.3299	81.8714	93.9614	58.2095	78.8967	60.0584	75.2407	80.4732	53.4267
PTLp2-3	58.0921	95.4045	81.7410	72.6722	81.8460	50.6133	66.2104	51.0629	66.7857	70.2914	47.2668
PTLp4	55.0250	92.8023	77.0028	62.9523	74.8402	46.1086	56.8595	41.2403	58.0889	63.5065	32.8669
PTLp5	52.2516	88.7169	72.7954	58.2079	68.6302	42.9095	51.9988	35.8931	50.8634	58.9865	28.2063
PTLp6a	36.3674	84.9704	62.4476	46.9232	58.3360	29.2241	38.8890	24.0720	34.7364	48.3880	18.0993
PTLp6b	30.0633	103.8801	60.6965	35.2669	48.9604	22.6301	22.2192	16.8809	24.5958	34.1245	30.3388
VIS1	69.9196	102.0593	91.2463	78.5475	92.2318	61.4781	74.7657	54.9845	73.3275	79.9044	49.4500
VIS2-3	63.6558	98.5069	85.7284	71.9084	82.9648	55.6786	70.9528	49.9917	67.8344	73.2113	43.2533
VIS4	52.7908	96.4879	78.4719	61.2177	73.2332	46.9306	62.4215	39.1845	56.6486	62.3253	33.1056
VIS5	50.8534	92.7374	76.3322	57.3552	68.8170	43.8845	54.7506	34.2708	51.6321	60.3923	26.8938
VIS6a	36.3915	85.8852	64.6474	44.9668	56.6797	28.9877	35.6863	22.1872	33.7134	47.1462	15.7238
VIS6b	29.0902	85.6710	60.7102	34.2073	47.7373	21.1892	26.9736	14.7846	24.3751	41.2816	11.1378
RSPd1	52.6564	89.5186	80.5692	58.3599	77.8830	39.1559	63.5280	34.6267	54.9004	66.3892	28.0873
RSPd2-3	40.9402	95.2736	72.3867	52.0513	67.1275	33.8702	44.4045	29.5808	45.1699	55.1655	22.4772
RSPd5	38.5724	93.5666	63.7973	47.3800	58.8357	27.7637	34.0440	22.9349	39.4406	49.0327	14.7491
RSPv1	50.1864	82.8674	72.1849	54.2506	70.5073	41.8494	48.6284	29.2588	48.3201	61.0292	22.3076
RSPv2-3	33.3340	87.4579	57.9402	40.4435	56.3577	26.4432	26.7938	18.1216	32.0922	46.1359	11.8571
RSPv5	44.4008	96.1547	71.7356	48.9030	63.8786	33.4080	47.3960	24.1843	41.2028	54.4177	17.9657
RSPv6a	36.5426	101.8875	67.3926	41.2091	55.9834	29.3124	41.0722	19.3019	33.5862	46.5789	12.5736
MOBgl	0.9903	76.4262	28.5322	2.9530	10.4518	0.6046	1.7457	0.3820	1.0264	2.6537	0.2283

MOBopl	1.5872	60.2314	19.2635	3.0992	7.4922	1.1570	2.1716	0.7408	1.6549	3.8717	0.6907
MOBmi	2.8073	73.9320	33.0399	5.3569	13.6506	1.7513	3.9287	1.2179	3.0136	6.8317	0.3388
MOBipl	2.7849	41.7033	12.8024	4.1635	8.3080	1.9675	2.4588	1.4128	2.9560	4.4958	0.4066
MOBgr	3.3379	55.1186	19.5793	6.0096	10.7172	2.5420	3.4571	1.6426	3.1840	6.3590	1.2816
AON1	35.5526	84.3160	71.5768	47.0895	62.1327	25.9038	34.8779	20.4185	33.2410	48.4374	14.0003
AON2	28.6462	78.3695	64.4387	37.9700	53.5190	21.4976	31.6479	16.5104	28.7761	39.7467	13.5864
PIR1	27.4805	60.6138	58.8950	32.4985	44.7256	21.0645	29.0662	13.2453	26.3501	38.4031	9.8615
PIR2	15.0539	69.5692	48.1972	20.7829	32.6349	10.1270	16.9220	6.9749	15.4500	25.5687	5.0844
PIR3	31.1286	93.6518	60.5380	34.4744	49.2536	22.5177	30.5042	14.5631	28.4166	40.3384	11.4668
CA1so	38.9583	89.4151	79.5916	60.7863	69.5896	32.6991	40.8469	33.6157	42.3375	55.4805	26.4840
CA1sp	24.0895	93.7390	88.1112	52.3302	72.1403	18.5070	25.2936	19.6606	28.2976	48.3733	19.6907
CA1sr	45.2843	95.9776	86.4686	69.4066	80.5439	40.2594	51.8050	42.5707	53.5878	65.0230	36.5516
CA1slm	43.7798	84.1737	83.4638	59.6494	68.4442	37.6117	48.2659	36.7246	49.4665	61.8147	31.0609
CA2so	6.5332	89.6096	61.8398	22.8749	35.3530	4.3642	7.1522	3.8174	5.5912	18.9752	2.6960
CA2sp	7.0222	95.0062	92.6114	40.4889	86.6158	4.1291	8.4354	4.3517	5.3575	34.4587	0.0000
CA2sr	10.0666	51.2122	50.4833	33.3545	47.1787	7.4774	6.4776	6.5871	10.6396	23.8148	5.1609
CA2slm	3.5030	111.4170	73.7925	12.6775	31.3478	1.7863	5.0277	1.7632	3.5203	12.1505	0.6358
CA3so	18.5091	58.1400	61.8665	34.0924	40.9891	14.1256	16.2689	9.7842	17.0783	35.2279	4.8757
CA3sp	9.9141	78.5037	50.3539	21.4865	36.8654	7.8272	9.4352	6.9893	10.3138	18.9578	4.0899
CA3sr	18.6267	58.0797	53.9170	39.7385	48.1649	14.7603	14.6633	13.4799	20.2348	37.5170	11.1235
CA3slm	16.4454	94.0231	90.2435	36.4766	59.0919	11.4608	8.9557	7.5763	14.7676	44.8836	6.2143
DG-mo	13.5697	67.7996	56.0066	33.2699	42.8541	9.8741	13.8811	10.9898	16.8276	28.0898	7.0159
DG-po	20.2777	56.8597	48.3317	34.9448	43.7282	18.0692	17.1964	14.6730	19.1308	32.1711	10.9040
DG-sg	10.0001	109.7307	68.7247	26.0751	56.1537	5.7106	11.6281	4.1417	9.5594	22.0797	4.1167
SUB	56.0602	102.9985	86.8157	68.6155	87.6948	48.2493	65.0418	43.0031	58.9672	71.5554	41.4683
CLA	34.2346	83.5061	67.5690	43.8500	57.9803	26.4892	33.7335	19.7668	33.1954	48.7176	13.2315
EPd	26.3664	78.5141	58.1325	32.5227	46.8530	20.3493	27.8143	13.0753	25.7716	38.5922	9.2289
CP	40.6669	103.8544	83.3181	54.0236	83.7560	29.6391	47.5797	23.4567	43.7171	61.4721	18.8054
ACB	29.1824	94.9393	75.7922	44.1948	71.3322	21.3144	37.2380	17.5953	33.9774	49.0989	14.9062
FS	42.9709	93.7202	74.6613	44.7286	70.8165	36.9882	51.2179	21.8598	39.3528	55.0634	19.0655
OT1	33.9564	84.2315	67.8432	42.5262	60.4518	23.6617	39.2482	19.6357	38.8366	47.9656	16.0399
OT2	19.2874	78.7531	61.6697	29.1051	51.7226	12.7025	28.0397	10.5737	23.6159	32.9222	10.6395
OT3	23.1245	82.5074	65.6704	31.8932	55.7031	15.9175	31.5541	11.5669	26.5602	38.5440	10.0665
GPi	43.7693	134.4427	99.1400	40.2631	67.2548	39.2145	50.1682	24.8228	41.3500	48.2455	16.0087
SI	40.3610	93.6326	73.6528	36.3552	53.3420	33.8470	46.2926	21.7622	37.8665	46.9177	11.4635
MA	21.3818	76.8382	63.3648	22.3799	37.7483	16.0452	22.8055	10.2346	21.3837	29.0115	9.6866
LD	9.6931	83.9710	66.0904	18.3528	38.4547	7.4869	10.3433	6.0876	9.6670	20.7013	4.9988
LP	15.0288	93.7502	73.3875	25.8441	51.0760	11.7118	17.8713	8.3692	14.7922	30.7744	6.0577
PO	4.9953	92.9735	73.1631	12.5434	40.9493	3.5464	5.6319	3.0108	5.0293	17.2446	3.0295
RT	18.0697	100.1610	67.0333	21.0666	37.1852	14.2107	18.6336	8.9953	19.3096	26.9493	4.0017
VPL	2.7405	95.4863	78.3708	9.7327	44.8005	1.9047	3.2394	1.3994	2.6480	12.7532	1.1353
VPM	1.8010	92.6663	62.2324	8.0240	41.8929	1.2020	2.1327	1.1856	1.9584	10.7804	1.1807
SPFp	28.6415	94.0923	62.5972	33.3115	57.7136	23.5816	26.5239	16.1099	29.3860	44.8433	10.7218

LHA	36.4781	87.4066	72.5510	36.3357	54.1669	30.1122	41.8268	19.5731	36.3029	46.1792	14.6678
STN	28.0090	97.6121	76.1013	31.0183	54.0865	22.9356	35.7035	15.1369	28.9435	41.4897	10.4509
ZI	26.5889	89.6953	62.4024	29.3206	47.7983	21.9746	28.0073	14.0949	27.0466	37.8857	9.4738
IC	27.0593	80.9861	57.9362	29.0655	41.9785	21.8676	29.8455	14.4133	26.6919	36.4023	12.0733
SCm	43.6820	103.2234	75.0884	40.2711	59.0844	35.9787	45.2280	23.8439	41.0746	50.2450	14.6673
SCs	39.6959	86.1328	69.9406	38.2996	54.6082	32.0639	42.0435	20.3686	37.0784	46.6082	14.7017
SNc	36.0788	82.8197	83.0859	36.8192	55.9002	30.5709	39.4314	20.6113	34.7839	45.2655	10.9128
SNr	46.2205	94.8854	85.5034	45.9056	60.4403	41.2602	52.9182	28.4203	43.6172	54.8125	24.1920
APN	25.8327	102.7870	52.8270	28.3324	46.7858	19.6945	26.3850	14.1094	26.8884	36.9460	16.7156
NOT	25.7879	78.5183	54.2473	29.7130	45.5139	22.2249	28.9967	13.5755	26.6336	38.9084	4.9654
PPN	33.0924	96.0165	98.4076	36.0520	57.6652	29.1866	39.6711	20.0205	33.6532	46.0665	11.1592
PPT	29.8174	75.4911	72.8866	32.9914	47.5246	25.0773	34.0947	16.0712	27.9764	38.6025	21.9343
RR	39.3292	110.1234	76.9607	37.4764	56.5920	31.8763	44.6346	22.9772	37.6230	46.5083	13.7222
MRN	44.3231	100.2583	81.3082	42.2295	63.1409	37.3826	47.1564	25.5639	41.8285	51.4761	17.6096
P	27.6264	95.5530	75.4458	31.5148	51.7333	22.2672	31.4827	14.8019	26.6871	38.8823	10.8604
MY	21.5714	97.8596	73.3158	27.4394	46.8258	17.7105	26.3928	10.8154	20.7853	32.6362	9.0202
IP	3.1249	106.0044	72.3278	10.6105	38.9749	1.8436	4.3738	1.2467	3.3252	13.7064	2.5901
ANcr2gr	6.4632	29.9044	19.0754	14.4016	16.5920	5.2686	6.2351	6.8339	6.8066	11.0245	4.9854
ANcr2mo	20.5722	47.1064	35.7091	25.4418	26.5828	16.6014	19.2820	11.4332	16.1563	22.8575	6.1305
CENT3gr	6.4924	70.8478	17.9283	11.1222	15.1777	5.0971	6.1209	4.6770	6.0468	8.6360	2.4563
CENT3mo	16.7957	74.2892	33.3475	22.4579	27.0229	13.7907	12.4650	10.0164	12.3282	22.9043	5.3790
CUL4,5gr	6.3040	59.7733	18.9243	13.0472	16.2406	4.8316	5.4396	5.9181	6.9109	10.4043	3.7148
CUL4,5mo	17.7887	77.4896	37.1450	23.7167	27.9332	14.6063	14.1577	10.3638	13.2488	22.9669	6.4931
SIMgr	7.7967	49.2183	22.6375	16.2139	19.1184	6.0521	6.6091	7.7344	8.5221	12.8704	5.4530
SIMmo	21.4503	66.4381	38.6648	26.7807	30.1589	17.3882	15.8877	11.7228	15.7918	25.1238	6.9062
PRMgr	5.3812	33.5498	16.5976	12.7721	14.9449	4.9248	4.8127	6.3929	6.3920	9.8960	3.5154
PRMmo	20.6397	48.2020	36.6573	23.9393	25.3701	16.5249	17.8065	10.5799	15.3829	22.9391	5.8990
COPYgr	5.8747	41.7190	16.5325	11.0603	14.5470	4.9198	4.9748	4.9284	5.5004	8.7599	3.3063
COPYmo	17.8973	40.0534	34.5196	22.7652	26.4095	14.3434	15.1459	9.7053	13.9757	22.1181	6.5272

Type 3 (PSD95 + SAP102) subtypes: subregions

	% remaining at day 7 compared to day 0																		
Abbreviation	**subtype 19**	**subtype 20**	**subtype 21**	**subtype 22**	**subtype 23**	**subtype 24**	**subtype 25**	**subtype 26**	**subtype 27**	**subtype 28**	**subtype 29**	**subtype 30**	**subtype 31**	**subtype 32**	**subtype 33**	**subtype 34**	**subtype 35**	**subtype 36**	**subtype 37**
ORB1	66.1849	78.2314	68.8587	78.1916	73.4531	66.3031	67.1127	68.0227	75.0333	63.0485	57.5868	73.9776	75.3050	75.1986	73.2109	93.5917	86.3662	68.1054	71.3753
ORB2-3	51.1245	67.6034	59.9320	63.9743	61.1151	57.0626	55.4705	57.2344	65.8604	50.6520	45.7052	64.3428	62.8797	64.7473	61.4988	88.5709	79.5903	57.5669	61.0978
ORB5	46.5312	60.4367	50.4793	57.7335	51.1804	48.1234	42.2503	48.9585	56.2453	40.5745	36.1719	53.7042	44.7065	53.5376	52.3091	84.2922	74.5691	48.3173	52.1027
ORB6a	39.5234	54.2991	42.5483	49.2831	42.2606	40.5144	33.9994	45.7952	47.4835	30.1502	29.8430	44.5412	39.3036	47.0842	43.1946	80.6190	70.2099	41.9711	43.0320
ORB6b	21.6484	52.0530	32.9036	37.2337	30.6357	29.3025	21.1456	39.3810	36.7240	20.6299	21.9673	33.0772	34.6948	34.7444	27.2734	72.2824	67.5677	31.1944	33.0023
FRP1	79.1063	83.4041	72.7367	74.1154	81.9365	76.9596	71.6093	70.8638	73.7751	64.9077	68.4497	76.3997	102.794	83.5302	73.9678	93.9898	89.3793	76.0923	74.8758
FRP2-3	52.7980	72.4971	65.5646	75.8807	66.8765	62.9093	58.9403	67.3239	66.5336	59.7781	53.3201	69.5095	70.9345	73.4488	69.4860	94.4952	86.2187	66.6687	66.5000
MO1	71.6037	83.0585	72.2405	71.4565	74.4366	71.3715	68.2411	65.1139	61.4216	68.2774	60.8692	75.4146	66.2457	77.5187	73.4604	93.8569	87.6478	72.3083	73.8821
MO2-3	59.6685	73.5875	63.9406	67.3364	65.7226	62.2678	59.1496	60.0584	71.3028	56.5179	49.8706	67.2078	59.5640	70.1570	66.0925	90.2165	82.9055	62.2989	66.0072
MO5	52.3651	65.4057	55.0695	61.0125	54.7022	53.0909	47.0020	54.5590	61.7638	44.2875	40.2842	57.2609	48.0270	56.6935	55.7778	87.6562	77.6239	52.8473	55.4765
MO6a	40.2884	52.9001	40.8137	45.1275	39.7686	38.4709	31.0586	44.2089	44.0575	28.8704	28.6000	39.9150	36.4479	45.6770	40.2787	80.2070	67.6274	40.2204	40.9756
MO6b	22.6045	42.5473	28.0733	33.0240	27.0039	26.3908	20.1068	33.3979	40.9309	19.2755	19.6439	26.5369	28.9519	33.8285	26.2168	76.3881	56.0148	27.1313	28.8662
SS1	60.5344	76.3995	66.8562	71.2983	71.0120	66.7212	64.6392	59.7585	65.9445	61.3704	54.4932	70.1334	62.3558	74.6704	69.0801	92.0265	82.8727	64.3387	69.5972
SS2-3	56.7797	68.0614	62.2141	65.2840	65.7149	61.5665	59.2484	55.6422	72.2482	53.5319	47.3287	65.9855	52.4503	69.4638	64.4242	87.3725	78.2629	59.0430	63.3414
SS4	43.9414	58.3731	50.3060	53.8030	51.7309	49.4842	45.4453	48.4700	57.3885	41.3159	35.3583	53.6398	41.2482	58.4826	51.8915	84.3165	68.7766	46.6962	50.0440
SS5	46.7558	58.8147	48.8601	50.7128	48.2414	47.2992	41.0548	46.9139	55.3778	38.2681	34.6857	50.5754	42.9106	52.4154	47.8569	82.8824	70.0698	45.6437	49.8491
SS6a	42.9509	48.1335	38.5342	40.7951	37.5810	36.2962	29.4797	41.0457	38.6976	27.0612	26.6408	37.5259	31.6829	43.4230	37.3972	79.0973	63.9548	37.3264	37.7306
SS6b	18.0116	36.7108	23.6517	26.1234	24.8578	23.1103	15.5431	33.6719	35.9151	15.2071	16.8306	24.1819	22.6644	30.6932	24.4228	79.6329	53.3581	23.5072	25.5554
PTLp1	76.0578	73.5034	67.0686	67.7428	68.7598	61.5681	64.1611	59.8069	61.0859	59.8259	49.8416	67.1912	83.3870	72.6245	69.8989	94.6772	81.6038	64.0999	65.4221
PTLp2-3	55.9765	66.9282	60.0283	59.2148	62.7121	58.4408	55.7588	58.0660	66.1170	51.9980	45.3635	63.4473	46.9399	68.6370	64.1563	88.8653	76.8600	57.0337	61.6680
PTLp4	74.6959	57.3567	58.5194	60.6028	56.4534	56.3514	57.5483	56.1173	58.5205	44.6373	42.5204	57.6767	64.8737	62.6061	61.1044	82.1417	72.6976	51.7040	57.2549
PTLp5	40.9978	56.1507	51.1686	52.4965	51.8404	49.6903	45.1268	50.5535	82.9547	39.1570	36.5141	51.9549	38.3891	55.5338	52.1099	85.7992	71.1688	47.9951	52.7220
PTLp6a	30.3519	45.7140	36.2089	36.5517	35.9468	35.3357	27.8308	37.9140	38.1922	29.8999	26.2079	37.2220	30.6474	45.5656	36.6497	76.4725	62.6762	38.6511	37.8859
PTLp6b	0.0000	36.3363	28.5290	27.4012	32.8291	25.3399	24.4388	40.3340	40.6647	20.0037	20.5975	31.1900	28.9937	39.1568	31.5694	82.7694	54.8052	28.8459	34.1891
VIS1	58.7528	72.1330	61.3174	64.9944	62.8006	59.5136	56.5582	56.9508	56.9762	52.0651	46.9173	63.9889	63.8153	69.0437	64.0221	89.2390	80.3795	58.4386	63.3170
VIS2-3	59.3134	65.6520	58.7378	64.4655	61.5148	56.7353	55.1382	56.6388	70.6140	50.5001	44.8665	62.4812	61.8570	66.2668	60.4588	86.8616	77.2015	55.3661	60.5451
VIS4	49.9679	59.4698	51.2373	57.8078	52.9798	49.5996	46.2438	50.3732	64.0418	41.7377	37.6910	54.6532	49.9426	58.1647	53.8596	84.0877	71.9120	48.8077	52.9987
VIS5	45.3813	55.3222	48.4824	55.3615	49.6687	46.3869	42.5862	48.7505	57.6422	37.6313	34.6012	50.1968	46.4647	52.4432	49.4949	81.4355	69.8867	45.7009	49.1594
VIS6a	31.6548	44.0155	34.8739	37.9849	35.0283	32.6714	26.5891	38.1555	41.3699	24.9432	24.5770	35.4944	31.6467	44.6793	34.4990	79.7500	61.1068	34.7064	36.3071
VIS6b	38.3204	38.6584	26.3180	30.4030	26.4123	23.5113	19.3839	34.8811	39.8455	14.7340	18.1263	25.0077	24.9369	35.6532	27.0534	76.1584	55.0456	26.3428	27.1794
RSPd1	47.7503	53.4055	47.7088	51.1175	51.2995	43.7619	44.5531	50.3055	45.5399	37.5191	31.9035	52.7656	43.6288	64.0974	52.1587	85.8840	70.1495	44.2956	50.3338
RSPd2-3	47.6569	52.3592	43.8733	45.2814	45.2863	44.2421	38.4454	45.6484	64.5840	29.4545	28.8627	45.2373	32.9747	58.5448	43.9657	81.5323	66.7021	39.2526	45.0353
RSPd5	25.5433	44.4335	34.2152	39.9948	39.0966	35.8570	26.1224	37.7558	59.5801	24.7501	22.6923	40.5976	37.0362	48.0691	37.1525	82.9911	62.5691	36.2715	37.1031
RSPv1	47.7239	52.3470	44.6363	47.1178	44.3537	39.4220	37.1492	52.4633	50.2456	28.9563	30.9715	47.6826	48.3268	50.6935	45.2435	76.4725	66.3802	38.3952	44.3944
RSPv2-3	43.3763	41.2312	28.5364	31.0648	30.1165	28.6350	19.4286	30.5488	30.5600	15.3743	19.4904	29.6069	32.0781	41.6983	25.1780	66.5953	52.3849	24.6898	31.0212
RSPv5	42.3603	47.0306	38.7595	44.4243	39.3830	34.7207	26.8665	45.1052	42.8709	23.1968	26.6937	40.8712	43.1021	46.4938	37.5856	77.4797	65.1741	33.2535	38.6923
RSPv6a	25.9982	40.9017	29.5757	35.1342	29.1623	27.7873	23.9274	37.3250	32.1934	18.5351	20.5937	32.3250	33.1046	38.8731	31.3986	73.6038	59.1840	29.0995	29.8761

MOBgl	1.1952	11.3577	1.0856	2.6062	1.5117	0.7891	1.0920	0.7176	19.6642	0.3617	0.3297	3.3541	1.3952	9.3872	1.1468	88.2179	11.5792	0.7289	1.4954
MOBopl	1.9057	9.7640	1.5023	2.0587	1.5158	1.7704	1.4903	1.5049	11.9638	0.9926	0.6988	2.5939	1.3626	4.7443	1.8505	66.4272	12.1448	1.2864	1.9582
MOBmi	4.6007	10.8465	2.2715	2.8446	4.4179	3.1737	4.3892	2.0561	32.1349	0.8991	1.2949	7.8068	3.8028	24.5120	3.7340	94.4426	11.1493	1.9850	3.9352
MOBipl	1.9075	9.6601	2.5336	2.9685	3.1937	2.3358	2.1150	1.9020	15.4365	2.2877	1.1598	5.2819	2.9803	13.3401	3.8578	53.9191	11.4068	2.1147	3.6537
MOBgr	5.0752	9.8376	3.8265	5.1865	4.3902	4.1382	3.2212	4.4053	19.7231	2.0608	1.9266	6.6205	2.4423	20.2106	3.7790	69.6111	13.8755	3.7138	4.6048
AON1	32.2796	56.2443	32.1635	37.2134	31.7699	30.5997	24.9102	30.2520	44.8703	22.4825	21.0305	32.3141	28.8596	40.2016	32.2483	81.4967	66.7540	30.7539	34.8660
AON2	22.8100	46.2414	28.3915	32.4643	28.0999	27.6378	21.6238	25.7779	44.4294	21.2899	16.9611	30.1830	28.2675	35.3363	29.4778	78.1759	55.8700	25.9186	31.2358
PIR1	18.7359	35.9112	22.8834	28.6447	23.8028	21.6824	19.6509	20.6688	33.4412	15.0925	13.5859	26.3813	26.9129	33.5435	25.0496	61.2469	44.0001	20.2340	23.5009
PIR2	14.4551	27.7435	14.4968	15.9482	13.2168	13.1480	10.3326	13.3366	28.1569	8.4492	7.4604	19.0442	10.1209	21.6744	15.2370	60.2618	36.3116	12.5915	15.6190
PIR3	35.1943	43.6572	27.0501	33.3316	25.0685	23.3128	19.5412	26.2648	43.4909	17.0221	16.1536	29.3580	27.0730	31.0720	26.4067	73.7482	53.4631	22.9752	27.7683
CA1so	36.9830	71.1088	46.9126	44.2125	43.1595	45.9850	37.5141	42.3991	40.4917	37.7715	35.3337	41.6331	37.5393	48.6163	44.6158	86.8526	78.9202	46.8654	49.0284
CA1sp	33.6087	73.5722	30.6729	26.2385	27.0067	28.0014	22.7354	28.0329	58.7603	23.5009	20.9342	27.6476	21.3814	45.2564	28.2850	91.3562	76.2311	31.4015	32.7609
CA1sr	48.5017	74.5669	53.6962	49.8894	50.8508	52.2988	45.7744	48.5406	52.9355	46.4796	40.7051	51.8964	46.4798	58.7810	53.2085	84.0903	81.3011	53.6480	57.5104
CA1slm	47.1541	72.7718	50.2038	51.6128	50.0548	50.4150	43.5749	50.8839	56.8583	38.0119	40.2665	50.4610	35.9547	52.8604	51.9535	79.8974	78.8315	49.1692	54.0073
CA2so	15.0169	65.4317	8.0487	7.7710	4.7068	8.1862	2.6094	6.3534	5.8678	4.7859	5.7606	5.3114	9.0255	2.9349	4.0309	86.6525	42.9979	7.0059	6.4002
CA2sp	30.8242	50.0000	11.1861	9.7033	5.9753	7.5874	6.8614	11.6810	39.9861	2.9180	7.1226	15.9512	10.0297	32.5624	5.5769	104.681	89.9058	12.6771	6.2326
CA2sr	8.8019	38.7263	12.9337	12.6623	8.2338	15.3949	6.1080	10.4281	16.9406	9.3018	9.4398	9.0687	6.3501	6.8528	8.0527	58.1415	61.0044	15.1191	10.7073
CA2slm	9.2901	53.5055	3.3923	4.8384	3.0094	4.1701	3.0040	5.7860	14.8375	2.3225	2.4585	3.7455	5.4023	5.2966	4.3667	49.6619	61.1494	3.9282	5.1976
CA3so	12.4525	44.7264	18.1267	18.9907	13.9242	16.5181	7.3761	18.9420	17.0400	12.1221	11.2255	14.3096	21.7785	13.5800	12.5824	79.5874	52.1868	16.2893	18.2724
CA3sp	8.4142	23.7557	9.9944	8.8469	8.9711	9.6530	7.2081	11.3137	22.2628	4.8449	5.9952	15.0347	5.3066	44.4846	9.1664	74.2944	36.8558	9.0570	11.6479
CA3sr	20.9378	52.5383	22.2336	19.0600	19.4671	21.9706	12.0278	22.7548	17.6120	18.5708	15.5828	20.7244	17.5652	25.4315	19.5118	69.8525	63.1497	26.1958	24.9646
CA3slm	0.0000	63.3306	13.7980	12.4370	12.0579	14.7236	8.1488	14.5575	17.9988	9.5682	8.8289	15.6464	17.7304	14.2516	13.9081	79.1027	70.1323	13.1445	16.5156
DG-mo	14.6340	44.1097	16.7515	16.7705	14.6038	15.9902	10.0951	15.2825	25.3726	10.7213	10.3416	15.1217	12.0517	20.3548	15.2844	69.3846	52.7473	15.8463	18.6839
DG-po	12.3563	48.6374	18.6430	16.2493	16.8667	15.8224	13.2558	16.7248	19.8613	15.4040	12.1067	18.8190	14.5270	34.2956	19.8443	71.4270	53.6363	19.4136	19.9444
DG-sg	3.5450	53.8895	12.9559	21.5315	14.0704	8.8506	6.6287	12.5270	51.8971	6.5348	6.8172	15.5298	10.8373	40.9858	8.5747	96.4733	52.0277	9.2154	9.4361
SUB	47.7309	69.1279	58.1419	52.9937	58.0539	56.1372	47.0683	55.0201	49.7356	45.2182	43.5035	57.3825	44.8319	50.4580	51.0025	92.6520	83.2817	55.6080	58.0396
CLA	32.2803	49.3634	34.3745	38.7418	33.2037	30.8395	24.1099	38.0515	38.3320	22.6458	23.1721	35.1114	33.6938	40.2830	34.5914	72.9482	64.7258	33.7368	35.7665
EPd	27.8721	41.9454	23.9241	30.6396	23.1011	21.5538	17.2596	26.5597	35.6631	15.0041	14.8236	26.6001	23.5068	30.4843	24.5407	70.8684	51.0787	22.3519	25.8663
CP	37.5628	61.7781	38.9337	44.8553	40.0992	35.7653	27.5896	42.9204	44.5552	26.4507	27.3838	42.0599	38.3309	45.3672	37.6534	84.2787	75.0542	39.5556	42.6797
ACB	33.3074	57.4987	30.8581	36.5487	31.8705	28.5478	22.0922	31.9431	46.1221	19.9049	20.0187	34.6194	27.9974	39.1074	30.5535	82.8242	68.6079	29.8013	35.2931
FS	57.8912	59.7643	27.6772	41.8742	35.8913	29.4342	34.7491	39.9738	58.0461	17.5326	21.2960	38.6203	32.6807	55.2486	36.1154	91.7453	69.2484	27.1883	34.1996
OT1	30.1400	45.8271	31.4529	39.0162	31.8056	29.0135	23.9501	33.2711	32.5490	20.8390	20.1467	33.8572	37.0747	31.9629	28.4962	75.4688	59.0466	29.4960	33.2278
OT2	19.4256	41.6487	19.9589	23.2359	19.9051	19.8958	12.9576	20.4887	35.6831	11.8562	10.9458	24.6271	18.2627	25.6912	18.1346	74.0265	53.9294	17.3585	22.7788
OT3	19.9077	44.3732	20.3095	29.5599	21.3889	20.8408	13.8181	20.1127	33.8222	12.7128	11.5162	25.7438	22.2000	28.0417	21.2900	73.2591	54.7007	18.3573	26.1401
GPi	46.0857	49.6579	34.2808	45.1895	38.9418	26.4477	32.0893	41.6451	65.2621	22.4485	26.6955	40.1925	36.2054	65.5467	42.5739	82.6827	67.2828	33.8861	34.5979
SI	34.3017	53.5243	28.6885	38.1957	32.3101	26.0360	30.2263	31.9960	41.9750	19.4300	20.5826	35.5099	28.8184	50.0723	33.0070	86.4974	55.0463	27.4298	31.7512
MA	24.3965	38.6089	15.0818	20.4668	16.6657	14.9830	12.3059	17.2752	28.6925	10.9470	10.4238	23.0879	13.9771	33.4957	17.1106	76.4550	41.2385	15.2927	17.4689
LD	13.9271	38.0098	10.6936	11.5883	10.5836	10.6396	8.5296	11.8945	38.9854	7.3542	7.2380	12.7470	10.4918	16.4506	10.4930	83.9976	54.8530	11.3364	11.7755
LP	17.6129	44.6793	18.9123	25.0090	18.6020	17.0361	13.4397	20.9433	42.6280	10.5759	12.9813	19.7238	19.5459	21.2417	17.9855	82.5386	61.0407	18.4456	18.8279
PO	11.1415	49.8035	7.1659	8.3531	6.3317	7.4184	4.1998	6.1479	39.8201	4.7635	4.3128	7.9863	8.2369	10.2036	6.0993	86.3346	60.5250	5.5850	7.5465
RT	14.5586	29.1071	14.1758	17.7108	15.5997	11.6745	10.8485	20.3247	45.4542	9.6863	9.8109	21.2076	15.4374	40.9786	17.0561	75.9444	35.1873	13.3627	17.0864
VPL	6.0598	28.2471	3.6606	4.5930	3.1534	2.9975	2.0156	4.4698	40.7918	1.9899	2.3416	5.2105	5.3505	7.0242	2.3116	101.567	37.1748	3.1538	3.4994
VPM	2.0370	47.0716	3.1819	3.3049	2.7059	3.3268	1.6735	2.0305	40.9201	1.6087	1.5015	4.0701	2.5215	6.0226	2.4664	92.8635	62.0616	2.2748	3.0729

SPFp	13.4049	41.7275	27.9114	40.3713	30.1617	26.5823	19.6117	32.8085	43.3566	19.2466	22.8630	37.5908	28.1321	40.8958	31.0195	93.8815	62.1586	31.8165	33.3579
LHA	32.4896	52.8086	27.6099	35.2159	29.4101	24.7844	25.1858	30.1491	40.2556	19.0421	19.3781	35.2028	25.6637	49.2584	30.7922	81.2105	54.6776	26.8970	31.5356
STN	19.6671	49.8271	23.8032	29.1117	23.0819	21.0446	18.8589	28.4332	39.0098	18.8339	19.0199	28.9583	20.8317	41.2806	26.3567	88.2062	49.5743	27.0810	26.0917
ZI	30.6758	47.9179	21.8434	28.4252	24.0658	18.2022	17.5540	28.7947	32.9738	14.8193	16.5008	29.3946	22.9074	57.4036	23.6069	79.4972	54.8111	24.1992	26.5984
IC	20.8458	36.5588	23.1711	28.2167	24.8132	20.5394	20.2731	26.3636	30.8939	15.9483	17.3612	28.3571	23.7198	47.4438	24.9647	69.6877	46.6357	23.9370	24.3785
SCm	30.4148	52.0921	33.9679	38.9625	34.7859	28.8228	29.5097	45.4368	41.3568	24.6752	27.0124	39.6839	36.1249	66.3871	39.1446	80.7239	64.8259	36.0732	37.2546
SCs	31.2011	48.8799	31.1236	38.7564	32.7758	27.2256	27.1549	37.7004	37.4163	20.4087	23.2433	36.7329	29.6908	53.2911	33.1468	75.7610	58.9648	32.1161	33.8831
SNc	26.5449	59.6397	29.0731	32.1757	29.3623	25.9394	25.1122	44.0764	38.1612	21.6628	23.2610	34.6589	29.1728	50.1217	32.7519	91.1967	67.0537	31.4321	34.0945
SNr	50.6744	64.3472	35.2526	43.4125	38.3006	32.2683	35.5869	40.0403	50.9411	27.3275	26.5679	40.1102	30.5319	59.5876	40.8975	86.8236	62.4724	36.4155	39.5231
APN	8.5517	42.4825	23.7539	31.3698	25.0604	18.2922	17.8908	31.7784	50.1659	17.8259	18.4319	31.2461	26.8512	50.0021	26.1402	76.9988	57.0666	23.0668	26.7876
NOT	40.2868	38.1329	22.1775	21.5696	25.3806	14.0082	17.5937	29.3850	41.4176	14.8591	18.0899	30.9051	22.1240	45.2820	30.7568	75.6716	46.7833	19.9675	25.5448
PPN	48.6274	53.2458	26.6248	35.0451	28.3628	22.2891	23.7030	37.3807	37.9328	18.6632	22.1733	33.3481	30.3645	63.9638	32.2748	90.3315	60.0795	31.7636	32.0124
PPT	0.0000	35.4084	19.0422	30.6758	23.5029	23.5558	16.9048	25.3752	42.7726	16.1570	16.8611	27.5371	22.8370	51.3672	21.9838	73.7091	56.7444	30.1647	26.4290
RR	45.1004	57.9223	30.3533	39.3249	33.0775	28.5998	25.3928	43.7039	37.3927	23.4299	25.4071	37.4865	30.3546	55.7444	28.8600	86.0593	57.7861	35.7429	38.6399
MRN	46.8639	56.6217	35.5330	40.7162	36.8836	30.2302	29.4260	44.6306	44.6600	26.6347	28.1362	40.7078	36.4834	64.3740	37.3143	83.8484	68.4267	38.7202	38.9671
P	11.6545	45.4517	21.8149	27.2760	23.0731	19.1856	17.7897	28.6431	31.0353	15.5014	17.6663	27.8528	22.5407	59.8043	26.1678	81.5698	52.9168	25.0468	25.1069
MY	22.6121	44.6151	19.4789	24.1059	18.8663	16.9296	15.2038	23.1269	29.6104	12.7578	14.3363	22.6608	20.2604	56.0054	21.1542	81.7741	54.5081	20.9064	21.2128
IP	2.1238	10.1287	3.3567	3.9253	5.1698	2.7473	2.7106	4.2761	25.7103	0.7636	1.8470	7.8401	2.0063	63.6482	2.4391	81.0816	22.2995	3.4747	4.3860
ANcr2gr	5.1574	17.4934	9.6785	10.3177	9.8101	9.5565	9.3816	6.3329	14.8923	7.9082	5.2750	8.9141	13.1476	32.4822	7.1794	73.1193	21.5199	8.8028	9.7388
ANcr2mo	24.0698	24.7361	20.3300	19.8055	19.4334	22.6431	16.2506	22.9772	15.5892	14.5643	14.3914	16.8430	14.5657	31.5104	18.5056	64.4986	29.1429	20.2744	19.5045
CENT3gr	4.7372	14.7910	8.5653	9.4211	11.1665	7.4724	5.6148	5.1270	29.2215	8.8407	5.3518	9.6995	2.0032	60.2597	7.8528	56.8660	19.2990	8.5054	7.1350
CENT3mo	13.1597	23.1099	18.3860	14.1735	18.3432	14.3175	13.3075	21.0578	27.2020	8.8687	13.7909	15.3481	14.8573	40.7231	17.9549	61.7188	31.3101	18.7917	16.8399
CUL4,5gr	5.9589	16.2692	8.6047	10.5209	9.0396	9.5338	8.3577	6.9713	21.3307	8.0805	5.4989	10.4840	7.4411	51.3091	8.4466	67.6374	21.0881	9.5053	9.8065
CUL4,5mo	18.8520	23.6274	18.3223	18.0850	19.3476	17.3762	15.5101	20.0998	25.9365	11.5515	14.2121	14.9614	12.6273	36.3764	18.6300	65.2469	31.6448	18.8694	18.8147
SIMgr	8.9977	17.2983	11.4739	10.8779	11.6856	10.3901	9.1708	7.1011	21.3970	10.2995	6.6769	12.5571	16.9505	40.9509	9.2254	75.1603	23.1900	11.9744	11.6791
SIMmo	23.4946	26.4662	21.2442	20.1477	21.8994	19.4007	15.8980	22.0223	20.9503	13.7356	16.2550	17.8411	18.7811	38.0544	17.5897	67.2921	32.9558	21.4032	20.1947
PRMgr	6.1506	15.2797	8.5237	8.1091	9.0905	8.7940	6.5598	5.9893	17.3317	7.2101	4.6300	9.2063	6.2601	30.5986	6.8882	71.9682	20.6121	8.6578	8.7326
PRMmo	21.0511	25.8577	20.4040	20.3925	19.8817	19.0880	15.7282	21.7021	18.7438	15.8495	14.7235	16.1275	16.6690	33.5478	17.9885	63.6895	33.0585	20.1662	19.3924
COPYgr	6.5684	12.9789	7.2135	8.7655	8.6260	7.5116	7.4007	5.2912	15.1793	6.7901	4.0219	9.2989	6.0537	34.7792	7.5197	63.0375	18.7964	7.6757	7.7649
COPYmo	21.2137	25.2701	17.9913	17.8533	18.2327	16.8137	14.1748	19.1663	16.3091	10.9248	13.0988	14.1511	17.7782	30.4010	14.7812	68.7469	31.7047	17.6152	17.5957

Appendix 10: Raw data for LPL synapse percentages across the brain. LPL synapses as percentage of total synapse number in 12 main brain areas and 110 brain subregions. Five synapse subtypes with longest PSD95-HaloTag lifetimes (subtypes 2, 3, 5, 34 and 35) were grouped to derive LPL synapse number. Subtypes densities (/100 μm^2) are provided for all 37 subtypes.

LPL synapse percentage: main brain areas

Abbreviation	Region name	LPL synapses % of total	LPL synapses (2, 3, 5, 34, 35)	Total subtypes
Isocortex	Isocortex	11.8857	12.6727	106.6210
OLF	Olfactory areas	3.0295	2.3059	76.1147
HPF	Hippocampal Formation	3.8026	4.4288	116.4678
CTXsp	Cortical subplate	4.4229	3.5933	81.2440
STR	Striatum	5.9480	5.2352	88.0162
PAL	Pallidum	1.7868	0.4234	23.6970
TH	Thalamus	0.7979	0.4840	60.6644
HY	Hypothalamus	2.1899	0.6764	30.8872
MB	Midbrain	2.3980	0.5853	24.4072
P	Pons	2.1011	0.3378	16.0762
MY	Medulla	2.1708	0.3783	17.4263
CB	Cerebellum	3.8958	1.5910	40.8377

Type 1 (PSD95-only) subtypes: main brain areas

Abbreviation	subtype1	subtype2	subtype3	subtype4	subtype5	subtype6	subtype7	subtype8	subtype9	subtype10	subtype11
Isocortex	2.7851	0.3489	0.3455	9.2092	6.9358	2.1857	0.3759	22.8661	5.9179	3.6926	1.5548
OLF	3.2042	0.1216	0.0829	3.5967	1.6035	2.9122	0.5030	15.5840	4.7841	1.4318	0.7121
HPF	3.7954	0.1315	0.1349	4.4372	2.6549	3.2924	0.5348	24.1485	7.9013	2.2865	1.8420
CTXsp	4.3197	0.2039	0.1246	4.2613	2.0189	4.0342	0.4548	19.8416	4.9630	1.3574	0.7998
STR	3.3668	0.2043	0.1521	4.4632	2.6945	3.1107	0.4532	22.4220	5.5804	1.7743	1.3543
PAL	1.8259	0.0618	0.0202	0.7844	0.2790	1.8707	0.2272	4.8485	1.5125	0.2044	0.0935
TH	4.2070	0.1100	0.0242	1.0174	0.2952	4.7875	0.2951	20.2541	4.0147	0.3043	0.5046
HY	2.4348	0.0790	0.0285	1.1593	0.4368	2.4900	0.3112	6.7736	2.0811	0.3127	0.1364
MB	2.0178	0.0495	0.0221	1.0089	0.3785	2.0111	0.2512	5.4619	1.8307	0.2780	0.1094
P	1.3499	0.0588	0.0151	0.4557	0.2096	1.3123	0.1822	3.3359	1.2988	0.1371	0.0585
MY	1.5265	0.0640	0.0169	0.5161	0.2412	1.5111	0.1934	4.1212	1.6011	0.1702	0.0793
CB	1.7259	0.0550	0.0708	2.5543	1.1822	1.7442	0.4175	9.7700	3.1218	1.1717	0.5701

Type 2 (SAP102-only) subtypes: main brain areas

Abbreviation	subtype12	subtype13	subtype14	subtype15	subtype16	subtype17	subtype18
Isocortex	0.9478	0.8832	0.3308	0.8779	4.4192	1.7005	0.1365
OLF	1.1954	1.8984	0.3673	1.1671	6.1311	2.5316	0.1923
HPF	1.8808	1.0501	0.5670	1.1652	6.1950	2.4006	0.1991
CTXsp	0.8520	0.6575	0.2522	0.8330	4.3040	1.3567	0.1238
STR	1.0562	0.6960	0.2747	0.8339	4.0851	1.4584	0.1147
PAL	0.2482	0.6401	0.0814	0.5640	2.0388	1.1060	0.0578
TH	0.5642	0.2004	0.2478	0.4563	2.9502	0.5803	0.0910
HY	0.2587	0.6531	0.0927	0.5272	2.0419	0.9453	0.0644
MB	0.1785	0.4959	0.0671	0.4148	1.4978	0.7543	0.0472
P	0.1195	0.5152	0.0481	0.3335	1.1418	0.6741	0.0387
MY	0.1180	0.4358	0.0446	0.3162	1.0906	0.5406	0.0341
CB	0.3760	1.6700	0.1493	0.7521	2.4805	2.0692	0.0955

Type 3 (PSD95 + SAP102) subtypes: main brain areas

Abbreviation	subtype 19	subtype 20	subtype 21	subtype 22	subtype 23	subtype 24	subtype 25	subtype 26	subtype 27	subtype 28	subtype 29	subtype 30	subtype 31	subtype 32	subtype 33	subtype 34	subtype 35	subtype 36	subtype 37
Isocortex	0.0705	0.7236	2.4816	0.3802	2.1388	1.3660	0.8895	0.7320	0.1457	0.8708	8.3175	2.7044	0.1272	6.7807	1.0781	0.5206	4.5219	2.5129	4.7457
OLF	0.0945	0.0787	1.2311	0.2939	1.4449	0.7093	0.9582	0.5934	0.2410	0.5477	4.5658	1.5270	0.0590	10.5284	1.0500	0.0538	0.4441	1.1084	2.5664
HPF	0.0655	0.2403	2.7271	0.6422	2.9524	1.4640	1.7049	0.9038	0.1709	2.0297	11.4729	4.3099	0.2077	11.2442	2.0067	0.1018	1.4056	3.0629	5.1377
CTXsp	0.0415	0.3642	2.0005	0.5145	1.8083	0.9810	0.8455	0.6261	0.1512	0.8845	8.7257	1.8243	0.2754	4.9168	0.7954	0.1181	1.1278	1.5772	2.9077
STR	0.0448	0.6235	2.2268	0.5027	1.9426	1.1868	0.9693	0.5556	0.1617	1.3275	9.2438	2.4381	0.2723	3.8695	0.9329	0.4862	1.6981	1.8629	3.5765
PAL	0.0180	0.0310	0.4872	0.1865	0.4729	0.2289	0.2602	0.1892	0.1125	0.1277	1.7909	0.4239	0.1716	1.6494	0.1457	0.0192	0.0432	0.1991	0.6754
TH	0.0087	0.0296	0.7909	0.2114	0.9663	0.3814	0.5664	0.2204	0.0649	0.5949	5.0954	0.8595	0.2697	7.4475	0.3640	0.0130	0.0416	0.6471	1.1874
HY	0.0254	0.0666	0.6729	0.2547	0.6306	0.3173	0.3395	0.2420	0.1621	0.1913	2.5544	0.5966	0.2305	2.1884	0.2070	0.0342	0.0979	0.2954	0.9538
MB	0.0193	0.0798	0.5617	0.2195	0.4796	0.2652	0.2387	0.1616	0.1338	0.1646	1.9339	0.5150	0.2780	1.1738	0.1455	0.0251	0.1101	0.2008	0.8265
P	0.0137	0.0401	0.3517	0.1660	0.3160	0.1565	0.1596	0.0774	0.1581	0.1032	1.0877	0.4033	0.2484	0.7322	0.0870	0.0185	0.0358	0.0891	0.5472
MY	0.0059	0.0396	0.3749	0.1638	0.3252	0.1710	0.1571	0.0750	0.1164	0.1211	1.1694	0.4078	0.2452	0.6337	0.0842	0.0177	0.0384	0.0983	0.5607
CB	0.0689	0.0774	0.6050	0.1933	0.5314	0.3697	0.3865	0.2831	0.2896	0.2035	1.7621	0.7614	0.0797	2.4792	0.3449	0.0121	0.2710	0.3544	1.7886

LPL synapse percentage: subregions

Abbreviation	LPL synapses % of total	LPL synapses (2, 3, 5, 34, 35)	Total subtypes
ORB1	13.8917	16.0797	115.7503
ORB2-3	13.4254	15.2173	113.3469
ORB5	10.3993	10.7646	103.5121
ORB6a	7.0082	6.6658	95.1143
ORB6b	3.2536	1.9535	60.0407
FRP1	14.3535	17.9724	125.2123
FRP2-3	13.8795	16.3286	117.6458
MO1	16.5181	21.6312	130.9541
MO2-3	16.3574	19.6065	119.8634
MO5	11.3784	11.3978	100.1709
MO6a	5.6572	4.9263	87.0808
MO6b	2.9278	1.8508	63.2151
SS1	15.8230	20.4704	129.3716
SS2-3	17.2209	21.0415	122.1857
SS4	13.0410	14.6130	112.0546
SS5	10.6660	10.7737	101.0102
SS6a	5.9428	5.3556	90.1181
SS6b	2.8870	1.6432	56.9167
PTLp1	14.9719	19.8005	132.2516
PTLp2-3	15.8563	19.7205	124.3703
PTLp4	13.4523	15.7631	117.1777
PTLp5	11.1340	11.8404	106.3447
PTLp6a	6.9249	6.6834	96.5119
PTLp6b	3.3006	1.9948	60.4372
VIS1	11.4224	13.8098	120.9016
VIS2-3	13.0877	15.9041	121.5191
VIS4	11.7863	13.6070	115.4477
VIS5	10.0473	10.8895	108.3821
VIS6a	6.1411	6.1571	100.2604
VIS6b	3.1280	1.7515	55.9954
RSPd1	7.0047	6.9055	98.5840
RSPd2-3	7.7615	8.1191	104.6081
RSPd5	6.6796	6.9764	104.4433
RSPv1	6.2223	4.8233	77.5166
RSPv2-3	4.4206	3.1074	70.2939
RSPv5	5.8439	4.7025	80.4687
RSPv6a	4.4870	2.9087	64.8257
MOBgl	1.6530	0.9303	56.2810
MOBopl	1.1505	0.8575	74.5360
MOBmi	2.0437	0.8868	43.3941
MOBipl	1.9378	0.9914	51.1622
MOBgr	1.9936	0.8510	42.6883
AON1	4.4072	5.1219	116.2167
AON2	5.1447	5.6822	110.4481
PIR1	4.5345	4.3554	96.0485
PIR2	4.2472	3.3478	78.8236
PIR3	3.6950	2.9678	80.3194
CA1so	3.9895	5.9662	149.5464
CA1sp	2.0876	1.4015	67.1341
CA1sr	5.8356	8.8865	152.2811
CA1slm	2.7097	3.1340	115.6598
CA2so	0.4917	0.5823	118.4261
CA2sp	2.7243	1.0996	40.3628
CA2sr	0.7121	0.7653	107.4599
CA2slm	0.2385	0.3139	131.6160
CA3so	0.8877	0.8660	97.5603

CA3sp	2.9880	1.5068	50.4301
CA3sr	1.9020	2.1267	111.8155
CA3slm	0.6088	0.8355	137.2249
DG-mo	2.2295	3.5696	160.1091
DG-po	2.0383	1.3459	66.0329
DG-sg	0.9331	0.3776	40.4647
SUB	9.5991	8.3673	87.1675
CLA	5.4857	4.7927	87.3681
EPd	3.5539	2.7368	77.0080
CP	6.3885	5.4290	84.9814
ACB	5.5462	5.3026	95.6076
FS	1.8770	0.3179	16.9351
OT1	7.4262	7.2228	97.2601
OT2	4.2090	3.6772	87.3639
OT3	4.3705	4.0039	91.6111
GPi	1.2620	0.1495	11.8439
SI	1.7573	0.4725	26.8861
MA	2.2853	0.8742	38.2517
LD	0.8438	0.6295	74.5972
LP	1.3971	0.9756	69.8344
PO	0.6991	0.4977	71.1885
RT	1.2111	0.2807	23.1801
VPL	0.5442	0.2968	54.5396
VPM	0.6498	0.4633	71.3000
SPFp	1.8390	0.5480	29.8005
LHA	2.4565	0.9050	36.8418
STN	2.1920	0.7113	32.4499
ZI	2.0570	0.4360	21.1969
IC	3.1362	0.9905	31.5813
SCm	2.5568	0.6347	24.8223
SCs	2.5380	0.9583	37.7568
SNc	1.8274	0.2887	15.7969
SNr	1.4297	0.2602	18.2020
APN	1.7799	0.3824	21.4851
NOT	1.6301	0.5474	33.5815
PPN	1.4781	0.2447	16.5537
PPT	1.9588	0.4852	24.7686
RR	1.4221	0.3082	21.6713
MRN	2.0768	0.3921	18.8794
P	2.1011	0.3378	16.0762
MY	2.1708	0.3783	17.4263
IP	1.6327	0.2665	16.3200
ANcr2gr	5.2292	2.6483	50.6444
ANcr2mo	2.8126	1.2214	43.4265
CENT3gr	3.8785	1.7224	44.4090
CENT3mo	2.1378	0.7481	34.9926
CUL4,5gr	5.3477	2.6579	49.7021
CUL4,5mo	3.0142	1.1338	37.6147
SIMgr	7.2507	4.0782	56.2457
SIMmo	3.5150	1.4213	40.4338
PRMgr	5.7292	3.0656	53.5087
PRMmo	3.1129	1.3644	43.8291
COPYgr	5.2658	2.6415	50.1633
COPYmo	2.9355	1.3190	44.9334

Type 1 (PSD95-only) subtypes: subregions

Abbreviation	subtype1	subtype2	subtype3	subtype4	subtype5	subtype6	subtype7	subtype8	subtype9	subtype10	subtype11
ORB1	2.4883	0.4306	0.3960	9.0583	7.9193	1.8028	0.3793	22.2915	6.0615	3.7858	1.6931
ORB2-3	2.4560	0.4438	0.4295	9.8623	8.4314	1.6926	0.3838	22.9394	6.5813	4.3569	1.7624
ORB5	3.1903	0.3619	0.3219	8.8933	6.0311	2.3869	0.4004	22.4884	6.0502	3.4213	1.3321
ORB6a	3.9283	0.2607	0.2099	6.7462	3.6794	3.3822	0.4252	22.9812	5.6899	2.3303	1.1555
ORB6b	3.6741	0.1575	0.0681	2.5391	1.0746	3.7932	0.3610	15.9751	3.6182	0.7083	0.5264
FRP1	2.3808	0.5316	0.4608	9.9329	9.1675	1.7351	0.4213	25.4413	7.0828	4.4942	2.2597
FRP2-3	2.5007	0.5286	0.4597	9.8663	9.0957	1.7453	0.3931	25.0200	7.1168	4.4924	2.1548
MO1	1.6322	0.5376	0.5023	11.2050	11.0471	1.1457	0.3469	25.0191	6.6684	5.0989	2.4626
MO2-3	1.8510	0.5444	0.5055	11.1505	10.6912	1.2526	0.3464	23.8322	6.5833	5.0008	2.1231
MO5	3.1236	0.3634	0.3370	9.3956	6.3526	2.3129	0.4134	21.9488	5.8505	3.4879	1.2721
MO6a	4.3268	0.1945	0.1603	6.2501	2.8298	3.9188	0.4399	22.5798	5.4680	1.8840	0.9854
MO6b	3.9349	0.1544	0.0691	2.9182	1.0618	4.0771	0.3768	17.0967	3.9026	0.7352	0.5694
SS1	1.5886	0.4751	0.4982	11.5591	10.6572	1.1751	0.3345	25.2251	6.3456	5.0999	2.3826
SS2-3	1.5470	0.5057	0.5454	11.7313	11.6376	1.0040	0.3182	23.2780	6.4585	5.3748	2.1715
SS4	2.1393	0.2719	0.4063	11.9730	8.4136	1.4656	0.3181	24.8500	6.0833	4.8314	1.7059
SS5	3.0954	0.3172	0.3196	10.0364	6.1760	2.2957	0.3820	22.7623	5.7360	3.6227	1.2570
SS6a	4.0286	0.1924	0.1708	6.7268	3.0290	3.5841	0.4116	22.9319	5.3153	2.0798	1.0346
SS6b	3.4838	0.1590	0.0585	2.5324	0.9082	3.6580	0.3520	15.2196	3.4318	0.6242	0.4904
PTLp1	1.7347	0.4208	0.5031	11.8035	10.6320	1.1852	0.3461	26.2063	6.5732	5.3058	2.4311
PTLp2-3	1.7642	0.4422	0.5132	11.9221	11.0766	1.1870	0.3312	25.0547	6.7917	5.5311	2.2650
PTLp4	2.1693	0.2470	0.4409	12.4160	8.9610	1.5114	0.3357	26.0282	6.4857	5.0249	1.8652
PTLp5	3.0129	0.2893	0.3450	11.0516	6.9020	2.1531	0.3563	23.7984	5.9591	4.0561	1.3640
PTLp6a	3.8002	0.2085	0.2058	8.1563	3.8217	3.1340	0.4108	24.0877	5.5048	2.6121	1.1133
PTLp6b	3.7163	0.1417	0.0863	3.0908	1.1666	3.7052	0.3725	16.6824	3.9220	0.7728	0.5591
VIS1	2.4008	0.2713	0.3555	9.5157	7.2897	1.8751	0.3831	24.2005	6.0903	4.0333	1.8835
VIS2-3	2.1597	0.3297	0.4203	10.4305	8.7303	1.5122	0.3317	24.0692	6.4345	4.6059	2.0124
VIS4	2.4060	0.2598	0.3605	10.6715	7.5712	1.7354	0.3345	25.0149	6.2501	4.4657	1.7729
VIS5	2.9407	0.2726	0.3034	9.9271	6.1265	2.1848	0.3563	23.4847	5.7626	3.6952	1.3650
VIS6a	3.6423	0.2197	0.1895	7.2471	3.3836	3.2129	0.3933	24.2275	5.4730	2.4243	1.2199
VIS6b	3.2138	0.1325	0.0615	2.5274	0.9411	3.3121	0.3245	14.4872	3.2459	0.6815	0.4903
RSPd1	3.6118	0.1652	0.2041	6.7485	3.8727	3.2883	0.4786	22.3136	5.4369	2.4965	1.1225
RSPd2-3	3.2205	0.2302	0.2369	7.9275	4.6531	2.6779	0.4109	23.8675	5.9028	3.0505	1.3864
RSPd5	3.3766	0.2131	0.2181	7.7427	3.8130	2.7903	0.3772	24.4839	5.4294	2.7388	1.2304
RSPv1	3.7119	0.1166	0.1362	5.0419	2.5487	3.3731	0.4588	16.8096	4.4148	1.6632	0.6115
RSPv2-3	3.4858	0.1425	0.0991	3.5650	1.7646	3.3536	0.4607	15.7946	4.1715	1.2424	0.6001
RSPv5	3.9564	0.1628	0.1326	5.2526	2.4508	3.6128	0.4540	18.7311	4.6286	1.6615	0.6872
RSPv6a	3.5855	0.1735	0.0925	3.7339	1.5322	3.4335	0.3994	15.4464	3.7448	1.0395	0.5372
MOBgl	2.3961	0.1022	0.0384	1.9509	0.7512	2.3483	0.6061	11.0198	4.6378	1.0875	0.5443
MOBopl	4.1012	0.0387	0.0275	2.8734	0.7293	3.9108	0.5021	16.2267	4.3826	0.8456	0.4637
MOBmi	2.1334	0.1407	0.0466	1.2135	0.6395	1.8103	0.3824	6.1386	2.6892	0.5176	0.1998
MOBipl	2.6223	0.0678	0.0428	1.6372	0.8046	2.3032	0.4223	7.8567	3.4830	0.7134	0.2164
MOBgr	2.2824	0.0636	0.0348	1.2727	0.6830	1.9331	0.3595	6.5269	3.0559	0.5447	0.2073
AON1	3.5032	0.1125	0.1617	6.7942	3.3473	3.1067	0.4637	25.8733	6.6145	2.7423	1.5078
AON2	3.2689	0.2826	0.2054	6.3947	3.5843	2.6715	0.4139	23.1262	6.1734	2.6797	1.4515
PIR1	3.2929	0.1344	0.1615	6.5602	3.1372	2.7635	0.5379	19.1030	5.4953	2.4600	0.9392
PIR2	3.6280	0.3283	0.1421	4.2182	2.2252	3.0227	0.5670	15.8600	4.9337	1.6403	0.7016
PIR3	4.5930	0.1645	0.1034	4.0962	1.7851	4.3706	0.5148	19.6863	5.1482	1.2966	0.7045
CA1so	3.7464	0.0882	0.1733	6.8405	3.8643	3.0127	0.5268	31.6415	9.6235	3.6724	2.6915
CA1sp	2.5143	0.1927	0.0670	1.5029	0.8311	2.4194	0.3833	14.0004	4.3835	0.8345	0.9658
CA1sr	3.4964	0.1466	0.2615	7.1898	5.1554	2.5929	0.5437	29.8086	9.8775	4.0218	3.0033
CA1slm	4.6618	0.0652	0.0940	5.3114	2.3388	4.0164	0.5249	27.3946	8.7958	2.6162	1.4717
CA2so	4.9406	0.0463	0.0231	1.2743	0.4128	5.2745	0.4920	26.7914	6.4306	0.6170	1.0055
CA2sp	1.7885	0.4327	0.0707	0.3481	0.5351	1.9255	0.3536	6.3182	2.2537	0.1939	0.1935
CA2sr	4.5400	0.0592	0.0283	1.2606	0.5105	4.9794	0.5335	22.7145	6.5667	0.5479	0.9967
CA2slm	5.0722	0.0178	0.0103	1.1225	0.2339	5.6242	0.4405	30.4890	7.0716	0.5620	1.2526
CA3so	4.0824	0.0604	0.0328	1.1961	0.5413	4.3995	0.4797	19.1200	6.1627	0.4933	0.9782
CA3sp	3.3169	0.4086	0.0847	0.8986	0.9012	2.6149	0.6109	9.1074	4.9484	0.6009	0.3987
CA3sr	4.7122	0.1172	0.0828	2.1090	1.3081	4.1329	0.7107	19.1957	8.3089	1.1191	1.2228
CA3slm	4.5197	0.0460	0.0275	1.3040	0.5054	5.2237	0.5465	27.7323	8.1919	0.5892	1.5882
DG-mo	4.1317	0.0793	0.1274	4.9812	2.5835	3.6415	0.6542	35.1718	11.2578	2.9954	3.2129
DG-po	4.9041	0.1428	0.0655	1.3437	0.9978	3.8201	0.7258	12.5773	6.9743	0.7879	0.5475
DG-sg	1.9208	0.0883	0.0273	0.3300	0.2206	1.9849	0.2619	7.8554	2.4655	0.1982	0.3648

SUB	3.5808	0.2109	0.2053	6.4818	4.1099	2.8847	0.4386	17.2697	5.1900	2.3542	0.8696
CLA	4.0048	0.2307	0.1533	5.2312	2.5914	3.7393	0.4112	21.6076	5.1453	1.7213	0.9679
EPd	4.5316	0.1844	0.1042	3.5803	1.6068	4.2393	0.4854	18.6083	4.8269	1.0952	0.6807
CP	3.3124	0.1919	0.1487	4.3767	2.6150	3.0302	0.3981	22.3940	5.2847	1.6582	1.3517
ACB	3.5926	0.2321	0.1621	4.8009	2.9348	3.3382	0.5238	24.4628	6.3923	2.0529	1.5290
FS	1.1068	0.0374	0.0108	0.4489	0.1795	1.1863	0.1258	3.7294	1.0188	0.1412	0.1162
OT1	2.7729	0.2356	0.2188	6.5835	4.0759	2.4222	0.5174	19.4628	5.2932	2.5468	1.1939
OT2	3.3292	0.2131	0.1378	3.5008	2.2153	3.1760	0.5823	18.8280	5.4643	1.5365	1.0367
OT3	3.7402	0.1914	0.1348	3.9191	2.2926	3.6344	0.5786	21.3825	5.7070	1.5657	1.1129
GPi	1.0802	0.0343	0.0074	0.2152	0.0898	1.1099	0.1155	2.5376	0.8674	0.0606	0.0389
SI	2.0319	0.0617	0.0222	0.9101	0.3137	2.0992	0.2538	5.4212	1.6437	0.2323	0.1056
MA	2.7528	0.1385	0.0424	1.5529	0.5846	2.7364	0.3828	8.1422	2.5294	0.4293	0.1735
LD	4.8714	0.0801	0.0296	1.9038	0.4517	5.3618	0.3700	24.1928	4.8296	0.5932	0.6583
LP	4.7872	0.0998	0.0413	2.1432	0.6292	4.9950	0.3204	22.1550	4.3059	0.5847	0.5739
PO	4.7906	0.1105	0.0238	1.2039	0.3136	5.4528	0.3290	24.0475	4.6524	0.3590	0.6259
RT	2.2362	0.0424	0.0121	0.6390	0.1837	2.2722	0.1495	6.6955	1.7302	0.1678	0.0974
VPL	3.7832	0.1115	0.0182	0.4615	0.1540	4.5354	0.2667	18.6945	3.6190	0.1467	0.4398
VPM	4.7965	0.1674	0.0277	0.7165	0.2503	5.6904	0.3424	24.2421	4.8223	0.2486	0.6168
SPFp	2.6201	0.0677	0.0224	0.9119	0.3321	2.6275	0.1846	9.1393	1.9817	0.2175	0.1769
LHA	2.7810	0.0885	0.0372	1.6257	0.5929	2.8395	0.3687	8.2129	2.3967	0.4146	0.1790
STN	2.0937	0.1302	0.0348	1.1188	0.4413	2.1871	0.3095	6.1097	1.9467	0.3062	0.1365
ZI	2.0235	0.0565	0.0181	0.6969	0.2851	2.0112	0.2184	4.9851	1.7321	0.2085	0.0792
IC	2.3756	0.0675	0.0368	1.6505	0.6667	2.2335	0.3773	6.5695	2.5206	0.5034	0.1656
SCm	2.2003	0.0532	0.0226	1.0132	0.3872	2.2120	0.2493	5.8094	1.8352	0.2635	0.1010
SCs	2.9012	0.0440	0.0333	1.8926	0.5931	3.0858	0.3428	9.3921	2.5413	0.4553	0.2060
SNc	1.3841	0.0364	0.0124	0.4499	0.1747	1.4197	0.1448	3.3751	1.0474	0.1116	0.0507
SNr	1.2886	0.0387	0.0121	0.4485	0.1749	1.3222	0.2121	2.9779	1.3638	0.1356	0.0665
APN	2.0508	0.0368	0.0133	0.7171	0.2561	2.0836	0.1603	5.7727	1.5752	0.1794	0.0827
NOT	2.9802	0.0352	0.0147	1.3295	0.3559	3.2289	0.2342	9.3776	2.0429	0.2641	0.1259
PPN	1.5664	0.0372	0.0102	0.4064	0.1599	1.5650	0.1421	3.8252	1.2879	0.1073	0.0552
PPT	2.3666	0.0441	0.0183	0.8186	0.2886	2.4342	0.2134	6.4915	1.7787	0.1992	0.0924
RR	1.9938	0.0254	0.0126	0.6318	0.2173	2.0496	0.1691	5.1165	1.6356	0.1710	0.0719
MRN	1.8441	0.0463	0.0153	0.6438	0.2412	1.8174	0.1671	4.6893	1.4247	0.1606	0.0700
P	1.3499	0.0588	0.0151	0.4557	0.2096	1.3123	0.1822	3.3359	1.2988	0.1371	0.0585
MY	1.5265	0.0640	0.0169	0.5161	0.2412	1.5111	0.1934	4.1212	1.6011	0.1702	0.0793
IP	1.0041	0.0759	0.0143	0.2734	0.1375	1.0863	0.2018	2.7625	1.1586	0.0910	0.0589
ANcr2gr	1.2485	0.0816	0.1253	3.3617	2.0817	1.0680	0.4522	10.9139	3.5201	1.8529	0.9573
ANcr2mo	2.4029	0.0452	0.0518	2.8123	0.8684	2.4188	0.5178	10.3818	3.4989	1.0059	0.3967
CENT3gr	1.3617	0.0480	0.0805	2.5759	1.2100	1.3795	0.2883	11.3409	3.0149	1.2658	0.7724
CENT3mo	2.3819	0.0296	0.0309	1.8494	0.5064	2.6287	0.3612	9.7926	2.9253	0.6249	0.3137
CUL4,5gr	1.2541	0.0729	0.1127	3.3095	1.9887	1.1647	0.3959	11.6345	3.4613	1.8172	0.9659
CUL4,5mo	2.1479	0.0349	0.0508	2.4745	0.7770	2.2533	0.4325	9.6338	3.1336	0.9284	0.3853
SIMgr	1.1081	0.1372	0.1844	4.1773	3.1068	0.8781	0.4875	11.7097	3.8950	2.3645	1.1632
SIMmo	1.9832	0.0413	0.0652	2.7932	0.9721	1.9275	0.5138	8.5279	3.2688	1.0798	0.3798
PRMgr	1.1701	0.1067	0.1371	3.6700	2.4679	0.9703	0.4903	11.4055	3.7956	2.1516	1.0615
PRMmo	2.1694	0.0354	0.0630	2.8982	0.9957	2.1002	0.5294	9.8457	3.4404	1.1499	0.4320
COPYgr	1.2124	0.0978	0.1189	3.4826	2.0960	1.0314	0.5247	10.7498	3.6236	1.8914	0.8916
COPYmo	2.1784	0.0374	0.0600	2.8152	0.9372	2.1528	0.5262	9.8918	3.3657	1.0689	0.4022

Type 2 (SAP102-only) subtypes: subregions

Abbreviation	subtype12	subtype13	subtype14	subtype15	subtype16	subtype17	subtype18
ORB1	1.2425	0.7793	0.4041	0.9591	5.1318	1.7058	0.1536
ORB2-3	0.9873	0.9928	0.3628	0.9013	4.6321	1.8022	0.1468
ORB5	0.9451	0.8862	0.3163	0.9032	4.6156	1.6714	0.1367
ORB6a	0.9024	0.7578	0.2882	0.8763	4.4061	1.6172	0.1311
ORB6b	0.5387	0.4521	0.1690	0.6381	3.1492	1.1062	0.0894
FRP1	1.2948	0.7723	0.3988	0.9147	4.7728	1.6351	0.1586
FRP2-3	0.9931	0.9028	0.3576	0.8653	4.2917	1.7345	0.1436
MO1	1.3248	1.0201	0.4493	0.9785	5.0336	1.9845	0.1603
MO2-3	1.0089	1.1427	0.3791	0.9121	4.5867	1.9749	0.1525
MO5	0.8369	0.8905	0.2911	0.8612	4.3106	1.6604	0.1292
MO6a	0.6969	0.6522	0.2368	0.7748	3.7252	1.4850	0.1050
MO6b	0.4940	0.4463	0.1710	0.6284	2.9841	1.1511	0.0929
SS1	1.2675	0.9360	0.4140	0.9496	4.8670	1.8443	0.1514
SS2-3	1.0179	1.2060	0.3997	0.9289	4.6404	2.0821	0.1548
SS4	0.7887	0.9050	0.3074	0.8168	3.8993	1.6481	0.1290
SS5	0.7929	0.8030	0.2768	0.8227	4.0247	1.5564	0.1202
SS6a	0.7642	0.6658	0.2569	0.8145	3.9278	1.5107	0.1175
SS6b	0.4789	0.3745	0.1444	0.5646	2.7761	0.9701	0.0782
PTLp1	1.2960	0.8709	0.4421	0.9496	4.8395	1.7355	0.1411
PTLp2-3	0.9579	1.0298	0.3853	0.8782	4.4172	1.8954	0.1475
PTLp4	0.8379	0.7857	0.3138	0.8230	3.9058	1.5230	0.1170
PTLp5	0.8010	0.7759	0.2854	0.8154	4.0338	1.4756	0.1359
PTLp6a	0.7970	0.7799	0.2661	0.8502	4.1809	1.6125	0.1230
PTLp6b	0.4359	0.3853	0.1543	0.6063	2.6044	1.0112	0.0826
VIS1	1.3210	0.8701	0.4184	0.9916	5.1571	1.7210	0.1529
VIS2-3	1.1579	1.0115	0.4119	0.9694	4.9343	1.9137	0.1576
VIS4	0.9346	0.7776	0.3350	0.8409	4.2817	1.5256	0.1327
VIS5	0.9770	0.7985	0.3404	0.8846	4.7065	1.5622	0.1385
VIS6a	0.9995	0.7784	0.3108	0.9183	4.6070	1.6532	0.1414
VIS6b	0.5173	0.4040	0.1596	0.6039	2.8322	0.9985	0.0794
RSPd1	0.9926	0.7817	0.3190	0.8156	4.2942	1.4642	0.1344
RSPd2-3	0.9760	0.8815	0.3390	0.8927	4.3844	1.6349	0.1319
RSPd5	0.9987	0.8330	0.3627	0.9384	4.6060	1.6378	0.1498
RSPv1	0.6513	0.7811	0.2421	0.7824	3.6750	1.4674	0.1204
RSPv2-3	0.6698	1.0357	0.2478	0.8835	3.7517	1.7835	0.1099
RSPv5	0.6197	0.8121	0.2376	0.7989	3.5427	1.5100	0.1136
RSPv6a	0.5051	0.5955	0.2052	0.6771	3.0599	1.1617	0.0920
MOBgl	1.0413	2.3369	0.3158	1.1285	5.5566	2.5740	0.1814
MOBopl	1.0173	2.1116	0.3518	1.2464	6.4074	2.8239	0.2063
MOBmi	0.8832	2.4948	0.2801	1.2649	5.9351	3.3413	0.2092
MOBipl	1.1486	2.3004	0.3210	1.3363	7.0751	3.2469	0.2105
MOBgr	0.9914	1.6086	0.2590	1.1257	5.9368	2.5646	0.1804
AON1	1.8583	0.7893	0.4679	1.1625	6.7030	1.8950	0.1790
AON2	1.6230	1.3443	0.5106	1.1055	6.7471	2.1298	0.2019
PIR1	1.3640	1.6101	0.4111	1.1351	6.0783	2.2674	0.1828
PIR2	0.9804	1.7934	0.3336	1.0125	5.3216	2.1780	0.1706
PIR3	0.8321	0.6357	0.2591	0.7866	4.3453	1.2989	0.1260
CA1so	2.0675	0.5710	0.6494	1.1753	6.2881	2.0497	0.1871
CA1sp	0.8937	1.4003	0.3389	1.0053	4.6506	2.2553	0.1601
CA1sr	2.4038	1.2371	0.7357	1.3595	7.0689	2.7088	0.2196
CA1slm	1.2114	0.7900	0.3970	1.0177	5.1559	1.9691	0.1482
CA2so	1.9864	0.6921	0.7245	1.3180	8.2726	1.8792	0.2164
CA2sp	0.6123	1.3549	0.2812	0.9990	4.9786	1.9037	0.1586
CA2sr	2.0734	0.9807	0.6758	1.4052	8.3483	2.3488	0.2509
CA2slm	2.2986	0.4615	0.7038	1.2943	8.5080	2.0525	0.2313
CA3so	2.6885	0.3461	0.6065	1.3380	7.3744	1.9838	0.1871
CA3sp	0.7473	0.8779	0.2336	0.8256	3.8388	1.7202	0.1272
CA3sr	3.2609	0.8539	0.7846	1.6814	8.6420	3.1420	0.2439
CA3slm	3.7269	0.4589	0.8250	1.6997	9.3500	2.7084	0.2673
DG-mo	2.7468	1.5562	0.8308	1.3784	7.8175	3.4667	0.2816
DG-po	1.1642	0.4656	0.3120	0.8225	4.1953	1.4331	0.1390
DG-sg	0.6848	1.7095	0.2497	0.7841	3.8235	2.3811	0.1820

SUB	0.8083	0.8587	0.2954	0.8338	4.1724	1.5591	0.1281
CLA	0.8972	0.6335	0.2610	0.8481	4.2718	1.4167	0.1220
EPd	0.8201	0.6753	0.2475	0.8233	4.3279	1.3193	0.1252
CP	0.9569	0.3897	0.2404	0.7113	3.4966	1.0881	0.0945
ACB	1.1217	0.9388	0.3012	0.9561	4.4910	1.8647	0.1327
FS	0.2068	0.2538	0.0527	0.3961	1.5245	0.6712	0.0371
OT1	1.6122	1.4658	0.4146	1.1800	6.2071	2.1160	0.1648
OT2	1.3528	1.8904	0.3921	1.1291	6.0397	2.4635	0.1874
OT3	1.3469	1.2227	0.3587	1.0985	5.7210	2.0672	0.1554
GPi	0.1160	0.1869	0.0346	0.2701	1.0110	0.4261	0.0275
SI	0.2894	0.7778	0.0948	0.6702	2.3782	1.3470	0.0665
MA	0.3754	1.0315	0.1339	0.7437	2.8914	1.5033	0.0925
LD	0.6392	0.2977	0.2937	0.5500	3.4633	0.7419	0.1088
LP	0.5245	0.1856	0.2497	0.4749	3.0726	0.5526	0.0918
PO	0.7192	0.1834	0.3030	0.5062	3.3981	0.6304	0.1002
RT	0.1537	0.1664	0.0632	0.2420	1.1764	0.3381	0.0385
VPL	0.5260	0.1820	0.2340	0.4325	2.7960	0.5515	0.0892
VPM	0.7327	0.2327	0.3174	0.5480	3.6602	0.6931	0.1134
SPFp	0.1620	0.1538	0.0748	0.2248	1.2829	0.2887	0.0392
LHA	0.3084	0.7549	0.1084	0.6185	2.4001	1.1683	0.0753
STN	0.3677	1.1411	0.1279	0.7072	2.8052	1.3514	0.0914
ZI	0.1293	0.3420	0.0522	0.3077	1.1397	0.4663	0.0372
IC	0.2332	0.8594	0.0915	0.5795	1.9608	1.1499	0.0649
SCm	0.1395	0.3720	0.0592	0.3311	1.2351	0.5358	0.0402
SCs	0.2634	0.5682	0.0921	0.5073	1.9301	0.9347	0.0600
SNc	0.1191	0.2903	0.0451	0.2857	1.1072	0.4676	0.0344
SNr	0.2369	0.6314	0.0728	0.5956	1.9608	1.1772	0.0555
APN	0.1205	0.1715	0.0431	0.2084	0.9765	0.2759	0.0293
NOT	0.1801	0.1931	0.0742	0.3042	1.4786	0.4041	0.0527
PPN	0.1157	0.2721	0.0511	0.2495	1.0073	0.3913	0.0342
PPT	0.1388	0.1806	0.0409	0.2240	1.1257	0.2841	0.0300
RR	0.1554	0.2030	0.0609	0.2742	1.2103	0.3971	0.0343
MRN	0.1032	0.2121	0.0438	0.2172	0.9243	0.3207	0.0300
P	0.1195	0.5152	0.0481	0.3335	1.1418	0.6741	0.0387
MY	0.1180	0.4358	0.0446	0.3162	1.0906	0.5406	0.0341
IP	0.1812	1.2886	0.0708	0.5751	1.6830	1.2364	0.0598
ANcr2gr	0.5235	2.3007	0.2091	0.9257	3.2116	2.8568	0.1478
ANcr2mo	0.4039	1.7230	0.1534	0.8599	2.7839	2.1261	0.0885
CENT3gr	0.4341	1.6080	0.1731	0.8298	2.9681	2.6808	0.1178
CENT3mo	0.2646	0.8611	0.0911	0.5812	1.7963	1.2283	0.0545
CUL4,5gr	0.4715	1.9956	0.1923	0.8604	2.9917	2.8039	0.1347
CUL4,5mo	0.3153	1.1720	0.1167	0.6742	2.1586	1.5753	0.0672
SIMgr	0.5385	2.4549	0.2310	0.9070	3.1663	2.9450	0.1521
SIMmo	0.4428	2.0194	0.1582	0.9356	2.9152	2.4226	0.0932
PRMgr	0.5189	2.6448	0.2263	0.9011	3.1690	2.9584	0.1535
PRMmo	0.4343	2.2118	0.1685	0.9186	2.8567	2.3881	0.0968
COPYgr	0.4761	2.7187	0.2155	0.9041	3.1461	3.0095	0.1487
COPYmo	0.4639	2.3241	0.1894	0.9657	3.0446	2.4924	0.1031

Type 3 (PSD95 + SAP102) subtypes: subregions

Abbreviation	subtype 19	subtype 20	subtype 21	subtype 22	subtype 23	subtype 24	subtype 25	subtype 26	subtype 27	subtype 28	subtype 29	subtype 30	subtype 31	subtype 32	subtype 33	subtype 34	subtype 35	subtype 36	subtype 37
ORB1	0.0696	1.1490	2.8818	0.4587	2.5513	1.5359	0.9648	0.8071	0.1488	0.9690	9.3843	3.5409	0.1297	7.2682	1.2699	1.2182	6.1155	2.8622	5.7425
ORB2-3	0.0824	0.8267	2.5687	0.3747	2.3358	1.3974	0.9039	0.7943	0.1592	0.8295	8.2023	3.2168	0.0661	7.3079	1.2503	0.6805	5.2322	2.7289	5.2246
ORB5	0.0743	0.6653	2.4270	0.4085	2.1380	1.2904	0.8684	0.8135	0.1491	0.8061	8.4726	2.5509	0.0911	6.4757	1.0863	0.3726	3.6770	2.4121	4.3807
ORB6a	0.0526	0.5960	2.4202	0.5017	1.9936	1.2332	0.8586	0.7074	0.1545	0.9885	9.5448	2.2685	0.2350	4.4051	0.9118	0.2062	2.3097	2.1186	3.8406
ORB6b	0.0141	0.3600	1.5885	0.4570	1.2686	0.7361	0.5944	0.3091	0.1190	0.8481	7.0693	1.2966	0.5713	2.0132	0.4511	0.0825	0.5708	0.9348	2.1176
FRP1	0.0876	1.2433	2.9018	0.4251	2.6870	1.6528	1.0439	0.7816	0.1601	0.9741	8.4712	3.8385	0.0818	8.3769	1.4620	1.5015	6.3109	2.9927	6.3645
FRP2-3	0.0868	1.0557	2.6474	0.3857	2.4085	1.4577	0.9271	0.6894	0.1736	0.9343	8.1015	3.4667	0.1194	6.6428	1.2863	0.9174	5.3273	2.6659	5.6905
MO1	0.0968	0.9291	2.7466	0.2935	2.5831	1.6458	1.0838	0.7827	0.1505	0.9338	7.5830	3.7417	0.0321	10.8565	1.4572	1.4607	8.0833	3.1985	6.6783
MO2-3	0.0875	0.8815	2.4959	0.2889	2.2689	1.4371	0.9146	0.7190	0.1550	0.8013	7.0881	3.2424	0.0367	7.7873	1.2203	0.9633	6.9021	2.8077	5.7280
MO5	0.0693	0.7782	2.3332	0.3868	1.9893	1.2566	0.7806	0.7401	0.1570	0.6963	7.5846	2.3452	0.0869	5.4302	0.9456	0.4112	3.9336	2.1885	4.2199
MO6a	0.0393	0.6045	2.2294	0.5102	1.7415	1.1231	0.7637	0.5836	0.1512	0.9503	9.0175	1.8766	0.3113	2.8638	0.7062	0.1211	1.6206	1.7224	3.4311
MO6b	0.0148	0.3247	1.6087	0.4730	1.2941	0.7748	0.6434	0.3169	0.1210	0.8908	7.6122	1.3180	0.5533	2.1494	0.4632	0.0497	0.5158	1.0125	2.2150
SS1	0.0815	0.9047	2.7720	0.2794	2.4936	1.6842	1.0819	0.7733	0.1409	0.9244	8.0077	3.5597	0.0354	10.9833	1.4126	1.2269	7.6129	3.3020	6.3244
SS2-3	0.0876	0.9129	2.5300	0.2613	2.2687	1.4812	0.9236	0.6893	0.1426	0.8032	6.9538	3.3307	0.0317	8.3526	1.2274	0.9007	7.4521	2.9253	5.9093
SS4	0.0862	0.7091	2.5050	0.2889	2.0225	1.4337	0.8539	0.7748	0.1191	0.7507	7.9264	2.6176	0.0419	6.7702	1.0937	0.3801	5.1411	2.7735	4.8133
SS5	0.0674	0.7320	2.4521	0.3830	2.0101	1.3312	0.7841	0.7643	0.1441	0.7448	8.3408	2.2830	0.0935	5.0705	0.9142	0.2852	3.6757	2.3352	4.2020
SS6a	0.0453	0.5722	2.3406	0.5001	1.8345	1.1826	0.8070	0.6173	0.1521	0.9974	9.7166	1.9525	0.2865	3.3028	0.7774	0.1156	1.8478	1.9560	3.5516
SS6b	0.0175	0.2549	1.4587	0.4376	1.1755	0.6989	0.5980	0.2896	0.1221	0.8384	7.1780	1.1646	0.5115	2.0217	0.4288	0.0438	0.4737	0.9899	1.9087
PTLp1	0.0773	0.8715	2.9109	0.2913	2.5842	1.7181	1.1927	0.7939	0.1233	1.0666	8.7619	3.7056	0.0457	11.0431	1.5110	0.9934	7.2512	3.4961	6.3974
PTLp2-3	0.0782	0.9331	2.6971	0.2947	2.3999	1.5420	0.9794	0.6856	0.1252	0.9132	7.7847	3.4286	0.0782	7.8874	1.2810	0.7182	6.9703	3.0763	5.9069
PTLp4	0.0638	0.8594	2.6782	0.3098	2.1711	1.5138	0.8723	0.7399	0.1055	0.8940	8.5798	2.8051	0.0695	6.5580	1.1367	0.3960	5.7182	2.9659	4.9492
PTLp5	0.0707	0.7830	2.6052	0.3915	2.0508	1.3954	0.8091	0.7773	0.1215	0.8298	8.6667	2.3516	0.1140	5.6744	0.9505	0.2438	4.0602	2.4690	4.3693
PTLp6a	0.0554	0.5774	2.4278	0.4470	1.9482	1.2085	0.8382	0.7206	0.1573	0.9378	9.7100	2.0438	0.2421	4.2290	0.8397	0.1258	2.3215	2.1834	3.8333
PTLp6b	0.0176	0.3222	1.5673	0.4248	1.2366	0.7642	0.6220	0.3243	0.1599	0.7701	7.0252	1.2299	0.4360	1.9220	0.4339	0.0407	0.5595	0.9886	2.0970
VIS1	0.0793	0.7205	2.8701	0.3963	2.5150	1.6999	1.1477	0.8524	0.1426	1.0866	9.5377	3.3532	0.1166	11.2633	1.4280	0.6074	5.2860	3.0883	5.7801
VIS2-3	0.0766	0.7454	2.8306	0.3479	2.4975	1.6139	1.0397	0.7694	0.1216	1.0481	8.7389	3.3843	0.0867	9.9092	1.3521	0.4964	5.9274	3.1409	5.7998
VIS4	0.0710	0.6788	2.7911	0.3542	2.3158	1.5798	0.9713	0.8068	0.1163	0.9825	9.2413	2.9717	0.0897	7.8904	1.2477	0.3340	5.0815	3.0988	5.1545
VIS5	0.0721	0.5911	2.6238	0.3682	2.2209	1.4479	0.9099	0.8314	0.1238	0.8934	9.0554	2.5130	0.0972	8.2554	1.1182	0.2330	3.9540	2.7371	4.5095
VIS6a	0.0601	0.4131	2.5286	0.4506	2.1025	1.3516	0.9850	0.8140	0.1491	1.1457	10.7819	2.2898	0.1798	5.9343	1.0565	0.0981	2.2662	2.5738	4.0381
VIS6b	0.0209	0.2049	1.5016	0.4191	1.2053	0.7154	0.6124	0.3484	0.1261	0.7794	7.0101	1.1679	0.4164	2.3929	0.4619	0.0411	0.5753	1.0421	1.9416
RSPd1	0.0701	0.4341	2.4619	0.4334	2.0916	1.3574	0.9854	0.7264	0.1662	0.9743	8.9627	2.4807	0.2323	8.7165	1.0341	0.2736	2.3899	2.0709	4.1820
RSPd2-3	0.0786	0.4015	2.5353	0.4143	2.1726	1.4089	1.0102	0.8407	0.1474	0.9879	9.4247	2.5137	0.1582	8.7741	1.0789	0.2147	2.7841	2.4155	4.4419
RSPd5	0.0888	0.4135	2.6469	0.4279	2.2944	1.5274	1.0723	0.9698	0.1488	1.0501	11.0868	2.4369	0.0997	7.2734	1.1437	0.1528	2.5795	2.6940	4.3967
RSPv1	0.0742	0.3142	2.0325	0.4330	1.7054	1.0973	0.7830	0.6773	0.2034	0.6751	7.3428	1.7875	0.2759	5.9815	0.7702	0.1745	1.8473	1.4928	3.2426
RSPv2-3	0.0853	0.1647	1.7387	0.4152	1.5654	0.8999	0.8281	0.6576	0.2286	0.6379	6.3318	1.6188	0.1999	5.7719	0.7338	0.1044	0.9968	1.2427	2.9105
RSPv5	0.0750	0.3429	2.2193	0.4415	1.8083	1.1769	0.8406	0.7911	0.1824	0.7422	8.2396	1.8133	0.2186	4.6113	0.7041	0.1263	1.8300	1.5667	3.3732
RSPv6a	0.0471	0.2502	1.7670	0.4219	1.5006	0.8925	0.7001	0.5813	0.1682	0.6183	7.0990	1.3160	0.2897	3.8715	0.5436	0.0633	1.0472	1.2181	2.4153
MOBgl	0.0759	0.0047	0.5812	0.1732	0.8534	0.4109	0.8371	0.3316	0.2852	0.2626	1.6375	1.0019	0.0218	8.4309	0.8467	0.0153	0.0232	0.3632	1.5077

MOBopl	0.1153	0.0175	1.1284	0.2983	1.3782	0.6259	0.9413	0.6423	0.2089	0.4115	4.3100	1.1706	0.0537	10.9493	0.8968	0.0084	0.0537	0.7528	2.3068
MOBmi	0.0577	0.0207	0.5708	0.2899	0.7524	0.2645	0.4800	0.2974	0.3479	0.1703	1.7765	0.7510	0.1106	5.1460	0.4440	0.0194	0.0405	0.2780	1.2561
MOBipl	0.0716	0.0250	0.6528	0.2938	0.8499	0.3223	0.5843	0.3321	0.2640	0.2026	2.1129	0.9345	0.0946	6.0921	0.5628	0.0145	0.0618	0.3721	1.5101
MOBgr	0.0377	0.0359	0.5931	0.3012	0.7587	0.2695	0.4730	0.2508	0.2262	0.2340	2.1768	0.8346	0.1644	4.5847	0.4574	0.0169	0.0528	0.3400	1.2500
AON1	0.0890	0.2475	2.5679	0.4874	2.6429	1.4672	1.4987	1.0723	0.1279	1.4128	10.9741	3.0309	0.0774	12.0790	1.8535	0.1199	1.3805	3.0231	4.7825
AON2	0.0903	0.2039	2.1054	0.3627	2.3518	1.1571	1.2536	0.8637	0.1848	1.0853	8.5399	2.6768	0.0422	15.6273	1.6854	0.1517	1.4583	2.5862	4.1071
PIR1	0.1581	0.1345	1.7582	0.3081	1.9342	1.0808	1.1718	0.8542	0.2586	0.6877	5.4467	2.0144	0.0255	14.8417	1.3512	0.1072	0.8149	1.5959	3.8705
PIR2	0.1238	0.1020	1.3306	0.3406	1.5820	0.7252	0.9247	0.6677	0.3670	0.4910	4.4791	1.6147	0.0453	11.4679	1.0188	0.0969	0.5552	1.1265	2.7068
PIR3	0.0588	0.2647	1.8435	0.5007	1.8043	0.8820	0.8950	0.7054	0.1651	0.6895	7.8000	1.6664	0.1894	6.2829	0.8212	0.1014	0.8134	1.3474	2.7413
CA1so	0.0612	0.2631	3.9616	0.7417	4.0955	2.2098	2.2118	1.3023	0.1191	2.6122	16.4439	5.8682	0.1505	13.5854	2.8945	0.0370	1.8034	5.1739	7.1420
CA1sp	0.0507	0.0455	1.5653	0.4193	1.8192	0.8192	1.1266	0.5873	0.2718	1.0398	6.5834	2.1651	0.1556	5.9699	1.1129	0.0352	0.2754	1.5618	2.7308
CA1sr	0.0742	0.4264	3.9454	0.7349	4.1381	2.1500	2.1169	1.2118	0.1214	2.6609	15.2800	6.2569	0.1441	12.4496	2.7833	0.1355	3.1875	5.1359	7.4970
CA1slm	0.0815	0.1229	3.1338	0.7390	3.0362	1.6028	1.4814	1.2539	0.1268	1.5006	12.5757	4.0164	0.2012	7.2492	1.8321	0.0238	0.6122	2.7265	5.3640
CA2so	0.0424	0.0269	1.9313	0.4144	2.6649	1.0957	1.8985	0.6806	0.1057	1.5354	10.5611	2.8280	0.1368	24.9796	1.7097	0.0038	0.0962	1.9273	3.3905
CA2sp	0.0370	0.0035	0.5637	0.2657	0.8482	0.2805	0.6264	0.2599	0.3723	0.2362	2.1723	0.7962	0.0986	7.2302	0.4944	0.0509	0.0103	0.3636	0.9513
CA2sr	0.0558	0.0410	1.9187	0.5345	2.6607	1.0281	1.9550	0.7210	0.1601	1.6415	10.2426	3.0592	0.1561	17.3377	1.6891	0.0066	0.1607	1.8600	3.4110
CA2slm	0.0324	0.0086	3.0705	0.7052	3.6514	1.4977	2.4813	1.1116	0.0774	2.5447	17.8668	4.2870	0.1780	16.4642	2.3725	0.0035	0.0484	3.1915	4.5767
CA3so	0.0270	0.0797	2.6467	0.8951	2.9609	1.2588	1.9914	0.7118	0.1169	2.9057	14.0765	4.0508	0.5360	5.3425	1.6096	0.0147	0.2168	2.0700	3.9785
CA3sp	0.0660	0.0399	1.0716	0.5092	1.3937	0.4684	0.7083	0.3896	0.3955	0.6233	4.1642	1.6803	0.2761	3.1083	0.6540	0.0553	0.0570	0.5734	1.9340
CA3sr	0.0688	0.1501	2.8001	1.0425	3.4869	1.3932	2.1620	0.9402	0.2514	2.6399	12.6236	5.0985	0.3296	6.8650	2.1622	0.0471	0.5716	2.4467	5.1080
CA3slm	0.0449	0.0550	3.5806	1.0357	4.1192	1.7700	2.9721	1.2045	0.1202	3.8675	19.6892	6.1903	0.3027	10.7255	2.7896	0.0188	0.2376	3.4404	5.7504
DG-mo	0.0901	0.1203	3.1330	0.6953	3.5931	1.8211	2.4444	1.0767	0.1289	3.2697	14.3625	6.2668	0.1489	20.7119	3.1857	0.0369	0.7425	4.2811	7.0851
DG-po	0.0553	0.0525	1.4942	0.6867	1.8704	0.5981	0.9542	0.4735	0.3369	0.9729	5.4720	2.4825	0.3863	4.3415	0.8576	0.0279	0.1120	0.7739	2.6658
DG-sg	0.0359	0.0073	0.6148	0.2544	0.8022	0.2848	0.5642	0.2409	0.2735	0.4855	2.6121	0.9694	0.1888	5.2985	0.4691	0.0166	0.0248	0.4672	1.3221
SUB	0.0570	0.6950	2.1922	0.4346	1.9414	1.1450	0.8099	0.6534	0.1574	0.7364	7.2801	2.2410	0.2081	6.3395	0.8417	0.4009	3.4404	1.8294	3.5126
CLA	0.0370	0.5066	2.3050	0.5215	1.9084	1.1459	0.8500	0.6155	0.1351	1.0981	9.9652	2.0868	0.3359	3.7183	0.8267	0.1523	1.6650	1.8826	3.3578
EPd	0.0457	0.2632	1.7936	0.5101	1.7372	0.8732	0.8439	0.6356	0.1634	0.7468	7.8863	1.6453	0.2357	5.7611	0.7740	0.0922	0.7493	1.3659	2.6039
CP	0.0219	0.8446	2.3731	0.5553	1.9049	1.2191	0.8362	0.4201	0.1367	1.5069	9.8757	2.5046	0.3956	2.1171	0.7622	0.5616	1.9118	1.7844	3.5104
ACB	0.0680	0.4042	2.2203	0.4775	2.0935	1.2294	1.1506	0.7534	0.1873	1.2176	9.3058	2.5603	0.1317	4.8484	1.1520	0.4366	1.5370	2.1221	3.8844
FS	0.0055	0.0344	0.4036	0.1411	0.3835	0.1775	0.2101	0.1159	0.0614	0.1883	1.7077	0.3562	0.1571	0.8326	0.1172	0.0220	0.0682	0.1838	0.5257
OT1	0.0973	0.3587	1.9212	0.3131	1.8940	1.2351	1.1477	0.7526	0.2073	0.8708	6.3165	2.2054	0.0596	11.5376	1.2588	0.4645	2.2280	1.9280	3.9805
OT2	0.1038	0.1656	1.6407	0.3631	1.8612	0.9357	1.2094	0.6894	0.2749	0.8984	6.5775	2.0055	0.0843	9.8411	1.2655	0.2494	0.8615	1.5771	3.2849
OT3	0.0881	0.2433	1.9166	0.4297	2.0389	1.0703	1.2721	0.7650	0.1893	1.0493	8.4318	2.1619	0.1031	7.6823	1.2633	0.2972	1.0879	1.9128	3.3787
GPi	0.0032	0.0097	0.2733	0.1182	0.2596	0.1161	0.1173	0.0659	0.0574	0.0857	1.0074	0.2632	0.2041	0.5791	0.0471	0.0079	0.0100	0.0748	0.3145
SI	0.0213	0.0388	0.5513	0.2059	0.5323	0.2614	0.2984	0.2225	0.1230	0.1410	2.0309	0.4609	0.1666	1.8626	0.1689	0.0219	0.0530	0.2331	0.7732
MA	0.0387	0.0389	0.7036	0.2608	0.7335	0.3550	0.4340	0.3390	0.1992	0.1794	2.6763	0.6487	0.1176	3.4707	0.2812	0.0351	0.0735	0.3569	1.0730
LD	0.0176	0.0359	0.9219	0.2388	1.1307	0.4791	0.6923	0.2987	0.0721	0.6616	5.5091	1.0166	0.2343	11.0092	0.4706	0.0142	0.0539	0.7723	1.5317
LP	0.0116	0.1016	1.0907	0.2744	1.1697	0.5235	0.6034	0.2829	0.0698	0.6643	6.4981	1.0024	0.3544	8.4080	0.4101	0.0280	0.1775	0.8853	1.4916
PO	0.0086	0.0250	0.9094	0.2315	1.1492	0.4350	0.6755	0.2566	0.0596	0.7675	6.2854	0.9991	0.2682	8.6281	0.4429	0.0135	0.0363	0.8302	1.4175
RT	0.0045	0.0361	0.5254	0.1708	0.4112	0.2091	0.1902	0.1053	0.0688	0.1863	2.3387	0.4665	0.3470	0.8251	0.0867	0.0085	0.0341	0.1645	0.5969
VPL	0.0067	0.0056	0.6545	0.1797	0.8608	0.3151	0.5234	0.1843	0.0600	0.5507	4.5589	0.7585	0.2314	6.6980	0.3279	0.0079	0.0052	0.5591	1.0103
VPM	0.0092	0.0077	0.8045	0.2105	1.1168	0.4096	0.6998	0.2447	0.0667	0.6851	5.5119	0.9726	0.2250	9.6620	0.4468	0.0100	0.0080	0.7178	1.2728
SPFp	0.0034	0.0931	0.5798	0.1847	0.5026	0.2323	0.2236	0.0929	0.0686	0.2803	2.9671	0.4993	0.4011	2.0132	0.1255	0.0271	0.0987	0.2737	0.6257

LHA	0.0344	0.0831	0.7807	0.2797	0.7414	0.3769	0.4040	0.3079	0.1740	0.2150	2.9922	0.6613	0.1994	2.6461	0.2591	0.0452	0.1412	0.3762	1.1533
STN	0.0418	0.0479	0.5845	0.2652	0.6261	0.2984	0.4127	0.2791	0.2525	0.1448	2.1115	0.6004	0.1475	3.5717	0.2773	0.0382	0.0668	0.2860	0.9908
ZI	0.0064	0.0613	0.4986	0.1991	0.4105	0.2223	0.1859	0.1175	0.1102	0.1497	1.7199	0.4917	0.3126	0.9277	0.0953	0.0205	0.0558	0.1413	0.6813
IC	0.0448	0.0974	0.6773	0.2797	0.6291	0.3397	0.3353	0.2733	0.2168	0.1536	2.0705	0.6558	0.1811	1.5771	0.2364	0.0364	0.1831	0.2796	1.2082
SCm	0.0122	0.1230	0.6439	0.2370	0.4920	0.2976	0.2171	0.1369	0.1281	0.2025	2.2001	0.5553	0.3774	0.9445	0.1244	0.0326	0.1391	0.2044	0.8945
SCs	0.0314	0.1279	0.8745	0.2871	0.7102	0.4389	0.3607	0.2837	0.1374	0.2693	3.3075	0.6931	0.2861	1.8809	0.2384	0.0395	0.2484	0.4108	1.2877
SNc	0.0057	0.0503	0.3942	0.1633	0.3225	0.1781	0.1565	0.0742	0.0948	0.1246	1.4342	0.3471	0.3168	0.8222	0.0726	0.0166	0.0486	0.1140	0.5044
SNr	0.0166	0.0229	0.3623	0.1788	0.3745	0.1801	0.2315	0.1417	0.1218	0.0828	1.0978	0.4127	0.1421	1.1861	0.1387	0.0115	0.0231	0.1112	0.5950
APN	0.0039	0.0573	0.5189	0.1844	0.4073	0.2063	0.1620	0.0874	0.0704	0.2117	2.1495	0.4402	0.3782	0.9707	0.0795	0.0155	0.0607	0.1750	0.5530
NOT	0.0068	0.1040	0.8464	0.2719	0.6036	0.3317	0.2924	0.1651	0.1087	0.3417	3.6796	0.5675	0.4704	1.6163	0.1412	0.0216	0.1201	0.3420	0.8746
PPN	0.0039	0.0305	0.3959	0.1592	0.3418	0.1642	0.1553	0.0793	0.0873	0.1343	1.5110	0.3825	0.3039	0.8120	0.0730	0.0114	0.0260	0.1098	0.4886
PPT	0.0020	0.0920	0.6273	0.2089	0.4671	0.2749	0.1900	0.0987	0.0784	0.2630	2.6345	0.5548	0.4529	0.9436	0.0862	0.0223	0.1119	0.2012	0.6892
RR	0.0029	0.0462	0.5373	0.2136	0.4599	0.2239	0.2054	0.1179	0.0605	0.1963	2.1540	0.4891	0.3911	1.2231	0.0939	0.0086	0.0443	0.1697	0.6041
MRN	0.0041	0.0770	0.4693	0.1727	0.3619	0.2014	0.1478	0.0740	0.0858	0.1671	1.7435	0.4104	0.3716	0.7833	0.0708	0.0204	0.0690	0.1336	0.5448
P	0.0137	0.0401	0.3517	0.1660	0.3160	0.1565	0.1596	0.0774	0.1581	0.1032	1.0877	0.4033	0.2484	0.7322	0.0870	0.0185	0.0358	0.0891	0.5472
MY	0.0059	0.0396	0.3749	0.1638	0.3252	0.1710	0.1571	0.0750	0.1164	0.1211	1.1694	0.4078	0.2452	0.6337	0.0842	0.0177	0.0384	0.0983	0.5607
IP	0.0217	0.0130	0.3008	0.1750	0.3104	0.1449	0.2042	0.1021	0.2553	0.0820	0.8516	0.3404	0.1540	0.6699	0.1149	0.0148	0.0240	0.0849	0.4968
ANcr2gr	0.0879	0.0546	0.5901	0.2102	0.6405	0.3898	0.5267	0.2723	0.4588	0.2499	1.3473	1.1113	0.0620	5.2010	0.5297	0.0131	0.3466	0.4220	2.2920
ANcr2mo	0.0944	0.1219	0.7272	0.2152	0.5660	0.4241	0.3723	0.3680	0.2261	0.1943	2.0744	0.6610	0.0533	1.8179	0.3182	0.0109	0.2451	0.3768	2.0200
CENT3gr	0.0577	0.0913	0.6946	0.2162	0.5825	0.4001	0.4250	0.3032	0.2534	0.2902	2.1823	0.9405	0.1178	2.4400	0.3496	0.0124	0.3716	0.4626	2.0687
CENT3mo	0.0346	0.1011	0.6435	0.1811	0.4684	0.3686	0.2818	0.2359	0.1359	0.2140	2.2754	0.5379	0.1244	1.0055	0.2080	0.0079	0.1733	0.3189	1.3547
CUL4,5gr	0.0885	0.0757	0.6746	0.2160	0.6330	0.4109	0.5077	0.3176	0.3949	0.2589	1.8017	1.1026	0.0720	3.7163	0.4760	0.0156	0.4679	0.4841	2.3604
CUL4,5mo	0.0531	0.1025	0.6146	0.1684	0.4774	0.3737	0.3185	0.2923	0.1558	0.1889	1.9893	0.5745	0.0577	1.4857	0.2623	0.0102	0.2608	0.3645	1.5331
SIMgr	0.0937	0.0869	0.6424	0.2103	0.6689	0.4455	0.5537	0.2974	0.5457	0.2537	1.4128	1.2753	0.0468	5.6507	0.5923	0.0257	0.6241	0.5005	2.7127
SIMmo	0.0828	0.1208	0.5927	0.1792	0.4951	0.3691	0.3575	0.3059	0.2533	0.1575	1.6086	0.6309	0.0321	1.8962	0.3436	0.0124	0.3303	0.3460	1.7798
PRMgr	0.0948	0.0472	0.5733	0.1945	0.6377	0.4064	0.5344	0.2905	0.5529	0.2207	1.1748	1.1899	0.0502	5.8067	0.5927	0.0170	0.3369	0.3885	2.4012
PRMmo	0.1006	0.1052	0.6731	0.1938	0.5547	0.4230	0.3876	0.3758	0.2756	0.1770	1.8249	0.6745	0.0310	2.3152	0.3531	0.0120	0.2583	0.3545	2.0054
COPYgr	0.1080	0.0525	0.5703	0.2168	0.6020	0.3814	0.5090	0.2920	0.6131	0.1872	1.1879	1.0717	0.0603	4.4506	0.5454	0.0153	0.3135	0.3573	2.2903
COPYmo	0.1158	0.1089	0.7237	0.2161	0.5940	0.4537	0.4207	0.4134	0.3045	0.1848	2.0048	0.7281	0.0336	2.4144	0.3911	0.0145	0.2699	0.3883	2.1342

Appendix 11: Raw data for PSD95 lifetime across the lifespan. Density- and intensity-based PSD95 half-life estimates for 12 main brain areas and 110 brain subregions in 3-week, 3-month and 18-month-old mice. Mean (+/-SD) are provided for day 0 and day 7 time points that were used to derive the half-life values.

		PSD95 puncta density (/ 100um2)			PSD95 puncta intensity (AU)		
		Half-life (days)			Half-life (days)		
Abbreviation	Region name	3W	3M	18M	3W	3M	18M
Isocortex	Isocortex	2.8914	6.6749	8.7032	2.2351	4.2334	4.5109
OLF	Olfactory areas	1.0545	1.4549	2.1285	1.4056	2.1599	3.1255
HPF	Hippocampal Formation	1.4356	2.8663	3.3464	1.7306	2.9371	3.3642
CTXsp	Cortical subplate	1.9681	3.6261	4.4754	1.6552	2.8227	3.1601
STR	Striatum	2.156	3.8304	4.8311	1.7383	3.1348	3.2657
PAL	Pallidum	2.3821	4.2791	6.5844	1.8424	3.4009	3.931
TH	Thalamus	1.1835	1.507	2.118	1.1751	1.6344	2.0667
HY	Hypothalamus	2.2051	3.8588	4.9586	1.8757	3.1509	3.5597
MB	Midbrain	2.2709	3.5144	5.5259	1.8991	2.6206	3.9623
P	Pons	1.9698	2.7881	4.1346	1.8379	2.6664	3.2952
MY	Medulla	2.1227	2.7032	4.1113	1.7469	2.3181	2.9897
CB	Cerebellum	1.3743	2.7174	4.9656	1.2559	2.1363	2.9331

	PSD95 puncta density (/ 100um2)											
	3W_Day0		3W_Day7		3M_Day0		3M_Day7		18M_Day0		18M_Day7	
Abbreviation	MEAN	SD	MEAN	SD	MEAN	SD	MEAN	SD	MEAN	SD	MEAN	SD
Isocortex	65.5778	5.7815	12.2452	8.6144	55.2158	13.5333	26.6914	12.9557	61.8908	3.2056	35.4410	5.9168
OLF	33.8431	10.6318	0.3398	0.2452	25.3013	11.8558	0.9010	0.7418	38.0384	13.3797	3.8925	4.0902
HPF	55.5627	11.3244	1.8922	2.5450	53.2215	23.8911	9.7930	7.8127	67.0375	5.1369	15.7262	4.3704
CTXsp	38.5330	7.3179	3.2746	2.4733	33.3836	11.8861	8.7581	6.2417	38.9142	5.2290	13.1604	3.8793
STR	50.0348	7.3697	5.2711	4.1257	41.6642	14.4496	11.7393	7.7103	47.0993	3.9492	17.2519	4.1241
PAL	11.1909	1.6661	1.4597	1.3318	8.3527	3.9061	2.6877	2.1835	9.9908	0.8875	4.7815	1.0782
TH	30.9778	8.1381	0.5136	0.8874	23.1868	13.7326	0.9268	1.1626	32.1780	4.6356	3.2558	1.7134
HY	17.0838	2.7280	1.8922	1.7444	10.4281	4.0294	2.9657	2.4710	13.1048	1.7306	4.9257	1.1734
MB	15.5700	2.3002	1.8381	1.6870	10.8125	3.8457	2.7186	2.0357	11.1585	1.2659	4.6374	0.9371
P	9.8394	1.5849	0.8380	0.9207	6.3674	2.6510	1.1173	1.1395	6.2929	1.0268	1.9463	0.7491
MY	12.7588	1.3774	1.2975	1.0531	7.5928	2.3921	1.2615	1.1719	8.9744	1.0905	2.7572	0.6715
CB	12.9209	1.3217	0.3784	0.4731	13.8160	3.0762	2.3170	1.8337	17.3000	1.6720	6.5115	1.4565

	PSD95 puncta intensity (AU)											
	3W_Day0		3W_Day7		3M_Day0		3M_Day7		18M_Day0		18M_Day7	
Abbreviation	MEAN	SD	MEAN	SD	MEAN	SD	MEAN	SD	MEAN	SD	MEAN	SD
Isocortex	6.3E+11	1.1E+11	7.2E+10	4.6E+10	5.9E+11	2.1E+11	1.9E+11	9.1E+10	6.7E+11	6.9E+10	2.3E+11	4.2E+10
OLF	6.0E+10	1.7E+10	1.9E+09	1.1E+09	8.1E+10	5.0E+10	8.6E+09	6.7E+09	8.4E+10	4.3E+10	1.8E+10	7.3E+09
HPF	9.2E+10	2.4E+10	5.5E+09	4.9E+09	8.5E+10	3.8E+10	1.6E+10	1.1E+10	1.2E+11	1.7E+10	2.9E+10	7.4E+09
CTXsp	1.0E+10	2.1E+09	5.3E+08	4.1E+08	1.0E+10	5.3E+09	1.8E+09	1.2E+09	1.3E+10	3.0E+09	2.7E+09	8.2E+08
STR	2.1E+11	4.3E+10	1.3E+10	1.0E+10	2.0E+11	1.0E+11	4.2E+10	2.8E+10	2.7E+11	3.7E+10	6.2E+10	1.7E+10
PAL	1.1E+10	2.6E+09	7.9E+08	6.7E+08	8.0E+09	4.8E+09	1.9E+09	1.5E+09	1.4E+10	2.5E+09	4.0E+09	1.0E+09
TH	5.6E+10	2.0E+10	9.0E+08	1.1E+09	4.4E+10	2.8E+10	2.3E+09	2.1E+09	6.2E+10	1.2E+10	5.9E+09	3.0E+09
HY	1.7E+10	4.3E+09	1.3E+09	1.1E+09	1.5E+10	8.3E+09	3.1E+09	2.7E+09	1.9E+10	4.0E+09	5.0E+09	1.4E+09
MB	5.7E+10	1.8E+10	4.5E+09	4.3E+09	5.4E+10	2.7E+10	8.5E+09	6.2E+09	5.6E+10	1.4E+10	1.6E+10	4.4E+09
P	1.8E+10	3.1E+09	1.3E+09	1.1E+09	1.6E+10	9.1E+09	2.6E+09	2.4E+09	1.8E+10	4.8E+09	4.2E+09	1.0E+09
MY	5.3E+10	9.2E+09	3.3E+09	2.4E+09	3.5E+10	1.5E+10	4.3E+09	4.0E+09	5.5E+10	1.2E+10	1.1E+10	4.0E+09
CB	3.5E+10	6.4E+09	7.4E+08	7.7E+08	3.6E+10	1.4E+10	3.7E+09	3.3E+09	5.2E+10	1.4E+10	1.0E+10	4.7E+09

		PSD95 puncta density (/ 100um2)			PSD95 puncta intensity (AU)		
		Half-life (days)			Half-life (days)		
Abbreviation	Brain area	3W	3M	18M	3W	3M	18M
ORB1	Isocortex	4.9909	13.3520	14.8222	2.9726	5.6079	5.7028
ORB2-3	Isocortex	3.4351	8.7183	9.9095	2.2513	4.5652	5.0304
ORB5	Isocortex	2.6971	6.1401	7.8983	1.9303	3.7529	4.1418
ORB6a	Isocortex	2.2228	4.6632	5.5640	1.7200	3.2431	3.3833
ORB6b	Isocortex	2.0000	3.5657	3.8209	1.6070	2.7836	2.6378
FRP1	Isocortex	5.4674	12.9528	17.9857	2.9328	6.5004	5.6549
FRP2-3	Isocortex	3.6137	11.2601	10.7578	2.4006	5.3109	4.7634
MO1	Isocortex	5.6808	17.2564	17.5079	3.0714	5.9267	5.8895
MO2-3	Isocortex	3.6955	11.1597	11.5869	2.3914	5.1010	5.0329
MO5	Isocortex	2.6863	7.1301	8.8445	1.9882	4.0593	4.5106
MO6a	Isocortex	1.7877	4.8175	5.3863	1.4479	3.2826	3.2237
MO6b	Isocortex	1.6896	3.9022	4.4566	1.4062	2.9933	2.9903
SS1	Isocortex	5.9540	11.8895	15.9240	2.9609	4.6557	5.4414
SS2-3	Isocortex	3.9466	9.0124	11.4419	2.3647	4.0442	4.7649
SS4	Isocortex	3.7573	5.9768	8.2615	2.1882	3.2886	4.3517
SS5	Isocortex	2.5290	5.3255	7.6404	1.8723	3.1366	4.0752
SS6a	Isocortex	1.7339	4.5563	5.1507	1.3938	2.8161	3.2718
SS6b	Isocortex	1.5648	3.5220	3.8901	1.3297	2.3083	3.3037
PTLp1	Isocortex	6.0996	11.8233	14.6454	2.9253	4.6770	6.2453
PTLp2-3	Isocortex	3.8903	9.1880	10.2042	2.4996	4.5112	4.4852
PTLp4	Isocortex	3.7355	7.3951	8.9753	2.1651	3.7674	4.1663
PTLp5	Isocortex	2.7835	5.4533	8.0692	1.9285	3.3718	3.7657
PTLp6a	Isocortex	2.0275	4.7512	5.6414	1.5749	3.0721	3.3070
PTLp6b	Isocortex	1.7629	5.0509	4.1933	1.3917	2.8703	3.2088
VIS1	Isocortex	5.0768	9.2777	12.2088	2.9555	4.4375	5.1829
VIS2-3	Isocortex	3.5544	9.5695	10.0376	2.2954	4.7909	4.3742
VIS4	Isocortex	3.2711	6.7199	9.0966	2.1120	4.1416	4.0887
VIS5	Isocortex	2.6306	5.1949	8.3941	1.8314	3.6443	3.9547
VIS6a	Isocortex	1.7371	4.1098	5.2433	1.4104	3.0970	3.1422
VIS6b	Isocortex	1.6170	3.9730	4.2959	1.3998	3.2458	2.8680
RSPd1	Isocortex	3.1455	5.4742	7.9726	2.1874	4.1111	4.0351
RSPd2-3	Isocortex	2.6745	4.9986	7.4580	1.9935	4.1034	3.8453
RSPd5	Isocortex	2.2114	4.0363	6.9076	1.7627	3.1408	3.6638
RSPv1	Isocortex	2.6416	4.9384	5.3494	2.0008	4.0772	3.1798
RSPv2-3	Isocortex	2.0156	3.2445	3.6099	1.5624	2.9450	2.7805
RSPv5	Isocortex	2.4200	4.0181	5.9133	1.8248	2.9560	3.4681
RSPv6a	Isocortex	1.8970	3.1655	4.8439	1.5745	2.5524	3.1723
MOBgl	Olfactory areas	0.0000	1.0468	1.4512	0.9263	1.0705	1.5183
MOBopl	Olfactory areas	0.9298	1.1704	1.8180	0.8974	1.0201	1.5073
MOBmi	Olfactory areas	1.0820	1.3304	2.1311	1.0349	1.1159	1.7744
MOBipl	Olfactory areas	1.1082	1.4266	2.1042	1.0434	1.1042	1.6816
MOBgr	Olfactory areas	1.1859	1.3910	2.6156	1.1879	1.1918	2.1571
AON1	Olfactory areas	2.5179	4.1269	5.4658	1.6511	2.9427	4.6796
AON2	Olfactory areas	1.5748	3.4281	4.7824	1.4999	2.2420	4.9542
PIR1	Olfactory areas	1.9085	3.3964	4.0985	1.5260	2.5000	2.7954
PIR2	Olfactory areas	1.3207	2.3886	3.5812	1.2048	2.0621	2.7459
PIR3	Olfactory areas	1.8002	3.2946	4.8473	1.6056	2.2713	3.4506
CA1so	Hippocampal formation	1.9146	4.3046	6.0703	1.5147	3.2954	3.7449
CA1sp	Hippocampal formation	1.2628	2.8858	3.5217	1.5557	3.0075	3.4140
CA1sr	Hippocampal formation	2.6520	5.5433	9.0539	2.0697	3.6909	4.5905
CA1slm	Hippocampal formation	3.1068	5.0302	8.1721	2.2311	3.4810	4.1441
CA2so	Hippocampal formation	0.8563	1.2439	1.3804	0.8565	1.2385	1.3789
CA2sp	Hippocampal formation	0.9233	1.7351	3.0391	1.1390	1.6280	3.3126
CA2sr	Hippocampal formation	1.0935	1.6193	1.6822	1.0245	1.6138	1.6373
CA2slm	Hippocampal formation	0.7879	1.1110	1.3319	0.8478	1.1439	1.3111

CA3so	Hippocampal formation	1.0589	2.1326	2.4801	0.9666	1.8739	1.9524
CA3sp	Hippocampal formation	0.9677	1.7398	2.5829	0.8819	1.6876	2.3644
CA3sr	Hippocampal formation	1.1243	2.1834	2.6226	1.0354	2.1080	2.1737
CA3slm	Hippocampal formation	1.0670	1.6346	2.0488	1.0950	1.8996	1.9102
DG-mo	Hippocampal formation	1.0647	2.2033	2.4740	1.0351	1.7717	2.2227
DG-po	Hippocampal formation	1.2528	2.5369	2.9454	1.0196	1.8965	2.3893
DG-sg	Hippocampal formation	0.0000	1.5346	2.4400	0.9082	1.5448	2.1315
SUB	Hippocampal formation	3.0834	5.7932	8.2157	2.1343	4.1857	4.7614
CLA	Cortical subplate	2.2056	3.5827	4.9481	1.7585	2.7991	3.8103
EPd	Cortical subplate	1.8688	3.5723	4.2571	1.5776	2.7052	2.7528
CP	Striatum	2.3691	4.0605	5.1560	1.8026	3.1143	3.2195
ACB	Striatum	2.0944	3.9387	4.7722	1.6784	3.0622	3.4593
FS	Striatum	2.3305	6.9889	5.4344	2.0260	3.9797	3.9712
OT1	Striatum	2.0281	3.7526	5.3872	1.7273	2.8135	3.2943
OT2	Striatum	1.4165	2.8917	3.6321	1.4620	2.6420	2.7813
OT3	Striatum	1.5856	3.4192	4.1231	1.4672	2.8489	3.1490
GPi	Pallidum	2.5461	2.9260	6.6479	1.9147	3.1239	3.8390
SI	Pallidum	2.5147	4.6154	6.9671	1.8830	3.6804	4.1117
MA	Pallidum	1.6746	3.1829	4.4185	1.5187	2.3975	3.2079
LD	Thalamus	1.5487	2.1277	2.9785	1.3043	1.6461	2.4073
LP	Thalamus	1.4819	2.3118	3.0666	1.2575	2.3971	2.5175
PO	Thalamus	1.2065	1.6218	2.3477	1.1494	1.5209	2.1118
RT	Thalamus	1.8017	2.4389	3.3903	1.4098	2.1504	2.6591
VPL	Thalamus	0.9284	1.1913	1.7473	0.9084	1.3609	1.6479
VPM	Thalamus	0.6875	1.0580	1.5046	0.8355	1.1449	1.5734
SPFp	Thalamus	2.1114	3.1715	4.5258	1.7426	2.5477	3.3013
LHA	Hypothalamus	2.5120	4.3838	5.4564	1.9889	3.7648	3.6679
STN	Hypothalamus	1.4249	2.7965	3.6364	1.3576	2.0068	2.9236
ZI	Hypothalamus	1.9428	3.4043	4.8121	1.6342	2.8884	3.4647
IC	Midbrain	2.0971	2.8745	4.6801	1.6939	2.3748	3.7358
SCm	Midbrain	2.3659	4.1152	5.3950	2.1982	2.7283	4.0249
SCs	Midbrain	2.1903	3.7384	5.8211	2.1887	2.4168	3.9618
SNc	Midbrain	2.1804	3.0771	4.4743	1.8517	2.8529	3.5152
SNr	Midbrain	2.9700	4.8254	6.9738	2.3312	4.1050	4.7251
APN	Midbrain	1.5617	2.7921	3.2606	1.5337	1.9074	2.9374
NOT	Midbrain	1.8310	3.5699	3.9203	1.7456	2.3931	3.9782
PPN	Midbrain	2.0967	3.5058	5.4346	1.8808	2.5985	3.7439
PPT	Midbrain	1.8745	3.5163	4.3619	1.9146	2.4626	3.2065
RR	Midbrain	2.0323	4.1025	5.3803	1.8193	2.8559	3.7511
MRN	Midbrain	2.3494	4.0625	6.0547	1.8429	2.9326	4.3434
P	Pons	1.9698	2.7881	4.1346	1.8379	2.6664	3.2952
MY	Medulla	2.1227	2.7032	4.1113	1.7469	2.3181	2.9897
IP	Cerebellum	0.9099	1.4301	2.0627	1.0571	1.5358	2.4695
ANcr2gr	Cerebellum	1.0097	2.7906	4.6643	0.8912	2.1195	2.6225
ANcr2mo	Cerebellum	1.6223	2.8422	6.4360	1.2881	2.3812	2.9576
CENT3gr	Cerebellum	1.0906	2.3842	4.0366	1.0363	1.6764	2.5977
CENT3mo	Cerebellum	1.8086	2.5211	5.2004	1.6180	1.8116	2.7305
CUL4,5gr	Cerebellum	1.1499	2.5513	4.2952	0.9835	1.8764	3.1993
CUL4,5mo	Cerebellum	1.8322	2.6272	5.5281	1.4674	2.0031	3.3444
SIMgr	Cerebellum	1.0052	3.3213	5.4354	0.9190	2.6965	3.3374
SIMmo	Cerebellum	1.7120	3.2498	6.4347	1.4259	2.5942	3.5642
PRMgr	Cerebellum	0.9993	2.7548	5.1671	0.9117	2.0680	2.8397
PRMmo	Cerebellum	1.6319	3.3380	7.8743	1.3513	2.4793	3.1324
COPYgr	Cerebellum	1.0026	2.7613	4.8261	0.9512	2.2138	3.1663
COPYmo	Cerebellum	1.6867	2.9514	7.3338	1.3384	2.6319	3.8298

	PSD95 puncta density (/ 100um2)											
	3W_Day0		3W_Day7		3M_Day0		3M_Day7		18M_Day0		18M_Day7	
Abbreviation	MEAN	SD	MEAN	SD	MEAN	SD	MEAN	SD	MEAN	SD	MEAN	SD
ORB1	84.0402	6.0638	31.7888	14.7893	62.8687	11.4417	43.7134	10.1226	67.3835	5.0799	48.5722	7.7371
ORB2-3	72.1464	5.1809	17.5703	10.3405	59.3126	13.8279	33.9976	11.1842	65.3183	4.9435	40.0303	6.4363
ORB5	63.6316	5.9118	10.5287	7.1022	53.5819	14.6930	24.3127	10.3227	60.7122	3.5916	32.8460	5.7014
ORB6a	52.2784	6.6439	5.8928	4.5986	45.3404	14.9908	16.0179	8.9564	51.5216	4.6193	21.5409	4.9507
ORB6b	21.4088	5.6506	1.8922	1.8558	23.0066	12.1634	5.9005	4.5664	12.6182	5.0425	3.5441	2.2158
FRP1	81.5127	8.0361	33.5593	13.1098	62.1839	11.9902	42.7557	19.7491	67.2321	6.0580	51.3353	6.7722
FRP2-3	71.7332	6.7625	18.7327	10.2934	59.0363	14.7934	38.3689	10.6226	67.6538	4.8307	43.0938	5.9540
MO1	85.5404	9.9548	36.4111	13.0883	67.2778	12.1222	50.7879	10.8619	72.3573	4.9794	54.8434	8.5199
MO2-3	74.2548	5.8186	19.9761	11.1657	61.1267	14.6468	39.5738	11.9611	68.8108	3.0443	45.2683	7.2966
MO5	64.1722	5.4570	10.5422	7.5069	50.6986	15.8797	25.6720	10.3920	57.3495	2.7197	33.1343	5.8834
MO6a	48.9536	5.4819	3.2438	2.8689	38.9490	15.8529	14.2262	8.0768	41.6389	3.1833	16.9156	4.8425
MO6b	11.4613	2.3879	0.6488	0.6116	21.7451	15.3823	6.2713	4.9863	6.8876	2.7225	2.3187	1.3667
SS1	84.9998	10.6400	37.6275	17.0731	69.6685	13.4310	46.3238	25.0742	73.1249	4.8940	53.9183	9.7246
SS2-3	72.0923	6.5896	21.0844	13.2390	64.4906	9.8576	37.6429	19.2467	69.6541	3.7211	45.5807	8.1516
SS4	71.2409	6.1658	19.5841	12.7786	62.1959	12.6550	27.6182	17.2005	67.9782	3.9078	37.7837	9.4773
SS5	63.3342	6.2188	9.2988	8.1391	54.6272	14.2378	21.9648	13.4972	60.8960	3.3905	32.2693	7.0826
SS6a	48.8184	6.3643	2.9734	3.3376	42.2048	16.2173	14.5505	10.6408	43.6068	4.2118	16.9997	4.8378
SS6b	8.4067	2.1769	0.3784	0.5005	19.9070	16.6429	5.0201	4.5660	5.6874	0.4536	1.6339	0.6127
PTLp1	87.1352	9.8820	39.3305	18.6506	69.1760	21.4804	45.8913	25.4664	76.2173	7.0155	54.7233	11.9260
PTLp2-3	73.9034	5.7316	21.2330	14.1531	64.4065	14.0416	37.9828	20.0892	72.4221	6.4712	45.0160	10.0399
PTLp4	70.5921	6.7118	19.2598	12.5070	63.4093	11.2112	32.9009	20.0404	70.2596	4.7075	40.9193	9.0935
PTLp5	67.8214	7.5716	11.8667	9.4722	62.1599	10.2356	25.5329	15.7972	66.8537	5.0935	36.6424	8.6841
PTLp6a	52.9677	6.7934	4.8386	4.1852	49.0647	12.8816	17.6707	12.5484	50.3971	4.6194	21.3247	6.8362
PTLp6b	11.2315	5.3906	0.7163	0.9192	21.1925	15.8660	8.1094	6.8836	7.2984	2.4605	2.2947	1.2642
VIS1	85.9729	7.1791	33.0592	18.8707	71.0622	12.7020	42.1224	20.1843	73.6331	4.3615	49.4852	7.5459
VIS2-3	73.7818	6.9417	18.8408	14.2568	60.9104	20.8680	36.6853	18.2710	72.0221	5.8424	44.4153	7.4946
VIS4	71.4841	8.6563	16.2188	12.6227	60.3217	21.9105	29.3019	17.0043	70.5948	4.2695	41.4119	7.2120
VIS5	64.2803	7.6933	10.1638	8.7605	61.6313	10.2049	24.2200	15.0627	67.2429	4.8514	37.7236	6.5280
VIS6a	50.3322	8.3634	3.0816	2.9937	52.2604	8.9228	16.0488	12.0092	58.3443	5.5862	23.1267	5.9229
VIS6b	19.0165	6.3786	0.9461	0.9804	25.1451	13.2869	7.4143	7.7335	17.9163	2.8694	5.7907	2.3825
RSPd1	74.2008	11.2688	15.8673	13.3076	60.2256	12.7867	24.8224	13.9231	63.0153	5.8445	34.2876	6.5680
RSPd2-3	64.5236	10.2587	10.5152	9.7348	59.2044	11.7267	22.4282	14.0816	65.5562	7.6500	34.2035	6.2843
RSPd5	56.8738	10.9034	6.3388	5.7957	58.1232	13.7759	17.4699	11.9389	65.8914	6.9552	32.6417	7.4319
RSPv1	60.8203	12.2722	9.6907	7.1601	39.6098	10.6863	14.8286	10.1971	44.5475	3.4044	17.9848	3.9757
RSPv2-3	39.3170	11.1111	3.5411	3.3916	28.4609	11.0648	6.3794	6.2579	35.1514	4.1510	9.1666	2.1999
RSPv5	52.5893	10.1196	7.0822	6.0583	46.3496	16.3436	13.8554	10.9998	46.9695	5.3870	20.6759	4.9652
RSPv6a	37.3302	6.5944	2.8923	2.8553	34.3357	15.0227	7.4143	6.6439	36.0489	6.5760	13.2393	4.9755
MOBgl	14.4888	4.3659	0.0000	0.0000	16.7130	9.2859	0.1622	0.1081	16.6204	3.7402	0.5870	0.1635
MOBopl	39.9342	8.1083	0.2163	0.2497	29.5954	12.3101	0.4685	0.4621	36.2579	2.6438	2.5139	1.1263
MOBmi	10.9515	1.4650	0.1236	0.1701	11.0596	4.0576	0.2883	0.3256	15.3538	2.3886	1.5755	0.6453
MOBipl	17.2382	3.8028	0.2163	0.3058	14.0563	4.5172	0.4685	0.4621	18.5975	2.2732	1.8536	0.7682
MOBgr	11.0905	1.5226	0.1854	0.2627	11.1214	3.5966	0.3398	0.4972	13.5156	1.4587	2.1144	0.9161
AON1	53.1048	16.7910	7.7309	5.9639	53.3732	21.3477	16.4710	10.4424	68.4756	6.8892	28.1846	8.1997
AON2	53.8327	8.4903	2.4714	1.7870	47.7913	20.1546	11.6054	8.8156	55.3708	4.9490	20.0752	8.1883
PIR1	59.0903	11.0400	4.6494	2.8354	43.6149	15.7735	10.4521	6.5858	57.9310	5.9190	17.7325	8.3081
PIR2	32.8700	4.7631	0.8341	0.7840	27.1123	13.0034	3.5501	2.8430	33.8431	3.7405	8.7311	4.2265
PIR3	48.5752	8.0160	3.2798	2.9695	32.6943	14.3397	7.4967	5.6832	42.9905	5.4945	15.7998	4.6274
CA1so	87.9211	15.2915	6.9741	8.5159	78.1984	29.9527	25.3321	18.7213	96.1880	7.2264	43.2500	12.1978
CA1sp	13.8670	4.3330	0.2973	0.4615	20.7480	11.1490	3.8616	3.8833	30.3507	5.5213	7.6528	3.3465
CA1sr	93.3119	13.2149	14.9753	13.1356	73.9815	24.8801	30.8311	18.9683	86.7054	5.0191	50.7347	10.5351
CA1slm	86.5946	8.0399	18.1650	16.8358	63.1810	25.1845	24.0810	19.6760	76.6390	4.9802	42.3249	9.3461
CA2so	50.7647	20.1182	0.1757	0.2828	45.0521	27.2038	0.9113	1.0628	65.4156	12.9100	1.9463	0.9865
CA2sp	5.1765	2.6081	0.0270	0.0765	3.7964	2.8234	0.2317	0.3085	7.5904	2.4713	1.5378	0.9329
CA2sr	43.4122	18.8050	0.5136	0.9457	33.3866	20.7457	1.6682	1.7467	54.8086	10.5059	3.0635	1.9783
CA2slm	76.6471	17.8272	0.1622	0.3790	47.4789	28.1930	0.6024	0.7059	77.5581	11.5179	2.0303	2.0392
CA3so	35.6542	12.8494	0.3649	0.7467	30.3591	16.6347	3.1202	3.1059	43.0878	9.4277	6.0910	3.1421
CA3sp	12.2046	2.9894	0.0811	0.1609	13.8160	7.9804	0.8496	0.9800	17.6893	3.8429	2.7031	1.4118
CA3sr	42.4931	12.9284	0.5677	1.1263	33.6389	16.0682	3.6454	3.5515	47.9102	7.9497	7.5327	4.4561
CA3slm	61.2393	17.7545	0.6488	1.2609	42.9857	24.5085	2.2088	2.2193	60.6798	10.9079	5.6826	3.8320
DG-mo	61.8475	16.9581	0.6488	0.9808	64.4065	33.2548	7.1208	6.0300	87.4407	8.2424	12.3022	3.6229

DG-po	23.3955	6.3994	0.4866	0.8235	21.6490	10.0536	3.1974	3.0119	30.3831	4.1135	5.8508	3.2574
DG-sg	2.2571	0.9381	0.0000	0.0000	5.1059	3.2955	0.2163	0.2163	10.5314	2.7487	1.4417	0.9238
SUB	53.7246	7.0471	11.1369	9.2734	46.5418	11.0010	20.1421	10.8034	50.3754	3.9706	27.9083	3.5403
CLA	40.1414	8.2146	4.4486	3.5793	40.0333	14.2867	10.3337	8.1685	42.4391	6.6201	15.9184	4.3726
EPd	38.1276	6.8582	2.8421	2.1314	29.4370	11.3110	7.5688	5.2776	37.4329	5.3346	11.9748	3.4405
CP	52.6028	8.5199	6.7848	5.6709	44.5956	14.7478	13.5002	8.4530	48.8293	3.0391	19.0540	5.0950
ACB	51.2648	6.1818	5.0548	3.8855	40.9794	15.8279	11.9555	8.2068	48.9158	4.5633	17.6965	4.5135
FS	5.3116	1.7677	0.6623	0.7891	5.1089	4.2363	1.5138	1.5189	4.6061	1.3468	1.8862	1.0746
OT1	53.4002	9.8925	4.8811	3.1433	41.7603	12.9649	11.4613	5.9788	46.8073	5.8326	19.0180	3.7379
OT2	33.2349	8.0965	1.0813	0.7594	27.0177	12.1266	5.0458	2.9923	37.0112	7.6201	9.7313	2.0686
OT3	36.8977	10.9184	1.7300	1.2794	30.7616	13.3741	7.4426	3.9665	40.6874	8.0532	12.5425	2.6879
GPi	5.2711	2.5376	0.7839	0.9097	5.6766	6.3583	1.0813	1.1027	5.6333	0.7904	2.7151	0.7577
SI	13.0291	2.0013	1.8922	1.6048	8.8392	4.1668	3.0893	2.3614	11.7640	1.3760	5.8628	1.1866
MA	17.1513	2.4959	0.9461	1.0006	12.2722	4.8060	2.6722	2.2618	14.5536	1.3707	4.8536	1.2190
LD	41.2362	8.0684	1.7976	2.7855	32.3294	17.6326	3.3055	3.9751	47.0452	5.6750	9.2267	4.9658
LP	37.8573	9.7851	1.4327	1.8564	28.7252	15.1844	3.5218	2.9853	42.7310	6.5053	8.7822	4.4790
PO	36.1948	10.1850	0.6488	1.0966	30.1549	17.2848	1.5138	1.7613	38.1465	5.5012	4.8296	2.6639
RT	16.7748	2.2915	1.1353	1.3014	10.1638	4.7991	1.3902	1.4870	11.8613	1.1051	2.8353	1.2302
VPL	30.1823	6.6686	0.1622	0.3790	18.1410	12.2551	0.3089	0.4299	28.9559	5.8128	1.8021	1.1132
VPM	31.3968	10.1782	0.0270	0.0765	24.2440	15.1153	0.2471	0.3625	35.6488	6.6105	1.4176	0.9798
SPFp	20.7195	4.5317	2.0814	2.2679	14.6930	6.3266	3.1820	2.6857	15.5484	2.1101	5.3222	1.7043
LHA	18.6516	2.7348	2.7031	2.2144	10.9326	4.4359	3.6145	2.8077	16.0782	3.7580	6.6076	1.1651
STN	17.0973	2.4591	0.5677	0.6832	12.4344	5.8493	2.1934	2.3280	13.3210	1.5162	3.5081	1.4737
ZI	14.1238	3.4411	1.1623	1.2816	9.2507	3.3182	2.2243	1.9965	10.1421	1.3191	3.7003	1.0396
IC	19.6788	2.3745	1.9463	1.8993	14.3686	5.3542	2.6568	2.0881	14.2293	2.3663	5.0458	0.9910
SCm	19.5436	3.7204	2.5139	2.2322	11.1489	3.9949	3.4291	2.4352	12.5209	1.4324	5.0939	1.1138
SCs	27.2475	4.1500	2.9734	2.5892	18.3813	6.5939	5.0201	3.7236	19.3544	1.6951	8.4097	2.1879
SNc	10.7584	2.0862	1.1623	1.1203	6.7278	2.9620	1.3902	1.2785	7.8174	0.9858	2.6431	0.7316
SNr	7.8931	1.4758	1.5408	1.2419	5.9108	2.4609	2.1625	1.6563	7.3958	1.1659	3.6883	0.6890
APN	18.1245	4.7659	0.8109	0.9373	10.8005	4.6237	1.8999	1.6157	15.4294	8.1540	3.4840	1.0837
NOT	21.2330	4.6735	1.5002	1.3707	11.7256	4.9307	3.0121	2.8989	17.6028	4.0440	5.1059	1.9744
PPN	11.7586	2.2172	1.1623	1.2972	7.5207	2.4698	1.8845	1.5429	8.3905	1.8653	3.4360	0.8476
PPT	17.4487	3.4060	1.3110	1.3609	10.6203	4.0191	2.6722	2.2721	13.1913	2.3474	4.3370	1.8762
RR	14.1238	1.8790	1.2975	1.3967	9.0224	2.6994	2.7649	1.9955	10.9531	2.4231	4.4451	0.8808
MRN	15.1375	2.6308	1.9192	1.7623	9.5871	3.2311	2.9039	2.0737	10.1205	1.1343	4.5413	1.0649
P	9.8394	1.5849	0.8380	0.9207	6.3674	2.6510	1.1173	1.1395	6.2929	1.0268	1.9463	0.7491
MY	12.7588	1.3774	1.2975	1.0531	7.5928	2.3921	1.2615	1.1719	8.9744	1.0905	2.7572	0.6715
IP	5.5955	1.5354	0.0270	0.0765	3.6763	1.4222	0.1236	0.1156	4.2926	0.7209	0.4085	0.1691
ANcr2gr	10.5692	1.3662	0.0865	0.1184	14.3961	2.7921	2.5301	1.5474	17.0477	1.1699	6.0241	1.2956
ANcr2mo	16.3539	2.4437	0.8218	1.0416	15.1015	3.2865	2.7392	2.3820	19.8770	3.0463	9.3528	2.0739
CENT3gr	10.5692	1.7774	0.1236	0.1701	14.8942	4.4170	1.9463	1.7657	18.8246	1.5772	5.6585	1.7568
CENT3mo	14.6278	1.6944	1.0002	1.1784	15.0294	4.5287	2.1934	1.7982	18.6299	2.3425	7.3285	1.6635
CUL4,5gr	11.0288	1.3026	0.1622	0.1917	15.7262	4.4276	2.3479	2.1604	20.5221	1.5340	6.6317	1.5367
CUL4,5mo	14.8942	1.4411	1.0542	1.2147	14.8852	3.7048	2.3479	1.8537	19.3760	2.3649	8.0553	1.8267
SIMgr	10.7990	1.4763	0.0865	0.1184	16.5895	2.4899	3.8493	2.9548	18.3813	2.3858	7.5282	1.4598
SIMmo	15.6376	2.2790	0.9191	1.0649	12.9930	1.5838	2.9194	2.1589	16.6242	1.9357	7.8210	1.0805
PRMgr	11.1098	1.0056	0.0865	0.1184	15.8583	2.1783	2.7248	1.7000	18.4353	1.2342	7.2083	1.7550
PRMmo	17.7595	1.9044	0.9083	1.1884	13.5697	7.3976	3.1717	3.0378	19.8229	3.6537	10.7044	2.0468
COPYgr	10.9341	0.8038	0.0865	0.1184	13.1604	4.0580	2.2706	1.5544	16.3114	1.7957	5.9685	1.2001
COPYmo	16.8945	1.6242	0.9515	1.1605	14.5505	4.0605	2.8113	3.9757	19.2771	2.3405	9.9475	1.4982

	PSD95 puncta intensity (AU)											
	3W_Day0		3W_Day7		3M_Day0		3M_Day7		18M_Day0		18M_Day7	
Abbreviation	MEAN	SD	MEAN	SD	MEAN	SD	MEAN	SD	MEAN	SD	MEAN	SD
ORB1	2.0E+10	2.7E+09	3.8E+09	2.1E+09	2.0E+10	7.9E+09	8.3E+09	3.4E+09	2.1E+10	4.4E+09	8.8E+09	1.9E+09
ORB2-3	4.0E+10	6.6E+09	4.6E+09	3.1E+09	3.5E+10	1.4E+10	1.2E+10	4.4E+09	3.8E+10	4.5E+09	1.4E+10	3.3E+09
ORB5	2.9E+10	4.9E+09	2.4E+09	1.8E+09	2.6E+10	1.2E+10	7.2E+09	3.6E+09	3.4E+10	5.9E+09	1.1E+10	2.5E+09
ORB6a	1.9E+10	3.7E+09	1.1E+09	9.7E+08	1.8E+10	8.2E+09	4.0E+09	2.5E+09	2.3E+10	3.8E+09	5.6E+09	1.5E+09
ORB6b	1.3E+09	4.1E+08	6.4E+07	5.6E+07	1.7E+09	9.9E+08	2.9E+08	2.3E+08	1.1E+09	3.7E+08	1.7E+08	8.3E+07
FRP1	3.9E+09	6.4E+08	7.4E+08	3.7E+08	3.6E+09	1.9E+09	1.7E+09	8.3E+08	4.4E+09	9.2E+08	1.9E+09	4.8E+08
FRP2-3	4.6E+09	9.7E+08	6.0E+08	3.7E+08	4.5E+09	2.1E+09	1.8E+09	8.3E+08	5.2E+09	1.0E+09	1.9E+09	4.0E+08
MO1	3.3E+10	6.8E+09	6.9E+09	3.3E+09	3.8E+10	1.4E+10	1.7E+10	7.0E+09	4.1E+10	5.8E+09	1.8E+10	3.4E+09
MO2-3	8.9E+10	1.7E+10	1.2E+10	7.4E+09	8.4E+10	3.3E+10	3.2E+10	1.4E+10	9.1E+10	1.2E+10	3.5E+10	6.3E+09
MO5	7.5E+10	1.6E+10	6.5E+09	5.2E+09	6.6E+10	2.8E+10	2.0E+10	1.0E+10	7.4E+10	7.8E+09	2.5E+10	5.5E+09
MO6a	1.4E+10	3.6E+09	5.0E+08	4.5E+08	1.4E+10	7.2E+09	3.1E+09	2.0E+09	1.4E+10	1.8E+09	3.0E+09	9.0E+08
MO6b	5.0E+08	1.5E+08	1.6E+07	1.5E+07	1.5E+09	1.2E+09	2.9E+08	2.4E+08	3.9E+08	1.4E+08	7.8E+07	5.0E+07
SS1	1.9E+10	3.1E+09	3.8E+09	1.9E+09	2.1E+10	7.9E+09	7.5E+09	4.7E+09	2.4E+10	2.3E+09	9.8E+09	2.3E+09
SS2-3	4.7E+10	9.5E+09	6.0E+09	4.2E+09	4.4E+10	1.4E+10	1.3E+10	7.6E+09	4.6E+10	4.7E+09	1.6E+10	3.4E+09
SS4	1.5E+10	2.8E+09	1.6E+09	1.1E+09	1.3E+10	4.8E+09	3.0E+09	2.0E+09	1.4E+10	1.3E+09	4.6E+09	1.3E+09
SS5	4.0E+10	7.8E+09	3.0E+09	2.7E+09	3.6E+10	1.3E+10	7.6E+09	4.9E+09	4.3E+10	4.1E+09	1.3E+10	3.3E+09
SS6a	1.2E+10	2.4E+09	3.7E+08	4.1E+08	1.3E+10	6.4E+09	2.2E+09	1.7E+09	1.2E+10	2.1E+09	2.8E+09	9.2E+08
SS6b	3.4E+08	8.4E+07	8.8E+06	1.0E+07	9.7E+08	9.4E+08	1.2E+08	1.1E+08	3.3E+08	1.4E+08	7.5E+07	5.1E+07
PTLp1	3.5E+09	6.4E+08	6.6E+08	3.4E+08	3.7E+09	1.8E+09	1.3E+09	8.1E+08	3.6E+09	7.1E+08	1.7E+09	4.4E+08
PTLp2-3	5.8E+09	9.6E+08	8.3E+08	5.8E+08	5.6E+09	1.6E+09	1.9E+09	1.1E+09	6.2E+09	7.7E+08	2.1E+09	4.6E+08
PTLp4	1.7E+09	4.3E+08	1.8E+08	1.3E+08	1.5E+09	4.0E+08	4.2E+08	2.8E+08	1.8E+09	2.1E+08	5.7E+08	1.5E+08
PTLp5	4.0E+09	8.7E+08	3.3E+08	2.7E+08	3.7E+09	8.6E+08	8.8E+08	5.8E+08	4.8E+09	4.6E+08	1.3E+09	3.3E+08
PTLp6a	1.3E+09	3.3E+08	5.9E+07	5.6E+07	1.4E+09	6.4E+08	3.0E+08	2.3E+08	1.5E+09	2.8E+08	3.4E+08	1.1E+08
PTLp6b	4.0E+07	2.1E+07	1.2E+06	1.4E+06	1.1E+08	9.7E+07	2.0E+07	1.9E+07	4.7E+07	3.5E+07	1.0E+07	5.9E+06
VIS1	2.5E+10	5.0E+09	4.9E+09	3.0E+09	2.6E+10	6.7E+09	8.6E+09	4.2E+09	2.8E+10	4.2E+09	1.1E+10	2.5E+09
VIS2-3	4.4E+10	1.0E+10	5.3E+09	4.4E+09	4.0E+10	1.7E+10	1.5E+10	7.4E+09	4.7E+10	9.2E+09	1.5E+10	2.7E+09
VIS4	1.7E+10	4.1E+09	1.7E+09	1.4E+09	1.4E+10	5.7E+09	4.4E+09	2.7E+09	1.7E+10	2.4E+09	5.1E+09	9.5E+08
VIS5	3.1E+10	7.3E+09	2.2E+09	2.0E+09	2.9E+10	8.4E+09	7.6E+09	4.8E+09	3.7E+10	5.9E+09	1.1E+10	2.0E+09
VIS6a	1.1E+10	2.7E+09	3.5E+08	3.6E+08	1.2E+10	3.4E+09	2.5E+09	1.9E+09	1.5E+10	2.8E+09	3.2E+09	9.0E+08
VIS6b	9.8E+08	3.8E+08	3.1E+07	2.9E+07	1.4E+09	7.6E+08	3.2E+08	3.2E+08	1.4E+09	2.3E+08	2.6E+08	1.1E+08
RSPd1	1.6E+09	6.1E+08	1.7E+08	1.3E+08	1.4E+09	6.1E+08	4.4E+08	2.9E+08	1.6E+09	6.7E+08	4.8E+08	1.6E+08
RSPd2-3	4.8E+09	1.1E+09	4.3E+08	4.0E+08	3.4E+09	1.5E+09	1.0E+09	6.6E+08	4.1E+09	1.2E+09	1.2E+09	2.7E+08
RSPd5	9.5E+08	3.1E+08	6.1E+07	5.4E+07	7.8E+08	3.4E+08	1.7E+08	1.1E+08	1.1E+09	2.9E+08	3.0E+08	7.4E+07
RSPv1	5.0E+09	2.2E+09	4.4E+08	3.3E+08	2.1E+09	8.9E+08	6.4E+08	5.6E+08	3.1E+09	1.2E+09	6.7E+08	2.1E+08
RSPv2-3	3.2E+09	1.4E+09	1.4E+08	1.3E+08	1.2E+09	5.5E+08	2.3E+08	2.4E+08	2.0E+09	4.9E+08	3.5E+08	9.5E+07
RSPv5	4.0E+09	1.7E+09	2.8E+08	2.6E+08	2.4E+09	1.2E+09	4.7E+08	4.2E+08	2.9E+09	5.7E+08	7.1E+08	2.0E+08
RSPv6a	2.4E+09	7.0E+08	1.1E+08	9.8E+07	2.1E+09	1.1E+09	3.1E+08	2.9E+08	2.3E+09	5.0E+08	5.0E+08	2.0E+08
MOBgl	4.3E+09	1.2E+09	2.3E+07	1.7E+07	5.7E+09	4.7E+09	6.2E+07	3.8E+07	1.0E+10	4.8E+09	4.2E+08	1.8E+08
MOBopl	1.2E+10	3.7E+09	5.6E+07	4.6E+07	1.6E+10	1.3E+10	1.4E+08	1.1E+08	2.8E+10	8.9E+09	1.1E+09	6.6E+08
MOBmi	1.4E+09	4.8E+08	1.2E+07	1.1E+07	1.5E+09	1.1E+09	2.0E+07	1.9E+07	2.8E+09	6.2E+08	1.8E+08	8.6E+07
MOBipl	1.6E+09	4.5E+08	1.5E+07	1.4E+07	2.1E+09	1.5E+09	2.5E+07	2.4E+07	3.5E+09	1.1E+09	2.0E+08	9.5E+07
MOBgr	4.2E+09	3.0E+09	7.0E+07	9.6E+07	5.3E+09	2.6E+09	9.1E+07	1.6E+08	9.6E+09	7.5E+09	1.0E+09	7.6E+08
AON1	1.7E+10	6.0E+09	9.0E+08	5.1E+08	2.5E+10	1.4E+10	4.7E+09	3.7E+09	2.2E+10	1.3E+10	7.7E+09	3.6E+09
AON2	9.3E+09	2.5E+09	3.7E+08	4.1E+08	1.7E+10	9.4E+09	1.9E+09	1.7E+09	9.5E+09	4.6E+09	3.6E+09	2.4E+09
PIR1	8.3E+09	1.3E+09	3.4E+08	2.0E+08	6.6E+09	4.2E+09	9.5E+08	6.2E+08	9.8E+09	1.3E+09	1.7E+09	8.9E+08
PIR2	5.4E+09	5.5E+08	9.7E+07	8.0E+07	4.1E+09	2.6E+09	3.9E+08	2.8E+08	6.7E+09	1.4E+09	1.1E+09	5.1E+08
PIR3	3.0E+09	6.1E+08	1.4E+08	1.4E+08	2.8E+09	1.8E+09	3.3E+08	2.4E+08	4.3E+09	8.7E+08	1.1E+09	6.3E+08
CA1so	1.3E+10	3.7E+09	5.3E+08	5.9E+08	1.2E+10	5.1E+09	2.7E+09	2.0E+09	1.8E+10	2.1E+09	4.8E+09	1.3E+09
CA1sp	1.8E+09	5.4E+08	7.9E+07	9.3E+07	1.8E+09	8.9E+08	3.7E+08	2.7E+08	2.5E+09	3.1E+08	5.9E+08	2.3E+08
CA1sr	2.1E+10	5.1E+09	2.0E+09	1.7E+09	2.0E+10	8.5E+09	5.5E+09	3.5E+09	2.7E+10	2.4E+09	9.5E+09	2.2E+09
CA1slm	1.2E+10	1.9E+09	1.4E+09	1.3E+09	7.9E+09	3.7E+09	2.0E+09	1.6E+09	1.0E+10	9.9E+08	3.2E+09	8.0E+08
CA2so	6.0E+08	2.8E+08	2.1E+06	2.9E+06	5.9E+08	3.8E+08	1.2E+07	1.2E+07	9.4E+08	2.5E+08	2.8E+07	1.6E+07
CA2sp	8.0E+07	3.2E+07	1.1E+06	1.8E+06	7.7E+07	6.2E+07	3.9E+06	4.2E+06	1.2E+08	4.7E+07	2.7E+07	1.8E+07
CA2sr	7.7E+08	3.3E+08	6.7E+06	9.1E+06	6.5E+08	4.3E+08	3.2E+07	3.5E+07	1.1E+09	2.1E+08	5.5E+07	3.4E+07
CA2slm	7.6E+08	1.8E+08	2.5E+06	4.0E+06	9.0E+08	6.2E+08	1.3E+07	1.5E+07	9.9E+08	2.0E+08	2.4E+07	2.3E+07
CA3so	2.1E+09	9.1E+08	1.4E+07	2.5E+07	1.7E+09	1.0E+09	1.3E+08	1.2E+08	3.1E+09	9.2E+08	2.6E+08	1.7E+08
CA3sp	1.0E+09	3.5E+08	4.2E+06	7.0E+06	1.1E+09	7.1E+08	6.1E+07	6.5E+07	1.5E+09	4.1E+08	1.9E+08	1.1E+08
CA3sr	2.9E+09	1.1E+09	2.7E+07	3.6E+07	2.1E+09	1.1E+09	2.1E+08	2.1E+08	4.5E+09	1.0E+09	4.8E+08	3.3E+08
CA3slm	5.0E+08	2.1E+08	6.0E+06	1.0E+07	4.2E+08	2.4E+08	3.3E+07	3.8E+07	6.9E+08	2.5E+08	5.4E+07	3.0E+07
DG-mo	2.0E+10	6.7E+09	1.9E+08	2.1E+08	2.1E+10	1.1E+10	1.4E+09	1.1E+09	3.3E+10	5.9E+09	3.7E+09	1.6E+09

DG-po	1.3E+09	5.0E+08	1.1E+07	1.6E+07	1.1E+09	5.8E+08	8.8E+07	8.4E+07	1.7E+09	3.3E+08	2.2E+08	1.4E+08
DG-sg	6.5E+08	3.7E+08	3.1E+06	3.7E+06	1.0E+09	6.5E+08	4.4E+07	3.9E+07	1.7E+09	3.3E+08	1.7E+08	1.1E+08
SUB	1.2E+10	3.1E+09	1.3E+09	1.0E+09	1.2E+10	4.4E+09	3.7E+09	2.0E+09	1.6E+10	3.3E+09	5.6E+09	9.1E+08
CLA	4.2E+09	1.2E+09	2.6E+08	2.0E+08	5.1E+09	2.5E+09	9.1E+08	6.5E+08	4.8E+09	1.6E+09	1.3E+09	4.6E+08
EPd	5.8E+09	1.2E+09	2.7E+08	2.1E+08	5.0E+09	2.8E+09	8.2E+08	5.4E+08	7.7E+09	1.7E+09	1.3E+09	3.6E+08
CP	1.3E+11	3.0E+10	9.0E+09	7.4E+09	1.3E+11	5.8E+10	2.7E+10	1.7E+10	1.7E+11	2.5E+10	3.7E+10	1.2E+10
ACB	5.5E+10	8.2E+09	3.1E+09	2.3E+09	6.2E+10	3.3E+10	1.3E+10	9.4E+09	7.4E+10	1.2E+10	1.8E+10	5.4E+09
FS	2.7E+08	8.1E+07	2.4E+07	2.2E+07	2.7E+08	1.9E+08	8.1E+07	7.5E+07	4.5E+08	2.1E+08	1.3E+08	7.2E+07
OT1	6.1E+09	1.4E+09	3.7E+08	2.2E+08	7.8E+09	5.9E+09	1.4E+09	8.9E+08	1.2E+10	2.8E+09	2.7E+09	3.5E+08
OT2	6.1E+09	2.1E+09	2.2E+08	1.4E+08	5.5E+09	2.9E+09	8.7E+08	5.2E+08	1.1E+10	2.5E+09	1.8E+09	5.3E+08
OT3	1.0E+10	3.3E+09	3.8E+08	3.1E+08	6.6E+09	3.7E+09	1.2E+09	6.4E+08	1.1E+10	2.1E+09	2.4E+09	6.2E+08
GPi	1.3E+09	6.1E+08	1.1E+08	1.1E+08	7.3E+08	4.3E+08	1.5E+08	1.6E+08	2.0E+09	6.4E+08	5.6E+08	2.2E+08
SI	8.2E+09	2.1E+09	6.3E+08	5.1E+08	6.0E+09	3.8E+09	1.6E+09	1.3E+09	9.7E+09	1.9E+09	3.0E+09	7.8E+08
MA	1.5E+09	2.8E+08	6.0E+07	6.9E+07	1.2E+09	7.3E+08	1.6E+08	1.4E+08	2.0E+09	5.2E+08	4.4E+08	1.5E+08
LD	5.3E+09	1.6E+09	1.3E+08	2.0E+08	4.9E+09	3.5E+09	2.6E+08	2.7E+08	6.3E+09	1.6E+09	8.3E+08	4.4E+08
LP	8.1E+09	4.3E+09	1.7E+08	1.6E+08	4.3E+09	2.8E+09	5.7E+08	4.9E+08	7.9E+09	2.4E+09	1.1E+09	7.6E+08
PO	1.5E+10	5.5E+09	2.3E+08	3.5E+08	1.5E+10	9.8E+09	6.2E+08	6.6E+08	1.7E+10	3.5E+09	1.7E+09	1.1E+09
RT	5.1E+09	1.2E+09	1.6E+08	1.8E+08	2.6E+09	1.6E+09	2.8E+08	2.9E+08	3.1E+09	6.0E+08	5.0E+08	2.3E+08
VPL	8.5E+09	2.1E+09	4.1E+07	6.3E+07	5.1E+09	3.8E+09	1.5E+08	1.6E+08	1.2E+10	4.0E+09	6.3E+08	4.1E+08
VPM	1.3E+10	5.4E+09	3.9E+07	5.1E+07	1.1E+10	7.1E+09	1.5E+08	2.0E+08	1.4E+10	3.4E+09	6.2E+08	3.7E+08
SPFp	2.1E+09	9.1E+08	1.3E+08	1.4E+08	1.8E+09	8.8E+08	2.6E+08	2.1E+08	2.0E+09	7.9E+08	4.6E+08	1.6E+08
LHA	1.2E+10	3.0E+09	1.1E+09	8.7E+08	8.3E+09	4.1E+09	2.3E+09	1.9E+09	1.4E+10	3.0E+09	3.6E+09	8.6E+08
STN	1.1E+09	3.0E+08	3.2E+07	3.6E+07	1.2E+09	8.2E+08	1.0E+08	1.0E+08	1.5E+09	3.8E+08	2.9E+08	1.5E+08
ZI	3.8E+09	1.2E+09	2.0E+08	1.9E+08	3.9E+09	2.7E+09	7.3E+08	7.3E+08	4.4E+09	1.2E+09	1.1E+09	4.5E+08
IC	2.2E+10	8.6E+09	1.3E+09	1.2E+09	2.0E+10	8.5E+09	2.6E+09	1.9E+09	1.8E+10	5.6E+09	4.8E+09	1.3E+09
SCm	7.4E+09	2.0E+09	8.2E+08	8.7E+08	7.8E+09	4.5E+09	1.3E+09	9.8E+08	9.1E+09	2.7E+09	2.7E+09	7.4E+08
SCs	5.6E+09	1.8E+09	6.1E+08	6.7E+08	8.5E+09	4.9E+09	1.1E+09	9.1E+08	8.5E+09	3.7E+09	2.5E+09	7.9E+08
SNc	1.8E+09	7.7E+08	1.3E+08	1.2E+08	9.0E+08	4.4E+08	1.6E+08	1.4E+08	1.2E+09	4.2E+08	3.0E+08	1.6E+08
SNr	4.0E+09	1.1E+09	5.0E+08	4.2E+08	3.2E+09	1.6E+09	9.8E+08	7.7E+08	4.9E+09	1.2E+09	1.8E+09	3.4E+08
APN	1.2E+09	5.1E+08	5.2E+07	5.8E+07	1.8E+09	1.4E+09	1.4E+08	1.2E+08	1.9E+09	6.9E+08	3.7E+08	1.2E+08
NOT	5.3E+08	2.2E+08	3.3E+07	3.6E+07	3.2E+08	1.8E+08	4.2E+07	4.0E+07	3.8E+08	2.1E+08	1.1E+08	7.3E+07
PPN	1.4E+09	6.7E+08	1.1E+08	1.3E+08	7.3E+08	5.0E+08	1.1E+08	9.3E+07	1.5E+09	4.1E+08	4.0E+08	2.2E+08
PPT	4.4E+08	1.7E+08	3.5E+07	3.7E+07	3.8E+08	2.0E+08	5.2E+07	4.5E+07	4.0E+08	3.1E+08	8.8E+07	4.2E+07
RR	9.0E+08	3.2E+08	6.2E+07	7.1E+07	5.1E+08	2.6E+08	9.3E+07	6.7E+07	7.8E+08	2.9E+08	2.1E+08	1.1E+08
MRN	1.2E+10	4.6E+09	8.6E+08	7.9E+08	9.6E+09	5.3E+09	1.8E+09	1.4E+09	9.5E+09	2.4E+09	3.1E+09	1.1E+09
P	1.8E+10	3.1E+09	1.3E+09	1.1E+09	1.6E+10	9.1E+09	2.6E+09	2.4E+09	1.8E+10	4.8E+09	4.2E+09	1.0E+09
MY	5.3E+10	9.2E+09	3.3E+09	2.4E+09	3.5E+10	1.5E+10	4.3E+09	4.0E+09	5.5E+10	1.2E+10	1.1E+10	4.0E+09
IP	1.2E+09	3.1E+08	1.3E+07	1.3E+07	7.0E+08	3.4E+08	3.0E+07	2.1E+07	9.9E+08	2.2E+08	1.4E+08	5.7E+07
ANcr2gr	1.2E+09	4.3E+08	5.1E+06	6.7E+06	1.1E+09	3.3E+08	1.1E+08	7.1E+07	2.4E+09	1.2E+09	3.7E+08	9.9E+07
ANcr2mo	1.8E+09	6.8E+08	4.1E+07	4.9E+07	1.3E+09	4.9E+08	1.7E+08	1.7E+08	2.8E+09	1.4E+09	5.5E+08	1.3E+08
CENT3gr	7.8E+08	3.5E+08	7.2E+06	1.1E+07	1.5E+09	9.9E+08	8.5E+07	9.8E+07	1.7E+09	8.9E+08	2.6E+08	7.9E+07
CENT3mo	9.7E+08	1.4E+08	4.8E+07	6.0E+07	1.7E+09	8.4E+08	1.2E+08	1.0E+08	2.2E+09	8.7E+08	3.7E+08	1.4E+08
CUL4,5gr	2.7E+09	5.3E+08	2.0E+07	2.1E+07	4.3E+09	2.2E+09	3.2E+08	3.0E+08	5.1E+09	1.1E+09	1.1E+09	4.0E+08
CUL4,5mo	3.6E+09	4.9E+08	1.3E+08	1.4E+08	4.1E+09	1.9E+09	3.6E+08	3.1E+08	5.0E+09	1.4E+09	1.2E+09	3.9E+08
SIMgr	3.7E+09	1.4E+09	1.9E+07	2.4E+07	4.4E+09	1.5E+09	7.4E+08	5.7E+08	6.9E+09	1.9E+09	1.6E+09	4.2E+08
SIMmo	4.5E+09	1.6E+09	1.5E+08	1.6E+08	4.8E+09	1.2E+09	7.5E+08	6.0E+08	7.4E+09	1.5E+09	1.9E+09	4.6E+08
PRMgr	2.0E+09	6.4E+08	9.8E+06	1.3E+07	2.1E+09	3.8E+08	2.0E+08	1.3E+08	4.2E+09	1.5E+09	7.6E+08	2.9E+08
PRMmo	2.9E+09	6.7E+08	8.1E+07	9.5E+07	2.4E+09	1.0E+09	3.4E+08	3.3E+08	5.0E+09	1.4E+09	1.1E+09	3.6E+08
COPYgr	3.7E+09	3.0E+08	2.2E+07	2.6E+07	3.9E+09	2.7E+09	4.4E+08	3.2E+08	5.6E+09	1.9E+09	1.2E+09	4.8E+08
COPYmo	4.0E+09	4.8E+08	1.1E+08	1.1E+08	3.8E+09	2.3E+09	6.0E+08	8.5E+08	5.7E+09	1.9E+09	1.6E+09	4.6E+08